# Mechanical Properties and Microstructure of Large Steel Forgings for Applications in the Energy Sector

**Edgar Ivan Saldana Garza**

*A thesis submitted in partial fulfilment of the requirements for the degree of Doctor of Philosophy*

# Abstract

Due to its optimal balance of strength and toughness, AISI 8630M low alloy steel forgings are extensively used as structural components for subsea applications in the oil and gas energy sector. However, considering the high pressures and low temperatures conditions in deep water environments the oil and gas industry has continuously been demanding higher reliability levels on the structural integrity of large steel forgings in order to avoid in-service premature failures. In particular, special attention has been given to the CTOD fracture toughness as a critical parameter for structural design.  Heat treatment is the last stage in the manufacturing sequence of large forgings and to certain extent, defines the metallurgical characteristics of final component. The cooling rate during industrial quenching treatment represents one of the most important processing parameters controlling the microstructure before tempering treatment.

The research programme involved industrial-scale experimental heat treatments in which large-scale forged segments with two different cross-sections (100 and 250 mm) were separately subjected to water, aqueous polymer solution and vegetable oil quenching and then tempered at 590°C, to evaluate the influence of cooling rate on the microstructure and mechanical properties produced under industrial conditions. Tensile, CVN and CTOD fracture toughness properties were measured at RT, -30 °C and 0°C respectively as per specification requirements. Microstructural evolution and fracture surfaces were evaluated by high resolution scanning electron microscopy. A CCT diagram was constructed by means of quenching dilatometry in order to validate the microstructural changes produced during industrial quenching.

In summary, the present investigation, showed that irrespective of the cross section, the faster, intermediate, and slower cooling times between 800°C and 500°C ($\lambda$, t $_{8/5}$) were obtained by water, polymer and vegetable oil respectively. Kinematic viscosity may be the main variable controlling the cooling performance of the different cooling media evaluated due to changes in the thermophysical properties of the quenchants. In addition, the predominant microstructures for the different thickness-quenchant conditions were found to be associated with mixtures of tempered bainite and tempered martensite. This was evidenced by the fact that the majority of

the industrial cooling curves fell within a similar microstructural region of the CCT (0.03 - 1˚C/s) dilatometric diagram which consisted of mixtures of martensite and bainite.

Accordingly, the mechanical properties evaluated were similar among the different thickness-quenchant conditions investigated. In this sense, all conditions evaluated showed strength and impact toughness properties well above the material specification limit for the selected forged component. It can be argued that the strength and impact toughness are controlled by changes in the distribution and size of carbide precipitates and packet substructure associated with the different fractions of tempered martensite and tempered bainite generated by changes in cooling rate. Accordingly, the higher strength and impact toughness values were observed at mixtures of tempered martensite (TM) and tempered bainite (TB) with proportions of 85% (TM) -15% (TB). The above due to partitioning effect of the acicular lower bainite on the austenitic grains in association with tempered martensite. Regarding the fracture toughness assessment, it can be argued that the yield strength variation between the selected specimens, along with the carbide size variation observed between tempered martensite and tempered bainite, were not large enough to induce significant changes leading to negligible variation in the final CTOD properties.

Construction of CCT diagrams by means of quenching dilatometry has proven to be an effective technique to predict the microstructures industrially produced at the central part of large forgings, although the unavoidable effect of macro segregation must be considered for comprehensive analyses. Finally, in spite of the fact that vegetable oil provided slow quench rate compared with those of water or aqueous polymer quenchants, it is true that the mechanical properties produced by this bio-quenchant were similar to those produced by water and polymer quenching. As such, this finding indicates the possibility of implementing vegetable oil as an alternative quenchant in material specifications used in the production of large scale forgings made of low alloy steels, in particular when a balance between mechanical properties, dimensional stability (distortion) and reduced crack susceptibility is desired after quenching and tempering.

# Acknowledgments

*"Yo no escribo para agradar ni para desagradar. Yo escribo para desasosegar"*

*José Saramago, 2009*

# Publications

- "Effect of Different Quench Media on the Microstructure and Mechanical Properties of Large-scale Low-Alloy Steel Forgings" Presented at the 16th International Metal Forming Conference". 18 – 21 September 2016, Krakow, Poland. DOI: 10.4028/www.scientific.net/KEM.716.270

- "Influence of Heat Treatment on Fracture Toughness of Structural Forgings" Presented at the 3rd Mediterranean Conference on Heat Treatment and Surface Engineering". 26 – 28 September 2016, Portorož, Slovenia

# Conferences

- Speaker: "Effect of Heat Treatment Parameters on Mechanical Properties of Low Alloy Steels" Presented at the Colloquium Innova Quench: Bridging the gap between fundamentals and applications in heat treatment, 4th November 2015, Monterrey, Nuevo Leon Mexico.

- Speaker: "Microstructure and Fracture Toughness of Critical Forgings for Subsea Applications" Presented at the National Student Conference in Metallic Materials". 29th June 2016, Sheffield, United Kingdom.

- Speaker: "Effect of Different Quench Media on the Microstructure and Mechanical Properties of Large-scale Low-Alloy Steel Forgings" Presented at the 16th International Metal Forming Conference". 18 – 21 September 2016, Krakow, Poland.

- Speaker "Influence of Heat Treatment on Fracture Toughness of Structural Forgings" Presented at the 3rd Mediterranean Conference on Heat Treatment and Surface Engineering". 26 – 28 September 2016, Portorož, Slovenia

.

# Contents

# List of Figures

# List of Tables

# Nomenclature

| | |
|---|---|
| $\gamma$ | Austenite |
| F | Ferrite |
| P | Pearlite |
| RA | Retained austenite |
| B | Bainite |
| M | Martensite |
| M/A | Martensite – Austenite constituent |
| FB | Featureless Bainite, |
| TLB | Tempered Lower Bainite, |
| TM | Tempered Martensite. |
| UB | Upper Bainite |
| LB | Lower Bainite |
| GB | Granular Bainite |
| PAGB | Prior Austenite Grain Boundaries |
| OEM | Original Equipment Manufacturers |
| UC | Upper Critical Cooling Rate |
| LC | Lower Critical Cooling Rate |
| $D_{cr}$ | Critical Diameter |
| PAG | Poly alkylene Glycol |
| PVP | Poly vinyl pyrrolidone (PVP) |
| $\lambda$ ($t_{8/5}$) | Cooling Parameter (s) |
| $CR_{Max}$ | Maximum Cooling Rate |
| $T_{CRMax}$ | Temperature at Maximum Cooling Rate |
| Bcc | Body centre cubic |
| Fcc | Face centre cubic |
| Ms | Martensite-start temperature (ºC) |
| Mf | Martensite-finish temperature (ºC) |
| CCT | Continuous cooling Transformation |
| Ac1 | Austenite start temperature on heating (ºC) |
| Ac3 | Austenite completion temperature on heating (ºC) |
| q | Heat Flow |

| | |
|---|---|
| K | Thermal conductivity (J/s m °C) |
| A | Cross sectional area ($m^2$) |
| $\Delta T$ | Thermal gradient (T2 – T1, °C) |
| L | Thickness (m) |
| H | hardness |
| R | Ideal Gas Constant |
| Q | Activation Energy |
| μm | Microns |
| Temperature | (ºC or K) |
| S | second |
| MPa | Megapascal |
| wt. % | Weight percent |
| Tons | (metric tons) |
| YS ($\sigma_{ys}$) | Yield Strength at 0.2% proof strength (MPa) |
| UTS | Ultimate Tensile Strength (MPa) |
| CVN | Charpy V-Notch |
| CTOD ($\delta$) | Cracking Tip Opening Displacement |
| DIC | Digital Image Correlation |
| XRD | X-ray Diffraction |
| EBSD | Electron backscatter diffraction |
| OR | Orientation Relationship |
| SE | Secondary Electrons |
| SEM | Scanning electron microscopy |
| TEM | Transmission Electron Microscopy |
| EDS | Energy Dispersive X-ray Spectroscopy |
| FEG | Field emission gun |
| $\delta_{el,BS}$ | Elastic Component |
| $\delta_{pl,BS}$ | Plastic Component |
| K | Stress Intensity Factor (SIF) |
| v | Poisson's ratio |
| E | Young's modulus |
| $r_{pl}$ | Plastic rotational factor |
| $V_{pl}$ | Plastic component of the clip gauge opening displacement |

| | |
|---|---|
| a | Crack Length |
| b | uncracked ligament width |
| Area | cross section area of inclusion |
| $\sigma_F$ | Fracture stress |
| $y_p$ | Effective work of fracture |
| C | size of the brittle nucleus |

# 1    Introduction

Steel continues to be a main element in the industrial development of the modern society. Industries such as the oil and gas, power generation and wind energy sectors, use steel due to its optimal combination of strength-toughness properties and low production costs. As illustrated in Figure: *1-1*, the offshore  industry uses low alloy steels for the fabrication of forged components for subsea applications due to the high pressures and low temperatures conditions in deep water environments [1].



Figure: 1-1 Schematic illustration of subsea system *[2]*.

However, as seen in Figure 1-2 the oil and gas exploration and production is continuously displaced to even more environmental challenging conditions such as ultra-deep waters and artic regions in order to satisfy the global energy demand [1, 3]. The aforementioned conditions have led the industry to design low alloy steel forged components with thicker walls to contain higher pressures in the critical components of the subsea systems [4].

The mechanical properties of low alloy steels are often governed by the chemical composition, geometry of the component, manufacturing route and the resultant microstructural features. One of the main concerns of thick-wall forgings is the microstructural heterogeneity developed through the thickness of the large-scale forging due to variations in the cooling rate along the geometry of the part during quenching treatment. The microstructural heterogeneity generated by the fluctuations in cooling rate can lead to non-uniform mechanical properties which in turn may affect the performance or functionality of the final component [5].
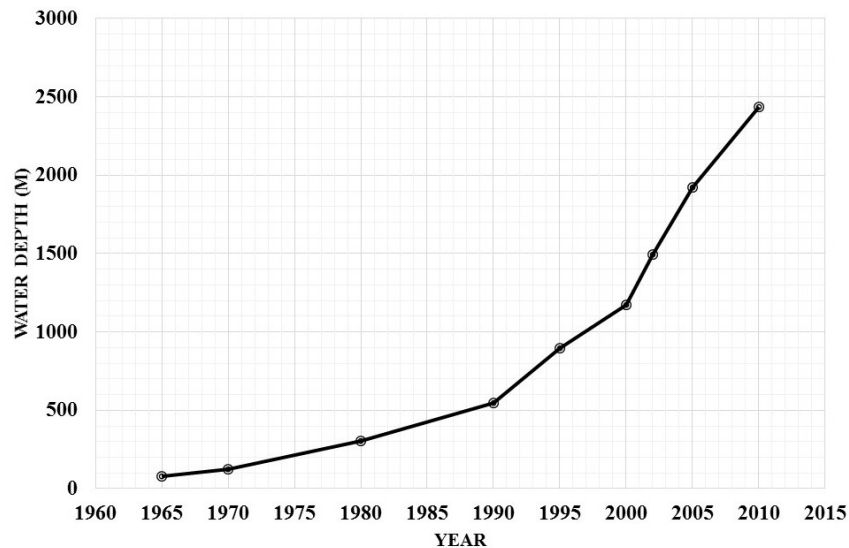
Figure 1-2: Increase in exploration and production of oil and gas in deep-waters in the Gulf of Mexico between 1960 and 2010 *[6]*.

The production of oil and gas from deep water wells provides technical challenges in the development of materials to provide safe and reliable service at reasonable cost. In this sense, large size forgings are required e.g. for blow-out preventers, subsea systems and connectors. They are usually made of alloy steel such as F22, 8630 and 4130 material grades. Nickel alloy weld overlay (grade 625) is applied on all process wetted areas to prevent corrosion.

Subsea flowlines are used for the transportation of crude oil and gas from subsea wells, manifolds, off-shore process facilities, loading buoys, subsea to beach, as well as re-injection of water and gas into the reservoir. Achieving successful tie-in and connection of subsea flowlines is a vital part of a subsea field development. Generally, these are vertical and horizontal tie-in systems.

Vertical connections are installed directly onto the receiving hub in one operation during tie-in. Since the Vertical Connection System does not require a pull-in capability, it simplifies the tool functions, provides a time efficient tie-in operation and reduce the length of Rigid Spools.
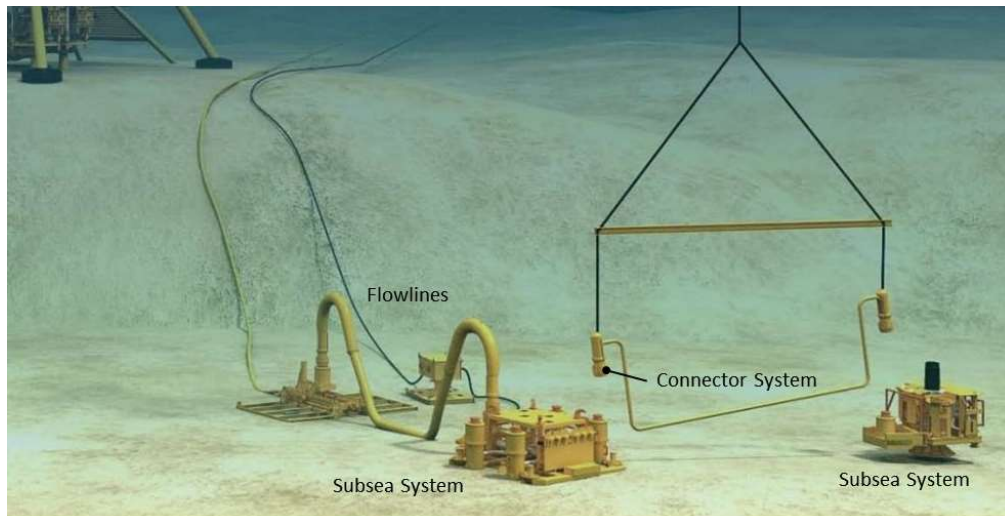
Figure 1-3: General overview of subsea and connection system *[7]*.

Stroking and connection is carried out by the Connector itself, or by the ROV operated Connector Actuation Tool (CAT) System. Factory adjusted reaction ring made of AISI 8630/8630 mod/1.6591 low alloy steel establishes precise, repeatable connector preload settings.

As mentioned previously, AISI 8630/8630 mod/1.6591, low alloy steel is frequently used by OEMs (Original Equipment Manufacturers) for the fabrication of structural components with high strength requirements. This material fully develops its mechanical properties by a combination of forging operations and heat treatment processes. The balance between strength and toughness for this steel is obtained by heat treatment cycles composed of normalizing, quenching and tempering treatments producing in consequence tempered martensitic or bainitic structures.
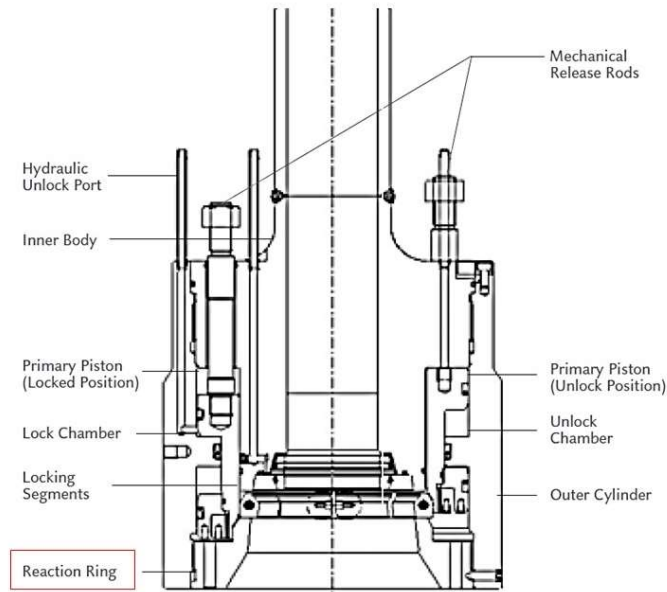
Figure 1-4: Schematic view of tie-in connection system including the reaction ring (AISI 8630M) component selected for the present study.

In general, the majority of international forgings suppliers are capable to produce thin wall forgings connectors in accordance with specifications for subsea equipment. However, the implementation of new designs including connectors with wall thicknesses greater than 100 mm and the implementation of new requirements such as CTOD (Cracking Tip Opening Displacement) fracture toughness testing, has hindered the production of thick- wall forgings within the specifications required by the oil and gas industry [8].

During the last years FRISA, and international forging company with facilities in Mexico and USA has been collaborating with major oil companies to produce large-scale connectors with a cost-benefit approach which involves increased service life of materials, restricted limits on mechanical properties and reduced production times. Additionally, these large-scale connectors are employed in subsea systems exposed to low temperatures and high pressures where a combination of high strength - high toughness is required in order to avoid in service failures. The company implemented different strategies to design robust manufacturing processes for large-scale forgings. These strategies covered modifications to chemical composition and steel-making parameters, changes in the forging-product design, and finally modifications in the cooling media employed on industrial quenching. During the evaluation stage of the different cooling media, vegetable oil, a non-conventional quenchant for large

forgings applications was used to validate its potential as replacement for established quenching media such as water an aqueous polymer. In spite of the fact that vegetable oil provides slow quench rates if compared with water or aqueous polymer quenchants, which are the most widely industrially accepted cooling media for large-scale forgings; vegetable oil was used as part of the modification strategies implemented by the company due to the following reasons: it is a relative low-cost quenchant that requires less bath maintenance in comparison with aqueous polymer. Additionally, with the increasing environmental regulations, vegetable oil, with its characteristics of high biodegradability has the potential to be used as an environmentally friendly quenchant for large scale forgings. Finally, the absence of film boiling stage during vegetable oil quenching may increase the cooling uniformity in large-scale forgings.

Although the results of the experimental forgings quenched in vegetable oil were satisfactory and within specification, the implementation of this bioquenchant as an accepted cooling media for critical forgings was not possible since the final user argued that there had been a lack of a thorough explanation of the specific causes that led to the aforementioned results including the metallurgical aspects and implications involved in using slow quenchants such as vegetable oil for large forgings. The unsuccessful implementation of an alternative quenchant for large-scale forgings, pointed out the need of the forging industry and major oil companies for systematic industrial research focused on the fundamental aspects of the manufacture process of large scale forgings.

The efficiency of quenching to achieve martensite or bainite is generally determined by a cooling curve testing where small (~12.7 mm diameter) standard probes usually made of Inconel are quenched to determine the cooling characteristics of commercial quenchants such as water, oils and polymer solutions [9]. However, as indicated by Kummar *et al*. [10] relevant quenching parameters such as steel chemical composition, phase transformations during cooling, and quenching tank agitation are not considered by these type of cooling curves testing since they are conducted under laboratory conditions. In this sense, it has been acknowledged [11] that a more suitable method to evaluate the relationships between cooling media, tank characteristics, and workpiece is to perform direct measurements of the cooling conditions during industrial quenching in a real workpiece. Consequently, this approach would allow to measure not only the cooling conditions inside a large forging but as well to evaluate the microstructure and mechanical properties developed after industrial quenching.

Furthermore, recently the forging company has focused its attention in the CTOD parameter since it has been difficult to identify the main manufacturing process variables controlling this property in large forgings. In addition, the company has struggled to develop correlations between CTOD parameter and CVN impact toughness. In this regard, Pous-Romero *et al.* [12] pointed the relevance of factors such as prior austenite grain size, tempering parameter and cooling rate variation on the strength and toughness of large scale forgings heat treated under industrial conditions. It is clear that a further understanding of the relationships between industrial heat treatment conditions, mechanical properties (strength, impact toughness and CTOD) and relevant microstructural features of large forgings is required in order to enable the development and production of large forgings that can comply with the string requirements of the offshore industry. The aims of the present research are:

- Determine the microstructures on relevant locations of large-scale forgings submitted to normalizing, quenching and tempering treatments under industrial conditions, and identify the main microstructural changes introduced in the large forgings due to modifications in the cooling conditions during quenching.

- Develop further understanding on the influence of industrial cooling rates and microstructure on the strength, impact toughness and CTOD properties of large-scale forgings industrially quenched in three different cooling media.

- Evaluate the effectiveness and implications of using Continuous Cooling transformation diagrams to predict the microstructures of large-scale forgings industrially heat treated.

The acquired knowledge obtained from this research is expected to be transmitted to the forging company to clarify the influence of industrial heat treatment conditions on the structural integrity of large forgings and as well to contribute to design robust heat treatments for subsea connectors. Finally, the results of this investigation are expected to contribute with the development of more realistic material specifications for subsea forgings considering the lack of knowledge of what can be achieved in terms of mechanical properties by using industrial heat treatment processes.

## 1.1 Thesis Structure

The structure of the thesis follows a coherent sequence necessary to develop a clear understanding of the broader context of the present research and its implications. Considering that this research work aimed to develop new technological processes, the literature review in Chapter 2, not only provides details of the scientific background of the project but also appraise the industrial and technological aspects involved in the manufacturing of large scale forging subjected to different quenching conditions. Relevant topics, such as heat transfer mechanisms during industrial quenching; phase transformations on both, continuous and exponential cooling, and the relationships between CTOD (Cracking Tip Opening Displacement) fracture toughness and key metallurgical aspects are covered in this section. Chapter 3, describes the production method of the experimental workpiece (large-scale forging segments) including relevant aspects of steel making, open-die forging, and ring rolling, machining and cutting operations involved in the manufacture of the part. The second section reports heat treatments carried out at industrial level to produce different cooling rates in large ring segments of AISI 8630M low alloy steel, whereas the third section describes the quenching dilatometric measurements carried out under laboratory conditions in order to assess the effect of cooling rate on the microstructure of AISI 8630M steel specimens. The last section provide information regarding the comprehensive mechanical testing and characterization plan conducted over the selected specimens.

In Chapter 4, the results of the quenching treatments conducted on three experimental ring segments separately quenched in water, aqueous polymer solution and vegetable oil, under industrial conditions are presented. By analysing the shape of the different cooling curves studied, it was possible to approximate the heat transfer stages taking place during quenching, such as vapour phase, nucleate boiling and convective heat transfer. In addition the main critical parameters such as the cooling time parameter ($\lambda$) and the maximum cooling rate (CRMax) were determined during the industrial quenching in an attempt to establish correlations with the microstructure and properties of the experimental ring segments. Finally the onset of the martensitic and bainitic transformations during industrial quenching were estimated by identifying the inflexions points in the cooling rates produced by the latent heat release.

In Chapter 5 the measured data obtained from the quenching dilatometer were used to determine the transformations temperatures for the different heating and cooling conditions which in combination with the microstructural characterisation allowed to build the continuous cooling transformation diagram for the selected material.

The effect of the different cooling rates on the mechanical properties and microstructures corresponding to the three segments quenched in water, polymer and vegetable oil after tempering treatment at 590°C for 10 hours are presented in Chapter 6. Finally a summary of the principal observations and economic impact of the research, and suggestions for future work are presented in Chapter 7.

# 2 Literature Review

## 2.1 Manufacturing Process of Large-Scale Forgings for the Oil and Gas Energy Sector

The production of large scale forgings is a complex manufacturing process which fundamentally involves steel-making, hot working, heat treatment and machining processes as illustrated in *Figure 2-1*. This complexity relies on the intrinsic dependence of the final mechanical properties of the forged component on the several processing parameters involved in the steel-making, hot working and heat treatment processes [12]. On this regard, forging companies require a strict control, monitoring and analysis of the relevant processing parameters in order to full-fill the requirements established by the offshore industry for the production of large-scale forgings. However, despite its relevance, the monitoring of processing parameters is not always feasible due to the difficulty to install measuring or recording devices either on the industrial equipment or directly in the component.
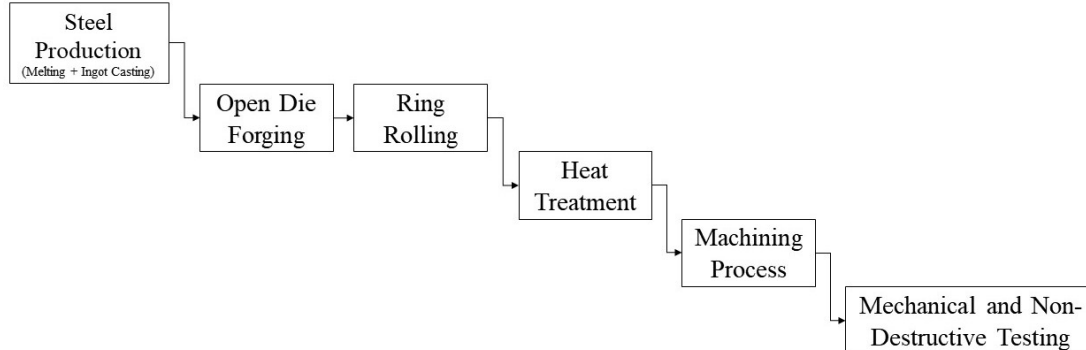


Figure 2-1: Typical manufacturing sequence for large scale forging connectors made of 8630 low alloy steel. (Courtesy of FRISA)

## 2.2  Steel Making

The steel making process constitutes a relevant part in the development and production of large scale forgings due to the fact that critical aspects such as non-metallic and segregation are generated during production of steel ingots.

Due to the higher solubility of oxygen in liquid iron the formation of non-metallic inclusions is inevitable in steelmaking process. On the other hand, Segregation refers, to the changes in chemical composition produced in liquid or solid phases during the solidification process.

Due to its detrimental effect on the hydrogen induced cracking and brittle fracture of low alloy steels, non-metallic inclusions and segregation are one the most important factors related to the steel making process [13, 14]. This section briefly describes the manufacturing process of steel ingots and the main processing parameters affecting the production high-quality ingots for the production of large forgings.

As seen in Figure 2-2, the steel making process starts by the melting different types of scrap in an electric arc furnace (EAF) with electrodes of different dimensions depending on the melting power input. Oxygen is injected to reduce carbon and phosphorus content during the scrap melting process in the EAF. During tapping of the furnace ladle, deoxidizers, fluxes and ferroalloys are added. In order to reduce the oxygen level, aluminium is added during tapping process to enable refining process. Once the tapping operation in the electric arc furnace is finished the raw liquid steel is moved to secondary steel making unit where the following operations are carried out:

- Full deslagging of the melt down slag
- Precipitation deoxidation with aluminium
- Start of arc-reheating and addition of new slag
- Alloying and superheating for vacuum treatment

The ladle is then moved to the injection-vacuum stations to carry out the following operations:

- Injection of calcium oxide (CaO) or calcium silicon (CaSi)
- Vacuum treatment with argon gas and induction stirring
- Final alloy trimming
- Temperature control

After finishing the vacuum degassing, the steel is bottom poured into the required ingot dimensions [15].



Figure 2-2:  Electric arc furnace located in the recently open melting shop of FRISA.
(Courtesy of FRISA)

In his work about the factors controlling the micro-cleanliness of bottom-poured ingots Manzo *et al*. [15]  established the main processing parameters involved in the steel making process of large low alloy steel ingots for forging applications:

- Hydrogen content
- Teeming temperature
- Teeming flux
- Teeming rate
- Hot-top design and volume
- Mold design
- Mold surface condition

- Refractory hollowware quality

- Argon shrouded teeming

- Ingot solidification time

- Hot transfer of ingots

- Ingot annealing

The section demonstrates that even a well understood and researched process such as steel making may still be challenging in particular when producing large ingots where the difficulty to control the main processing parameters at industrial-scale level is increased. However, as explained in the following section, it should be pointed out that subsequent processes such as open die forging and ring rolling might aid to reduce, until certain extent the detrimental effect of non-metallic inclusions in the mechanical properties of large forgings.

## 2.3 Hot Working (Forging and Rolling)

Hot working is regarded as a critical step in the manufacture of structural components [16]. The plastic deformation produced during hot working allows the obtention of the geometry of the component and a more homogeneous microstructure, that in combination with subsequent heat treatment define the final mechanical properties of the component. *Figure 2-3* illustrates the open die and ring rolling processes of critical components for subsea applications.
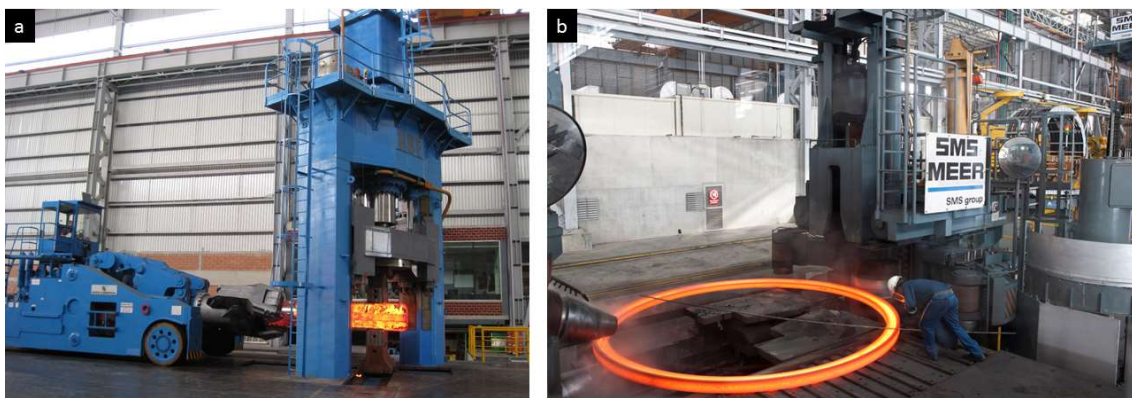


Figure 2-3: a) Open die and b) ring rolling processes of critical components for subsea applications (Courtesy of FRISA).

The grain microstructure of low alloy steels submitted to forging is dependent on the recovery, recrystallization and grain growth mechanisms taking place during (dynamic recrystallization) and after (static recrystallization) hot working process. In turn, these mechanisms are affected by key forging parameters such as degree of plastic deformation, temperature, time and design of deformation passes [17].

As seen in Figure 2-4, during hot working process, the heterogeneous grain structure of the ingot is refined and orientated in the direction of the main material flow. In addition, the plastic the deformation generated during hot working is responsible for the closure of internal voids related to the ingot solidification. Besides the enhancement in grain size uniformity and void closure, the plastic deformation as well contributes to the reduction of non-metallic inclusion by breaking them into smaller particles and redistribute them uniformly along the part [18]. Furthermore, high plastic deformation levels also contribute to reduce the thickness of segregated bands after hot working process [19].

However, when producing large forgings is not always possible to achieve high degrees of plastic deformation and internal penetration required to produce void closure and uniform microstructure [20]. Usually these issues are caused either by technological limitations on the hot working equipment or by cost constraints to acquire larger ingots.
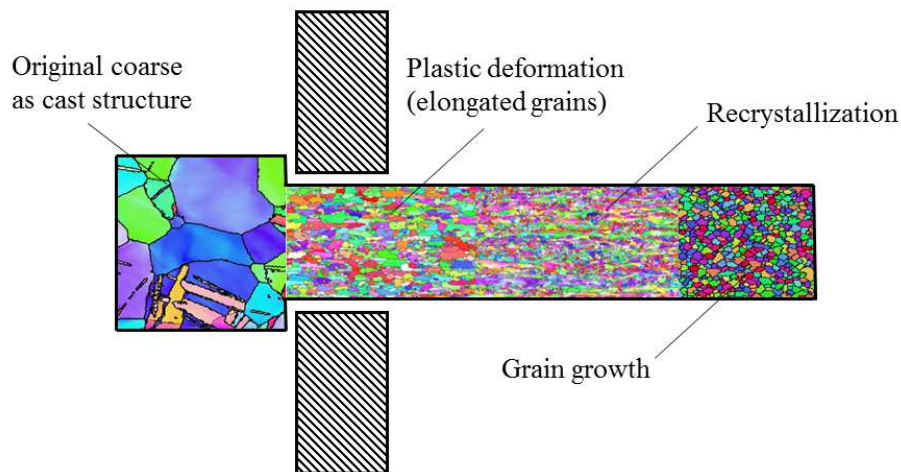


Figure 2-4: Schematic illustration of recrystallization and grain growth mechanisms taking place during open die forging process *[21]*.

The problem of penetration and plastic deformation inside large steel forgings was studied by Ali [22]. In this research, it is stated that the penetration of plastic deformation in 34CrNiMo6 steel large scale forgings is higher in the surface of the part and decreases with depth up the central zone, leading to heterogeneous grain size distribution along the part thickness producing large variation in the mechanical properties even after heat treatment.

Despite the improvement on its properties after hot working, large forgings cannot be used in the "as-forged" condition since the microstructure and mechanical properties are still not within the specification requirements for subsea applications. Accordingly, further processing is required in order to develop the bainitic and martensitic structures that provides the essential mechanical properties for subsea connectors.

## 2.4 Heat Treatment

Heat treatment is the last thermal process in the manufacturing sequence of large steel forgings that determines the final microstructure and mechanical properties of the component [23]. The design of heat treatment process consists in the definition of critical parameters such as of heating rate, temperatures, soaking times and cooling rates in order to achieve the desired microstructure and mechanical properties. These parameters have been widely researched over the last four decades, however with the continued development of new heat treatment technology including massive furnaces and quenching tanks to satisfy the demanding requirements of the offshore industry there is uncertainty in the forging industry to guarantee the mechanical properties of large scale forgings due to the potential microstructural variation associated to with heat treatment of large forgings.

### 2.4.1 Normalizing

There are three main concerns about the microstructure of large forgings after open-die forging and ring rolling operations. First, the grain flow is preferentially oriented depending on the severity of the plastic deformation on the longitudinal or transverse axis of the forging. This microstructural anisotropy results in different mechanical properties between the longitudinal or transverse orientations of the forging. Second, due the cooling rate variation experienced during cooling down process after hot working operations, a heterogeneous microstructure

could be formed along the wall-thickness of the forging leading in consequence to variation in the internal structure [24]. In this sense, normalizing treatment has the potential to reduce the heterogeneity and microstructural anisotropy developed after hot working due to its ability to homogenize and refine the structure of low alloy steels. Normalizing involves heating the material from to austenitic phase (face-centered cubic structure), holding it at austenitizing temperature until complete transformation is reached along the dimensions of the forging and finally cooled down in air to room temperature. In terms of microstructure, a ferritic-pearlitic microstructure is usually expected on large scale components after normalizing treatment [24].

As a result of the high forging temperatures (1100°C - 1250°C) employed during hot working operations, a coarse grain structure is produced in the part after forging process, however this coarse structure is in fact refined after normalizing process by using temperature between 900 and 950˚C. *Figure 2-5* shows the microstructural evolution of a EN355B low carbon steel flange before ("as-forged" condition) and after normalizing treatment. The grain refinement effect of normalizing treatment can be clearly seen.
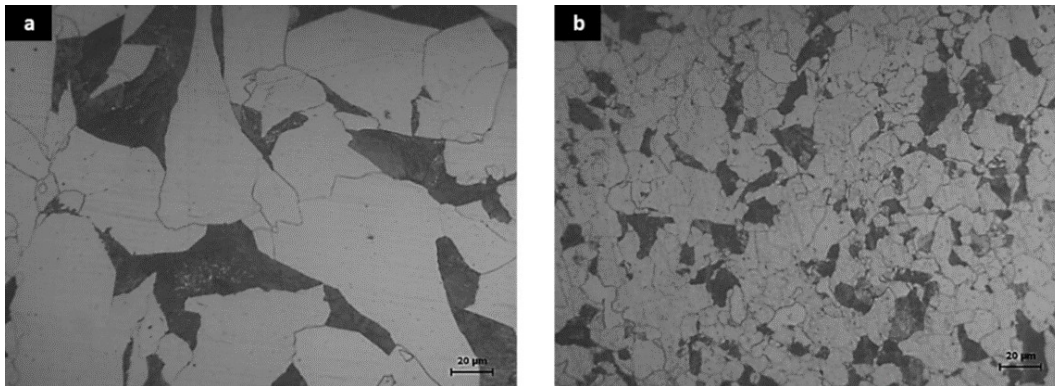


Figure 2-5: Light microscopy images of EN355B low carbon steel forging a) after forging and b) after normalizing treatment.(Courtesy of FRISA)

The main processing parameters of normalizing treatment are: heating rate, temperature, soaking time and cooling rate. The heating rate depends on the heating capacity and control of the furnace while the temperature is determined based on the chemical composition of the material. In turn, the soaking time and cooling rate depend on the thickness and mass of the material [25]. Usually, 8630M low alloy steel forged components for offshore applications are normalized between 900°C-930°C with soaking times of 60 minutes per 25 mm thickness. The low austenitizing temperatures, in combination with the dissolution of carbides and the

formation of fine aggregates of ferrite and pearlite, represent the main mechanisms responsible in the refinement and homogenization of the microstructure after normalizing treatment [25].

## 2.4.2 Quenching

### 2.4.2.1 Introduction

Although, as previously mentioned, the microstructure of large forgings is significantly optimized after normalizing, quenching treatment is still required in order to promote the phase transformations required to achieve the desired properties in the final component. *Figure 2-6* shows an example of how a large ring looks during industrial quenching process.



Figure 2-6: Industrial quenching process of a rolled ring carried out in cylindrical tank (Courtesy of FRISA).

Quenching can be regarded as a key technological process used in the forging industry to tailor the microstructure and properties of low and high alloy steels [26]. This complex process can be summarized as follows: initially the component is heated to its austenitic range, then after the soaking time is over, the material is removed from the furnace and transferred to a quenching tank where the component is immersed in a quench medium to promote fast cooling in order to avoid the development of undesired structures [27]. If the cooling rate is fast enough, the austenitic structure may transform into meta-stable structures such as martensite or bainite depending on the non-equilibrium cooling conditions generated during quenching, the

chemical composition and section size of the forging. Nevertheless, this basic description does not reveal the intricacy of quenching in which relevant heat transfer mechanisms occur in the surface of the forging and the cooling media during cooling from the austenitizing temperature [24, 28]. This complexity is further discussed in the following section.

*2.4.2.2   Heat transfer mechanisms during quenching – Wetting kinematics.*

Since the boiling temperature of the quenching medium is often lower than the initial temperature of the material being cooled, heat transfer during quenching is frequently associated with boiling [11]. As schematically explained in *Figure 2-7*, during quenching in liquid media, three phases of heat removal usually take place. The first stage is the generation of a vapour film immediately after full immersion of the workpiece. The second stage is nucleate boiling whereas the third stage is convection heat transfer. In the first stage, after full immersion, the high temperature (between 700-950°C) of the workpiece allows the vaporization of the quenchant, promoting the formation a vapour blanket in the interphase between surface of the component and the coolant. Due to the insulating effect of the vapour blanket, the cooling rate in the first stage of quenching is relatively slow. Eventually, the breakdown of the vapour film takes place when the temperature of the workpiece falls below the Leidenfrost temperature (the temperature above which the vapour film stage takes place) leading to the nucleation boiling stage. The release of vapour bubbles produced by the evaporation of the liquid in contact with the surface of the component results in high cooling rates due to strong convection produced during the nucleate boiling stage. Finally, when the temperature of the metal is lower than the boiling point of the quenchant, slow cooling rates are produced in the workpiece associated to the wetting effect taking place over the surface of the component. Additionally, on this last stage the slow cooling rate are controlled by the rate of convection and the viscosity of the liquid [24].
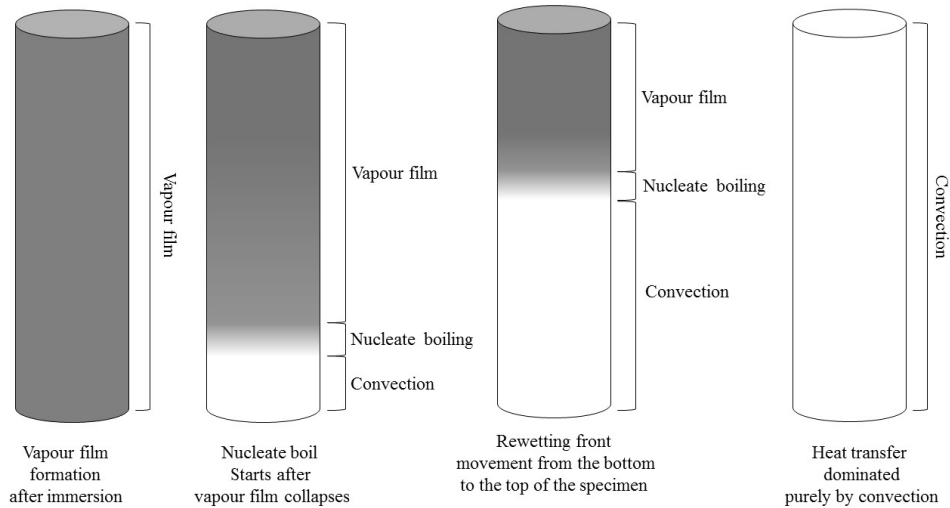
Figure 2-7: Schematic illustration of wetting kinematics during quenching process *[26]*.

Wettability is defined as the tendency for a liquid to spread on a solid and it's characterized by the degree and the rate of wetting. The degree of wetting indicates the extent up to which the liquid wets the surface [11]. It is well established that the cooling characteristics during quenching are strongly affected by the wetting-front process occurring on the surface of a material during quenching. As summarized by Hernandez-Morales et al. the velocity and geometry of the wetting front as well as the shape of the workpiece are important factors controlling the time-temperature distributions within the workpiece. Consequently, the heterogeneity level of the rewetting process associated to the aforementioned factors can lead to non-uniform hardening and some other quenching problems such as distortion and quench-cracking [29]. *Figure 2-8*, shows an example of wetting process taking place during quenching as a function of time.
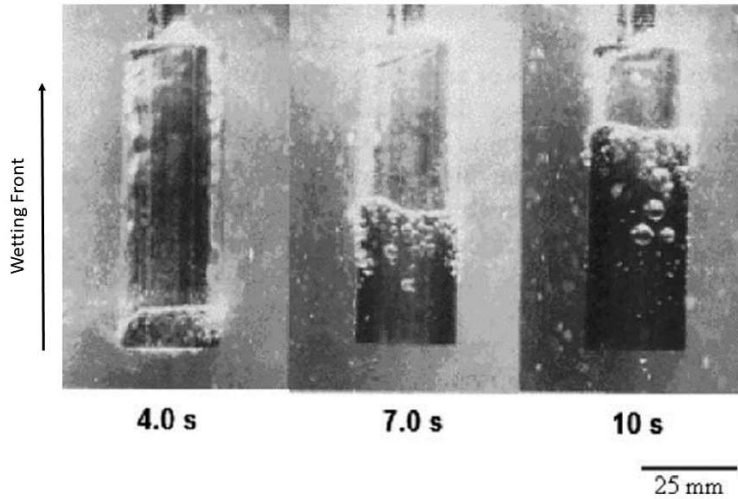
Figure 2-8: Wetting process of a cylindrical Cr–Ni-steel specimen 25-mm diameter100 mm quenched from 850°C into distilled water at 30°C with an agitation rate of 0.3 m/s *[30]*.

The use of wetting kinematics to evaluate the cooling performance of quenching medium is demonstrated in the work of Prabhu *et al.* [31]. They investigated the applicability of pongamia pinnata vegetable oil as cooling medium for industrial heat treatment. Based on this study it was found that the early collapse of the vapour blanket promotes a fast rewetting during quenching of pongamia vegetable oil resulting in higher heat transfer rates during nucleate and convective cooling stages. *Figure 2-9* shows the wetting kinematics of an Inconel probe quenched in pongamia pinnata, palm and mineral oil where a uniform wetting front can be observed in the probe quenched in pongamia pinnata oil.
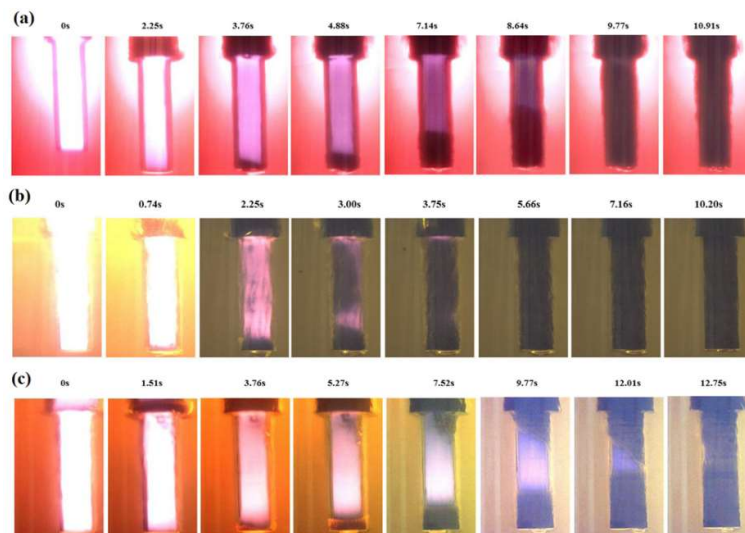


Figure 2-9: Wetting kinetics of Inconel probed submitted to quenching in  (a) pongamia pinnata (b) palm and (c) mineral oils *[31]*.

*2.4.2.3   Quenching fluids*

The quenching power can be defined as the ability of cooling media to extract heat from a workpiece to achieve the microstructure and mechanical properties desired. In this context, extracting heat from the surface, and even from central zones of the workpiece represents the main requirement that should be met by every quenchant to guarantee the achievement of "fast" microstructures such as martensite or bainite  that allow the obtention of high strength and toughness after heat treatment [11].

Water is an economical cooling media that has been used for years in the forging industry for quenching of parts with simple geometries like blocks, cylinders and rings. Due to its high specific heat of vaporization and high specific heat capacity, water is capable to develop high heat transfer rates during quenching. This characteristic is particularly attractive for steels with low hardenability where high cooling rates are required to avoid the formation of pearlitic and ferritic structures. However, the high cooling rates produced by water quenching can induce residual stresses in the part that may lead to distortion and cracking. Furthermore, water requires strict temperature controls and high agitation flow to enable its maximum quenching power [11].

When minimum distortion is required, and the strength and toughness are not critical for the performance of the material, mineral oils can be an alternative to water due to its cooling uniformity, low quenching power and thermal stability. However, the use of mineral oils is restrictive due to its high fire hazard severity and detrimental effects on the environment [9].

Aqueous polymer quenchants represent an alternative between water and mineral oils since a wide range of cooling rates can be achieved by controlling the polymer concentration, bath temperature and intensity of agitation [27]. The use of polymer solutions such as poly alkylene glycol (PAG), poly vinyl pyrrolidone (PVP), enables the development of high strength and toughness comparable to those of water quenching but with the advantage of low distortion levels. The reduced distortions obtained after quenching in aqueous polymer solution are due to the formation of a polymer film during quenching which promotes uniform cooling near to the martensitic transformation point [32]. The main disadvantage of using aqueous polymer solutions is that strict maintenance and monitoring of the quenching tank required in order to

avoid the degradation of the viscosity of the polymer media which may cause a reduction in the heat transfer rates. Additionally, high temperature of the tank, low agitation, oxidation and contaminants such as oils and lubricants are the main factors promoting degradation in aqueous polymers [9].

With increasing environmental regulations in the forging industry, vegetable oils have attracted great attention due to its characteristics of high biodegradability. Souza *et al.* [33] Studied the cooling performance of different vegetables oils such as canola oil, cottonseed oil, corn oil, sunflower oil, and soybean oil. It was found that the heat transfer during quenching with these particular vegetable oils was completely dominated by convection and no presence of vapour film and nucleate boiling stages were observed. The absence of vapour film and nucleate boiling during vegetable oil quenching can be explained by the fact that the boiling point of vegetable is extremely high in comparison with water and polymer. These results highlighted the possibility that vegetable may not require the use of expensive and complex agitation systems to break the vapour film since as mentioned, vegetable oil does not experience vapour film and nucleate boiling during quenching [33]. However other authors such as Prabhu [34] have in fact detected the presence of nucleate boiling stage during quenching with different vegetable oils. Further, they reported that the maximum heat transfer coefficient occurred within the nucleate boiling stage during quenching.

The cooling performance in small specimens and wetting kinematics of water, aqueous polymer, vegetable and mineral oils has been well researched for over 30 years [11, 9, 35, 32]. Nonetheless, during the last decade nanofluids have attracted the attention of many researchers [36, 37]. Usually the production of nanofluids for quenching is carried out by mixing CuO, $Al_2O_3$ and $TiO_2$ particles (average size < 100 nm) in base fluids such as water. The fundamental reason why nanofluids have become of research interest is due to its high heat transfer coefficient and thermal conductivity in comparison with conventional coolants such as water, polymer solutions and oils [37]. Prabhu and Ramesh [38] indicated that the wetting kinematics and critical heat flux during boiling stage of conventional fluids can be enhanced by the incorporation of nanoparticles. The enhancement of the heat transfer conditions by using nanofluids can in consequence foster the microstructure and mechanical properties of low alloy steels. However, the application of nanofluids has yet not been proven to be effective at industrial level.

*2.4.2.4   Critical Variables*

In practice, one of the main challenges in heat treatment is related to the myriad of factors that per se influence the quenching process including: quenching tank design (agitation system, dimensions, temperature control, distance from the furnace to the quenching tank, etc.), chemistry, geometry and surface finish of the component, and as mentioned before, the characteristics of the cooling media used during quenching. In general, the industry has been trying not only to monitor but as well to control some of these critical factors during industrial heat treatment. However, due to the great number of parameters involved in the analysis of industrial quenching, it is often difficult to determine with a decent degree of accuracy which factor or set of factors are in fact responsible, for example for the inferior mechanical properties observed in a large forged component after heat treatment. In this context the present section attempts to describe the most important parameters involved in quenching process under industrial conditions.

2.4.2.4.1   Cooling rate

If a low alloy steel is submitted to a slow cooling rate from its austenitizing point, pearlite and ferrite microstructures will precipitate in the material. Nevertheless, these microstructures are not suitable for components with high strength - high toughness requirements since these type of structures possess a coarse grain structure that is detrimental for the strength and toughness of low alloys steels. On the contrary, when higher cooling rates are applied to low alloy steels during quenching, the formation of bainite and martensite is promoted. The preferential distributions of carbides and the relatively fine gran structure and substructure of martensite and bainite allow the achievement of superior strength and toughness properties compared to those of ferritic-pearlitic structures [39]. This explanation highlights the relevance of cooling rate to determine the microstructure and mechanical properties of low alloy steels [9].As illustrated in *Figure 2-10*, the plot shows the influence of cooling rate in the microstructural evolution represented in a continuous cooling transformation diagram (CCT). The upper critical (UC) cooling rate is the minimum cooling rate at which martensite can be formed, whereas, with further increasing in the cooling rate, there is a limit in which pearlitic structure starts to be inhibited. This limit is the lower critical (LC) cooling rate [24]. It is important to point out that the "noses" of the bainitic, pearlitic and ferritic ranges, can be shifted to the right

side of the CCT diagram by increasing the amount of alloying elements such as manganese, chromium and nickel and by the effects of segregation [19]. This displacement may allow the obtention of martensite even with slower cooling rates. However, increasing the alloying elements in low alloy steels forgings not only increases the steel-making costs but as well increases the possibility of cracking and distortion during or after quenching.
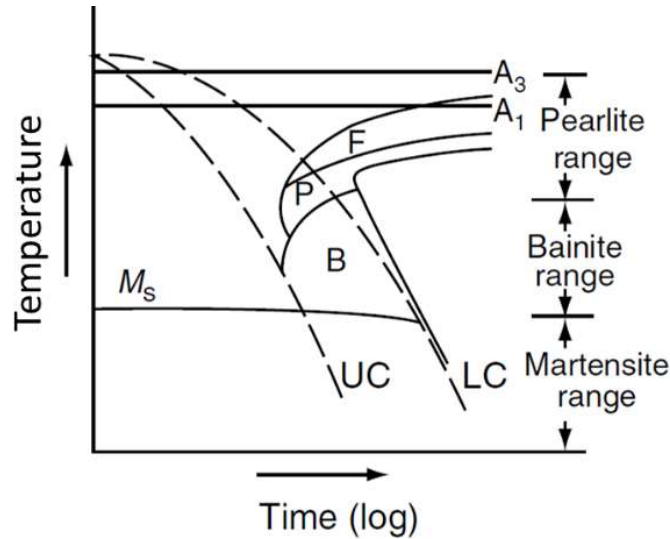


Figure 2-10: Schematic CCT diagram of 1040 steel, F (Ferrite), P (Pearlite), B (Bainite), Ms (Martensite Start), UC (Upper Critical Cooling Rate), LC (Lower Critical Cooling Rate) *[24]*.
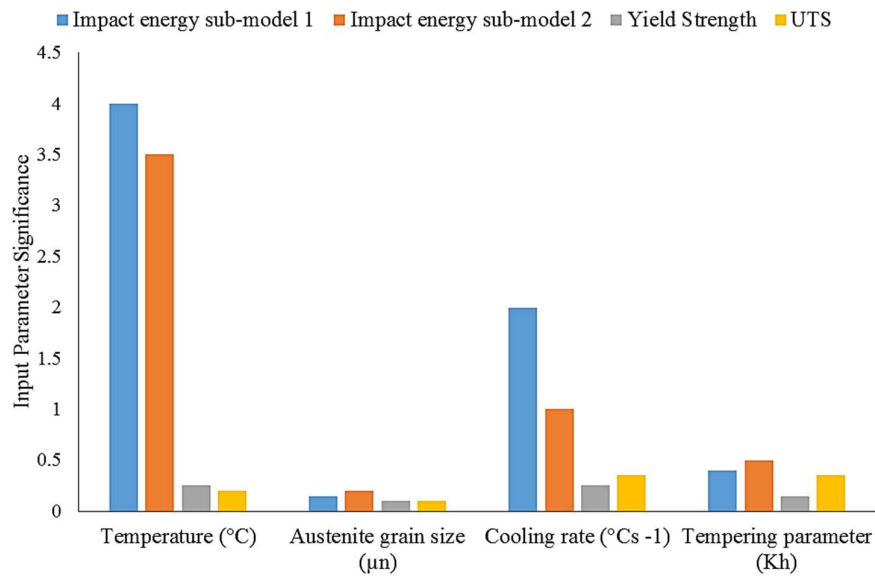


Figure 2-11: Relevance of critical parameters on strength and toughness *[12]*.

Pous-Romero et al. [12] Developed a method based on neural networks to predict the strength and toughness of A508 low alloy steel large forgings. In this work, industrial experimental data were collected and used as input data for the neural network model. As illustrated in *Figure 2-11*, they found that with exception of testing temperature, industrial cooling rate is one of the most important parameters controlling the performance of the material.

In order to enhance the structural integrity of 34CrNiMo6 large scale forgings, Hughes [40] and colleagues developed a heat transfer model to predict the cooling conditions and mechanical properties on specific locations along the geometry of the forged component. Initially, the heat transfer model was used to predict the cooling rates at different locations of a 480 mm billet, then representative samples were heated and then cooled down according the cooling rates predicted by the heat transfer model. After cooling, the samples were tempered and impact toughness tested. The results corresponding to the cooling - rate impact toughness correlation are displayed in Figure 2-12. Based on this study, it was concluded that the increasing formation of martensite as the cooling rate is increase lead to superior impact energy in the specimens after tempering.

The methodology developed by Hughes to predict the toughness of 34CrNiMo6 steel appears to be a practical alternative to correlate cooling rate and mechanical properties at industrial level, however, in this work the effect of segregation on the samples cooled at different rates was not considered in the analysis of the results. As explained later in this chapter, if segregated and non-segregated samples are cooled down at the same rate, different microstructures can be produced after cooling even if the same cooling rate was applied for both samples [36].
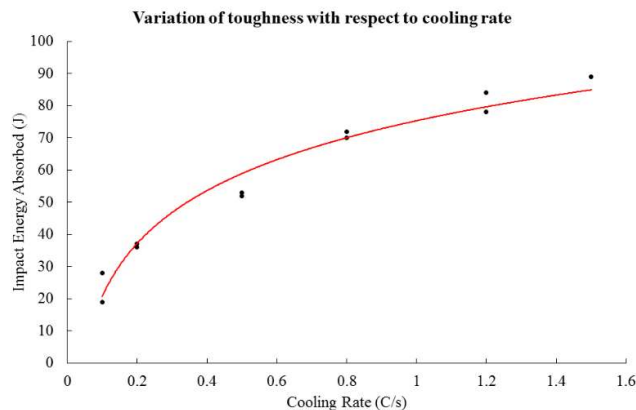


Figure 2-12: Dependence of impact toughness with respect to cooling rate during quenching of 34CrNiMo6 low alloy steel, adapted from *[40]*.

## 2.4.2.4.2   Quenching tank temperature

An increase in the temperature of the cooling media is expected during quenching process, especially when large components with excessive weight are immersed in the quenching tank. As reported by Fontecchio *et al.* [41]  the temperature rise during immersion quenching may cause a detrimental effect on the wetting kinematics of different quench media which in consequence may adversely affect the final properties of the part. For example, as the tank temperature is increased during water or polymer solution quenching, the thickness of the vapour film becomes larger generating a reduction in the cooling rates during the vapour film, nucleate boiling and convection heat transfer stages. This reduction in the cooling rate may be responsible for the formation of diffusional products such as pearlite and ferrite. This is the reason why a restriction of maximum 55˚C on the bath temperature is usually is suggested by polymer quenchant suppliers when PAG (Polyalkylene glycol) polymer solution is selected as preferred cooling media. The reason behind this temperature restriction is due to the polymer chains might chemically dissociate from the water solution provoking a loss of the inherent cooling characteristics of the polymer solution. Finally, the standard practice suggest a temperature range of 50-65°C for mineral and vegetable oils to avoid deterioration in the cooling rate conditions during industrial quenching [9]. The effect of quenching tank temperature on the cooling rate of Inconel 600 specimens quenched in water can be seen in Figure 2-13.

Besides the restrictions in temperatures and times during heat treatment cycles, some material specifications for large scale forgings for offshore applications have strict requirements on the bath quenching temperatures in order to avoid undesirable mechanical properties after heat treatment. Accordingly, the temperature requirements of the quenching tank before quenching, either in water or in polymer solutions, must be in the range of 20 - 25°C, whereas, the temperature of tank once the quenching process is finished, shall not exceed 35°C. In order to fulfil these sorts of requirements, forging and heat treatment companies must install heat exchangers to maintain the temperature of the quenching tanks within the specified requirements.
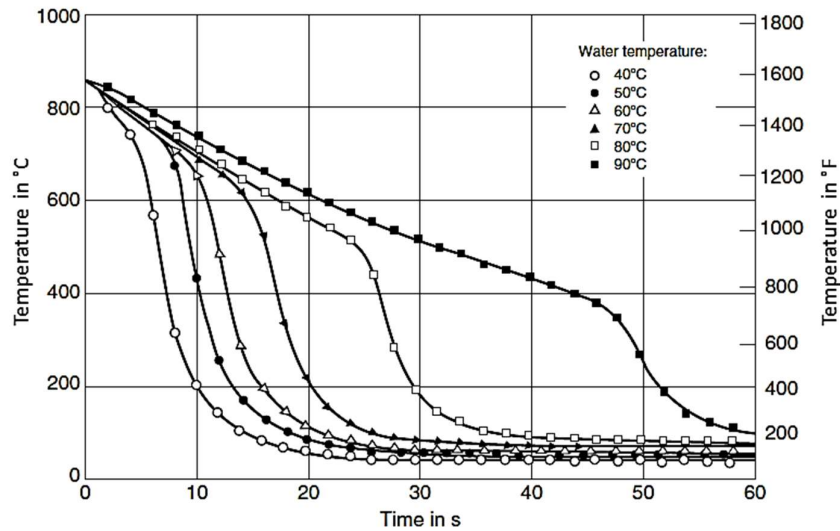
Figure 2-13: Effect of bath temperature on cooling curves measured in the center of an Inconel 600 probe (12.5-mm diameter x 60 mm) quenched into water flowing at 0.25 m/s *[24]*.


2.4.2.4.3  Intensity of agitation


As mentioned, one of the most vital aspects during the design process of quenching technology is the agitation system [9]. Its relevance is due to the fact that a high flow velocity during immersion quenching induces an instability in the vapour film stage by decreasing its duration, and at the same time, increasing the heat transfer by convection during quenching.

The reduction of the vapour film allows to obtain higher cooling rates between the vapour film stage and nucleate boiling stage [24]. *Figure 2-14*, shows the effect of agitation on the cooling rate of Inconel probes (diameter = 12.5 mm, length = 60 mm) submitted to quenching in PEG (Polyethylene Glycol) aqueous polymer solutions. Furthermore, *Figure 2-15*, illustrates the hardness results produced after quenching a test-piece (diameter = 30 mm, height = 105 mm) in a tank with agitation rates of 0.25 and 1.2 m/s. It is clear that superior hardness penetration can be achieved by using higher agitation rates (1.2 m/s) during polymer quenching at 20°C.
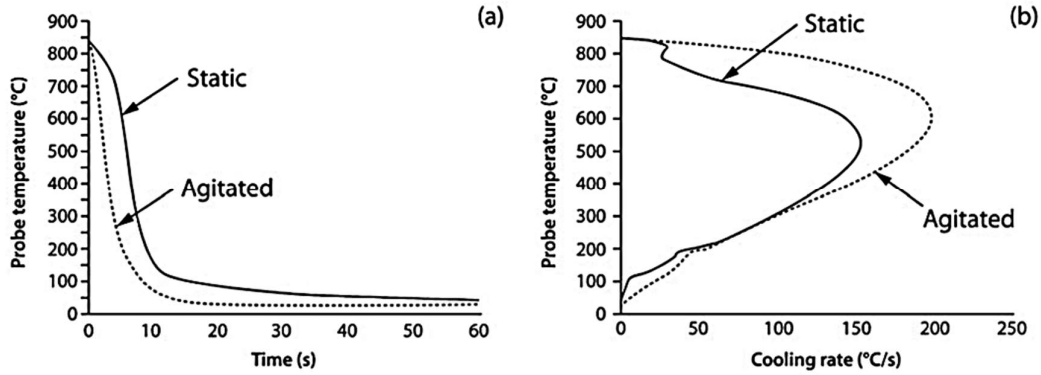
Figure 2-14: Cooling data for a 10 % solution of PEG-6000 tested at 30°C: (a) temperature/time curves; (b) temperature/cooling rate curves *[42]*.
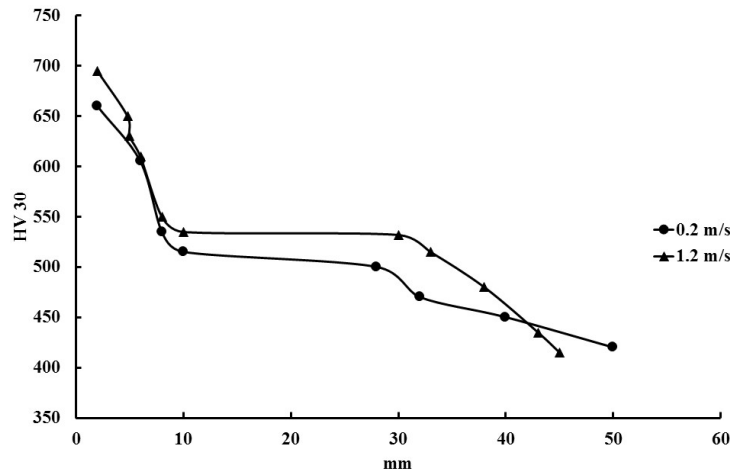


Figure 2-15: Hardness penetration in the wedge sample (AISI 5038) steel influence of the velocity of the liquid, adapted from *[11]*.

### 2.4.2.4.4   Cooling uniformity

Another critical parameter involved in the quenching process of large forgings is the cooling uniformity. During industrial quenching, heterogeneous hardness distributions can be developed due to non-uniform fluid flow inside the quenching tank [43]. Agitation flow measurements taken at different depths inside of an industrial quenching tank property of FRISA are illustrated in Figure 2-16. Usually these type of measurements are carried out by immersing an anemometer in the desired locations inside the quenching tank. Referring to this figure, the results indicate that the average agitation flow at 150 cm depth is approximately 0.15 m/s while the measurements at 50 cm result in an average flow of 0.35 m/s.

The higher agitation flow observed at 50 cm depth could be due to the proximity of the agitation source to the area selected for agitation measurement. It is evident that near to this area the agitation intensity would be expected to be high in comparison with the 150 cm depth measurement where the intensity of the agitation is reduced as the distance from the agitation source is increased.
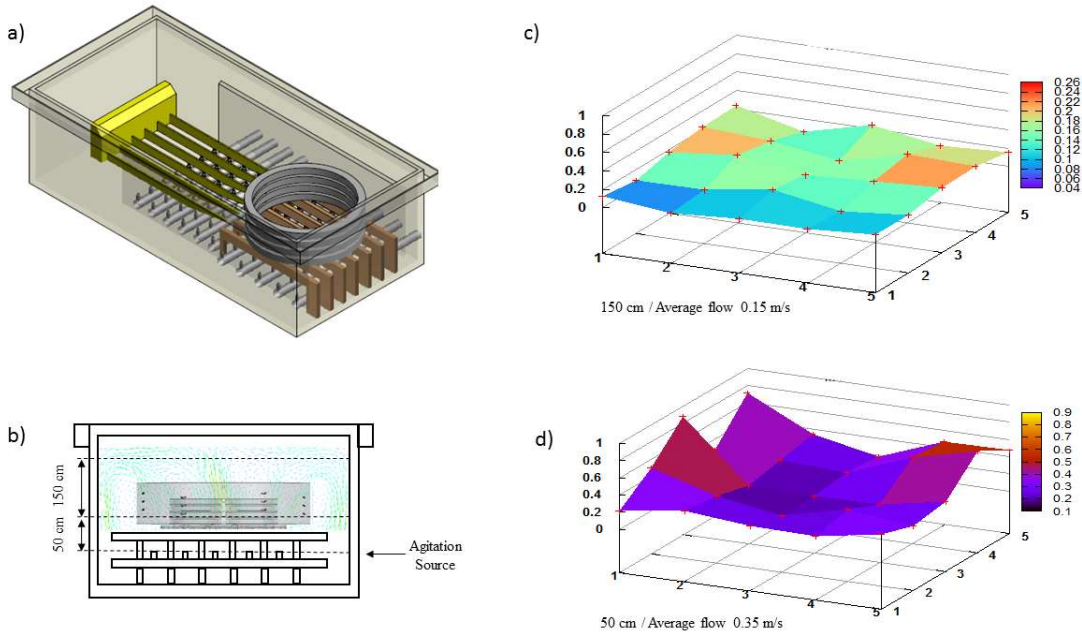


Figure 2-16: a) Schematic design of industrial quenching tank, b) locations to measure agitation flow inside quenching tank, c) agitation flow measures at 150 cm depth and d) agitation flow measurements at 50 cm (Courtesy of FRISA).

In addition, the flow rate uniformity of the cooling media in a quenching system mainly relies on the type of agitation and the design of the flow baffles. For example, as shown in *Figure 2-17*, immersion quenching tanks for processing of large forgings are usually agitated either by propellers or submerged nozzles systems depending on the quenching tank dimensions as well as the intensity and uniformity of agitation required.

Figure 2-17: : Illustration of (a) propellers and (b) nozzles for the agitation of liquid quenchants (Courtesy of FRISA).

2.4.2.4.5   Effect of Thickness

There are several alternatives to achieve the desired microstructure and properties on thin-wall components. Modifications such as; increasing alloying elements, increasing the plastic deformation during hot working or increasing the cooling rate during quenching can contribute to achieve optimal microstructures that eventually allow the obtention of the desired mechanical properties. However, in the case of forgings with large cross sections the cooling rate at the central part of the components is limited by the thermal conductivity of the material. As illustrated in *Figure 2-18* , as the cross section of cylindrical steel specimens subjected to quenching is increased the cooling time becomes larger [44]. Due to the slow cooling rates produced in thick-wall sections, undesired microstructures such as pearlite and ferrite could be formed in the center of the part after heat treatment leading in consequence to non-uniform distribution of strength and toughness properties along the geometry of the forging. One of the alternatives available to overcome this limitation is to increase the alloying elements in the material by increasing the amount of martensitic transformation at center of the forging. However, this alternative is not always feasible due to cost constraints involved in increasing expensive alloying elements such as chromium, nickel and molybdenum. As expected, the section size of the forged component also affects the wetting kinematics due to the slow cooling rate during quenching process. Fernandes and Prabhu observed that during quenching of 1040 steel specimens with  diameters of 44 mm and 28 mm, the nucleate boiling stage was significantly delayed in the thick specimen in comparison with the thin one [45].
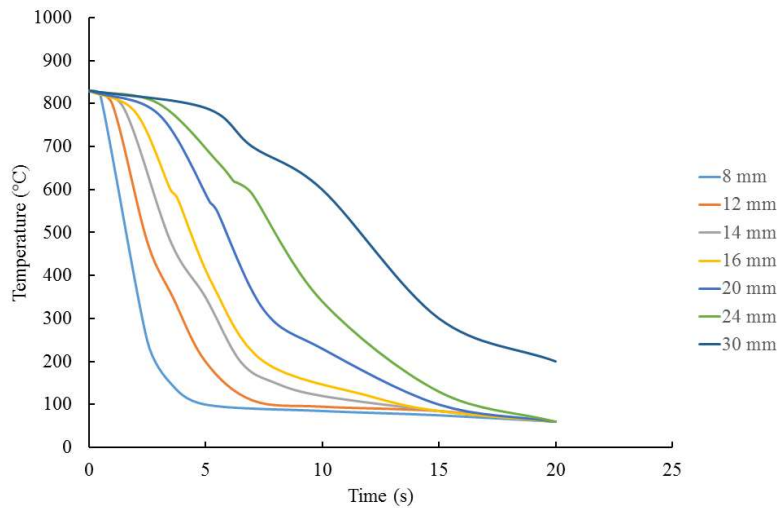
Figure 2-18: Plot showing the effect of diameter of experimental cooling curves at the center of the selected steel specimens, adapted from *[44]* .

2.4.2.4.6  Quenchant selection – Viscosity

The viscosity of a fluid can be defined as its resistance to flow. The performance of the vast majority of cooling media is in fact affected by its dynamic viscosity [11]. Usually a cooling media with high viscosity is associated with low heat transfer rates, while a quenchant with low viscosity is related to high heat transfer rates.  In turn, viscosity changes with temperature and usage. Ramesh and Prabhu investigated the effect of thermal conductivity and viscosity of water, mineral, brines and polymers solutions during quenching process by using standard ISO/DIS 9950 Inconel 600 quench probe. Cooling curve analyses showed that the change in thermophysical properties of the quench media had significant effect on the cooling history of the quench probe indicating that viscosity was the most important characteristic controlling the cooling performance of commercial cooling media [46]. The thermal conductivities and viscosities of the selected quenchants used by the aforementioned authors is elucidated in *Table 2-1*.

| Cooling media | Thermal conductivity (W m $^{-1}$ K $^{-1}$) | Kinematic viscosity (mm $^2$ s $^{-1}$) |
|---|---|---|
| Water | 0.594 | 0.801 |
| 2%NaCl (brine) | 0.581 | 0.812 |
| 4%NaCl (brine) | 0.575 | 0.839 |
| 2% PVP (polymer) | 0.574 | 1.185 |
| 4% PVP (polymer) | 0.570 | 1.829 |
| Mineral Oil-1 | 0.128 | 17 |
| Mineral Oil-2 | 0.135 | 42 |

Table 2-1. Thermophysical properties of selected quenchants, adapted from *[46]*.

2.4.2.4.7  Hardenability

As briefly explained earlier in this section, the forging and heat treatment industries apply the concepts of hardenability, critical cooling rate and ideal critical diameter to improve the mechanical properties at center of large forgings. The relations between these metallurgical concepts can be elucidated as follow; The lowest rate of cooling at which a martensitic structure is formed is called critical cooling rate. For example, an unalloyed steel requires high cooling rates to produce martensite at its geometrical center, whereas, an alloyed steel with the same dimensions will produce martensite at the same position with relatively lower critical cooling rates. This effect can be understood by the hardenability concept, which can be defined as the ability of the material to reach either a certain hardness or martensite level along the cross section of the component [24]. On this regard, the chemical composition is the most important factor determining the hardenability of a material. The elements Cr, Mo, Mn, Si, Ni and V all retard the phase transformation from austenite to ferrite and pearlite. The most commonly used elements are Cr, Mo and Mn. The retardation is due to the need for redistribution of the alloying elements during the diffusional phase transformation from austenite to ferrite and pearlite. Carbon controls the hardness of the martensite. Increasing the carbon content increases the hardness of steels up to about 0.6wt%. At higher carbon levels, the formation of martensite is depressed to lower temperatures and the transformation from austenite to martensite may be incomplete, leading to retained austenite. The solubility of the elements varies between the different phases, and the interface between the growing phases cannot move without diffusion of the slowly moving elements. There are quite complex interactions between the different elements, which also affect the temperatures of the phase transformation and the resultant microstructure. Steel compositions are sometimes described in terms of a carbon equivalent which describes the magnitude of the effect of all of the elements on hardenability. An alloyed

steel with high hardenability will consequently require lower cooling rates to produce martensite at the center of the part compared to steels with low hardenability. Finally, hardenability is often estimated by using the critical diameter (*Dcr*) parameter which can be regarded as the largest bar diameter in which full hardening is produced along the cross section of the part. An example of a hardenability testing is illustrated in *Figure 2-19*.
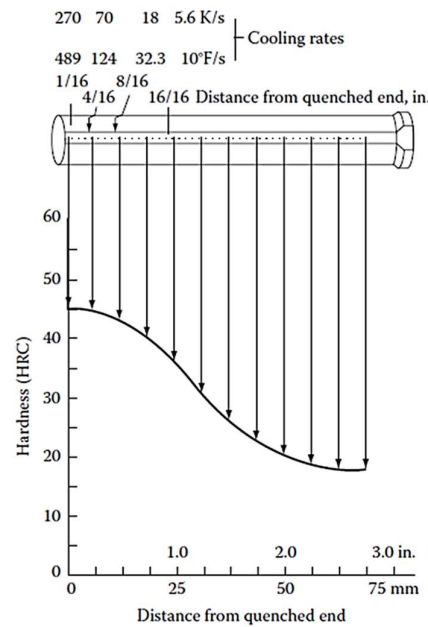


Figure 2-19: Measuring hardness on a Jominy test specimen (100 mm long by 25 mm diameter round bar) austenitized between 870-900˚C and quenched in water and plotting hardenability curves *[11]*.

2.4.2.4.8   Summary

As explained at the beginning of this section, it is clear that quenching can be treated as a complex heat transfer phenomenon in which many variables related to quenching tank design, cooling media, geometry and chemistry of the part, contribute in some degree to the overall performance of quenching treatment. However, as explained in the following section, the tempering treatment is as well a crucial step in the heat treatment process of large scale forgings due to its ability to reduce the high internal stresses and brittle microstructures associated to the martensitic transformation.

### 2.4.3 Tempering

Tempering treatment is required after quenching process since the as-quench martensite is brittle, hard and consequently not suitable for structural applications. Tempering consists of heating the previously obtained martensitic structure to a determined temperature for a specific time period and the cooling in still air. The tempering time is calculated based on the thickness of the part, usually one hour per inch (25 mm) of thickness of the component, while the selection of the tempering temperature depends on the desired mechanical properties [24]. Abdollah-zadeh and Salemi in reference [47] investigated the effect of tempering temperature on the strength and toughness of a NiCrMoV steel by austenitizing selected specimens at 870°C for 1 h, quenched in oil and then tempered between 200 - 600°C. It was observed that the rising temperature causes a reduction in the yield strength and ultimate tensile strength. On the other hand, as illustrated in *Figure 2-20*, a reduction in the toughness is observed as the tempering temperature in increased. The reduced yield strength and increased toughness observed on the specimens as tempering temperature was increased is associated to a reduction in the residual stresses and high dislocation density inherent to the martensitic transformation. Further, the as-quench martensite is transformed into tempered martensite during tempering which consists of a acicular ferrite matrix with carbides precipitates located either in the prior austenite grain size boundaries or within the lath substructure [48]. It is noteworthy to mention that the maximum temperature used during tempering treatments must be below the lower critical temperature $A_{c1}$ (austenite start temperature transformation on heating) in order to avoid austenite transformation.
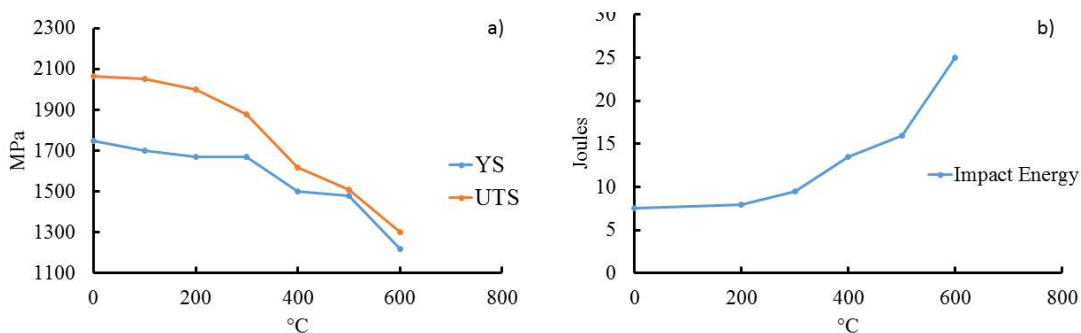


Figure 2-20: Variation of a) yield, ultimate tensile strength and b) impact toughness with tempering temperature, adapted from *[47]*.

The tempering process of martensite involves three main process associated to reconstructive modes that involve movement of atoms. The initial stage of tempering (100-200°C) involves the formation of $Fe_{2.4}C$ carbides also known as $\mathcal{E}$-carbides. During the second stage, the retained austenite from the previous quenching operation transforms into a mixture of ferrite and cementite between 200-350°C. The third stage occurs between the ranges of 250–750 °C. In this temperature range, depending on the chemical composition of the material, the formation of either $Fe_3C$ cementite or $M_3C$ carbides takes place, leading to the termination of the bct (body-centered tetragonal) tetragonality of martensite and progressively reducing its stress level [24].Consequently, the dimensions, morphology, chemistry, distribution and orientation of the carbide precipitates formed during tempering of a martensite structure determine the mechanical properties of the material.

### 2.4.3.1 Tempering embrittlement

As indicated by Arabi and co-workers, the segregation of impurities (P, S, Sn, As, and Sb) to grain boundaries during tempering in the range of 370-550° can reduce the impact toughness of low alloy steels [49]. This phenomenon is known as temper embrittlement and can be produced either by cooling the material at slow cooling rates or by isothermal heating in the temperature range previously mentioned. The formation of brittle phases produced by the migration of impurities generally promotes embrittlement at grain boundaries which may cause intergranular failure on the component. Industrially, temper embrittlement might cause reworks (repetition of heat treatment cycles) and potential rejection of the part if the toughness is not improved even after repeating the heat treatment process. In particular, forged components with large cross sections can be subjected to slow cooling rates from the tempering temperature selected. In order to avoid this, usually large forgings are cooled down in water instead of air in order to avoid the critical interval of temperature (370 -550°C). However, cooling in media different that of air, is not always accepted as standard practice in some material specifications for large forgings used in offshore applications since cooling in water may induce residual stresses in the part after heat treatment. Another alternative used by the industry to cope with temper embrittlement is to increase the purity of the low alloy steel by reducing the composition of detrimental elements such as P, S, Sn, As, and Sb, this in turn may reduce the sensitivity of the material to temper embrittlement [49].

*2.4.3.2   Critical Parameters on Tempering*

The hardness, strength and toughness properties are quite sensitive to tempering temperature
and tempering time parameters since the formation of carbides generated by the diffusion of
carbon and alloying elements is dependent on temperature and time parameters [50]. Besides
temperature and time, the cooling rate and chemistry of the material are also critical tempering
parameters. Due to the variety of chemical compositions and dimensions of forged components
for oil and gas applications, the heat treating industry employs different methods to determine
the effect of temperature-time parameters on the properties of low alloy steels.  As indicated
by Canale et al. [51], one of the most used methods to predict hardness based on tempering
parameters is the Holloman-Jaffe equation:

$$H = f\left[t \exp^{-\frac{Q}{RT}}\right] \qquad (1)$$

Where:

H = hardness

t = the time at tempering temperature

T = the tempering temperature (absolute)

R = the ideal gas constant

Q = the activation energy for the structural changes involved in the tempering process of the steel

f = an appropriately selected function.

The Holloman-Jaffe equation has been a useful method for many years to determine the effect
of tempering temperature and time for steels under isothermal conditions (only the time at the
tempering temperature), However, this equation does not address the non-isothermal
conditions (total time in the furnace) experienced during industrial tempering which includes
the heating and cooling process during the complete tempering treatment. These limitations
may to lead to erroneous predictions of hardness due to the fact that critical stages during
tempering such as the heating up and cooling-down processes are not considered for the
quantification of the tempering-time parameters.

### 2.4.4    Advances on Heat Treatment Simulation

Due to the importance of quenching technology in defining the final properties of structural components, Computer Fluid Dynamics (CFD) has been used recently to evaluate the uniformity and intensity conditions of flow rate during immersion quenching. Currently the majority of the state of the art quenching systems installed in forging and heat treatment companies are initially designed using CFD techniques. CFD was used by Bogh to evaluate the flow heterogeneity of nozzles located in different positions inside the tank during immersion quenching [52]. It was determined that by using CFD it is possible to predict the liquid flow characteristics during immersion quenching. *Figure 2-21*, illustrates the high flow velocity near to the quenching nozzles (agitation source) and how it's gradually decreased as the distance from the nozzles in increased.
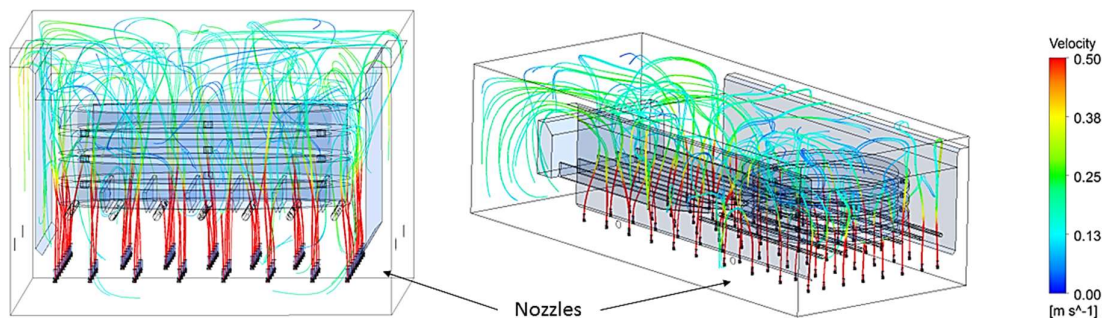


Figure 2-21: Streamline variation in an industrial quenching tank indicating the variation of agitation flow around the quenching zone, (Courtesy of FRISA).

## 2.5    Continuous Cooling Transformations

The time-temperature dependence of phase transformations is graphically represented by transformation diagrams. The kinetics of phase transformation of steels is generally described by TTT (time-temperature-transformation) and CCT (continuous-cooling-transformation) diagrams. The TTT diagram measures the degree of transformation at an isothermal temperature by cooling specimens as rapidly as possible from the austenitic zone to a determined constant temperature between Ac$_3$ *and Ms* critical points. However, these diagrams are not suitable for industrial heat treating of since during cooling, the temperature and the rate of cooling are not constant along the thickness of the part [9].

### 2.5.1 CCT Diagrams

A CCT diagram quantifies the rate of microstructural transformation as a function of time and temperature by heating up predetermined specimens to the austenitizing temperature, and then cooled down at constant cooling rate. As seen in *Figure 2-22*, the start and the end of the phase transformations during continuous cooling are determined by dilatometry with the volume change resulting from the start and finish of phase transformations. The construction of this diagram is carried out by representing the selected cooling rates on a time-temperature plot and overlapping the start and finish phase transformation points on each cooling curve profile. Finally, the transformation temperatures points for all the cooling rates are connected as illustrated in *Figure 2-23*. The microstructural evolution during continuous cooling is often validated by performing a metallographic analysis on each specimen subjected to the different continuous cooling rates [53].
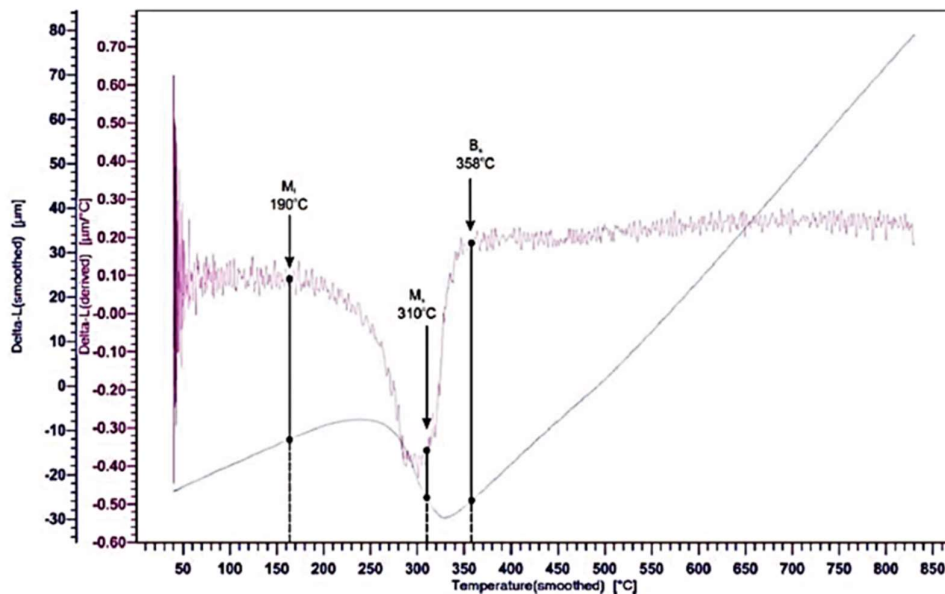


Figure 2-22: Dilatometry plot of a 37MnNiMo6-4-3 low alloy steel indicating the phase transformation temperatures associated to the formation of mixtures of martensite and bainite during continuous cooling *[54]*.
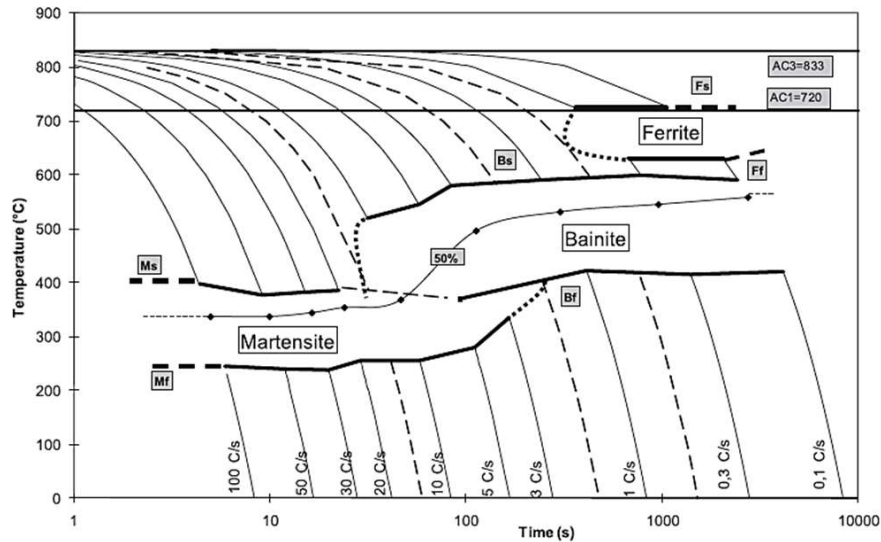
Figure 2-23: Continuous cooling transformation diagram of an A508 type RPV steel (Wt. %: 0.25 C, 1.2 Mn, 0.72 Ni, 0.49 Mo and <0.05 Cr) austenitized at 1100°C for 30 minutes. The dotted lines represent the critical cooling rates of the different phases *[55]*.

## 2.5.2 Continuous Cooling Versus Exponential Cooling

According to the above mentioned it is clear that construction of CCT diagrams by means of dilatometry is useful tool for the design of heat treatments and microstructure prediction. However, the determination of phase fractions during industrial quenching (exponential cooling) of large-scale parts by using CCT diagrams can be ambiguous. Investigations carried out in steels demonstrated that considerable variations in the phase fractions of bainite can be obtained by applying constant and exponential cooling rates even if the cooling time for both, the constant and exponential rates is similar [56]. As seen before, despite the advantages of using CCT diagrams for the prediction of microstructures under different cooling conditions, direct measurements of the microstructure and properties in the real part continues to be one of the most effective and reliable methods to establish relationships between microstructure, properties and cooling conditions during industrial heat treatment. Although it is also true that a better correlation between the specific cooling rate applied and its corresponding microstructure can be obtained by using CCT dilatometry related to small dimensions of the dilatometric specimen.

## 2.6   Phase Transformations during Heat Treatment

As seen in the previous sections, the heating and cooling rates involved in the heat treatment of low alloy steels strongly influence the microstructure and properties of the forged component. This section aims to point out the main microstructures produced on large forgings after heat treatment. The microstructure evolution of steels during heating or cooling can be described in function of its mechanisms of transformation. In this sense, Bhadeshia [57] proposed a classification system for microstructures of steels based on the mechanisms of transformation as illustrated in *Figure 2-24*. The generation of allotriomorphic ferrite, idiomorphic ferrite, massive ferrite, pearlite, carbide, and austenite is carried out by reconstructive transformations. This type of transformation involve uncoordinated diffusion of substitutional atoms through a determined temperature range but without compositional changes. On the other hand, Widmanstätten ferrite, acicular ferrite, bainite and martensite occur by displacive transformations, where the structural arrangement of atoms is altered by an invariant plain strain-shape deformation without diffusion of iron or substitutional solutes during the transformation process [58].
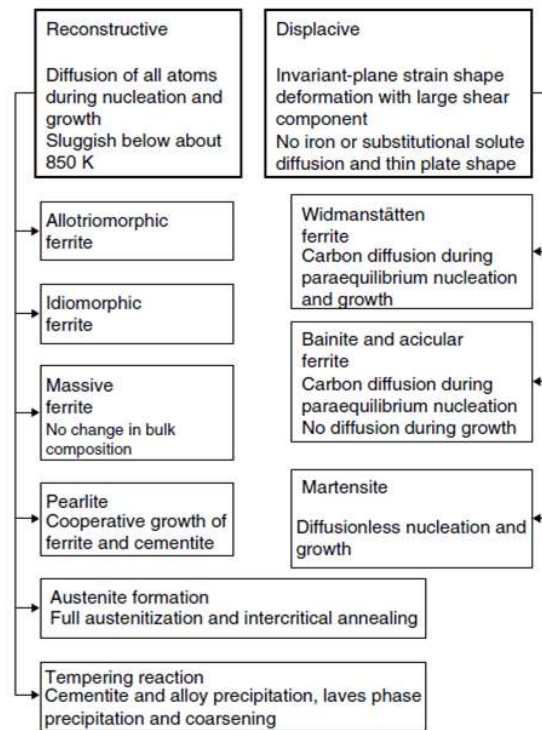


Figure 2-24:  Classification of steel microstructure evolution during heating and cooling based on the mechanism of transformation adapted from *[24]*.

### 2.6.1    Characteristics of Martensitic and Bainitic Phase Transformations

#### 2.6.1.1    *Morphology of Martensite*

Due to the high cooling rates produced during quenching, the FCC (faced centered cubic) austenite structure, can be transformed into BCT (body center tetragonal) martensitic structure. The martensitic transformation can be regarded as a difussionless process (no atomic movement) where the austenite lattice is deformed during cooling and a large shear and volume expansion are induced in the transformed area. This is the reason why the mechanism of transformation of martensite is referred as difussionless shear transformation process. Additionally, the morphology of martensite consists of thin plates or laths due to spatial restrictions during its formation [39]. It is well known that martensitic laths are crystallographically related to the parent austenite by the Kurdjumov–Sachs (K–S) orientation relationships in which the prior austenite grain is subdivided into packets and blocks of martensitic laths respectively. Accordingly, the strength and toughness properties are influenced by these packets and blocks and the mode in which these microstructural features partition the austenite grain [59].

The following aspects also represent important features of martensitic transformation [24]:

- The carbon content on austenite and martensite is equivalent even after transformation.
- The lattice structure of martensite in the as-quench consists of a supersaturated solid solution of carbon in ferritic iron.
- Martensite transformation occurs athermally along a specific temperature range, regarded as martensite start temperature (Ms) and martensite finish temperature (Mf). The Ms and Ms Points are in turn dependent on the chemical composition of the alloy steel.
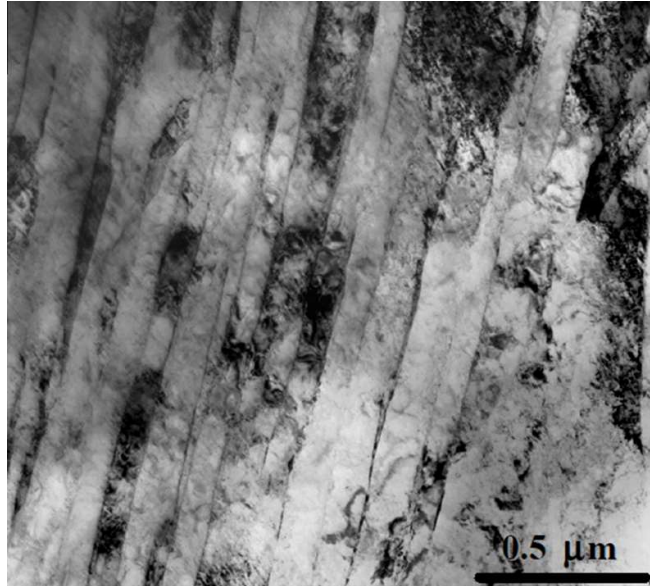
Figure 2-25: Transmission electron micrograph showing packet lath morphology of as-quench martensite *[60]*.

### 2.6.1.2   *Morphology of Bainite*

The transformation mechanisms related to the formation of bainite remain controversial even nowadays [61]. One line of thought [62, 63] suggests that bainitic transformation is of displacive nature. On the contrary, some other researchers [64, 65] propose a diffusion-driven transformation mechanism. As pointed out by Fielding in reference [61] the controversy is still open considering that both schools of thought agree that "direct experimental evidence for either theories are difficult to obtain". In general, lower and upper morphologies are the two main forms of bainite produced in steels isothermally heat treated. Lower and upper bainite are morphologically differentiated by the distribution of carbide precipitates formed at low and high transformation temperatures. As illustrated in *Figure 2-26* and *Figure 2-27*, the structure of upper bainite consists of parallel ferritic plates with cementite precipitated along the plate boundaries. Usually upper bainite is formed at transformation temperatures between 400 and 550°C.  During this period, cementite precipitates from the remaining austenite between the ferritic laths (interlath morphology). Lower bainite is quite similar to that of upper bainite, however the main difference in lower bainite is that cementite precipitates within the ferritic plates (intralath morphology). In addition, the intralath carbides are orientated at some angle to the major axis of the plate according to its Bagaryatski orientation relationship. In general, the transformation temperature range for lower bainite takes place between 400 and 250°C [39].
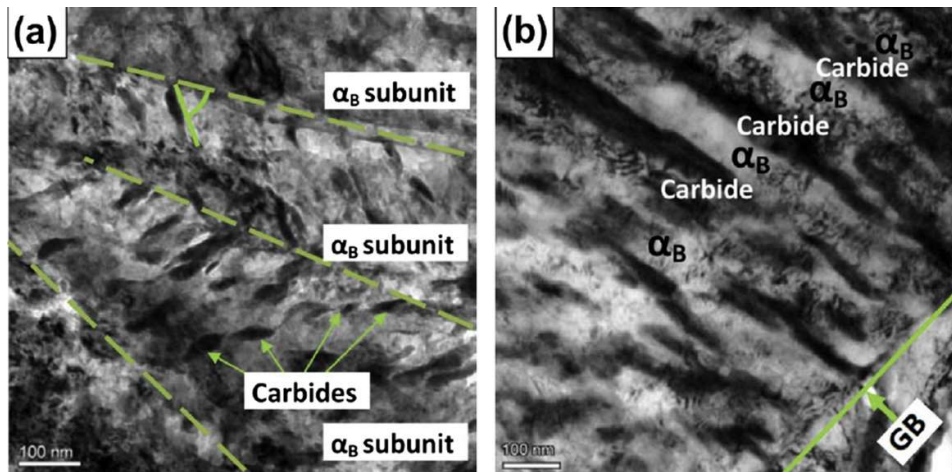
Figure 2-26: TEM micrographs corresponding to 100Cr6 steel showing (a) lower bainite at 260˚C for 2500 s, (b) upper bainite at 500˚C for 1200 s; :$\alpha_B$ bainitic ferrite, GB: grain boundary *[66]*.

However, the classical morphologies of bainite produced by isothermal treatment are not always suitable to be compared with the bainitic microstructures formed during continuous cooling. In this sense, Bramfitt and Speer [67], demonstrated the presence of continuous cooled bainitic microstructures which are not easily defined in terms of any of the "classical" bainitic morphologies such as lower and upper bainite. For example, a non- classical bainitic structure consisting of both intralath and interlath carbides cooled at a rate of 7500˚C/min was reported by the authors. As result of this investigation the authors proposed a classification system based on into three categories depending on whether the acicular ferrite is related with (a) intralath precipitates, (b) interlath particles/films, or (c) isolated regions of secondary transformation products such as M/A constituent.

The mechanical properties of bainite are also sensitive not only to the distribution but as well to the size of the carbide precipitates in which lower bainite usually exhibit higher toughness in comparison with upper bainite due to fine dispersion of carbides associated to the slow carbon diffusion rate experienced by these particles into the residual austenite [68]. Finally, as elucidated by Barbacki, the following microstructural aspects of the bainitic structure also influence the mechanical properties of low alloy steels [69]:

- Packets of lathlike ferrite grains with low disorientation between grains within a packet variable, but generally high, dislocation density.
- Solid solution hardening, mainly by carbon, nitrogen and substitutional alloying elements.
- Regions of martensite and retained austenite of enhanced carbon content between the ferrite laths.
- Large carbides at ferrite lath, packet and prior austenite grain boundaries and smaller carbides dispersed within the ferrite laths.
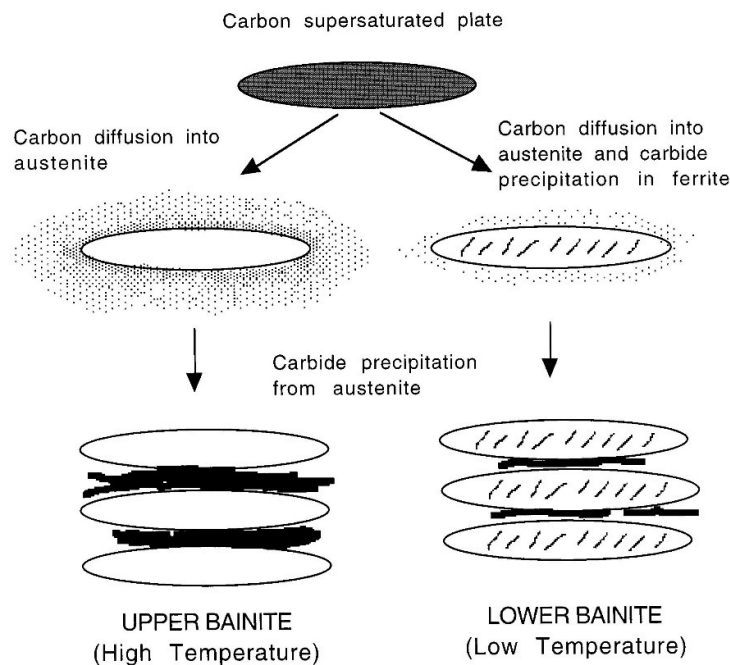


Figure 2-27: Schematic representation of upper and lower bainitic transformations during cooling *[39]*.

### 2.6.2 Tempering of Martensitic and Bainitic Structures

One of the most important factors associated to the tempering of bainitic and martensitic mixtures is the fact that bainite undergo auto-tempering during quenching. In this context, some of indications of auto tempering process are associated the relocation of carbon from the supersaturated ferrite into the residual austenite, and the fast precipitation of carbides during the bainitic reaction.

As illustrated in *Figure 2-28*, the microstructure at the central part of a 100 mm cross section 8630M steel forging after polymer quenching consists of mixtures of as-quench martensite and bainite. It can be appreciated that there is no carbide precipitation in the martensitic structure. This absence of carbide precipitation is due to the fact that carbon still remains in the highly-stressed supersaturated Fe-C solution.

On the other hand, the presence of carbide precipitates is evident in the bainitic structure due to the auto tempering effects mentioned previously. Usually this type of mixed structures can lead to low fracture toughness since that as-quench martensite is highly unstable due the high stresses induced by carbon in the BCT structure and the high dislocations density. In order to increase the mechanical properties, large forgings with mixed structures, must be tempered in order to promote the precipitation of carbides by reducing residual stresses and dislocations density in the martensitic structure.

The simultaneous tempering of martensite and bainite structures affect them to a different extent. At the beginning of the tempering process the bainitic microstructure already contains cementite or carbide precipitates inherent to its phase transformation during quenching. With martensite, the tempering process effectively induces an initial precipitation of cementite located between the lath boundaries. The afore mentioned discrepancy in the initial conditions of each microstructure has an effect on the sensitivity of each structure during and after tempering process due to fact that unlike martensite, bainite only contain small amount of carbon in solid solutions. In consequence only a few changes occur in the recovery and morphology of carbide precipitates on bainite during tempering. On the other hand, since most of the carbon remains in the solid solution of martensite, during tempering the strength of martensite is reduced dramatically as carbon precipitates from the solid solution during

tempering. *Figure 2-29*, shows the variation of cementite size as a function of tempering time in which as the tempering time is increased, the bainitic structure maintains a fine carbide size in comparison with martensite. In summary, as elucidated by Bhadeshia in reference [57]: "The bainitic microstructure is coarse to begin with because of the tempering inherent in the formation of bainite. With martensite the tempering induces the precipitation of cementite, with considerable intra lath cementite and a larger overall number density of particles. Therefore, the coarsening rate is much larger for martensite; the bainitic microstructure shows greater stability to tempering. A consequence is that the matrix microstructure remains fine over a longer time period for bainite than for martensite".

As indicated by Zhang and Knott [70], the relevance of the distribution and size of carbide precipitates in martensitic and bainitic structures is based on the fact that these microstructural features have a strong influence on the fracture toughness of low alloy steels. Correspondingly, small carbides are associated to a lower stress since the ferritic matrix is capable to deform plastically instead of fracturing, while large carbides are more prone to generate cleavage initiation sites in the cementite-ferrite boundaries due to the less ductility experienced by the matrix in the presence of large particles. However it is also important to mention that prior research has demonstrated that effective grain size on martensitic structures is finer than that of bainite leading in consequence to superior toughness properties for martensitic structures [71].
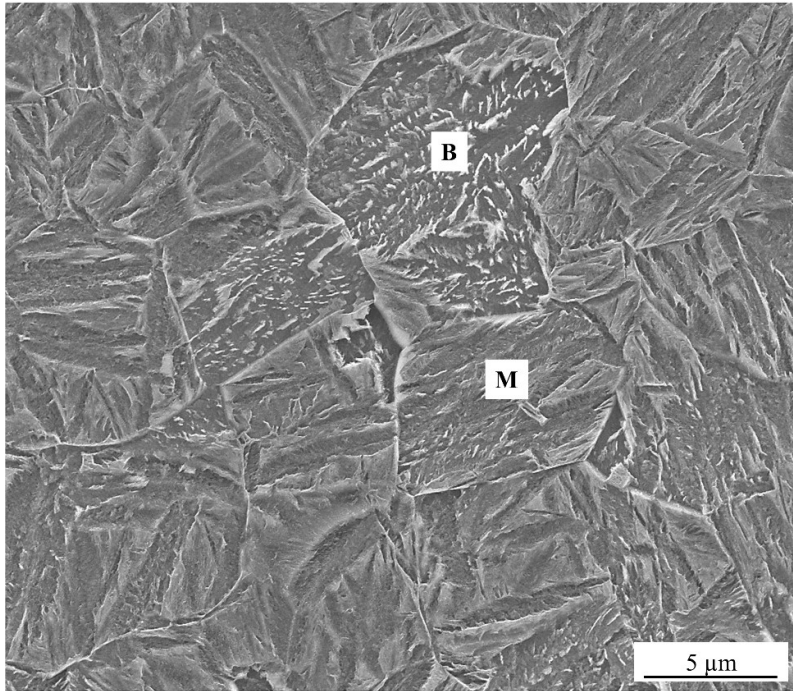
Figure 2-28: Microstructure with mixtures of (M) martensite and (B) bainite corresponding to 8630Mod alloy steel specimen continuously cooled at 0.5 °C/s using Dilatometry technique *[72]*.
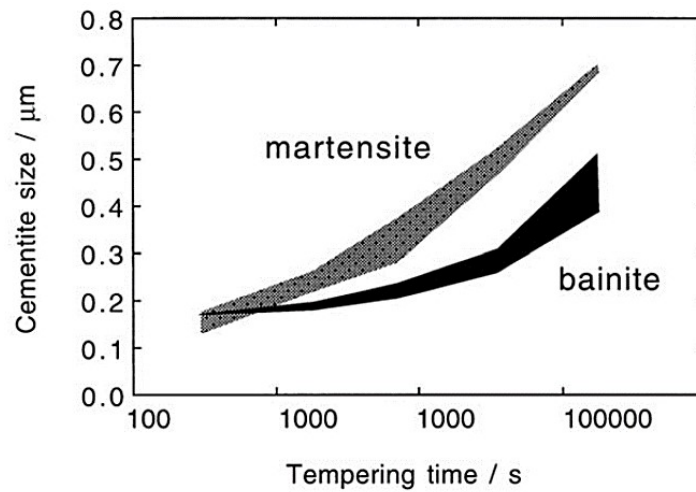


Figure 2-29: Variation of cementite size as a function of tempering time at 700°C The data are for a Fe-0.45C-0.22Si-0.62Mn Wt% steel, the bainite was produced by isothermal transformation, *[57]*.

## 2.7　Mechanical Properties of subsea forgings

The mechanical properties requirements for subsea forgings are designed in according with the environmental and reservoir conditions established on the subsea system. Accordingly, this section describes the main mechanical properties required by the offshore and subsea industry and its relevance on the design of oil and gas structures.

### 2.7.1　Yield Strength and Ultimate Tensile Strength

The offshore and subsea systems are complex structures which consist of several components with specific functions. Due to the increasingly movement of oil and gas exploration to ultra-deep waters, the overall weight and dimensions of these structures and components has become larger. In consequence the critical components, either in the offshore or subsea systems are subjected to heavy loads and high stresses during operation [3, 73]. In this sense, the yield strength and the ultimate tensile strength are used by the offshore designers for general structural design of subsea and offshore components.

From a metallurgical perspective, yield strength and ultimate tensile strength are intimately related to the plastic deformation characteristics of the steel. In turn, the main mechanism responsible for the plastic deformation of steels is the movement of dislocations. In this regard, the free and easy movement of dislocations during the application of tensile loads can lead to low strength properties. However, the strength of low alloy steels can be significantly enhanced by reducing or hindering the free movement of dislocations, increasing in consequence the external loads required to trigger plastic deformation. Correspondingly, the main mechanisms involved in the obtention of superior yield and tensile strength by restraining dislocation motions are; strengthening by grain size refinement, solid solution strengthening and strain hardening [74].

### 2.7.2 Impact Toughness and CTOD Fracture Toughness

During service, offshore and subsea components can experience low and high speed impacts from different sources such as ship impacts, explosions or dropped objects. On this regard, the ability of the material to absorb the energy involved in these sorts of impacts without fracturing represent a critical performance characteristic of offshore and subsea components [75].

#### 2.7.2.1 *Impact Toughness*

The oil and gas industry has used the Charpy V-notch impact testing for around 100 years to evaluate the toughness of steel components. The impact toughness testing measures the energy absorbed by a standardized notched specimen subjected to a sudden application of an impact loading [76].

After impact testing, generally two types of fracture modes can be produced on the broken specimens. These failure modes are frequently regarded as ductile and brittle fracture. Ductile mechanism is often desired on subsea components since when a component fails in a ductile fashion the material undergoes a large amount of plastic deformation before fracturing. Consequently, a component subjected to ductile deformation before breaking can be either replaced or subjected to preventive maintenance before catastrophic failure which may cause leaking oil to the marine environment. On the other hand, brittle fracture occurs rapidly without any deformation before fracture reducing the possibilities to enable any replacement of maintenance in the structure. These type of failure have been responsible for the most catastrophic environmental damages in the oil and gas industry during the last 3 decades. As indicated by Abd-Allah and co-workers, the brittle fracture behaviour of a material subjected to impact testing is enhanced by increased stress triaxiality, low temperatures and high strain rates [77].

## 2.7.2.2 CTOD Fracture Toughness

As mentioned previously, CVN test can be regarded as a simple, economic and standardized method which is commonly used to determine the DBTT (ductile-brittle transition temperature) of low alloy steels [78]. Nevertheless, offshore designers cannot use CVN test for quantitative safety assessment since it only measures the absorbed energy necessary to cause complete failure under plane stress conditions. On the other hand, the CTOD test in fact determines the fracture toughness of a material by measuring the critical value of the stress intensity factor ($K \approx \sqrt{\pi \alpha}$, where "σ" is the applied stress and "α" the crack length*)* at the crack tip of the specimen under plane strain conditions [79]. Considering this, the offshore industry has recently incorporated the CTOD test a critical material requirement for large forgings used on subsea applications.

Besides the fundamentals differences mentioned above, fracture toughness is affected by the temperature, strain rate, crack tip (notch blunt or sharp crack) and the geometry of the specimen (thickness effect). The apparent changes in fracture toughness due to variation in specimen dimensions and crack tip shape are not quantified at all by CVN test, since, according to the standard method for impact testing, the CVN specimen always must be fabricated with a 0.25 mm blunt notch with a thickness of 10 mm as illustrated in *Figure 2-30* [75].
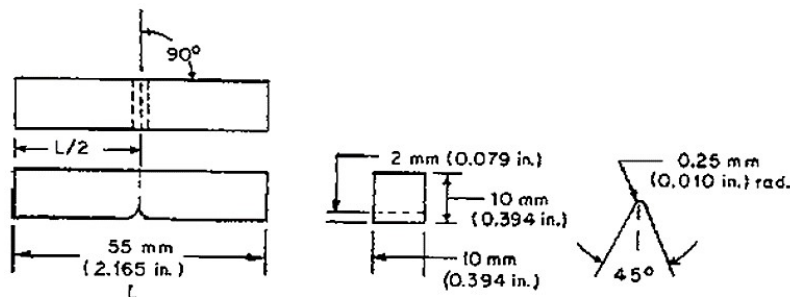


Figure 2-30: Standard full CVN specimen according to ASTM A370 *[80]*.

One of the most important advantages of the CTOD testing is the fact the specimen sizes can approximate the actual thickness of the final component, allowing a more accurate prediction of the performance of the material. It is important to point out that as the thickness of the specimen is increased, the fracture toughness results in lower values. This is due to the fact that as the thickness is increased the material at the centre of the fatigue pre-crack is subjected to plane strain conditions, being unable to plastically deformed therefore leading to low fracture toughness [81, 82]. As mentioned, this so-called thickness effect is not considered in the CVN test since the specimen is always 10 mm thick as is carried out according to the corresponding specification standard.

Regarding the effect of crack tip geometry, Ritchie et al. [79], suggested that the variations between CVN and fracture toughness testing can be associated to a different response of the microstructure to the crack tip geometry, in particular to different stress distributions in the sharp crack and blunt notch. Finally, Chen et al. [83] investigated the effect of grain size and carbides size on the cleavage fracture of blunt notched and pre-cracked specimens made of low carbon steel. It was found that the cleavage crack propagation in notched specimens is controlled by the grain size, while the carbide particles are the main factor governing cleavage cracking on pre-cracked specimens.

### 2.7.2.3   CTOD Equation according to British Standard BS7478

δ CTOD parameter is determined by using the following equation [84]:

$$\delta_{BS} = \delta_{el,BS} + \delta_{pl,BS} \tag{2}$$

$$\delta = \frac{K^2(1-v^2)}{2\sigma_{ys}E} + \frac{r_{pl}bV_{pl}}{r_{pl}b+a+z}$$

Where, $\delta_{el,BS}$ represent the elastic component of $\delta_{BS}$, while $\delta_{pl,BS}$ is the plastic component of $\delta_{BS}$, K is the stress intensity factor, $v$ is the Poisson's ratio. $E$ is the Young's modulus, $\sigma_{ys}$ is the 0.2% proof strength, $r_{pl}$ is the plastic rotational factor, $V_{pl}$ is the plastic component of the clip gauge opening displacement, $Vg$, $a$, is the crack length, $b$ is the uncracked ligament width and z is the distance if the knife edge measurement point from the front face SEB (single edge notch bend) specimens [85].

As seen in *Figure 2-31*, the physical meaning of CTOD can be explained by the degree of crack blunting displayed at the crack tip where the larger the crack blunting and mouth opening, the better the material resistance to crack propagation resulting in high CTOD values. On the contrary, a low CTOD value reflects a brittle-type behaviour with small or null extension of crack blunting [81]. CTOD can be considered as a strain-based estimate of fracture toughness. However, it can be separated into elastic and plastic components. The elastic part of CTOD is derived from the stress intensity factor, K. In some standards, the plastic component of CTOD is obtained by assuming that the specimen rotates about a plastic hinge. The plastic component is derived from the crack mouth opening displacement (measured using a clip gauge). The position of the plastic hinge is given in test standards for each specimen type.
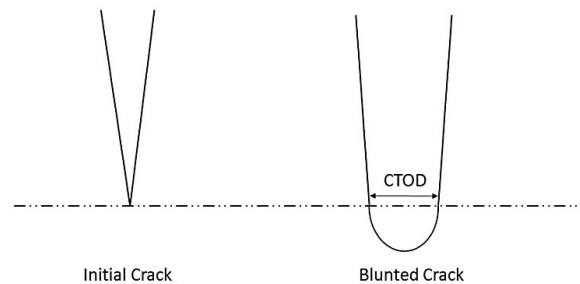


Figure 2-31: The physical meaning of CTOD *[86]*.

## 2.7.2.4 Fracture Modes

Depending on factors such as loading history, environmental conditions and material quality, the fracture modes of steels can be either ductile or brittle. As seen in *Table 2-2*, brittle failure can occur either by transgranular cleavage (crack propagation through grains) or intergranular separation (crack propagation along grain boundaries).

As explained by Knott [5] in his work on cleavage fracture on structural steels, ductile (plastic collapse) and brittle failure are the two main failure mechanisms that can affect the integrity of structural components. However brittle fracture is of greater importance since this failure mechanism occurs rapidly with little or no indication of plastic deformation which can lead to human, environmental and financial losses.
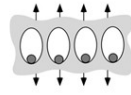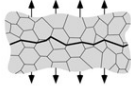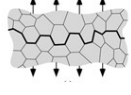
| Fracture Mode | Failure Mechanism | Stress-Temperature Conditions | Schematic Fracture Mechanism |
|---|---|---|---|
| Ductile Fracture | Nucleation, growth and coalescence of voids generated at inclusions or second phase particles (carbides) | High temperature or Low stress | |
| Transgranular Cleavage | Rapid crack propagation on specific crystallographic planes | Low temperature or High stress-strain | |
| Intergranular Separation | Propagation along grain boundaries | Low temperature or High stress-strain | |

Table 2-2: Failure mechanisms on steels, adapted from *[81]*.


## 2.8 Metallurgical Factors Controlling Fracture Toughness of Low Alloy Steels

The fracture toughness of low alloy steels is not only affected by the microstructure produced after heat treatment. Metallurgical aspects such as non-metallic inclusions and segregation inherent to the steel making process, as well as the grain size distribution achieved after hot working processes, represent critical processing parameters which also affect the structural integrity of large forgings. This section aims to provide a review on the main metallurgical factors controlling fracture toughness of low alloy steels.


### 2.8.1 Influence of Non-metallic Inclusions

Any type of fracture requires a stress concentrator to enable the structure to fail either in ductile or brittle fashion. In this sense, non-metallic inclusions, which are unavoidable oxidation products from the steel making process, can be regarded as stress-concentrating features, since its size strongly affects the fracture mechanisms of crack initiation and propagation as illustrated in Figure 2-32, shows cleavage micro crack nucleated from a particle (MnS non-metallic inclusion) and arrested in the surrounding matrix.
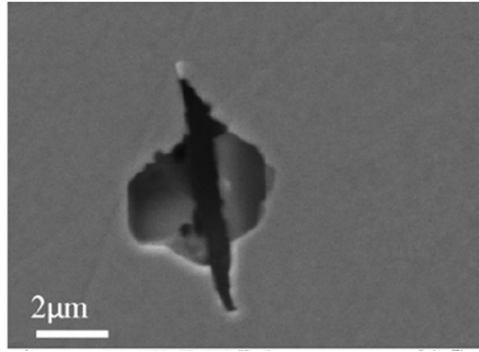
Figure 2-32: Cleavage micro crack nucleated from a particle (MnS inclusion) and arrested in the surrounding matrix *[87]*.

$$K_{max} = 0.5\sigma_0 \sqrt{\pi\sqrt{area}} \tag{3}$$

Where:

$K_{max}$ = Stress Intensity Factor

$\sigma_0$ = Stress amplitude

Area = cross section area of inclusion

In addition, under loading conditions non-metallic inclusions might act as crack initiation sites decreasing the fracture toughness of the material by reducing its fracture stress as the size of the inclusion is increased as illustrated in

*[88, 5]*.

$$\sigma_F = \{\pi E'_{yp}/C\}^{0.5} \tag{4}$$

Where:

$\sigma_F$ = Fracture stress

*E = Young's Modulus*

*yp = Effective work of fracture required for the brittle micro crack to extend into and cross the ferritic matrix*

*C = size of the brittle nucleus*

### 2.8.2 Influence of Segregation

On the solidification process of low alloy steels, alloying elements are heterogeneously distributed in the dendritic structure leading to compositional variations along the ingot. This compositional variation is usually regarded as macro or micro segregation [89]. One of the main effects of segregation is the formation of a banded structure upon solidification on the ingot. As seen in *Figure 2-33*, under the optical microscope, two types of bands, one bright and one dark, are generally found in segregated low alloy steels. Different alloying elements such as chromium and nickel, can either enrich or deplete these bands leading to compositional variations. As reported by Penha et al. [19], large compositional variations on the banded structure, can lead to the formation of non-uniform microstructures such as martensite or bainite on each band, leading to non-uniform mechanical properties in the final component even after heat treatment.

Furthermore, Pickering and Bhadeshia investigated the effects of as-cast macro segregation on the microstructure of a representative section of a large SA508 Grade 3 steel forged component submitted to continuous cooling. They concluded that after quenching the segregated areas led to distinct microstructures such as lower bainite, martensite-austenite islands, and some Widmanstätten ferrite while the microstructure of the non-segregated area consisted mostly of Widmanstätten ferrite. In addition, it was also observed that the distinct microstructures developed on the segregated and non-segregated areas led to hardness variations in the as-quenched and as-tempered conditions [90].



Figure 2-33: Chemical Segregation observed on a quenched and tempered 8630 low alloy steel, (Courtesy of FRISA).

### 2.8.3 Influence of Effective Grain Size

The beneficial effect of grain size refinement lies on the fundamental fact that grain size boundaries and sub-boundaries (packets and blocks), act as obstacles, limiting or retarding the fast cleavage crack propagation along {100} planes, enhancing the fracture toughness of fine-grained steels as consequence of increasing the resistance to brittle crack propagation [91]. As illustrated in *Figure 2-34*, lath martensite has a complex hierarchical microstructure, in which prior austenite grain structure consists of several packets. These packets in turn contain blocks which are further partitioned by laths [92]. In general, each one of these structural units possess, either high or low angle boundaries depending on their misorientation angle. According to Wang et al. [93] the microstructure unit controlling cleavage crack propagation in lath martensitic steels, is the high-angle packet structure rather than the low-angle prior austenite grain boundaries. High-angle boundaries are more effective than low-angle boundaries retarding or deviating cleavage cracks since more energy is required for the propagating crack to cross a large angle boundary. In general, a high-angle boundary has a misorientation angle larger than 15° where the effective grain size can be defined as the smallest microstructural unit over which the cleavage crack propagates in a continuous manner [93, 94].
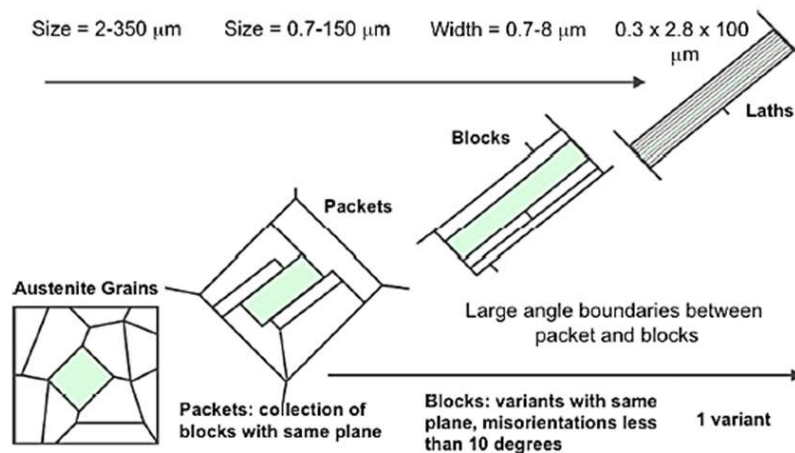


Figure 2-34: Hierarchical microstructure in martensitic structure, adapted from *[92]*.

As elucidated in *Figure 2-35* , EBSD (Electron Back Scatter Diffraction) is one of the most powerful characterization techniques to determine the effective grain size by measuring the misorientation angle of grain size boundaries and sub-boundaries. However, several authors have pointed out the difficulty to use EBSD to determine the effective grain size on quenched and tempered low alloy steels  due to the complex similarities (orientation relationships) in of tempered martensite and tempered bainite [95, 71].
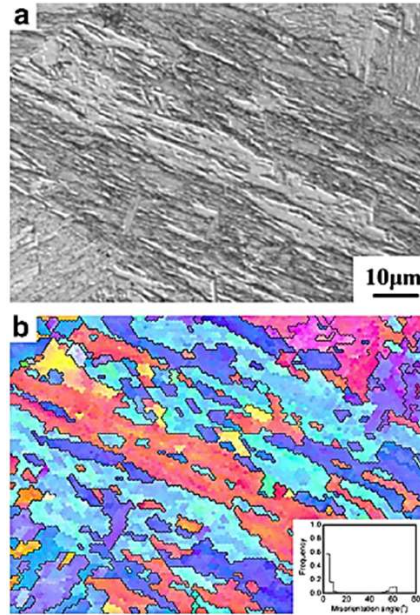


Figure 2-35: Light microscopy image (a), and EBSD image (b) showing orientation relationships. The black lines indicates high-angle boundaries (misorientation angle > 15°), from *[93]*.

### 2.8.4   Influence of Microstructure

The main microstructural change of industrial interest developed after tempering is the evolution of carbides precipitates due to its strong correlation with the final properties of the component [57]. Carbide particles in steels are usually characterized through their crystallography, chemical composition, size, morphology, and distribution. To determine the chemical composition of the carbide metallic constituent (M), energy dispersive x-ray spectroscopy (EDX) along with transmission electron microscopy (TEM) is mainly used. In this sense $M_3C$ is the predominant carbide type in low-carbon, low alloy steels in the absence of strong carbide-forming elements as illustrated in *Figure 2-36* [96]. In general, the microstructure of 8630M large low alloy steel forgings after heat treatment consists of mixtures

of martensite and bainite in the as-tempered condition. As seen in *Table 2-3*, the size of cementite changes according to the type of microstructure and heat treatment history. Bowen et al. [97] investigated the effect of martensitic and bainitic structures on the cleavage fracture of A533 pressure vessel steel after heat treatment. It was found that, the fracture toughness in auto-tempered martensite is higher than that of upper and lower bainitic structures. The superior toughness exhibited by the auto-tempered martensite is associated to fine distribution of carbides precipitated in the martensitic structure. On the contrary, the coarse carbide distribution of the bainitic structures lead to detrimental fracture toughness results.
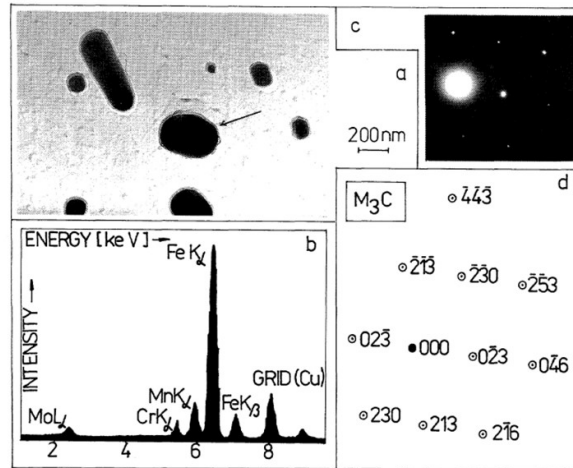


Figure 2-36: TEM characteristics of $M_3C$ carbide: (a) morphology of analysed particle, (b) EDX spectrum, (c) electron diffraction pattern, (d) evaluation of diffraction pattern *[96]*.

| Microstructure | Mean cementite size / nm | Coarsest particle / nm |
|---|---|---|
| Auto-tempered martensite | 14 | 36 |
| Tempered martensite | 38 | 110 |
| Severely tempered martensite | 230 | 600 |
| Upper bainite | 220 | 1000 |
| Mixed upper and lower bainite | 230 | 720 |

Table 2-3: Cementite particle size as function of microstructure *[97]*.

The effect of carbide thickness (*C*, in equation 4) on the local fracture stress (the critical stress for the fast propagation of a micro crack into the ferritic matrix) is elucidated in *Figure 2-37*, where the fine distributions of carbides in martensite result in local fracture stresses of 3100–4000 MPa, whereas that of coarse bainite is between 1100–2200 MPa. According to this evidence it's clear that, due to its carbide size distribution, bainitic structure is more brittle than tempered martensite.
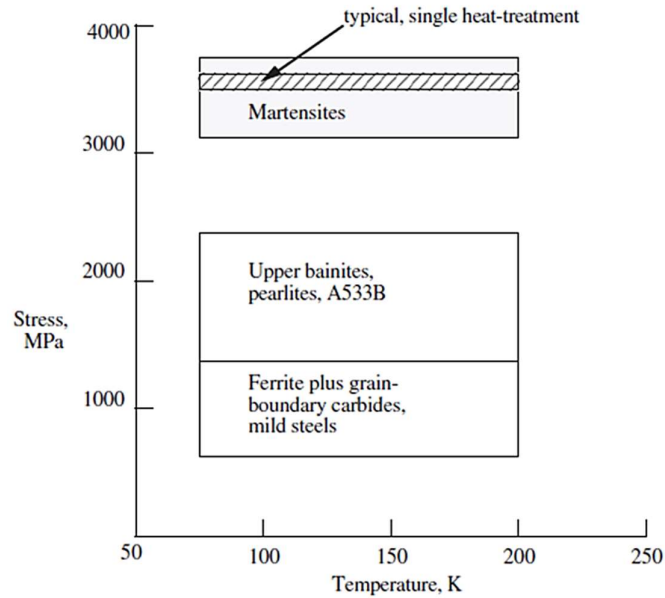


Figure 2-37: Distribution of fracture stresses as a function of temperature for different microstructures. The values of $\sigma_F$, which are, at most, weakly dependent on temperature, fall into two classes: some 3200–3800MPa for the fine distributions found in auto-tempered martensites and lower bainites; 1200–2200MPa for the coarser upper bainites and other ferrite/carbide mixtures *[97]*.

### 2.8.5 Summary

The appraisal of the literature presented in this chapter, highlights the complex relationships between processing route, microstructure and properties of low alloy steels. In particular, how the structure and properties of low alloy steels can be altered by modifying relevant metallurgical parameters such as chemical composition (steel making), degree of deformation (forging) or cooling rate (quenching). Furthermore, the relevance of heat treatment as an essential step in the manufacturing route of large forgings is elucidated, considering the complexity of the mixed microstructures produced after quenching and tempering, and more importantly how these microstructural features affect the fracture toughness properties of the final component. However, there is still a lack of understanding on the effect of industrial heat treatment conditions on the microstructure evolution of thick-wall forgings and how these microstructures influence relevant properties such as CTOD parameter. The present research attempts to cover quenching processes by using three different cooling media and subsequent tempering treatments of thick-wall forgings to explore the effect of industrial cooling conditions on the microstructure and mechanical properties of subsea connectors as illustrated in the following chapters.

# 3 Experimental Procedure

## 3.1 Introduction

In heat treatment operations, many variables are involved in determining the performance of large forgings for subsea applications. Quenching processing parameters such as heating rate, austenitizing temperature, soaking time, transfer time (transfer of the workpiece from the furnace to the quenching tank), dwelling time (period of time at which the workpiece remains inside the quenching tank) and cooling rate, have a great impact on the microstructure and properties of the material subjected to heat treatment. Under industrial heat treatment conditions, knowledge is scarce regarding the variation on cooling rate and its effects on the fracture toughness properties of thick wall forgings made of 8630M low alloy steel. Considering this, the experimental work was designed in order to provide information on the microstructure and mechanical properties evolution by changing the cooling rate during quenching process of large ring segments. The cooling rate changes were induced by using three different cooling media (water, aqueous polymer solution and vegetable oil) with different heat removal rates. In addition, the microstructures obtained during the industrial experimentation were validated by producing a CCT diagram under laboratory conditions using dilatometric techniques.

The first section of this chapter describes the production method of the experimental forging including relevant aspects of steel making, open-die forging, and ring rolling, machining and cutting operations involved in the manufacture of the experimental part. The second section reports heat treatments carried out at industrial level to produce different cooling rates in three ring segments of 8630 modified low alloy steel. The normalizing treatment of the three segments was carried out at FRISA (Monterrey, Mexico) using a temperature of 900°C for 5 hours. Then each ring segment was austenitized at 890°C for 6 hours and then separately quenched in water, aqueous polymer and vegetable oil. The heat treatment (normalizing, quenching and tempering) process of the two segments quenched in water and aqueous polymer was carried out at FRISA, while the heat treatment process (quenching and tempering) of the segment quenched in vegetable oil was carried out at SORBIT (Lecco, Italy). All the experimental ring segments were subsequently tempered at 590°C for 10 hours and the cooled down in still air.

The third section explores the effect of cooling rate on the microstructure of 8630 steel specimens by means of quenching dilatometry under laboratory conditions. The dilatometric measurements were carried out in TA Instruments (Hüllhorst, Germany) whereas the specimens were machined down at Sheffield University. The last two sections describe the comprehensive mechanical testing (tensile, impact and CTOD testing) and characterization performed over the specimens removed from selected locations on the three ring segments after tempering treatment.

### 3.1.1   Material selection

Since the forging company (FRISA) wanted to further comprehend the effects of using conventional and non-conventional cooling media for the quenching process of large forgings, and their implications on its mechanical properties; a double cross section connector was selected for this research. These type of forging connectors are generally employed as structural components in offshore and subsea systems [7]. After machining process, which represents the last step in the manufacturing route, the forged connector has an approximate weight of 1500 kg and consists of two cross sections of 100 and 250 mm respectively, as illustrated in *Figure 3-1*.
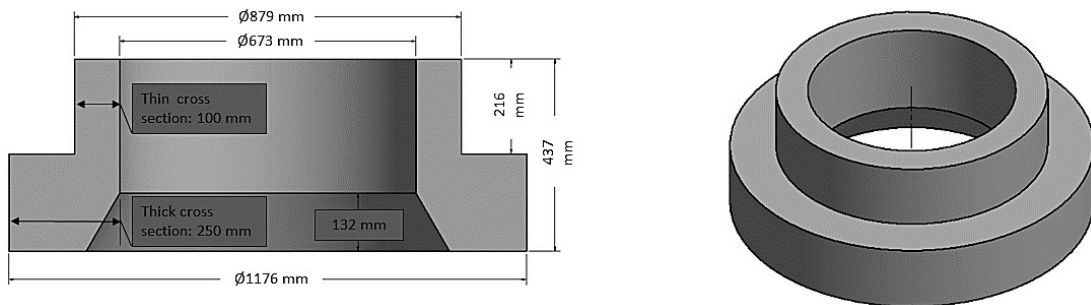


Figure 3-1: Dimensions of double cross section forged connector selected as experimental workpiece.

As shown in Table 3-1, the chemical composition of the selected component corresponds to an AISI 8630 modified low steel. In order to meet specification requirements, 8630M steel connectors are normalized, quenched and tempered to produce a balance between strength and toughness after heat treatment. In combination with carbon, carbide formers elements such as

chromium and molybdenum are added to 8630M steel to increase its hardenability. In addition, molybdenum also contributes to reduce temper embrittlement. 8630M steel is also alloyed with nickel, a non-carbide alloying element, to increase hardenability and enhance toughness *[24]*.

| Element | Value (W%) |
|---------|-----------|
| C | 0.33 |
| Mn | 0.93 |
| P | 0.007 |
| S | 0.001 |
| Si | 0.30 |
| Ni | 0.84 |
| Cr | 0.99 |
| Mo | 0.40 |
| V | 0.005 |
| Cu | 0.14 |
| Al | 0.026 |
| Hppm | 1.0 |
| Ti | 0.003 |
| Ca | 0.0010 |
| Co | 0.013 |

Table 3-1: Chemical composition of AISI 8630 Modified low alloy steel (Appendix A).

The mechanical properties requirements specified for large forgings used in subsea applications are illustrated in Table 3 2. The minimum and maximum YS requirements are 750 and 900 MPa correspondingly, while the minimum UTS is 900 MPa. The minimum and average impact requirements are 28 and 42 J respectively. Finally, it is important to point out that there is not a CTOD fracture toughness parameter established in the materials specification (final user) applied for this application, however internally (FRISA), an aim value of δ = 0.25mm was established by the company based on CTOD requirements for similar applications.

| Yield Strength (MPa) | Ultimate Tensile Strength (MPa) | CVN Impact Toughness (J) at -30°C | δ CTOD Fracture Toughness (mm) at 0°C [aim value] |
|---------|---------|---------|---------|
| 760 (min) | 900 (min) | 28 (min) | 0.25 (min) |
| 900 (max) | N/A | 42 (avg.) | N/A |

*Table 3-2:* Material specification for large forgings used in offshore applications.

## 3.2 Production Method of Large-scale Experimental Ring

### 3.2.1 Introduction

The manufacturing process of the experimental forging is schematically illustrated in *Figure 3-2*, initially a 22 Ton tapered ingot was converted into a forged bar through a series of hot working operations. The cylindrical block required to produce the experimental part was removed from the center of the bar length via saw cutting and then transformed into a square ring by means of ring rolling operations. After ring rolling, and contour machining the full-scale ring was saw cut into three equal segments of 530 kg each. On this regard, considering the effect of mass on the cooling rate, finite element simulations were carried out to validate the representativeness of the ring segment (~530 kg) in comparison with the full ring part (~1600). According to the simulation in Appendix B:  Quenching Simulations ,the mass/dimensions of the experimental ring segment proposed, were capable to satisfactory reproduce the cooling rate conditions of a full scale forging. After saw cutting the three ring segments were normalized, austenitized and then each segment was separately quenched in water, vegetable oil, and aqueous polymer solution respectively. Finally, after quenching, the segments were tempered at 590°C for 10 h followed by cooling in still air.
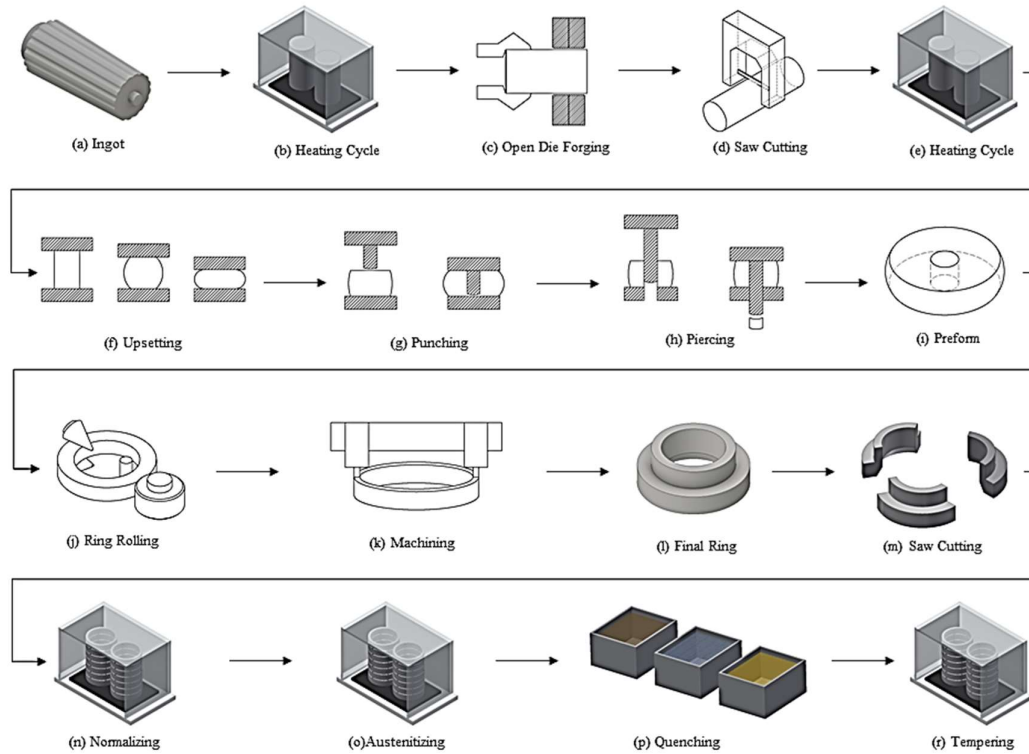
Figure 3-2: Manufacturing route for experimental rolled ring 8630 modified low alloy steel.

## 3.2.2   Steel making process

The weight and dimensions of the tapered ingot used to fabricate the experimental forging are displayed in *Table 3-3*. The ingot was initially electric furnace melted, then ladle refined and subsequently vacuum degassed, followed by bottom pouring into a tapered big ingot mold. The big end up design of the ingot geometry optimize the cleanliness and soundness of the ingot. According to the steel-making supplier, the surface hardness of the ingot after thermal treatment was lower than 285 BHN.

| Characteristic | Value |
|---|---|
| Top Dimension (mm) | 1219 |
| Bottom Dimension (mm) | 965 |
| Mean Area (sq. mm) | 36957 |
| Length (mm) | 3505 |
| Weight (Ton) | 22.74 |

Table 3-3: Ingot weight and dimensions.

### 3.2.3 Open-die Forging and Ring Rolling

The ingot was initially heated in a gas furnace up to 1300°C (forging temperature) in an oxidising atmosphere (air). After the heating cycle was completed, the ingot was forged on a 5000 - ton hydraulic open die press using a series of forging and heating operations to produce a 610 mm diameter billet. Due to confidential reasons, details about forging operations, dimensions and deformation steps, were not available to be displayed in this document.

As displayed in *Figure 3-3*, after open die forging, a ˜2- ton section (cylindrical block) was removed from the center of the billet length via saw cutting and subsequently heated, preformed and ring rolled to produce the experimental ring. In this regard, the cylindrical block was removed from the center of the billet length to reduce as much as possible the effect of segregation located at the top and bottom sides of the tapered ingot [98]. After being removed from the billet, the cylindrical block was charged directly into a gas furnace and heated up to 1250°C, after heating time was accomplished, the billet was removed from the furnace and transferred to a 4500- ton hydraulic blanking press to perform the upsetting, punching and piercing operations. Illustrations of the real open die and ring rolling processes in FRISA industries are shown in *Figure 3-4*.
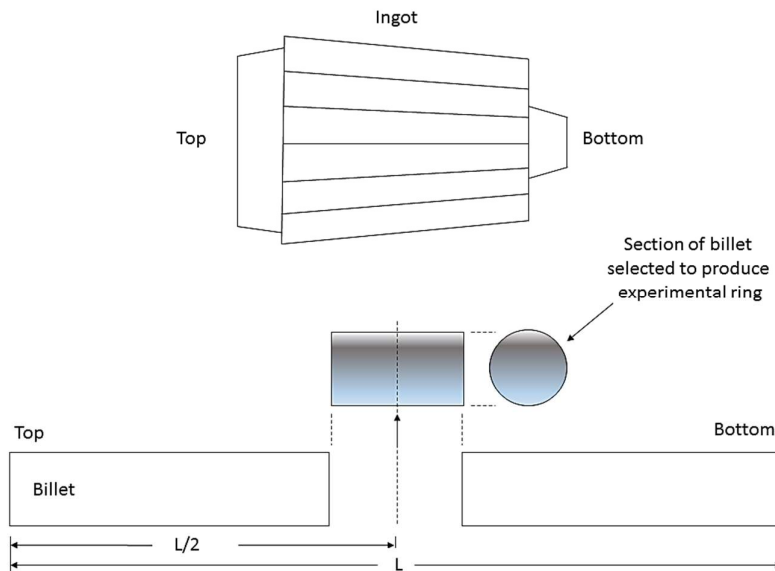


Figure 3-3: Section of the forged billet removed to fabricate experimental ring.

### 3.2.4 Machining and Sectioning of Ring Segments

After ring rolling, the experimental ring was cooled down until room temperature and subsequently machined according to the dimensions in Figure 3.1 with an approximate final weight of 1600 Kg. Although initially, the experimental proposal was to fabricate three full-scale rings to be separately quenched in the three selected cooling media, it was eventually realised that cutting three sections from different locations in the billet would inevitably result in different level of segregation on each one of three experimental rings. Considering the effect of segregation on the microstructure of steels during quenching [90] and its potential to mask the real effect of cooling rate changes on the mechanical properties, a decision was made to produce only one experimental ring which would be subsequently cut into three equal segments to reduce as much a possible the effect of segregation. As illustrated in *Figure 3-6*, the double-cross section ring was segmented into three equal sections of approximate 533 kg using an industrial saw cutting machine. The weight of the three segments was further verified using a precision industrial scale resulting in a final weight of 530 kg +/- 2 kg (tolerance) for each ring segment.
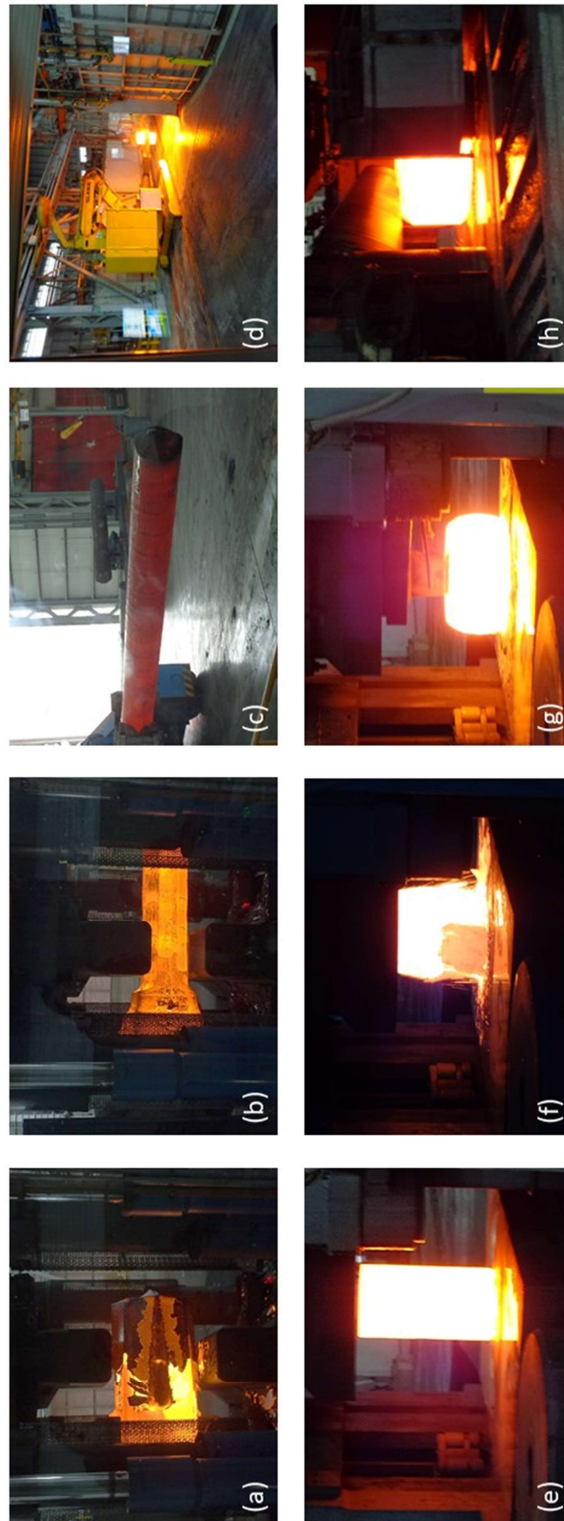
Figure 3-4: Open die and ring rolling processes in FRISA Industries. (a) start of open die process (cogging operation), (b) end of open die process (cogging operation), (c) forged bar after cogging, (d) section of the forged bar being removed from furnace to start ring rolling, (e) start of upsetting operation, (f) end of upsetting operation, (g) punching and piercing operations, and (h) ring rolling operation. (Company archive)

## 3.3   Industrial Heat Treatment of Ring Segments

As illustrated in *Figure 3-5*, after hot working, machining and saw-cutting operations, the three ring segments were industrially heat treated (normalizing, quenching and tempering) using different quenchants to examine the effect of industrial cooling rates on the microstructure and properties of 8630M low alloy steel.
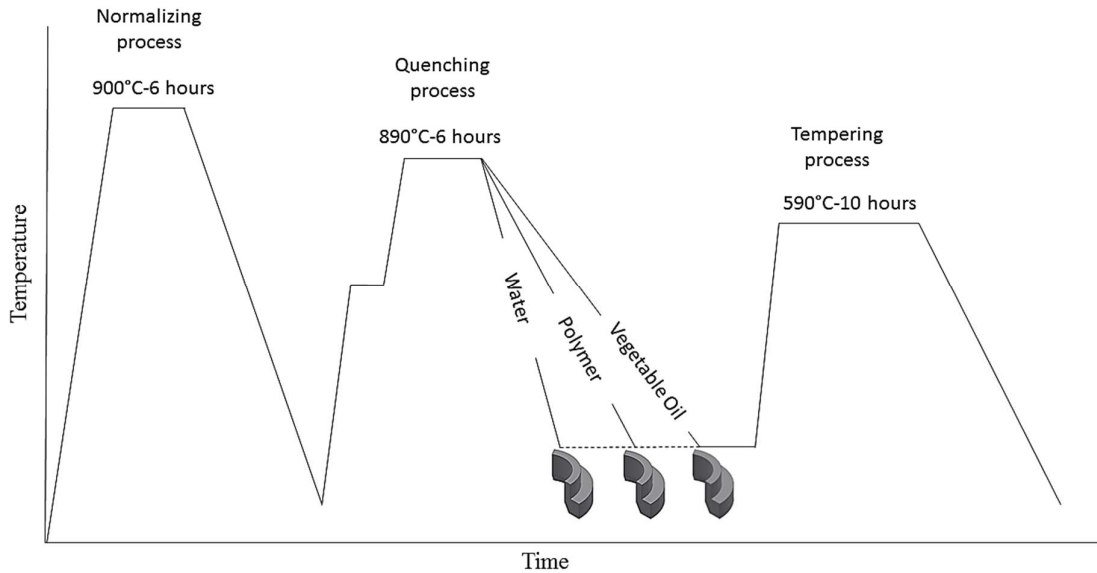


Figure 3-5: Scheme of industrial heat treatment for the 8630 modified low alloy steel ring segments.

### 3.3.1   Normalizing Treatment

In order to refine the prior austenite grain size coarsened due to the high temperatures used during hot working operations, the three ring segments were normalized in FRISA at 900°C for 5 hours and then cooled down in still air to room temperature. The selected normalizing temperature was in according with the specification requirements whereas, the soaking time was defined based on the thicker section (critical section, 250 mm) of the ring segments using a time-thickness ratio of 1/2 hour per 25 mm of thickness. The normalizing process of the three ring segments was carried out in chamber furnace heated by natural gas with a 15.0-ton capacity. The temperature tolerance and uniformity of the furnace were monitored according the API 6A Annex M 20th Ed. method.
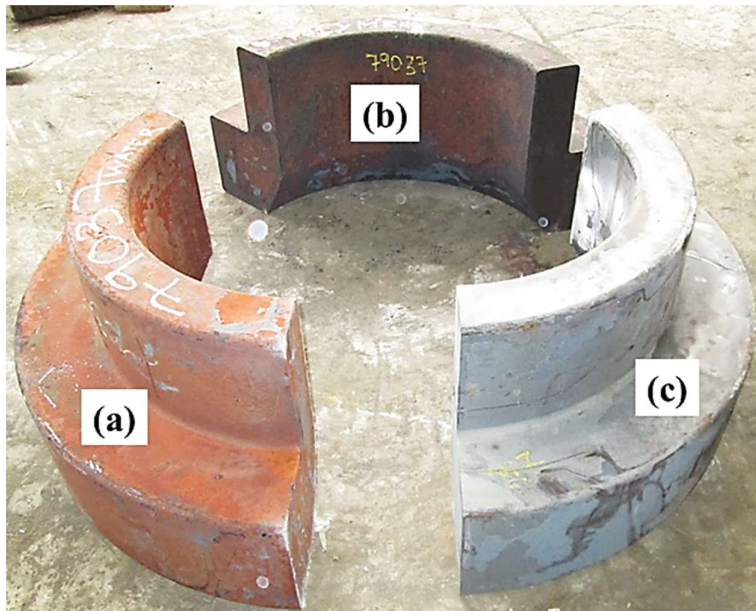
Figure 3-6: Experimental large-scale ring segments after saw-cutting operation: (a) ring segment for water quenching, (b) ring segment for polymer solution quenching and (c) ring segment for vegetable oil quenching.

### 3.3.1.1 Microstructure after Normalizing treatment

A 12 mm thick slice was removed from one of the ring segments after normalizing to evaluate its microstructure. One cubic-shape specimen (10 mm x 10 mm x 10 mm) was cut near to the centre of the thick cross section as seen in *Figure 3-7*, then mounted and prepared using metallographic methods described in 3.6.1.
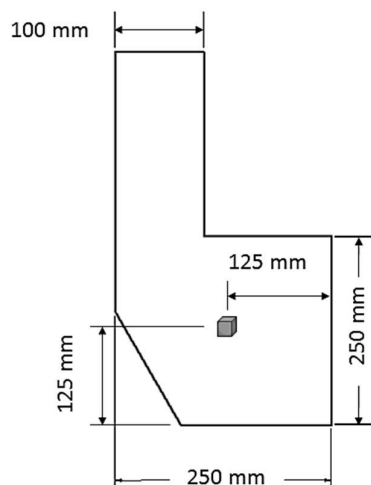


Figure 3-7: Specimen position for SEM characterization after normalizing treatment.

The specimen was pre-etched for 3 seconds with 3% Nital solution then immediately re-etched with 10% Sodium Metabisulfite solution for a period of 20 seconds. As seen in *Figure 3-8* the microstructure mostly consisted of pearlite, with a small amounts of granular bainite.
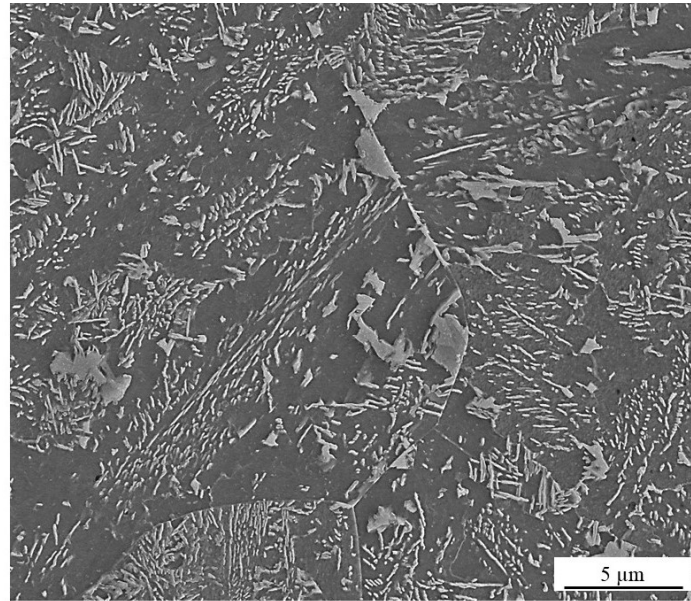


Figure 3-8: SEM Image of 8630M low alloy steel ring segment specimen normalized at 900°C for 5 hours and cooled in still air showing mostly pearlitic structure.

### 3.3.2 Quenching in Water, Aqueous Polymer, and Vegetable Oil.

After normalizing process, one segment was packed and shipped to SORBIT (Italy) to carry out the quenching process in vegetable oil; whereas the other two segments remained in FRISA (Mexico) for subsequent quenching in water and aqueous polymer solution as seen in *Figure 3-9*. In order to examine the effects of cooling rate produced by the different quenchants, two K-type thermocouples were inserted into each ring segment to measure the temperature-time conditions during the three quenching processes. Two 3.2 mm holes were drilled at the mid-wall location of the 100 and 250 mm cross sections to a depth of 125 mm as shown in *Figure 3-10*, then the thermocouples were inserted into the holes and insulated with ceramic fiber to prevent liquid infiltration during quenching operations. The measured cooling curves were recorded by using a QUADTEMP2000 4-channel data-logger with a sampling rate of 1 per second. *Figure 3-11*, illustrates the specification of data logger and K-type thermocouples used to measure the temperature-time conditions during industrial quenching.



Figure 3-9: Image of the industrial quenching tanks at FRISA: (a) polymer quenching tank and (b) water quenching tank (company archive).
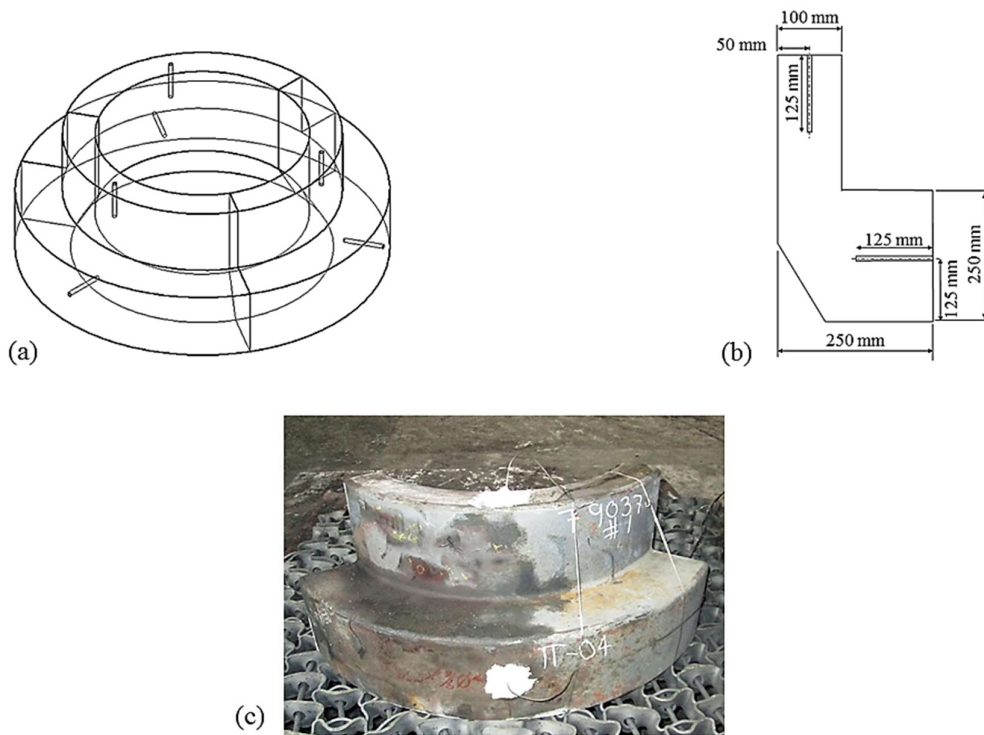
Figure 3-10: Schematic (a)isometric and (b)transverse view of the three ring segments with thermocouples holes, and (c) real experimental ring segment with thermocouples inserted on the thin and thick sections.



| Specification | |
|---|---|
| Accuracy (K type thermocouple) | ± 0.5°C |
| Temperature Resolution | 0.1°C |
| Type K Thermocouple Range | -260 to 1370°C |
| Maximum Thermocouple Resistance | 1000 Ω |
| Recording Interval | 4/sec to 1/day |
| Time Accuracy | ±1 min/month |
| Sensitivity | 41 µV/°C |

Figure 3-11: Specification of data logger and type K-type thermocouples used to measure the temperature-time conditions during industrial quenching of experimental ring segments *[99]*.

The data logger applies a calibration equation to convert the voltage to temperature. The most accurate way to fit the thermocouple data is by using rational polynomial functions as elucidated in Equation 5 , where $T$ represents the thermocouple temperature (°C), $v$ is the thermocouple voltage (in millivolts), and $T_0$, $v_0$, and the $p_i$ and $q_i$ are coefficients [100].

$$T = T_0 + \frac{(v - v_0)(p_1 + (v - v_0))(p_2 + (v - v_0))(p_3 + p_4(v - v_0))}{1 + (v - v_0)(q_1 + (v - v_0))(q_2 + q_3(v - v_0))} \qquad (5)$$

### 3.3.2.1 Evaluation of cooling capacity of quenching media

Before proceeding to carrying out the industrial quenching of the three experimental ring segments, the cooling capacity of the three quenchants used in this research was evaluated under laboratory conditions by using an IVF® smart quench quenchometer, with 12.5 mm diameter 8630 low alloy steel probes as illustrated Appendix C. The probes were heated to 875°C and then separately quenched for 80 s in water, hazelnut vegetable oil, and 10 % aqueous solution of a PAG (Polyalkylene glycol) polymer. As elucidated in *Figure 3-12*, the maximum cooling rates for, water, aqueous polymer solution and vegetable oil were 87.6, 67.1 and 60.8°C/s respectively. The results indicate that water media produced the higher cooling rate, in contrast vegetable oil developed the slower cooling rate while the cooling rate of aqueous polymer solution was between those of water and vegetable oil.
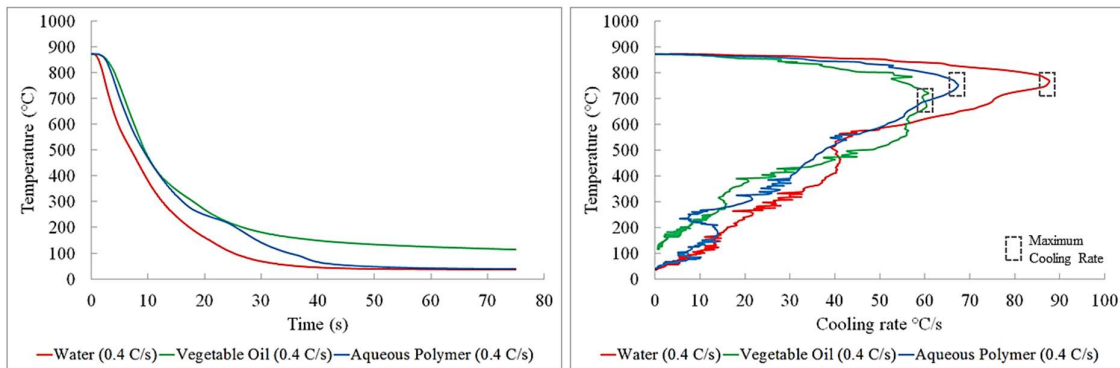


Figure 3-12: Cooling curves and cooling rate plots of Ø12.5 mm 8630M low alloy steel specimens quenched in water, aqueous polymer solution and vegetable oil.

### 3.3.2.2 As-quenched microstructure of ∅12.5 mm specimens after quenching in different cooling media

A 2 mm thick slice was removed from each one of the 12.5 mm probes after quenching under laboratory conditions to evaluate their microstructure. One penny-shaped specimen (12.5 x 2 mm) was cut near to the tip of the three steel probes, then mounted and prepared using metallographic methods described in 3.6.1.

The specimens were pre-etched for 3 seconds with 3% Nital solution then immediately re-etched with 10% Sodium Metabisulfite solution for a period of 20 seconds. *Figure 3-13*, shows a typical as-quenched martensitic structure formed in the three probes quenched in water, polymer solution and vegetable oil.
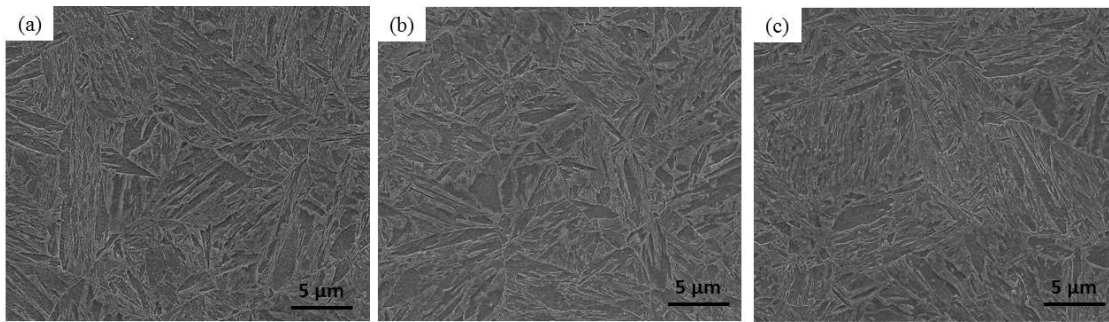


Figure 3-13: As-quenched martensitic structures of the small 8630M steel probes quenched in (a) water, (b) polymer solution and (c) vegetable using the IVF smart quenching system.

### 3.3.2.3 Water quenching process

The first ring segment was subjected to quenching in water media with a viscosity value of 0.987 $mm^2$/s. Initially the ring segment was charged into a furnace preheated at 650°C for 1 hour, to promote uniform temperature distribution and then the temperature was raised to 890°C and hold it for 6 hours to obtain austenite structure all along the geometry of the part. A chamber furnace heated by natural gas with a 15.0-ton capacity was used for the austenitizing process and the temperature tolerance and uniformity of the furnace were monitored according the API 6A Annex M 20th Ed. Method. As seen in *Figure 3-14* (a), after the soaking time was concluded, the ring segment, in its austenitic condition was removed from the furnace, transferred to quenching tank in 65 s and immersed into water media for approximate 2 hours

in order to reduce the temperature at the centre of the thick section (250 mm) below the martensite start transformation point. The quenching tank used for water quenching has volume of 90 m$^3$ and counts with a propeller system to uniformly circulate the fluid to agitation levels of 0.30-0.60 m/s average. Finally, the temperature of the water at the start and completion of the quenching process were 25 and 29°C respectively.

### 3.3.2.4   *Polymer quenching process*

The second ring segment was subjected to quenching in a 10 % aqueous solution of a PAG (Polyalkylene glycol) polymer with a viscosity value of 2.93 mm$^2$/s. Initially the ring segment was charged into a furnace preheated at 650°C for 1 hour, to promote uniform temperature distribution and then the temperature was raised to 890°C and hold it for 6 hours to obtain austenite structure all along the geometry of the part. A chamber furnace heated by natural gas with a 10.0-ton capacity was used for the austenitizing process and the temperature tolerance and uniformity of the furnace were monitored according the API 6A Annex M 20th Ed. Method. As seen in *Figure 3-14* (b), after the soaking time was concluded, the ring segment, in its austenitic condition was removed from the furnace, transferred to quenching tank in 65 s and immersed into polymer solution for approximate 2 hours in order to reduce the temperature at the centre of the thick section (250 mm) below the martensite start transformation point (Ms). The quenching tank used for water quenching has volume of 90 m$^3$ and had propeller system to uniformly circulate the fluid to agitation levels of 0.25-0.50 m/s average. Finally, the temperature of the polymer solution at the start and completion of the quenching process were 23 and 26°C respectively.

### 3.3.2.5   *Vegetable oil quenching process*

The last ring segment was subjected to quenching in hazelnut oil with a viscosity value of 42.33 mm$^2$/s as shown. Unfortunately, the preheating step of 650°C-1 h of this latter segment was not reproduced due to difficulties to control the temperature of the furnace during heating. In this setup the ring segment was heated directly to 890°C and hold it for 6 hours to obtain austenite structure all along the geometry of the part. After the soaking time was concluded, the ring segment, in its austenitic condition was removed from the furnace, transferred to quenching tank in 50 s and immersed into vegetable oil for approximate 2 hours in order to reduce the

temperature at the centre of the thick section (250 mm) below the martensite start transformation point. The quenching tank used for water quenching has volume of 70 m3 and counts with a propeller system to uniformly circulate the fluid to agitation levels of 0.30-0.70 m/s average. Finally, the temperature of the vegetable oil at the start and completion of the quenching process were 49 and 54°C respectively. No pictures of the quenching process were allowed to be taken inside SORBIT facilities.
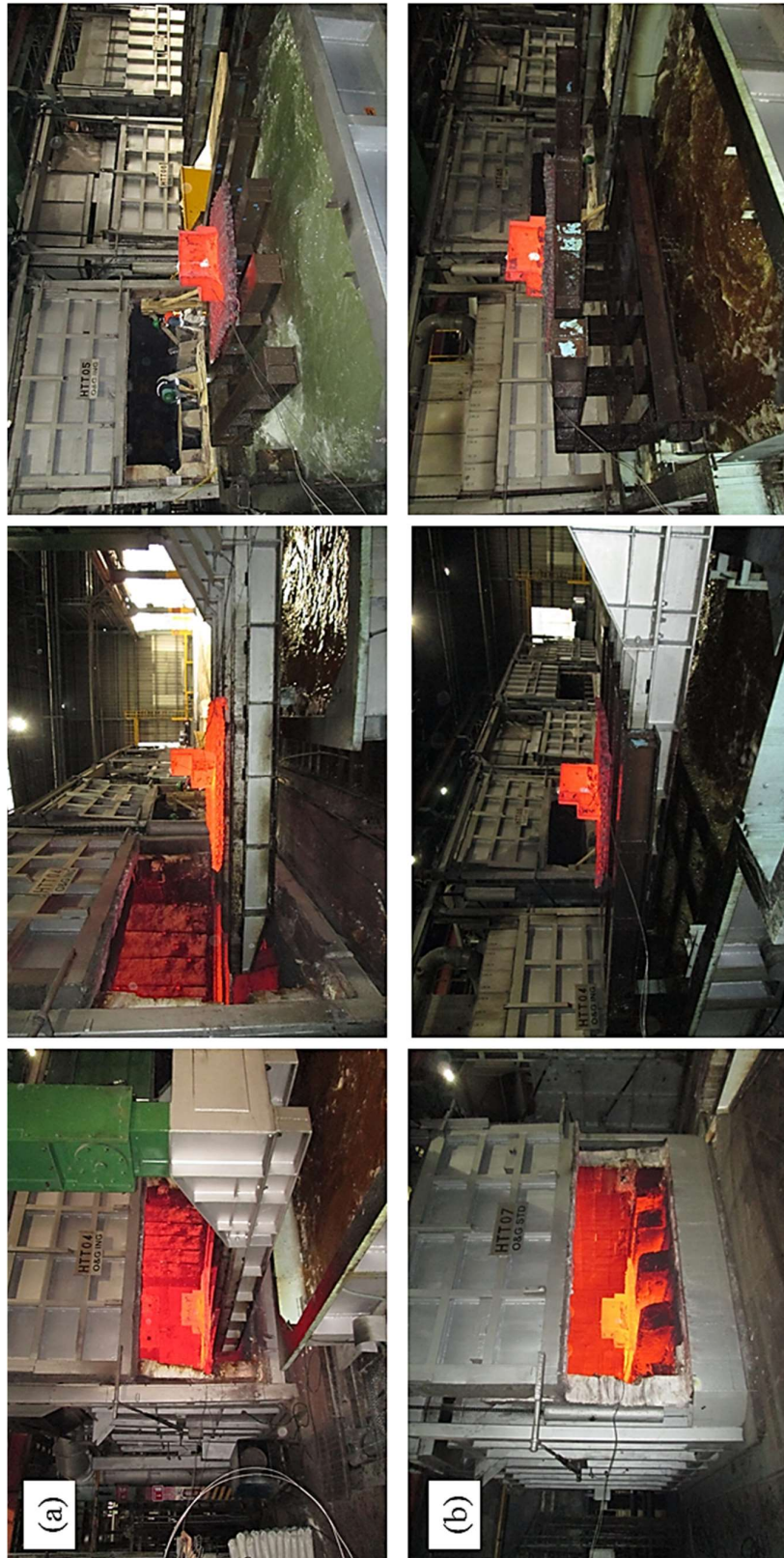
Figure 3-14: Illustration of the (a) water and (b) polymer solution quenching processes of 8630M low alloy steel ring segments carrying out in FRISA.

### 3.3.3  Tempering Treatments

After quenching process, the ring segment quenched in vegetable oil in SORBIT (Italy) was send back to FRISA (Mexico) to be subjected to tempering along with the two ring segments quenched in water and aqueous polymer solution. The three ring segments were then tempered at 590°C for 10 hours and then cooled down in still air to room temperature. Although the tempering temperature range (566 - 650°C) indicated in the material specification was not too restrictive, the selected tempering temperature was determined by using regression equations used for the company to estimate the appropriate tempering temperature to achieve yield strength values above 750 MPa and CVN impact properties above 28 J.As shown in *Figure 3-15*,  these type of regression equations, employ historical data such as key heat treatment parameters, chemical composition and mechanical properties results as input parameters to correlate tempering temperature and mechanical properties. On the contrary the soaking time of 10 hours was strictly defined in the material specification. The tempering process of the three ring segments was carried out in a chamber furnace heated by natural gas with a 15.0 t capacity. The temperature tolerance and uniformity of the furnace were monitored according the API 6A Annex M 20th Ed. method.
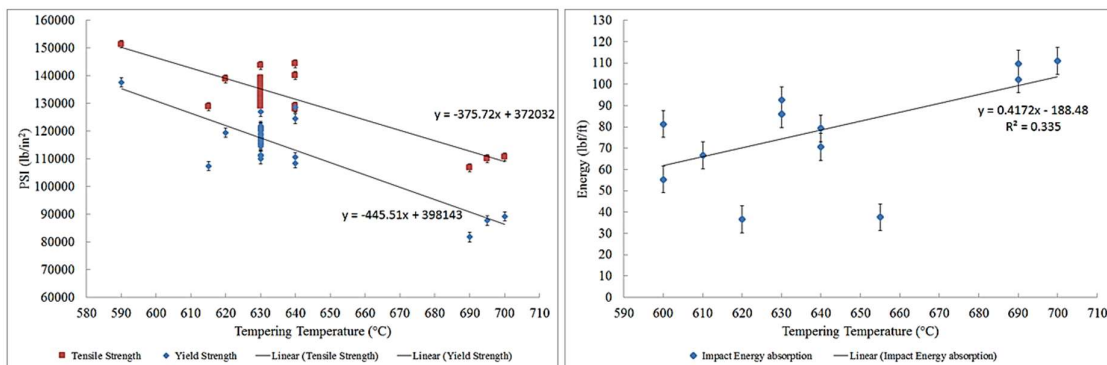


Figure 3-15: Relationships between YS, UTS and CVN with tempering temperature designed for 170 -250 mm thick-wall forgings made of 8630M low alloy steel (company data).

## 3.4   Dilatometry Measurements of AISI 8630 Low Alloy Steel

Dilatometric investigations were carried out at TA Instruments Laboratories (Hüllhorst, Germany) using a quenching dilatometer DIL805 A/D. Samples were cut from the centre of the thick (250 mm) cross section of a slice removed from the experimental forging after normalizing treatment. Hollow cylindrical specimens of 4 mm x 2 mm x 10 mm were then machined in Sheffield University according to DIN 2310 – IK standard as illustrated in *Figure 3-16*.
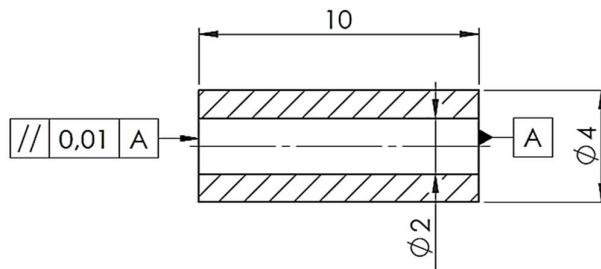


Figure 3-16: Quenching hollow sample used for dilatometric studies.

After machining process, the specimens where packed and shipped to TA Instrument laboratories for subsequent dilatometric work. An induction system was used to heat the specimens at 890°C for 10 minutes using heating rate of 500°C/min. Following to holding time, the specimens were continuously cooled over a range of cooling rates from 0.01 to 50 °C/s. Additionally, one specimen was firstly heated at constant rate of 2°C/min to determine the transformation temperatures on heating ($A_{c1}$ and $A_{c3}$) of the selected steel.

Considering that the decomposition of austenite into different transformation products such as ferrite, pearlite, bainite and martensite is accompanied by a change in specific volume associated to lattice structural changes during cooling; it is feasible to determine the start and finish transformation temperatures for the aforementioned transformation products. The start transformation point can defined as the temperature at which the linear thermal expansion first deviates from linearity.  Location of the point at which the deviation occurs is obtained by extrapolating the linear portion of the thermal expansion curve. Similarly, the transformation finish temperature is determined by extrapolating the linear portion of the curve after

transformation [53]. An example of the decomposition of austenite into bainite and martensite can be seen in *Figure 3-17*.
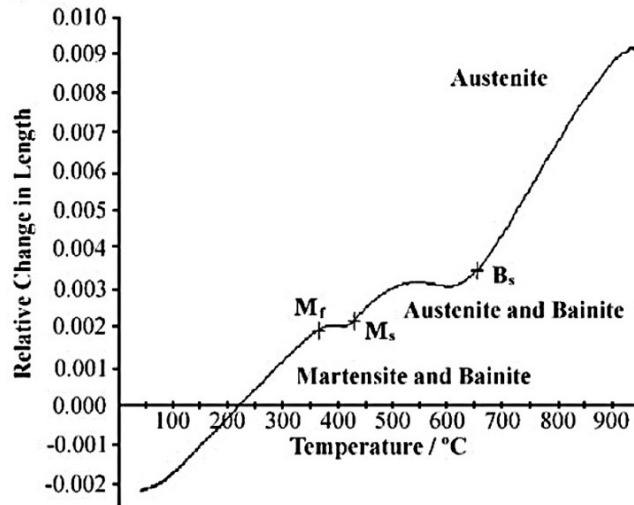


Figure 3-17: Cooling dilatometric curve showing start and finish transformation temperatures for low carbon manganese steel (Fe – 0.07C–1.56Mn–0.41Si) after cooling at a rate of 234 K s/-1. *[53]*

Plots of length change against temperature during cooling were obtained after quenching dilatometry, then the start and the end of the phase transformations were determined based on the volume changes resulting from the initiation and termination of phase transformations. Finally, the selected cooling rates were represented on a time-temperature plot, overlapping and connecting the start and finish phase transformation points on each cooling curve profile. After cooling, the specimens were cut and metallographically prepared for subsequent microstructural characterization. The metallographic evaluation of the specimens prior to the dilatometric measurements revealed an average prior austenite grain size of 8-8.5 per ASTM E112 for the different specimens evaluated.

## 3.5 Mechanical Testing

Tensile, impact and CTOD testing were performed on specimens removed from the experimental pieces using different combinations of cooling media (water, aqueous polymer and vegetable oil) and cross sections (100 and 250 mm). However as illustrated in *Table 3-4*, not all the conditions could be assessed by CTOD testing mainly due to economic constraints. Nevertheless, an attempt was made to cover the most relevant conditions based on the variations observed on the yield strength properties, considering the well-known correlation between this property and CTOD parameter. This relationship (Yield strength – CTOD) will be further explained in the following chapters.

| Ring segment | Cooling media | Tempering temperature (°C) | Cross Section (mm) | Specimen | Tensile Testing | Impact Testing | CTOD Testing |
|---|---|---|---|---|---|---|---|
| 1 | Water | 590 | 100 | 1 | ✓ | ✓ | ✓ |
| | | | 250 | 2 | ✓ | ✓ | * |
| | | | | | | | |
| 2 | Polymer | 590 | 100 | 3 | ✓ | ✓ | ✓ |
| | | | 250 | 4 | ✓ | ✓ | ✓ |
| | | | | | | | |
| 3 | Vegetable Oil | 590 | 100 | 5 | ✓ | ✓ | ✓ |
| | | | 250 | 6 | ✓ | ✓ | * |

Table 3-4: Summary of mechanical tests performed on the experimental ring segments after heat treatment. Specimens 2 and 6 were not subjected to CTOD testing.

### 3.5.1 Extraction Location of Specimens

After tempering treatment, specimens for tensile, impact and CTOD testing were taken from the ring segments previously quenched in water, polymer and vegetable oil. The material to fabricate the tensile and impact specimens was removed from the mid-thickness of the 100 mm and 250 mm wall sections as close as possible to the measuring point of thermocouple as shown in *Figure 3-18* and *Figure 3-19*.
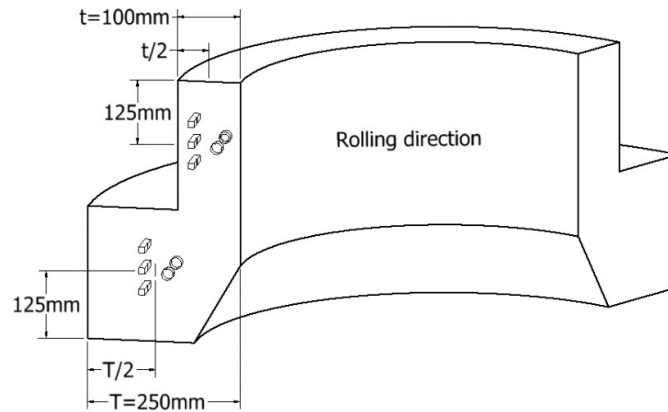


Figure 3-18: Position sampling of (a) tensile and (b) impact and specimens on the ring segments.



Figure 3-19 Sampling location zone for (a) tensile, impact and (b) CTOD testing specimens on the ring segments. Units in millimetres.

### 3.5.2    Tensile Testing

In order to determine the tensile properties of the ring segments subjected to the different cooling conditions, tensile tests were carried out at room temperature using a 300 kN hydraulic universal testing machine (Tinius Olsen). Round tension specimens according to ASTM standard E8/E8M − 16a [101]  were machined with the following dimensions: gauge length (G) of 50 mm, diameter (D) of 12.5 mm, radius of fillet (R) of 10 mm and length of reduced section (A) of 56 mm. The specimens were machined along the transverse rolling direction as this direction represents the minimal (critical) grain flow orientation in the experimental rolled ring.

### 3.5.3    Impact Testing

Impact tests were carried out at -30°C using a pendulum impact tester model IT406, Tinius Olsen. V-notch specimens according to ASTM standard E23 − 16b [102] were machined with the following dimensions: length (L) of 55 mm, width (W) of 10 mm, thickness (T) of 10 mm, notch radius of 0.25 mm and notch angle of 45° The notch of the impact specimens was orientated along the transverse rolling direction of the experimental rolled ring. A low temperature chamber cooled by propylene glycol and dry ice was used to induce the required temperature. All the tensile and impact tests were carried out in FRISA Laboratories. *Figure 3-20* shows the tensile and impact specimens after machining process.
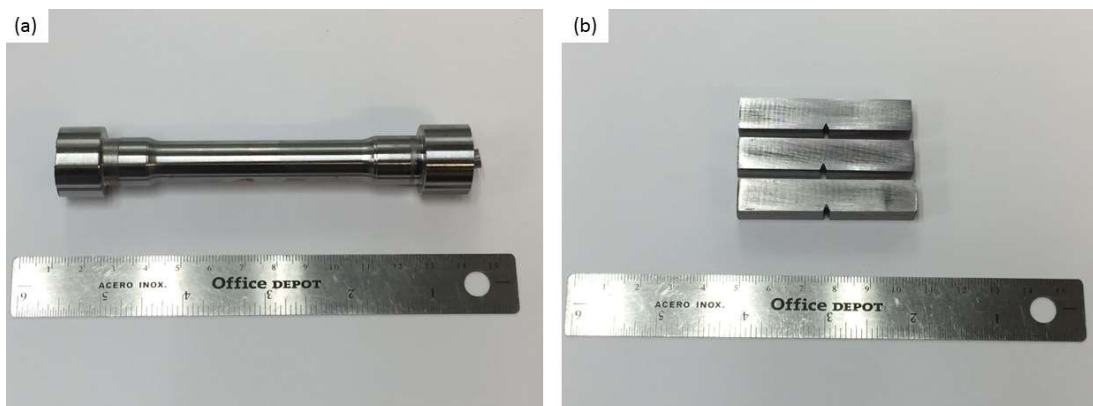


Figure 3-20: Illustration of (a) tensile and (b) impact specimens after machining process.

### 3.5.4   CTOD Testing

Compact Tension C (T) specimens with integral knife edges were machined from the forging segments in accordance with latest version of BS7448 Part 1 [84]. The specimens were removed from the mid-thickness of the 100 mm and 250 mm cross section next to the thermocouple locations as shown in *Figure 3-21* and each specimen had a nominal thickness of 25 mm and an effective width of 50 mm (see Appendix D).
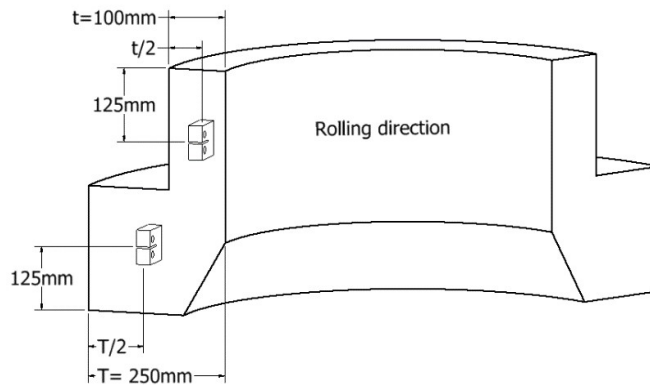


Figure 3-21: Position sampling of CTOD specimens on the ring segments.

The specimens were notched by electro discharge machining (EDM) and fatigue pre-cracked to a target *a/W* value of 0.5 (where *a* is the initial crack length and *W* is the effective width). All specimens were orientated in a similar manner as for the impact testing using in the L-C (Longitudinal-Circumferential) direction and tested at 0°C using an INSTRON 8500 B107 servo hydraulic machine. A low temperature chamber cooled by nitrogen was used to induce the required temperature and two thermocouples were welded to the specimens to control and monitor the temperature of the specimens. The CTOD parameter for specimens 1 to 6 was determined according to Equation 2 at the first attainment of maximum force. *Figure 3-22*, illustrates C (T) specimen 1 inside the chamber after fracture toughness testing.
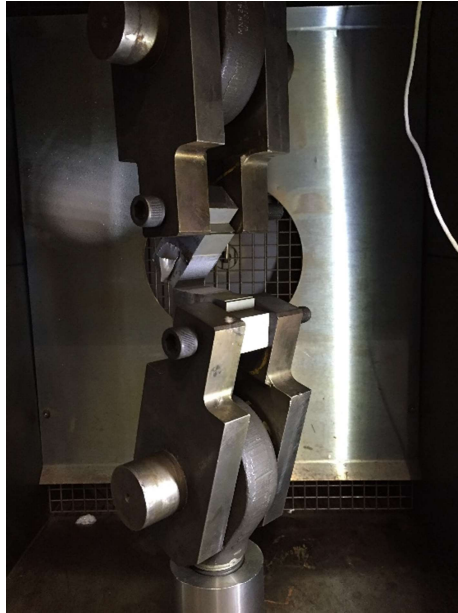
Figure 3-22: illustration C(T) specimen 1 inside the chamber after fracture toughness testing.

## 3.6   Materials Characterization

### 3.6.1   Optical and Scanning Electron Microscopy (SEM)

Specimens for microstructure characterization were polished up to 0.05 µm by using an automatic grinding and polishing equipment. Detailed sample preparation steps are illustrated in *Table 3-5*. After finishing the polishing process, the specimens were cleaned with distilled water and ethanol and subsequently pre-etched for 3 seconds with 3% Nital solution, then immediately re-etched with 10% Sodium Metabisulfite solution for a period of 20 seconds. After etching process, the specimens were placed in a desiccator for further optical and SEM evaluation. The microstructure evaluation and fracture surface analysis was carried out on the crack propagation face of the broken CVN and CTOD specimens. The light microscopy examination was carried out using a microscope (Leco DM 400) whereas the scanning electron microscopy examination was conducted using a FEI Inspect-F50 scanning electron microscope field emission gun (FEG) operated at 20kV with a spot size (dp) of 2.0 and a working distance range of 9 – 12 mm.

| Surface | Abrasive/Size | Load (N) | Speed rpm/Direction | Time (minutes) |
|---|---|---|---|---|
| Sic Paper | 120 to 1200 / water cooling | 27 | 320/ Comp. | 3 |
| Diamond Cloth | Diamond suspension / 3 μm | 25 | 110/Comp | 10 |
| Diamond Cloth | Diamond suspension / 3 μm | 25 | 110 | 10 |
| Chem. Cloth | Colloidal silica / 0.05μm | 25 | 110-150 | 5 |

Table 3-5: Sample preparation steps for analysis by optical and SEM microscopy.

### 3.6.2   Fracture Surface Analysis

The fracture surface analysis was carried out on the ductile and brittle zones as illustrated in *Figure 3-23*. The fractographic analysis was conducted using FEI Inspect-F50 scanning electron microscope field emission gun (FEG) operated at 20kV with a spot size (dp) of 2.0 and a working distance range of 9 – 12 mm. Before SEM examination, the fracture surfaces were fully immersed in xylene and isopropanol and successively immersed in an ultrasonic bath for 20 minutes to remove the oil (protective coat) and any other potential source contamination.
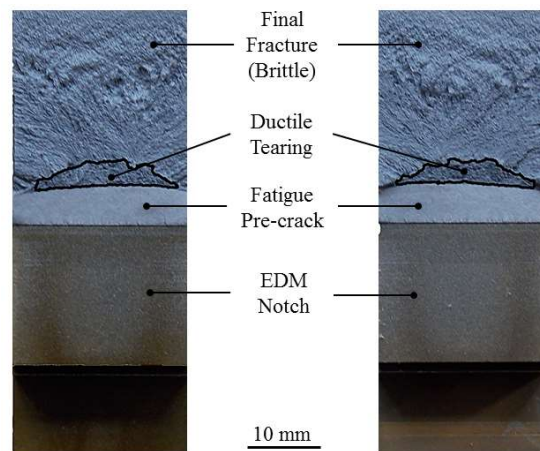


Figure 3-23: Two fracture surfaces of a  Compact tension C (T) specimen after CTOD testing indicating distinctive zones.

### 3.6.3   Grain Size Evaluation

Although, grain size evaluation is out of the scope of this study due to the forging conditions an austenitizing temperatures were the same for the three ring segments; some grain size measurements were carried out on some specimens after tempering only for information purposes.

Revealing prior austenite grain boundaries on low alloy steels after tempering can be difficult particularly if the phosphorus content of the material is low and tempering temperatures used are high [103]. However, Vander Voort [103], successfully etched tempered low alloy steel specimens by using a hot solution consisting of  picric acid (saturated with water),  1ml hydrochloric (HCL) acid and  14.18 gr of Nacconal90G® (wetting agent). In this sense, material near to crack propagation faces on the  CVN  specimens was removed and metallographically prepared as described in section 3.6.1. The mounted samples were then etched using a modified version of the Vander Voort procedure as illustrated in *Table 3-6*.  The grain size measurements were carried out in an image analyser (Omni Met, Buehler) using linear intercept methodology according to ASTM E112 − 13 [104].

| Step | Process |
|------|---------|
| 1 | Mix picric acid with water and stir for 20 minutes (saturated solution) |
| 2 | Add 5-7 ml of HCL to 500 ml of the saturated solution |
| 3 | Heat solution between 80-90°C |
| 4 | Immerse the specimen into the solution for 40-80 s |
| 5 | Wash and dry thoroughly |
| 6 | Light back polish on stationary cloth with 0.5 μm  alumina to remove excess etching if needed |
| 7 | Wash and dry thoroughly |

Table 3-6: Etching procedure to reveal PAGB on AISI 8630M low alloy steel specimens after 590°C.

The results corresponding to the grain size measurements carried out on a CVN specimen corresponding to the thick section (250 mm) of the forging segment quenched in polymer and tempered are illustrated in *Figure 3-24* and *Figure 3-25*. As seen in these pictures, the material analysed specimen showed an average prior austenite grain size of 18 μm.
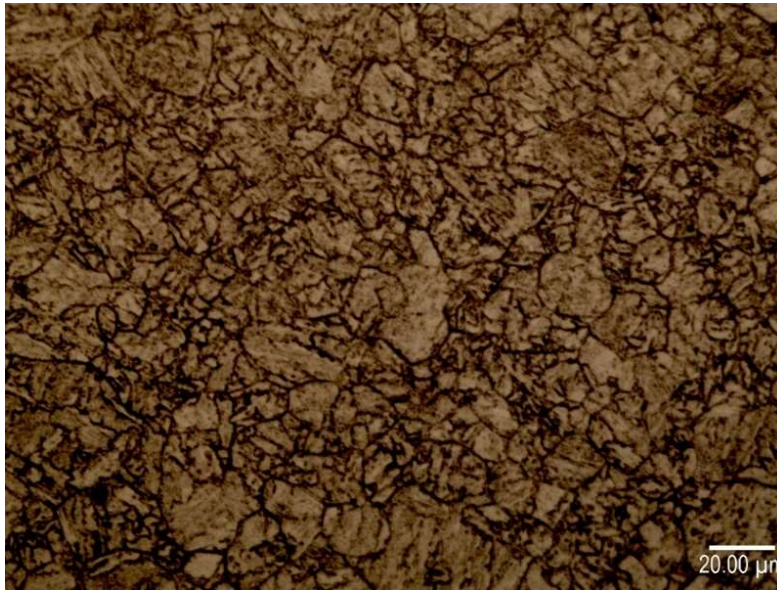
Figure 3-24: Quench and tempered AISI 8630M steels showing grain boundaries in specimen 1. Etched according Vander Voort Method. 500X.
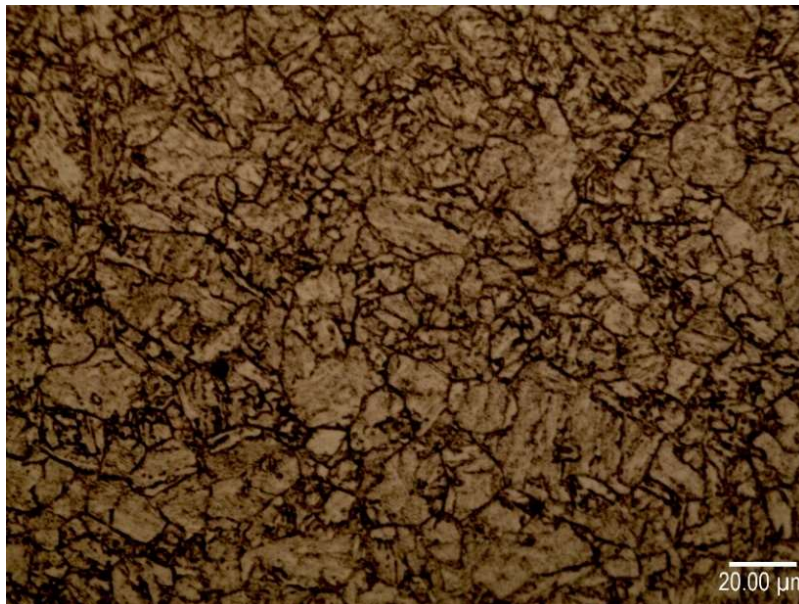


Figure 3-25: Quench and tempered AISI 8630M steels showing grain boundaries in specimen 2. Etched according Vander Voort Method. 500X.

### 3.6.4 Microstructural Evaluation

As reported by several authors [95, 71, 105] , determine the percentage of constituents for mixtures of martensitic and bainitic structures can be complex a task due to the great morphological similarities between tempered martensite and tempered bainite. As explained below, a method proposed by Kim et al. [105] and Ramesh et al. [106] was followed. On their work about characterization of tempered bainitic and martensitic microstructures, Kim and co-workers quantitatively characterize the microstructure of quench-and-tempered specimens in the as-quenched condition; since by doing this it is actually possible to distinguish between martensite and bainite. The above, bearing in mind that on the as-quench condition, martensite lacks of carbide precipitation whereas extensive carbide precipitation can be easily observed on bainite after quenching. However, using this method directly on the experimental parts used in the present investigation, would be extremely difficult, considering that, in practice, is very difficult saw-cutting large sections of material after quenching due to its high surface hardness and due to technological limitations associated to the saw-cut equipment. In this context, Ramesh and Prabhu [106], successfully quantified the microstructures produced during quenching in different cooling media by superimposing measured cooling curves of (W) water and (PS) polymer solutions on a CCT diagram as displayed in *Figure 3-26*.
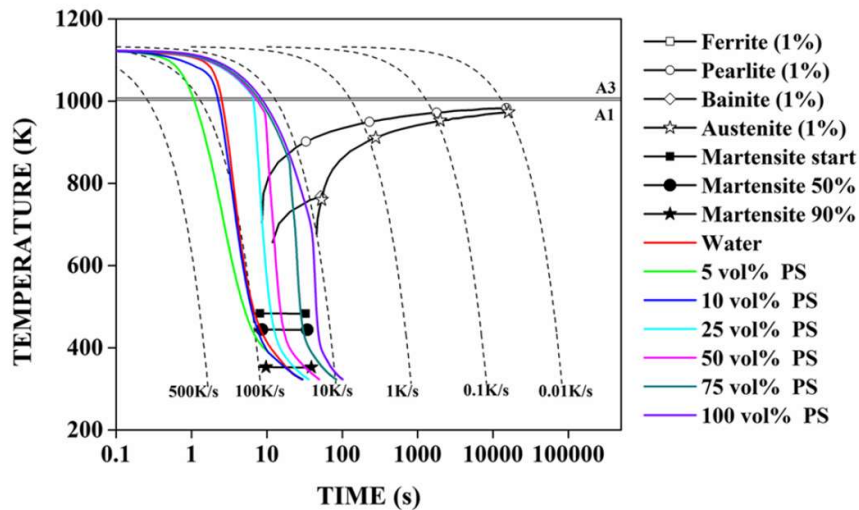


Figure 3-26: CCT curve of AISI 1080 steel along with measured cooling curves of (W) water and (PS) polymer solutions quenching.

Based on this study a decision was then made to estimate the phase fractions of the industrially heat treated segments by overlapping the industrial cooling rates on the CCT diagram produced by dilatometry for the AISI 8630M steel used in this research as illustrated in Chapter 5. Subsequently, the dilatometry specimens associated to the industrial cooling curves were metallographically prepared and characterized by using the method proposed by Kim et al. described above. Finally, the microstructures were manually selected and identified using Image J software. Then a colour white was assigned to the martensite structure and black colour was assigned for the bainite structure then the software determined what fraction of the area of the image was black and what fraction was white, resulting in the obtention of volume fraction measurements for the analysed specimens. Finally, it is important to point out, that the accuracy of the method proposed might not be accurate enough when estimating the constituent's fractions on the experimental forging so a level of certainty related to the constituents fractions might be expected.

# 4 Effect of Water, Aqueous Polymer and Vegetable Oil Quenchants on Cooling Characteristics of Ring Segments Industrially Heat-Treated

## 4.1 Introduction

This chapter presents the results of the quenching treatments conducted on three experimental ring segments separately quenched in water, aqueous polymer solution and vegetable oil, under industrial conditions. The cooling conditions during quenching strongly determine the microstructure and properties after heat treatment, where in general, depending on their position on the CCT diagram and the chemistry of the material in question, a fast cooling rate is associated to martensite, whereas a slow cooling rate might be associated to the formation of structures such as ferrite or pearlite. In addition, relevant heat transfer mechanisms occurring during quenching, such as vapour film, nucleate boiling and convective cooling can be estimated by analysing the shape of the cooling curves produced during quenching. In this regard, several methods such as the ASTM D6200-01(2012) [107] , ASTM D6482-06(2016) [108] and ISO 9950 [109] standard test methods have been developed for determination of cooling characteristics of water, aqueous polymers and oil quenchants. However, these methods present some limitations since they are performed under laboratory conditions using small Inconel probes and do not reflect the real cooling conditions of an industrial quenching process which is strongly affected by the agitation system, tank design, and geometry of the part being quenched. Considering this, the purpose of this study was to characterise the cooling curves developed during a real industrial quenching process of large ring segments quenched in different cooling media. For the sake of simplicity, the six combinations of cooling media and cross sections investigated in this research were defined as "conditions" and each "thickness-cooling" condition, in turn was identified as follows: "100-W" and 250-W" respectively stand for the 100 and 250 mm cross sections of the ring segment quenched in water, whereas "100-P" and 250-P" stand for the 100 and 250 mm cross sections of the ring segment quenched in polymer, finally "100-O" and 250-O" stand for the 100 and 250 mm cross sections of the ring segment quenched in vegetable oil. Furthermore, from this section on, the 100 mm cross section of the ring segments might refer as "thin section" and the 250 mm cross section might be correspondingly referred as "thick section".

## 4.2 Results

### 4.2.1 Cooling characteristics on the 100 mm section of the ring segments

#### 4.2.1.1 Cooling curves

Before quenching in water, polymer and vegetable oil the thermocouples registered austenitizing temperatures of 887, 894 and 889°C in the thin section of the three segments. Respectively as illustrated in Figure 4-1. During the first 50 s, the drop in temperature at the center of the thin section of the segments quenched on the different cooling media was very small. The slight drop in temperature during this period indicates the transfer of the ring segments from the furnace to their respective quenching tanks. The average temperature drop recorded during this period was around 5°C for the three conditions. After 70 - 75 s the ring segment quenched in water was fully immersed into the agitated cooling media. At this point the thermocouples indicated a temperature of 825 - 840°C. On the other hand, the ring segment quenched in polymer was fully immersed at a time of 60 - 65 s with a corresponding temperature of 880-884°C. The ring quenched in vegetable oil was fully immersed at a time of 55 - 60 s with a corresponding temperature of 885 - 888°C. Once the quenching process started for the three segments, it could be observed that from 800 to 500°C (cooling time parameter, λ), water and vegetable oil generated the faster and slower cooling times corresponding to 154 s and 253 s respectively, while an intermediate cooling time of 231 s between those of water and vegetable oil, was achieved by aqueous polymer.

Approximately between 420 and 350°C (black dots in Figure 4-1) a change in the slope was observed in three cooling curves. This alteration in the cooling regime is attributed to the effect of latent heat release due to the onset of phase transformation in the material during quenching. On this regard, the approximated start transformation temperatures for the segments quenched in water, polymer and vegetable oil were 353, 369 and 405°C respectively. Finally, at temperatures near to 100°C, an isothermal step could be observed in the water and aqueous polymer curves, which can be associated to the boiling point of water. This phenomenon was not observed in the vegetable oil since its boiling point is much higher than those of water and aqueous polymer solution.
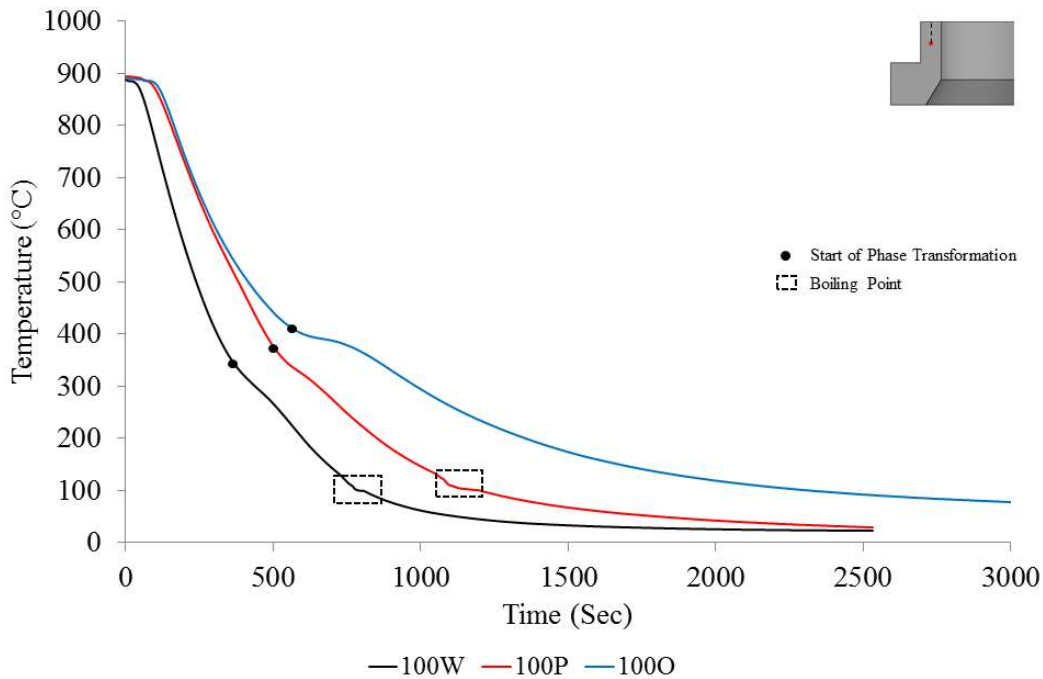
Figure 4-1: Cooling curve profiles recorded by the thermocouples located at the center of the 100 mm cross sections of the ring segments quenched in water, polymer and vegetable oil.

### 4.2.1.2 Cooling rates

The first derivatives (change rate of temperature with time) of the cooling curves for the three cooling conditions studied in this research were determined in order to observe with more detail the wetting kinetics, and phase transformations during industrial quenching as a function of temperature. Figure 4-2 shows the cooling rates produced on the thin section of the ring segments quenched in the different media.

Once the quenching started, the cooling rates for the three ring segments were very similar regardless of the cooling media, however after cooling rate values around 1°C/s were reached, the three segments starting to experience changes in their cooling rate pattern. As the temperature decreased, the effect of the different cooling media became stronger, leading to different maximum cooling rates of 2.17, 1.52 and 1.61°C/s on thin section of the segments quenched in water, polymer and vegetable oil respectively. It is noteworthy to mention that the maximum cooling rate reached by polymer was lower than that of vegetable oil. This was unexpected considering the higher transfer rates usually obtained with aqueous solutions of polymer. After reaching the maximum cooling rate, an expected reduction on the rate of

cooling is observed in the water, polymer and vegetable quenchants due to the prior onset of the nucleate boiling stage, however the cooling rate curve corresponding the polymer quenching exhibited a small hump around 500°C which could be attributed to the reformation of a polymer film during nucleate boiling [32]. Around 470°C, an even smaller hump was observed on the cooling curve corresponding the vegetable oil, the reason for this it's not clear however it might be argued that a similar thermal arrest mechanism as the one describe above occurred during the nucleate boiling stage with vegetable oil. As stated previously, between 420°C and 350°C the latent heat effects due to the onset of the phase transformations were clearly displayed in all the cooling curves and cooling rate profiles. In this sense, According to the continuous cooling transformation diagram for AISI 8630 low alloy steel built by Atkins [110], the transformation temperatures generated during industrial quenching in water, polymer and vegetable oil may be related to the onset of bainite and martensite. Finally, as previously described in section 4.2.1.1, the peaks associated to the boiling point of water and polymer around 100°C were also observed in their corresponding cooling rate profiles.
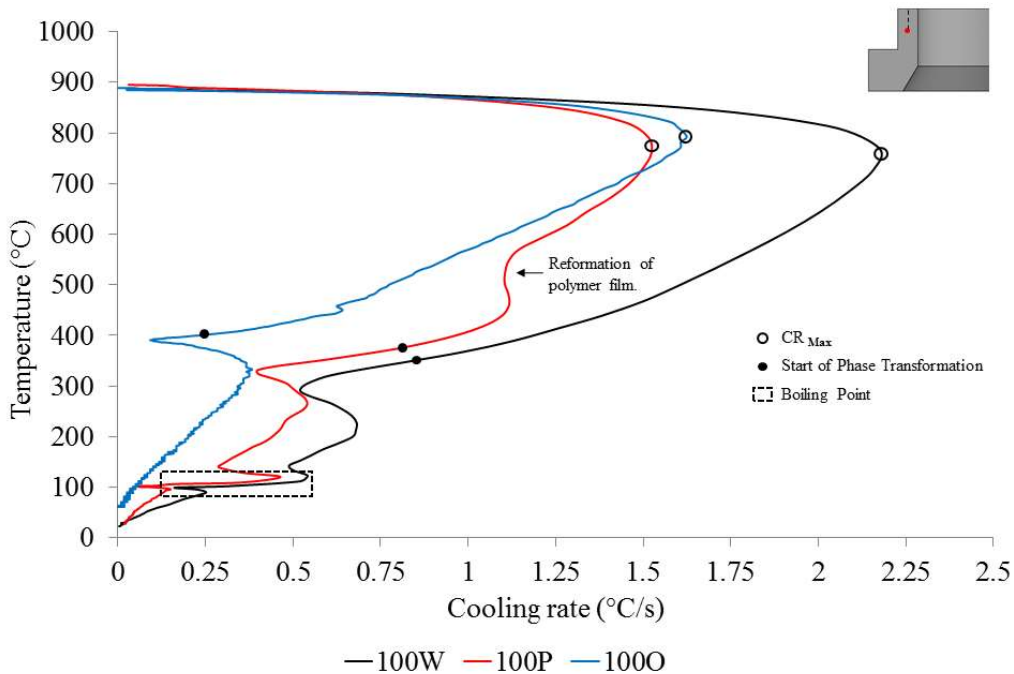


Figure 4-2: Cooling rate profiles recorded by the thermocouples located at the center of the 100 mm cross sections of the ring segments quenched in water, polymer and vegetable oil.

**4.2.2 Cooling characteristics on the 250 mm section of the ring the segments**

*4.2.2.1 Cooling curves*

Before starting the quenching process in water, polymer and vegetable oil the thermocouples registered austenitizing temperatures of 893, 899 and 889°C in the thick section of the three segments as illustrated in Figure 4-3. In a similar fashion like section 4.2.1.1 during the first 50 s, the drop in temperature at the center of the thick section of the three ring segments was very small. The slight drop in temperature during this period indicates the transfer of the ring segments from the furnace to their respective quenching tanks. The average temperature drop recorded during this period was around 5°C for three conditions. After 70 - 75 s the ring segment quenched in water was fully immersed into the agitated cooling media. At this point the thermocouples indicated a temperature of 885 - 890°C. On the other hand, the ring segment quenched in polymer was fully immersed at a time of 60 - 65 s with a corresponding temperature of 883 - 897°C. The ring quenched in vegetable oil was fully immersed at a time of 55 - 60 s with a corresponding temperature of 880 - 885°C. Once the quenching process started for the three segments, it could be observed that from 800 to 500°C (cooling time parameter λ), water and vegetable oil generated the faster and slower cooling times corresponding to 387 s and 608 s respectively, while an intermediate cooling time of 515 between those of water and vegetable oil, was achieved by aqueous polymer.

Approximately between 450 and 480°C a change in the slope was observed in the three cooling curves. As mentioned, this alteration is attributed to the effect of latent heat release due to the onset of the phase transformations during quenching. The estimated start transformation temperatures on the thick section of the segments quenched in water, polymer and vegetable oil were 460, 475 and 474°C respectively. Finally, at temperatures near to 100°C, the isothermal step due to the boiling point of water and polymer observed in the thin sections was also observed in the corresponding cooling curves of the thick sections.
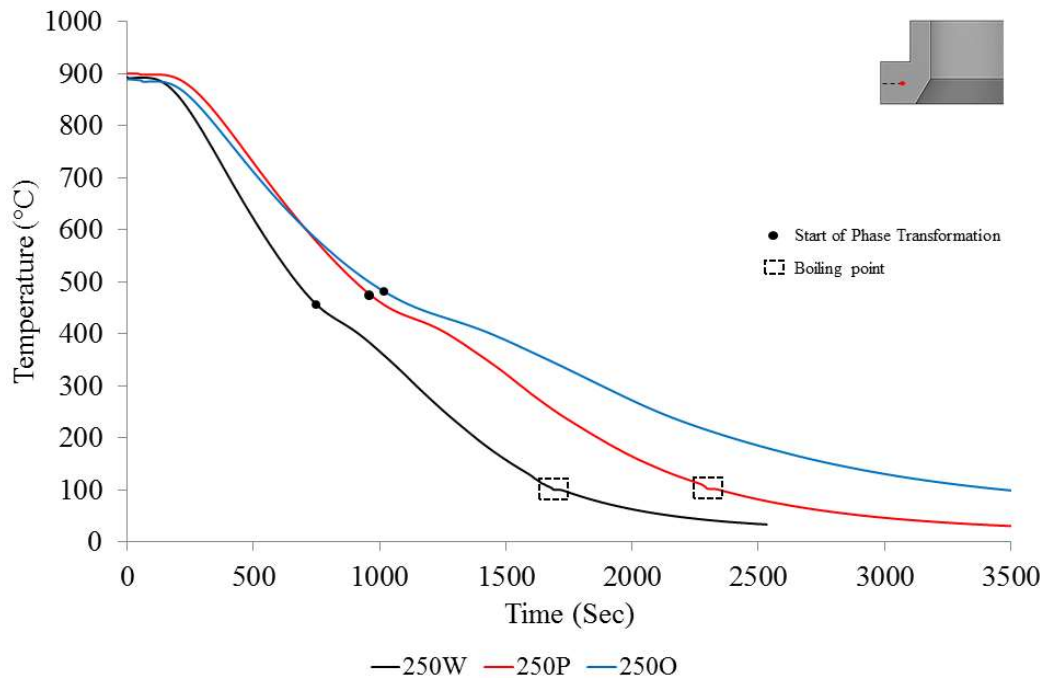
Figure 4-3 Cooling curve profiles recorded by the thermocouples located at the center of the 250 mm cross sections of the ring segments quenched in water, polymer and vegetable oil

### 4.2.2.2   Cooling rates

Figure 4-4, illustrates the cooling rates on the thick section of the segments quenched in the different cooling media.

Once the quenching started, the cooling rates for the three ring segments were very similar regardless of the cooling media, however after a cooling rate of 0.4°C/s was reached, the three segments starting to experience changes in cooling rate. As the temperature decreased the effect of the different type of quenchants became stronger, leading to different maximum cooling rates of 0.80, 0.65 and 0.60°C/s on the thick section of the ring segments quenched in water, polymer and vegetable oil respectively. Opposite to the behaviour observed in the maximum cooling rates of the thin sections, where polymer produced a lower maximum cooling rate than that of vegetable oil. The maximum cooling rate on the thick section reached by aqueous polymer was higher than that the maximum cooling rate on the corresponding thick section quenched in vegetable oil. This is an expected behaviour considering the superior heat transfer characteristics of aqueous polymer in comparison with vegetable oil. After reaching their corresponding maximum cooling rates, an anticipated reduction on the rate of cooling is

observed in the water, polymer and vegetable quenchants due to the prior onset of the nucleate boiling stage. Unlike the cooling rates of the thin sections quenched in vegetable oil and polymer media illustrated in section 4.2.1.2, the cooling rates of the thick sections cooled in vegetable oil and polymer did not show any disruption between 700 and 500°C. The continuous reduction - without any disruption - of the cooling rate between 700 and 500°C for the three quenchants could be explained by the fact that the thick sections are capable to contain more heat than the thin sections therefore stabilizing the effect of the vapour film, allowing a "natural" cooling rate reduction between 700 and 500°C. The latent heat effects due to phase transformation are clearly displayed in all of the cooling rate profiles between 350 and 410°C. According to the continuous cooling transformation diagram for 8630 low alloy steel built by Atkins [110], the transformation temperatures generated during industrial quenching in water, polymer and vegetable oil may be related to the onset of bainite transformation. Finally, as previously described in section 4.2.1.1, the peaks associated to the boiling point of water and polymer around 100°c are also observed in their corresponding cooling rate profiles.

Figure 4-4: Cooling rate profiles recorded by the thermocouples located at the center of the 100 mm cross sections of the ring segments quenched in water, polymer and vegetable oil.

97

## 4.3 Discussion

### 4.3.1 Cooling stages

As seen in section 4.2, characterizing the cooling conditions for water, polymer and vegetable oil during industrial quenching is complicated since two phenomena such as wetting kinetics (quenching stages) and phase transformations are occurring almost simultaneously. However as seen below relevant metallurgical aspects could be identified by analysing the shape of the six cooling rates studied in this research. On this regard, *Figure 4-5* illustrates the stages of cooling produced in the thick section of the ring segment during industrial quenching in aqueous polymer. Where vapour phase, nucleate boiling and convective heat transfer stages can be observed. For the sake of brevity, only the cooling rate analysis corresponding to the thick section quenched in polymer is shown below since similar cooling stages were observed on the rest of the thickness-cooling conditions evaluated.
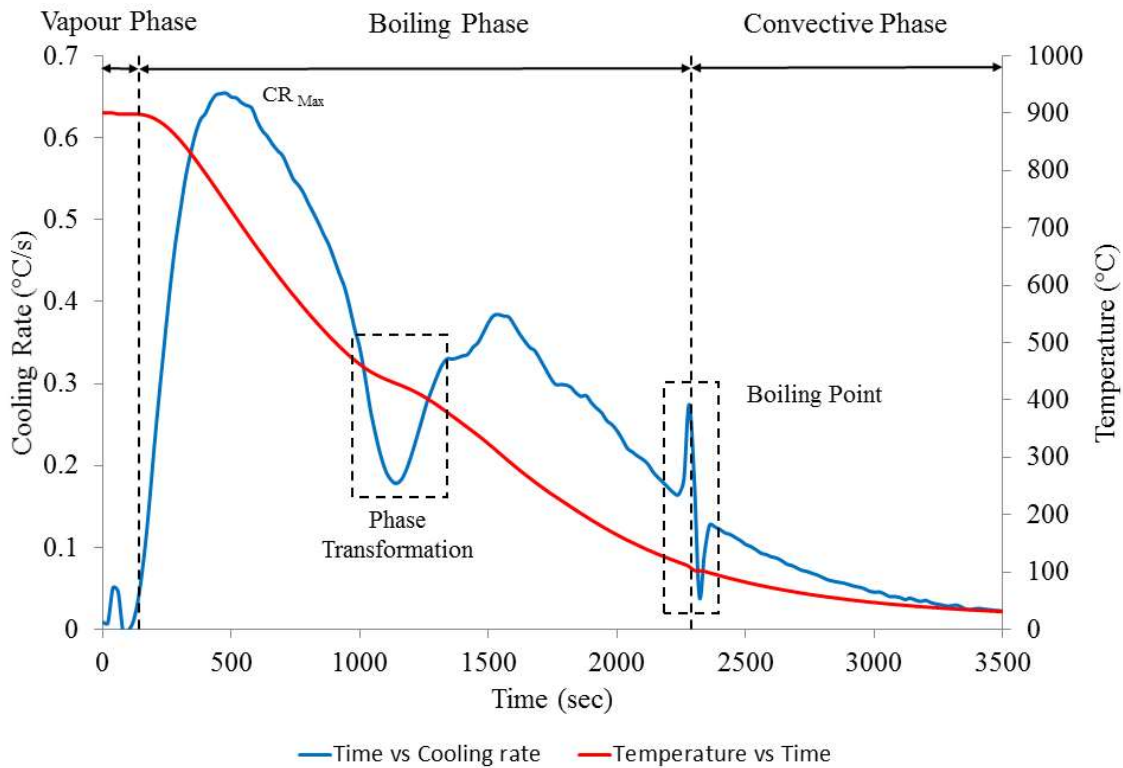


Figure 4-5: Plot of cooling rate and temperature as a function of time during quenching of the ring segment (thick section) in an aqueous polymer solution.

The vapour phase stage was estimated based on the fact that during this stage slow cooling is promoted either by the formation of a vapour blanket during water or polymer quenching or by the formation of a strong heated liquid layer during vegetable oil quenching, as explained in the work of Ramesh and Prabhu [27]. Whereas the boiling phase was determined considering that this stage results from the collapse of the vapour blanket (water and polymer) or the heated liquid layer (vegetable oil), leading to fast cooling during and maximum cooling rates. Finally as indicated by Ikkene and colleagues [42] , slow cooling is experienced once the temperature of the different media reached their boiling point, which marks the beginning of the convection stage.

The prior analysis might be valid for all the cooling conditions due to the similarities found in the cooling regimes for the six cooling rates. Additionally, the cooling stages were estimated based on the fundamentals of wetting kinematics on quenching, and are in line with the work of Prabhu and Fernandes [111], about heat transfer mechanisms during quenching treatment.

### 4.3.2   Effect of type of quenchant on cooling conditions

The cooling time parameter ($\lambda$) and the maximum cooling rate ($CR_{Max}$) are among the most important quenching parameters controlling the mechanical properties of steels forgings after industrial heat treatment. As explained in section 2.4.2.4, long cooling times associated to slow cooling rates during quenching could lead to low strength and toughness properties on the component due the formation of undesired microstructures such as ferrite and pearlite. In turn, short cooling times associated to high cooling rates are capable to produce high strength and toughness after quenching due to the formation of martensitic and bainitic structures. In this sense, considering the results obtained during industrial quenching, where water, polymer and vegetable oil produced the fastest, intermediate and slowest cooling times on both cross sections, it is important to elucidate which the main variables are controlling the cooling performance of the different cooling media used in this research.

Prabhu [46] carried out a number of cooling curve analyses on Inconel probes in order to determine the effect of the thermal and physical properties on the cooling performance of water, polymer and mineral oils. It was determined that the dynamic viscosity is the most important aspect governing the cooling performance and quench severity of the different cooling media investigated.   In addition Ma [112], established that the maximum cooling rate of oil

quenchants is increased as the viscosity is decreased. This can be explained by the fact that as the viscosity of a determined cooling media is decreased, its motion is increased leading to a stronger boiling stage which in turn is reflected as an increase in the heat transfer coefficient and shorter cooling times during quenching.

In agreement with the results of Prabhu [46] and Ma [112], in the present investigation, similar relations between viscosity and critical cooling parameters were obtained during industrial quenching as illustrated in Table 4-1, where a decreasing viscosity results in shorter cooling times and higher cooling rates.

However, as described in the previous chapter, the maximum cooling rate corresponding to the thin section of the segment quenched in polymer (100 - P) was the only parameter that does not follow this tendency, where a lower maximum cooling rate was obtained compared to that of vegetable oil, this, in spite of the lower viscosity of polymer. Possibly this is due to the higher sensitivity of the polymer film to variations in agitation and temperature compared to that of vegetable oil [42]. These variations observed on polymer quenching, could lead to heat transfer oscillations at different locations of the component. On the contrary, the convective heat transfer regime and the strong heated layer formed during quenching in vegetable oil might provide more uniform thermal gradients between the part and the quenchant [46, 36].

As seen in *Figure 4-6*, other aspects can be explained on the basis of viscosity and wetting kinetics during industrial quenching. For example, the small disruption (dotted square in *Figure 4-6*) in the cooling rate of the thin section quenched in polymer can be due to the reformation and dissolution of an unstable polymer film which consequently alters the vapour and nucleate boiling regimes in the thin section of the ring segment [32, 113]. On the contrary, the thick section quenched in the same media does not undergo this reduction since it is capable to contain more heat than the thin section by stabilizing the vapour film, allowing a "natural" cooling pattern [114].
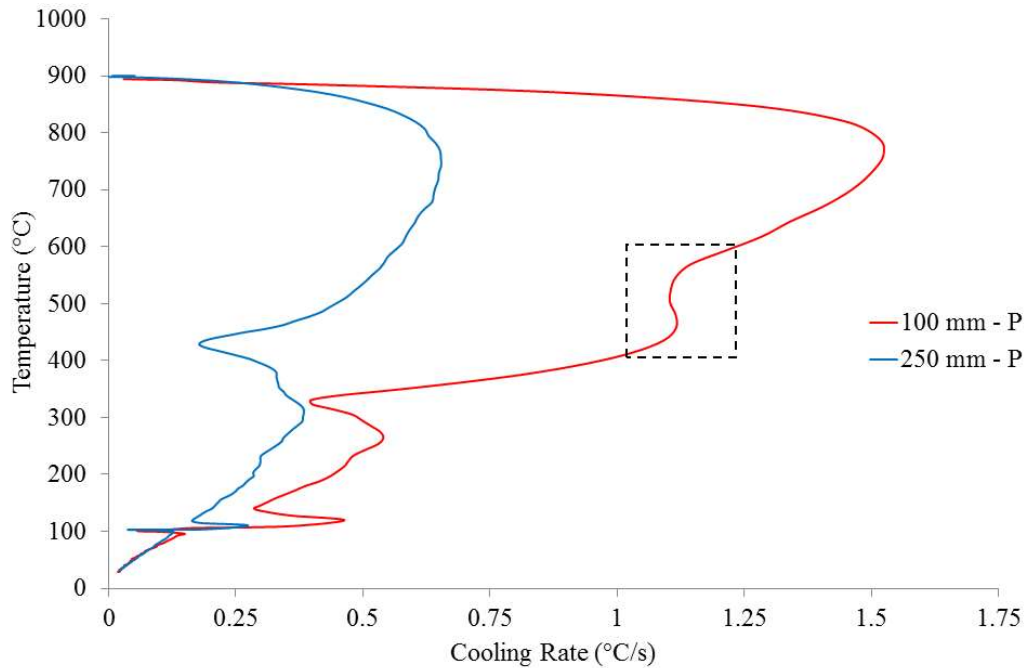
Figure 4-6: Cooling rate as a function of temperature in aqueous polymer quenching.

Table 4-1 illustrates the main critical parameters determined during the industrial quenching of the experimental forgings. On this regard it can be concluded that the differences in the cooling conditions on both, the thin and thick sections of the ring segments quenched in the three cooling media can be elucidated in terms of the wetting kinetics and viscosities of each quenchant where high heat removal rates were obtained with water due to high instability of the vapor film which collapses in a short period of time and therefore generates high heat transfer rates. On the contrary, the slow cooling produced with vegetable oil can be attributed to the formation of a strong and uniform heated liquid layer around the part reducing the thermal gradients and heat transfer during quenching. Aqueous polymer, in turn, produces a polymer film during quenching which encapsulates and stabilizes the vapour blanket reducing the thermal gradient between the liquid and the part leading in consequence to cooling times between those of water and vegetable oil [42, 27].

| Identification | CR Max (°C /s) | T CRMax | λ (s) | Estimated transformation start temperature (°C) | Viscosity (mm²/s) |
|---|---|---|---|---|---|
| 100W | 2.17 | 721 | 154 | 353 | 0.987 |
| 100P | 1.52 | 755 | 231 | 369 | 2.93 |
| 100O | 1.6 | 760 | 253 | 405 | 42.33 |
| | | | | | |
| 250W | 0.85 | 771 | 387 | 460 | 0.987 |
| 250P | 0.65 | 751 | 515 | 475 | 2.93 |
| 250O | 0.6 | 760 | 608 | 480 | 42.33 |

*Table 4-1:* Critical cooling parameters and viscosity of water, aqueous polymer and vegetable oil.

As mentioned previously, viscosity strongly affects the heat transfer characteristics of cooling media during quenching, where the heat transfer coefficient tends to decrease as viscosity increases. Besides this, the cross section of the component represents another important aspect controlling the heat transfer conditions during quenching. The combined effect of these two variables is incorporated in the cooling time parameter, and its effect on the maximum cooling rate produced for the different conditions during industrial quenching are illustrated in *Figure 4-7*.
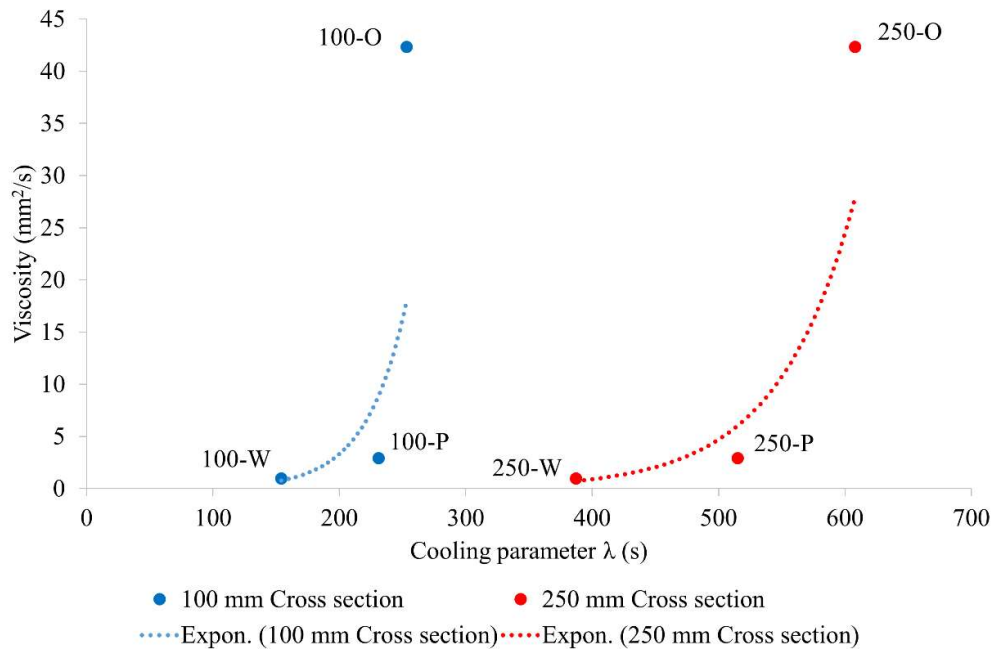


Figure 4-7: Plot of viscosity against cooling time parameter (λ) for the different thickness-cooling condition.

### 4.3.3 Microstructural evolution

As expected, the microstructure evolution during the industrial quenching of the ring segments was affected by the wetting kinetics produced by water, polymer and vegetable oil [115]. As can be seen in Figure 4-2 to Figure 4-4, the cooling rates for the different conditions were very similar during the initial period of quenching. Possibly, during this stage the thermal properties of the material have not changed yet, and regardless of the cooling media, the thin and thick sections of the three ring segments were still in the austenitic condition [10]. At the onset of austenite decomposition, the effect of the different type of quenchants became more pronounced along the thin and thick sections resulting in different cooling regimes for each thickness - cooling condition. When plotting the $CR_{Max}$ against the transformation start temperature, it can be elucidated that, as the maximum cooling rate is increased, the transformation start temperature for the different conditions is decreased as displayed in *Figure 4-8*. This can be explained by a decreasing atomic diffusion rate as the cooling rate is increased [116]. These observations are similar to the results obtained by Zhao et al. [117]. As stated previously, the probable onset of the bainitic and martensitic reactions for the different thickness – cooling conditions were estimated by identifying the inflexions points in the cooling rates produced by the latent heat release. These estimations are in line with the work of Cerda et al. [118]. Nevertheless, as described in the following chapter, the transformation temperatures were further validated via dilatometric analysis (CCT diagram).
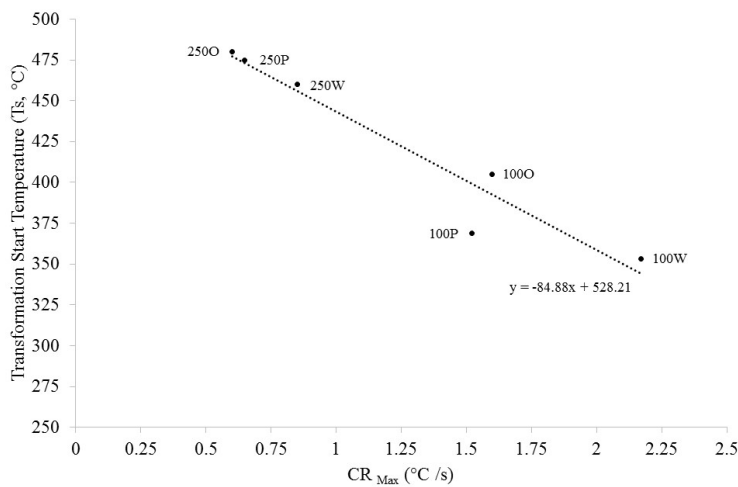


Figure 4-8: Plot of CR $_{Max}$ against transformation start temperature for the six thickness – quenchant conditions.

### 4.3.4   Effect of Thickness

When comparing the cooling curves of the thin and thick sections quenched in the same cooling media, it is possible to observe the effect of the section size on the cooling conditions and its subsequent influence on the transformation temperatures. Figure 4-9, illustrates the cooling curves corresponding to the six thickness – cooling conditions investigated. As described in Equation 6, the differences in the cooling conditions observed in the thin and thick sections of the ring segments quenched in the different media can be explained by the fact that the heat transfer rate during quenching is strongly influenced by the wall thickness of the part, where, as the thickness is increased the heat transfer is decreased producing longer cooling times associated to slower cooling rates.



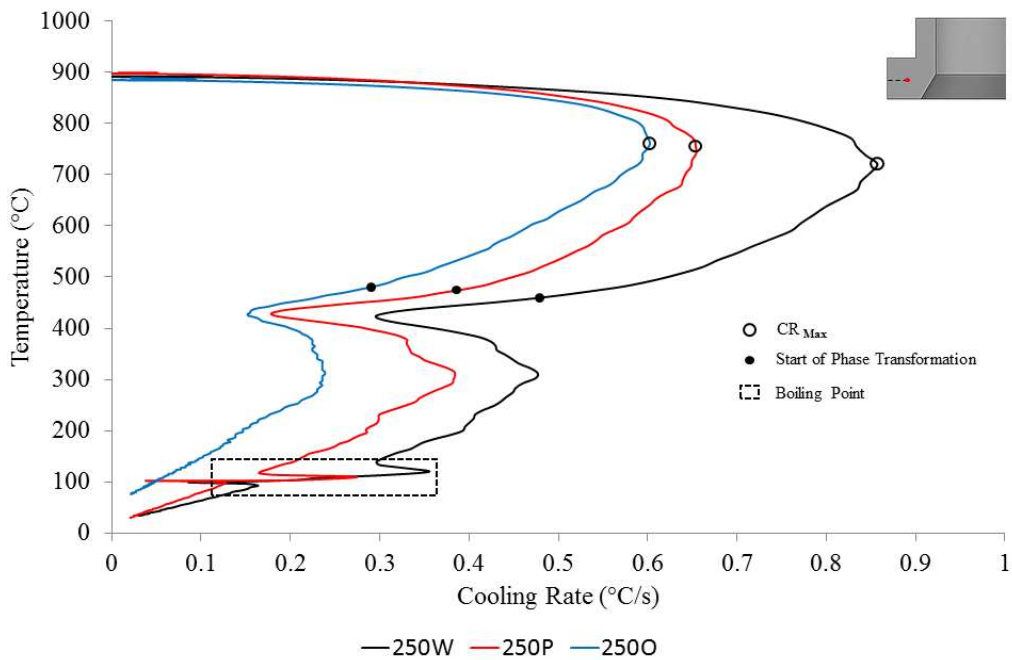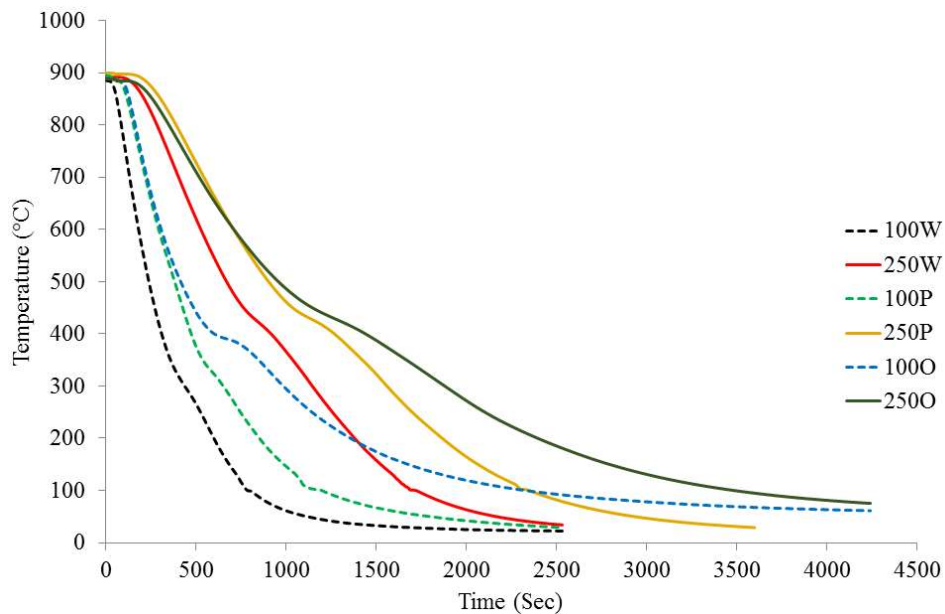Figure 4-9: Cooling curve profiles recorded by the thermocouples located at the center of the 100 and 250 mm cross sections of the ring segments quenched in water, polymer and vegetable oil.

$$q = \frac{KA\,(\Delta T)}{L} \tag{6}$$

Where:

q = Heat flow

$K$ = Thermal conductivity (J/s m°C)

A= Cross sectional area ($m^2$)

$\Delta T$= Thermal gradient ($T_2 - T_1$, °C)

L= Thickness (m)

# 5 Development of a Continuous Cooling Transformation Diagram for and AISI 8630 Modified Low Alloy Steel using Dilatometry

## 5.1 Introduction

As demonstrated by Ramseh and Prabhu [106] on their work about cooling performance during immersion quenching, it is possible to quantify the effect of quenching media on the microstructure by superimposing experimental cooling curves on a CCT diagram with chemistry of interest. However, despite the technological relevance and widely use of AISI 8630M low alloy steels on the offshore industry, it is very difficult to find accurate CCT diagrams on the scientific literature that possess similar composition and also similar grain size as the one used in this research. Considering this, a CCT diagram for the selected steel was developed by means of dilatometry, first, in order to establish correlations between continuous cooling rate and microstructure under controlled conditions and second, to estimate the microstructures produced during industrial quenching.

A large range of cooling rates can be developed through the cross section of large forgings during industrial quenching. In turn, these cooling rates, in combination with the chemical composition and the austenitizing conditions define the microstructure of the component after quenching. Recently, attention has been focused on the mechanical properties at the centre of the cross section of large forgings since this region represents one of the most critical aspects affecting the overall performance of the component due to the low mechanical properties and undesired microstructures such as pearlite and ferrite associated to slow cooling rates produced in this region of the forging. Although, inserting a thermocouple into a forging it is still one of the most reliable methodologies to evaluate the real microstructure produced on the forging after quenching; it is not always possible to use this method mainly due to time and economic constraints. Therefore, the use of CCT diagrams might represent a valuable metallurgical tool to establish correlations between cooling rate and microstructure which can be subsequently used to predict the microstructures at different locations inside large forgings after quenching. In this sense, it is important to mention that cooling curves produced during industrial quenching are of exponential nature (i.e. a maximum cooling rate is reached during quenching)

and evidently the cooling rate is not constant during the quenching process, on the other hand the cooling rates used to construct the CCT diagram are in fact constant during the cooling-down process. However as explained in reference [56], there is evidence which indicates that remarkable differences on the volume fraction of bainite could be observed between constant and exponential cooling rate.

## 5.2   Results

### 5.2.1   Analysis of Dilatometer Data

The measured data obtained from the dilatometer were used to determine the transformations temperatures for the different heating and cooling conditions. *Figure 5-1* to *Figure 5-6*, displays selected dilatometer curves showing critical transformation temperatures such as austenite, bainite, bainite-martensite and martensite transformation points.

As seen in *Figure 5-2*, the $A_{c1}$ and $A_{c3}$ temperatures were 724 and 798°C correspondingly. These temperatures were determined by heating the specimen at a rate of 10°C/min. As seen in Chapter 4, the austenitizing temperature used for the industrial heat treatment of the experimental forgings was 890°C. This temperature might look high if compared with the $A_{c3}$ temperature obtained from the dilatometer testing, however the selection of this temperature was defined considering the temperature dropped experienced during the transfer of the part from the furnace to the quenching tank. $A_{c1}$ and $A_{c3}$ transformation temperatures obtained by dilatometry were compared against a CCT diagram for AISI 8630M steel developed in JMatPro software with a grain size number of 8-8.5 ASTM at an austenitizing temperature of 890 °C as shown in *Figure 5-1*. The calculated $A_{c1}$ and $A_{c3}$ temperatures were 729 and 768°C respectively, indicating a variation of 5° and 29°C respectively with respect to the experimental results obtained by dilatometry. In their work on kinetics of austenite formation, Cota et al. [119], found that the critical temperature for austenite formation increases with increasing heating rate, so it could be argued that the differences between the experimental and calculated $A_{c1}$ and $A_{c3}$ temperatures observed in the present work could be associated to variation in the heating rates used during the dilatometric testing.
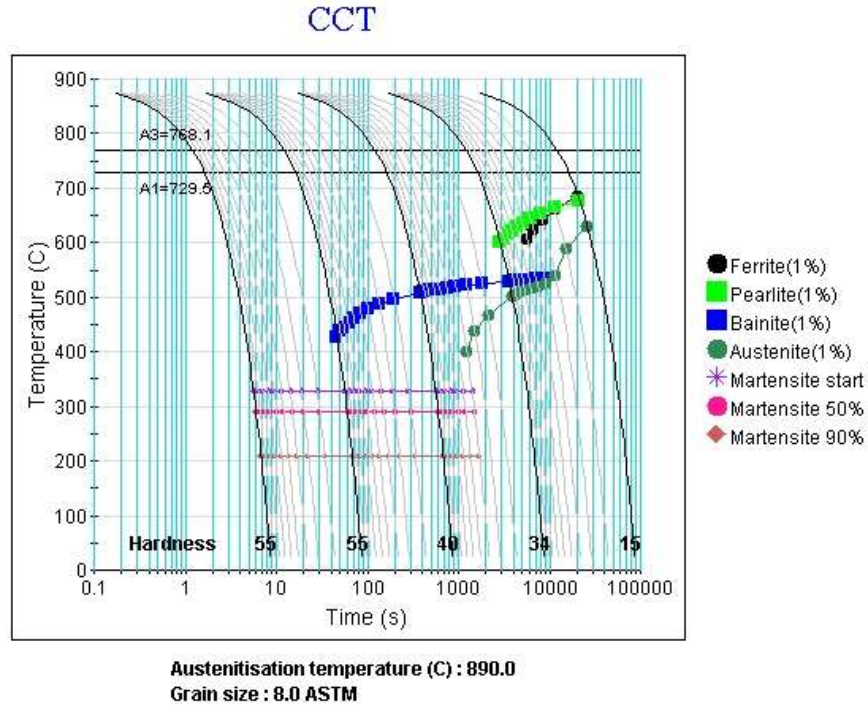
Figure 5-1: CCT diagram for AISI 8630M steel with grain size of 8 ASTM at austenitizing temperature of 890 °C (JMatPro software).

As illustrated in *Figure 5-3* when a cooling rate of 0.05 ˚C/s is applied, a complete bainitic transformation between 488.5 (B$_s$) and 300.5˚C (B$_f$) can be observed. Full bainite transformation was also observed on the specimens cooled down a rates of 0.10 and 0.20˚C/s, whereas the specimens cooled below 0.05˚C/s showed mixtures of, ferrite-pearlite and presumably granular bainite.

Although not clearly displayed on the dilatometric curves corresponding to the range of 0.3 to 1.0 ˚C/s (*Figure 5-4*) the presence of mixtures of martensite and bainite was confirmed by microstructural analysis. In this regard, due to the complexity involved to determine the Ms point directly from the dilatometric curves, the first derivative of the dilatation curve was determined. The advantage of using this technique is that small amounts of phase transformation can be detected on the first derivative curve [120]. As seen in *Figure 5-5*, approximately at 318˚C, a disruption associated to the formation of martensite (M$_s$) can be observed on the first derivative of the dilatation curve. This methodology was also used to determine the Ms Temperature on the specimens cooled at 0.3 and 0.5˚C/s which also formed

mixed structures of martensite and bainite and its applicability is further demonstrated in references [120, 121]. It should be pointed out that determination of the start transformation temperatures for the martensite on the specimens with mixed constituents might not be accurate enough due to the approximate nature of the methodology applied to determine the Ms points on the specimens with mixed constituents. Finally, a full martensitic structure is produced when the cooling rate is increased above 2˚C/s as illustrated in *Figure 5-6*.
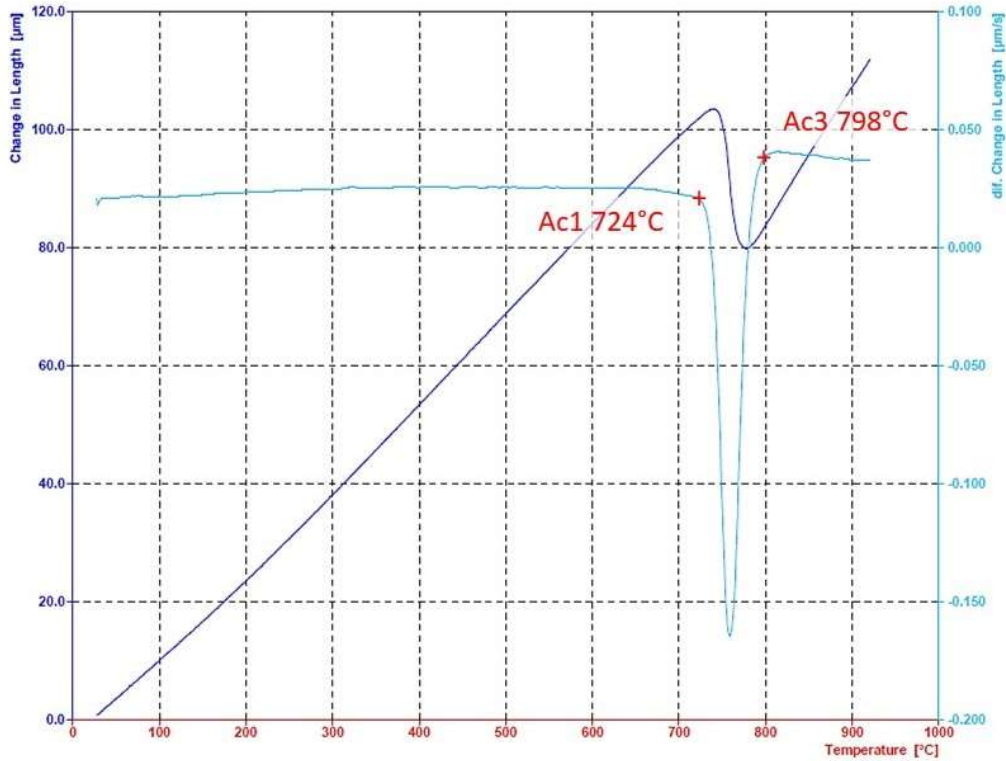


Figure 5-2: Dilatometric curve with corresponding first derivative on heating at a rate of 10˚C/min to determine Ac1 and Ac3.
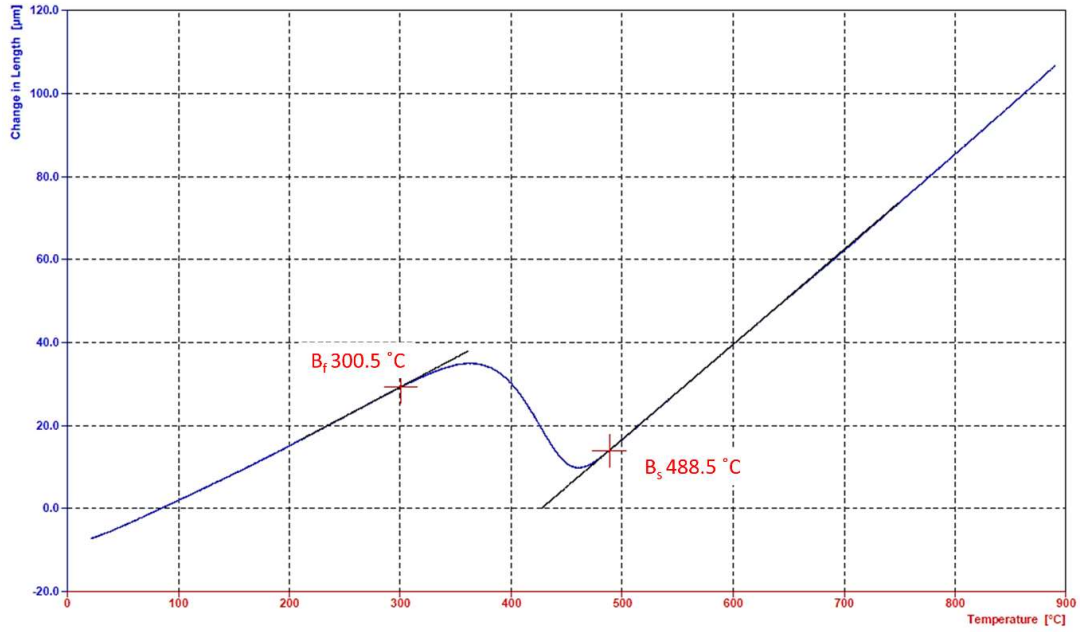
Figure 5-3: Dilatometric curve on cooling at 0.05˚C/s from 890˚austenitising temperature showing full bainitic transformation.
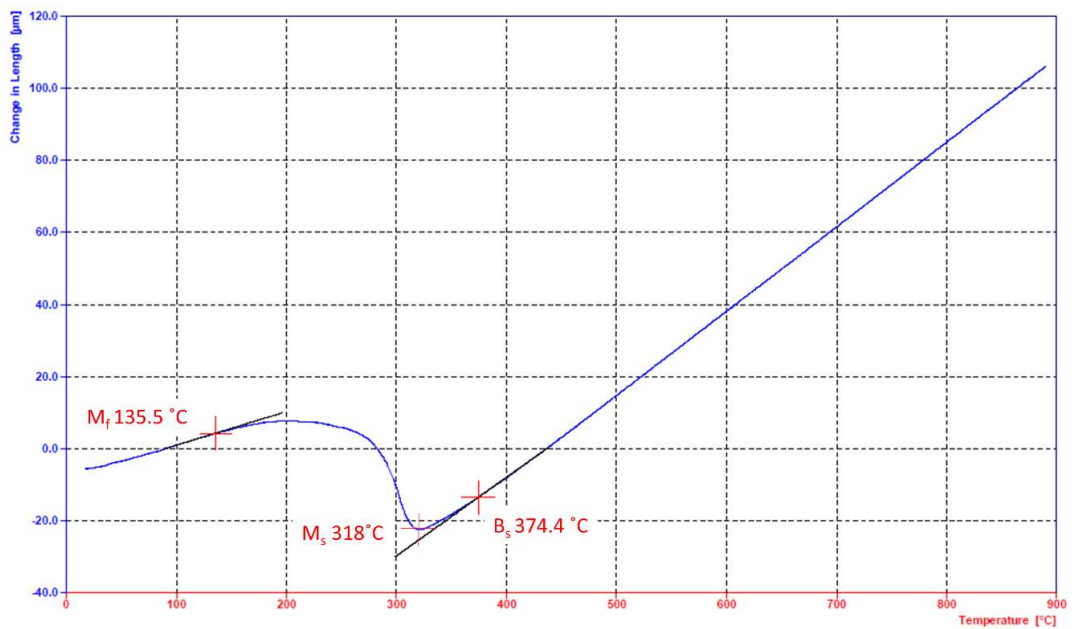


Figure 5-4: Dilatometric curve on cooling at 1.0˚C/s from 890˚austenitising temperature showing bainitic and martensitic transformation.
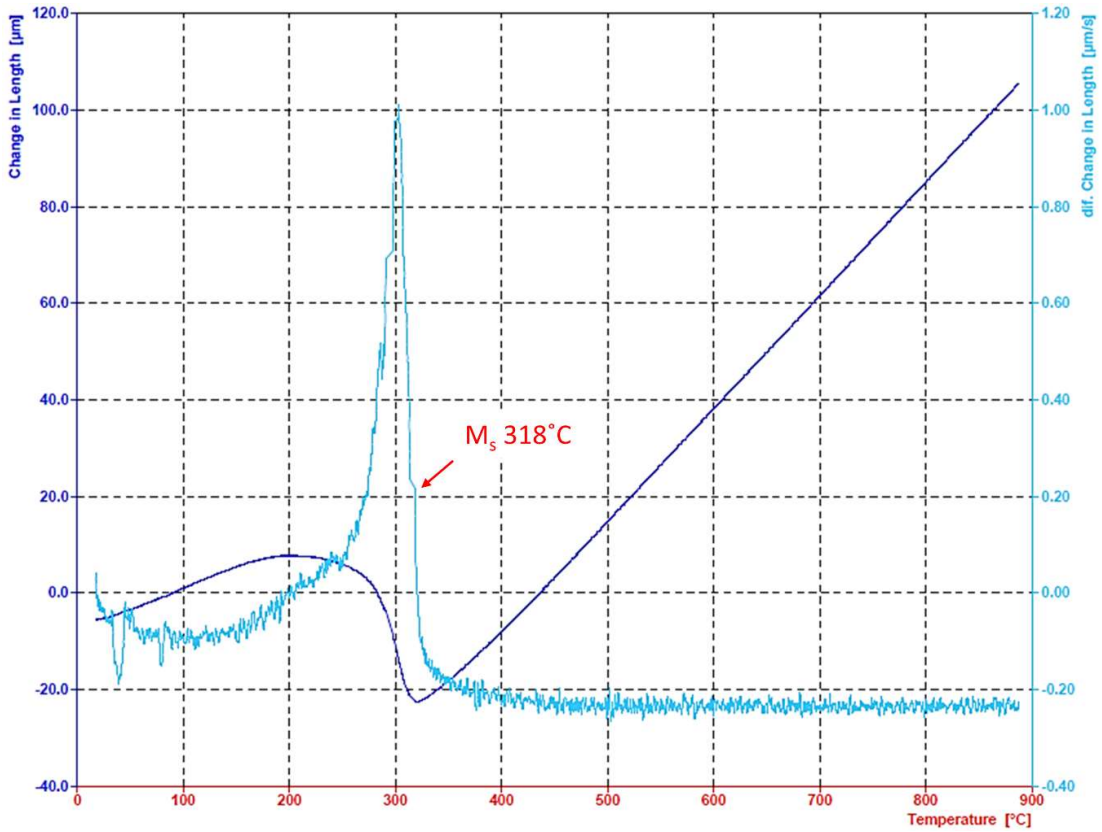
Figure 5-5: Estimation of Ms point by the first derivative of the dilatation curve.
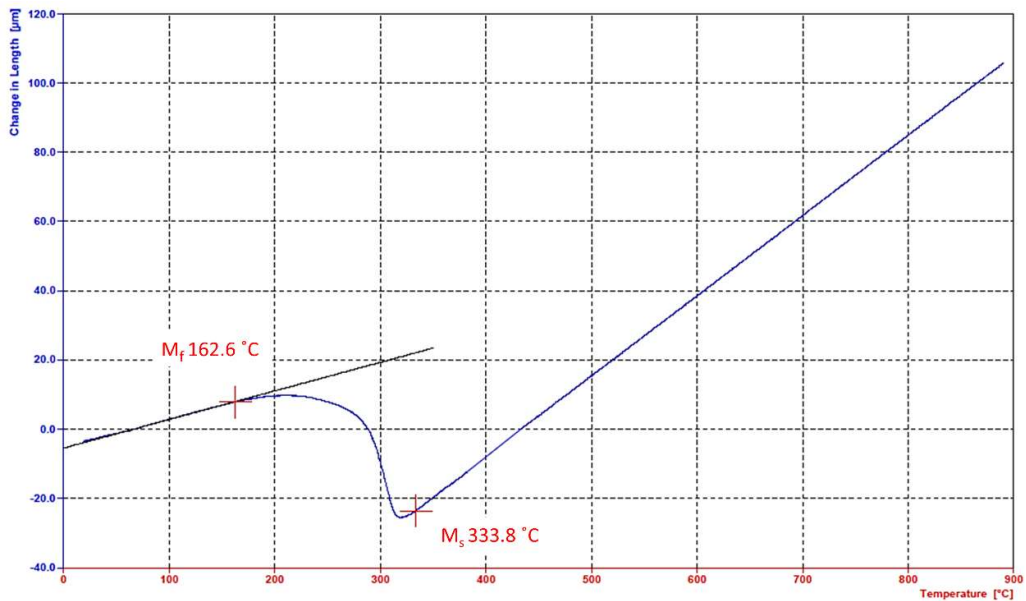


Figure 5-6: Dilatometric curve on cooling at 2.0˚C/s from 890˚austenitising temperature showing full martensitic transformation.

### 5.2.2   Effect of Cooling Rate on Microstructures

The transformation reaction temperatures (start and finish points) obtained from the dilatation curves were superimposed on the corresponding cooling profiles and plotted in the form of a continuous cooling diagram as illustrated *Figure 5-7*. According to the transformation points, the formation of ferrite pearlite and bainite occur along slow cooling rates ranging from 0.01 to 0.03˚C/s. industrially, these type of microstructures are expected to be produced at the center of large forgings, slowly cooled in air during normalizing treatment. Whereas, full bainitic microstructure is perceived at cooling rates between 0.03 and 0.2˚C/s with and average start transformation temperature of 490˚C. As the cooling rate is increased from 0.3 to 1˚C/s, mixtures of bainite and martensite are the dominant microstructure in the aforementioned range. With further increasing cooling rates above 2˚C/s, a full martensitic structure is generated at temperatures below 330˚C (average $M_s$ in this cooling rate range).
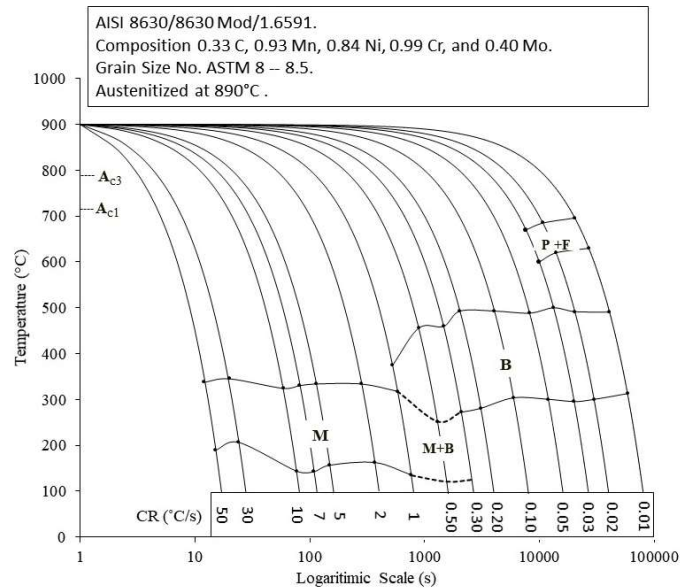


Figure 5-7: Continuous cooling transformation diagram for AISI 8630M built by quenching dilatometry.

In order to identify the microstructures related to the different transformation temperatures observed during continuous cooling, selected dilatometric specimens were examined by means of SEM as illustrated in *Figure 5-8* to *Figure 5-13*. In this regard, *Figure 5-8* and *Figure 5-9*, illustrate the microstructural complexity developed at slow cooling rates. It can be seen in this figures that the microstructure of the specimen cooled down at a continuous rate of 0.03˚C/s, mainly consists of degenerated pearlite and presumably granular bainite. Similar morphologies of degenerated pearlite on continuous cooling were reported by Shanmugam et al. [122] and its formation mechanisms are also addressed by the author. Essentially, the formation of degenerated pearlite involves the nucleation of cementite at the boundaries between austenite and ferrite, and the reason why no layer structure is observed on degenerated pearlite is associated to the scarce carbon diffusion available to promote a lamellae structure as the one observed on classic pearlite. Habraken in the late 50s firstly described granular bainite on continuous cooled steels which consisted of coarse ferritic plates with granular aspect and islands of retained austenite and martensite [123]. Eventually it was confirmed that the coarse ferritic plates observed by Habraken were in fact bainitic ferrite with small regions of austenite associated to low carbon concentration [57]. The mechanisms of formation of granular bainite are similar to those of bainite, although carbide precipitation is not observed on granular bainite since during cooling carbon migrates to the parent austenite leading to the formation of islands of carbon-rich regions of austenite upon cooling [124].

The classic morphology of lower bainite is illustrated in *Figure 5-10*. As is well known the main characteristic of this morphology of bainite is the extensive carbide precipitation within the bainitic lath which is arranged in a single crystallographic variant with an angle of 60˚ from the main bainitic lath axis [57]. Similar morphologies of lower bainite formed on continuous cooling are reported elsewhere [125].At intermediate cooling rates, the specimen cooled at a rate of 0.5 ˚C/s displays a microstructure which consists of a mixture of lower bainite and martensite as illustrated in *Figure 5-11*. The differentiation between these two microstructures is made on the basis that bainitic transformation involves extensive carbide precipitation during cooling, on the contrary no precipitation shall be observed on the as quench martensite microstructure since the carbon remain within the supersaturated solid solution after quenching [126]. *Figure 5-12*, shows a high resolution image of the same specimen (0.5˚C/s) at the interface between lower bainite and martensite, where the absence of carbide precipitation is evident on the martensite, on the contrary extensive carbide precipitation is observed on the

bainitic structure. At higher cooling rate above 2˚C/s, full martensitic structure is the dominant microstructure as illustrated in *Figure 5-13*. The detailed mechanisms of formation of bainite and martensite were already defined in section 2.6.1. In general, the microstructural observations listed above are in line with the work of Radwański [127]. In this work, the author develops a methodology to characterise the morphology of diverse constituents of multiphase steels by using field emission gun scanning electron microscopy (FEG-SEM).
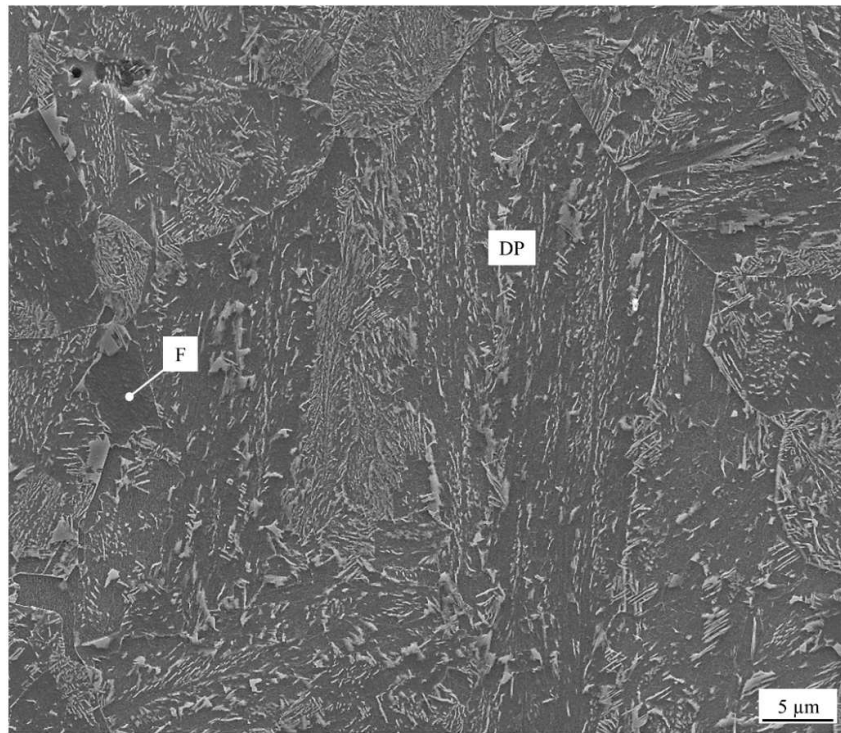


Figure 5-8: Low magnification SEM micrograph showing (DP) degenerated pearlite and (F) ferrite on specimen continuous cooled at rate of 0.03 ˚C/s.
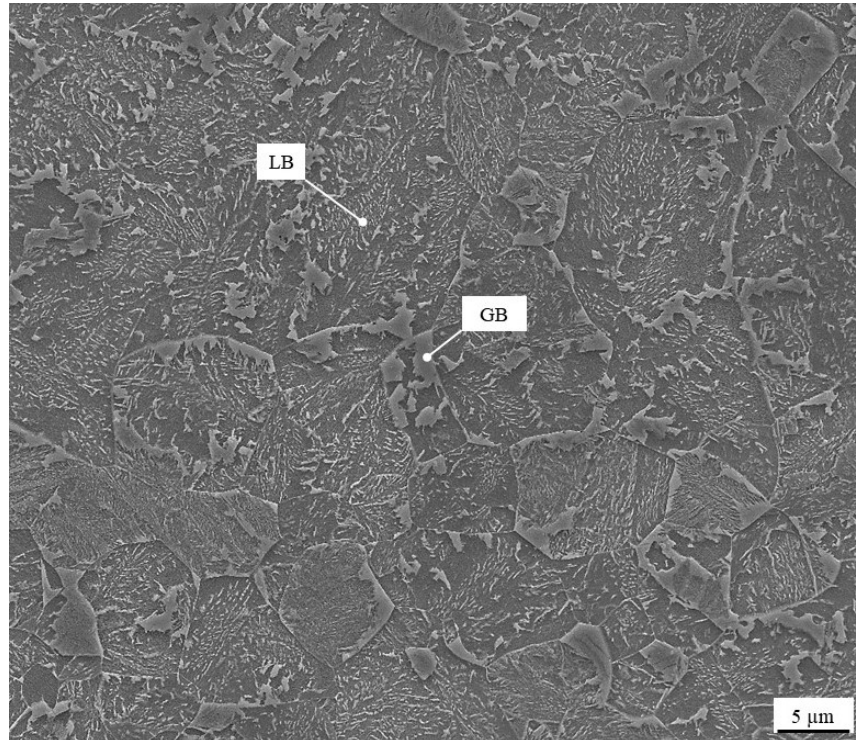
Figure 5-9: Low magnification SEM micrograph showing (LB) lower bainite and granular bainite constituent on specimen continuous cooled at rate of 0.03 ˚C/s.
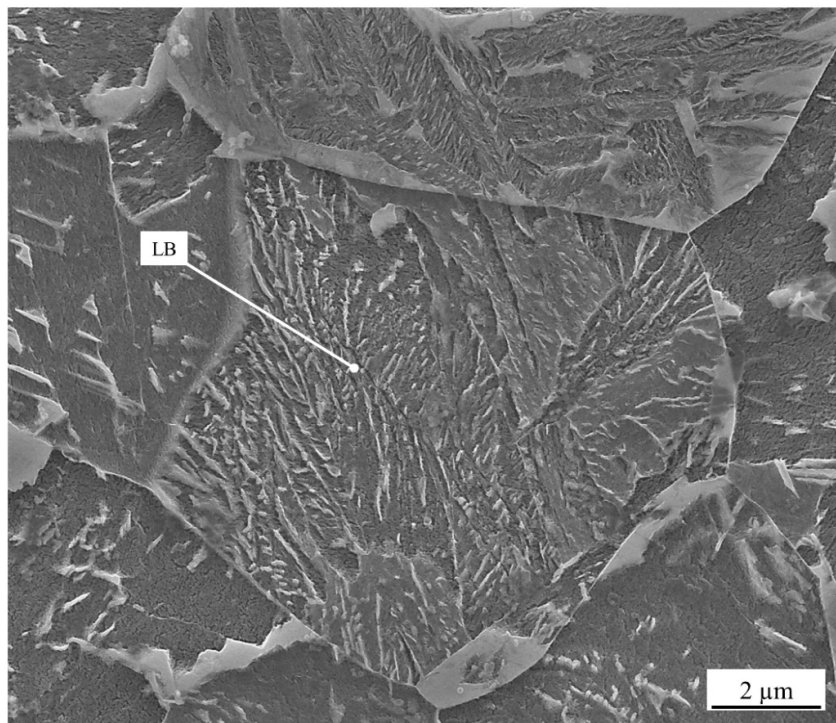


Figure 5-10: High magnification SEM micrograph showing (LB) lower bainite, on specimen continuous cooled at rate of 0.03 ˚C/s.
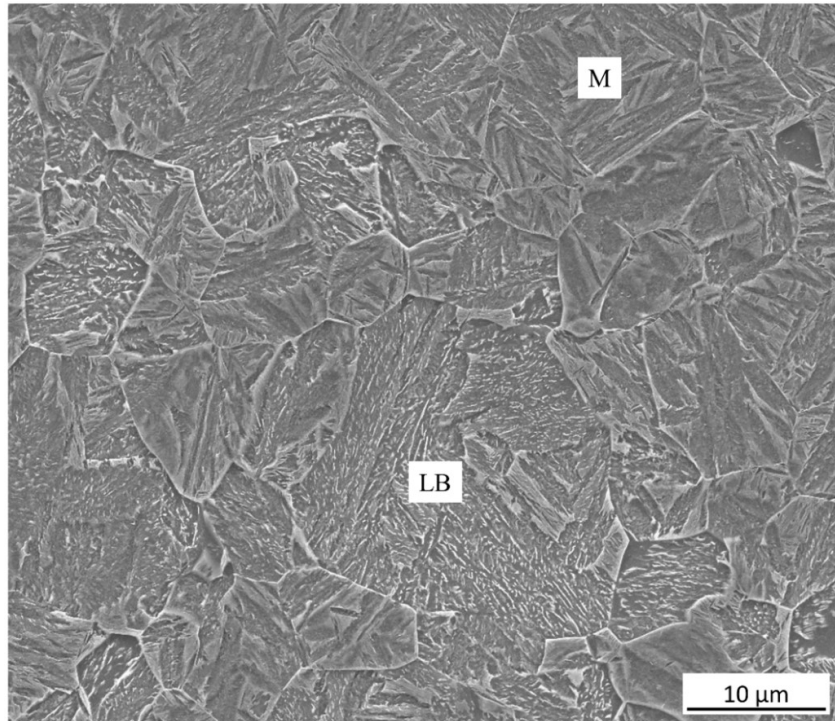
Figure 5-11: SEM micrograph showing (M) martensite and (LB) lower bainite on specimen cooled at a rate of 0.5 ˚C/s.
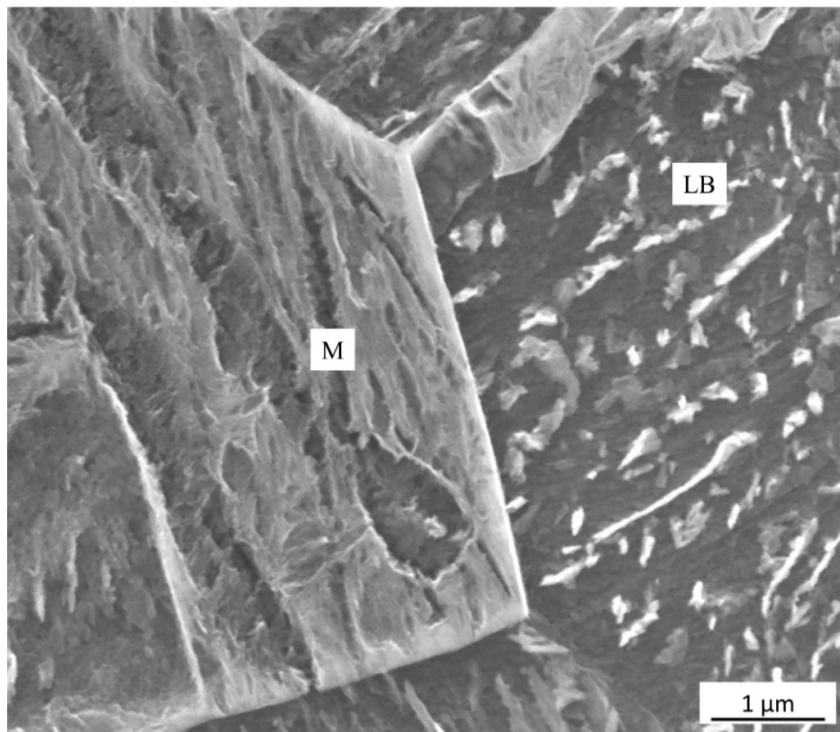


Figure 5-12: High magnification SEM micrograph showing (M) martensite and (LB) lower bainite on specimen cooled at a rate of 0.5 ˚C/s.
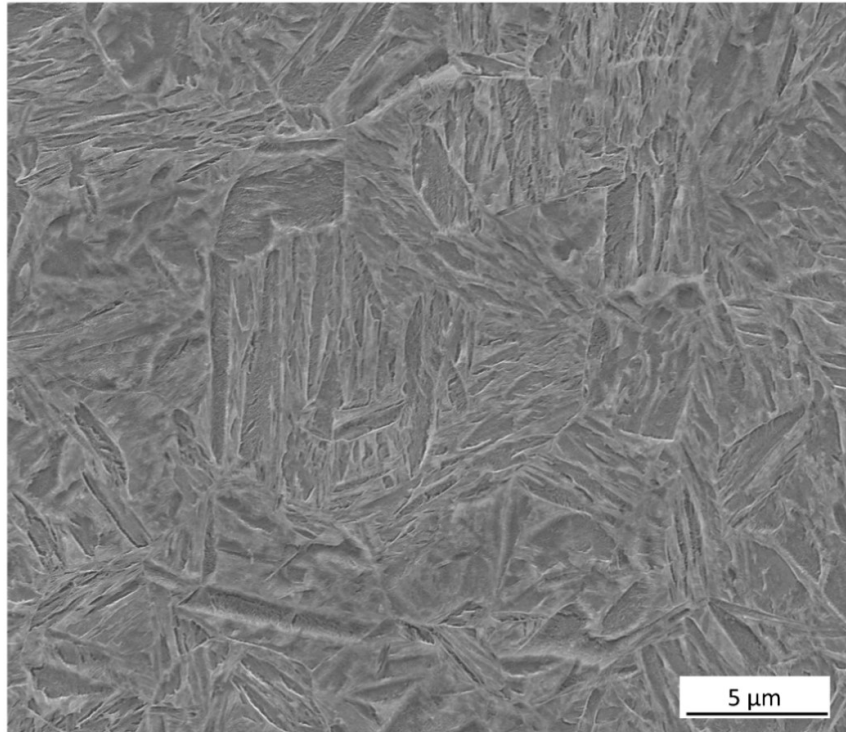
Figure 5-13: SEM micrograph showing full martensite on specimen cooled at a rate of 2 ˚C/s.

### 5.2.3 Comparison of Industrial and Continuous cooling curves

With the CCT diagram defined in the previous section, it is now feasible to evaluate the effect of the different industrial quenching conditions on the microstructure of the selected steel. To evaluate this effect, the cooling curves measured during industrial quenching in water, polymer and vegetable oil were superimposed on the CCT diagram built by dilatometry as elucidated in *Figure 5-14*. Surprisingly, despite the different cooling conditions promoted by water, polymer and vegetable oil, mostly, all the cooling curves fell within the mixed region (˜0.03 to ˜1˚C/s) of martensite and bainite, with the only exception of 100-W condition which cooling curve fall between continuous cooling rates of 1 and 2 ˚C/s associated to a full martensite structure. Considering that the highest cooling rate of all the industrial cooling conditions was in fact developed on the 100-mm section quenched in water, it reasonable to expect that the microstructure of 100-W condition consisted of a full martensite structure, which was produced as well at high continuous cooling rates. As the cooling rate is decreased, the first industrial cooling curve which apparently enters the mixed region of martensite and bainite is 100-P condition. Furthermore, it can be seen on the CCT diagram that the cooling profile of 100-P condition is close to the continuous cooling profile corresponding to 1˚C/s. On the other hand, the cooling curves corresponding to 100-O and 250-W conditions can be observed between continuous cooling rates of 0.5 and 1˚C/s. Finally, the slow industrial cooling curves corresponding to 250-P and 250-O conditions, are within the range of 0.3 to 0.5˚C/s.

The phase fraction of the continuous cooling specimens associated to the different industrial cooling curves were determined in an attempt to predict the microstructures present under industrial conditions as illustrated in *Table 5-1*. The specimen cooled at 2˚c/s, associated to 100-W condition, showed a fraction of 100% martensite. Whereas the martensite fraction on the specimens cooled at 1˚C/s (100-P), 0.5˚C/s (100-O and 250-W) and 0.3˚C/s (250-P and 250-O) were 85%, 48% and 19% respectively. It is clear that as the cooling rate is decreased from 2˚C/s to 0.3˚C/s, the amount of martensite decreases with a corresponding increase in the fraction of bainite. In their work on Ni–Cr–Mo low alloy steels, Lee and co-workers [128] also reported that a decreasing cooling rate effectively reduces the amount of martensite while increasing the amount of bainite.
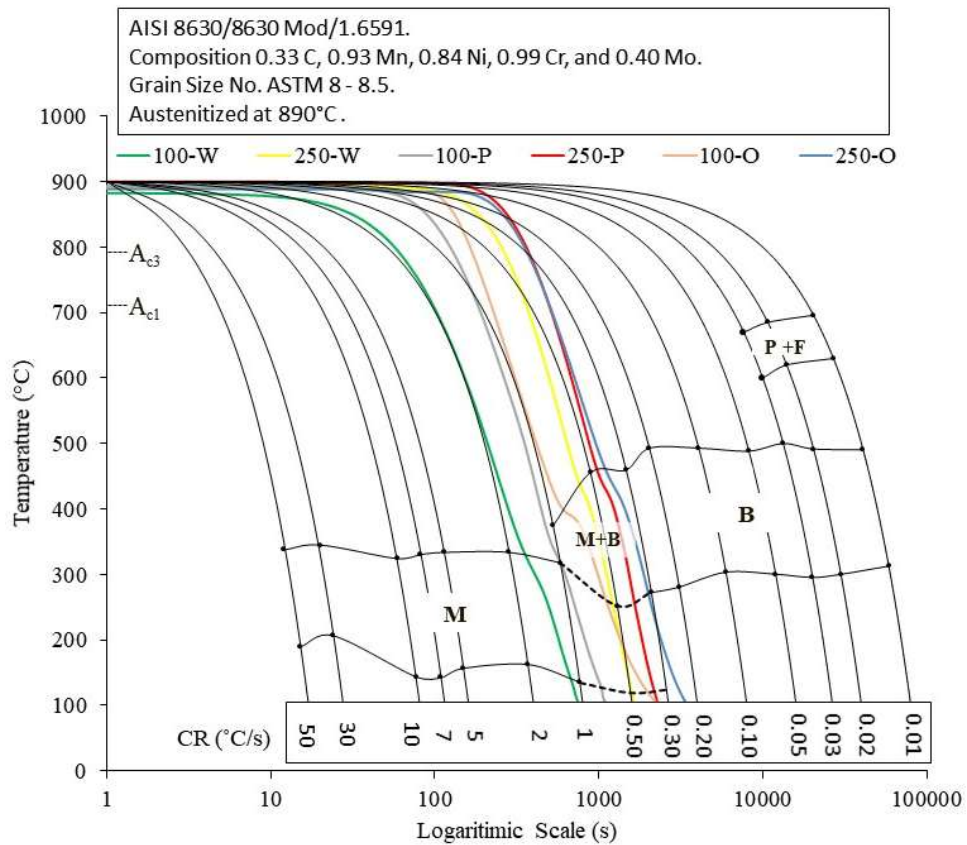
Figure 5-14: CCT of 8630 mod. Steel along with measured industrial cooling curves of water, aqueous polymer and vegetable oil media.

| Continuous Cooling rate (°C/s) | Bainite (%) | Martensite (%) | Industrial cooling condition associated to continuous cooling rate |
|---|---|---|---|
| 0.3 | 81 | 19 | 250-P and 250-O |
| 0.5 | 52 | 48 | 100-O and 250-P |
| 1 | 15 | 85 | 100-P |
| 2 | 0 | 100 | 100-W |

Table 5-1: Phase fractions of martensite and bainite on mixed region of the CCT diagram and industrial cooling conditions associated to continuous cooling rate.

## 5.3  Discussion

According to the results described above, the cooling rate appears to be determinant in controlling the phase transformations taking place on AISI 8630M low alloy steels during quenching. At very slow cooling rates (<0.03˚C/s) ferrite and pearlite are the dominant constituents. On the contrary the formation of full martensite is promoted at high cooling rates (>2˚c/s). Interestingly, at the intermediate cooling region of the CCT diagram, martensite and bainite both coexist between rates of cooling in the range of 0.3 and 1˚C/s. In this sense, it can be concluded that the the majority of the industrial cooling curves fall within the range of martensite-bainite structure on the CCT diagram. Thus, the discussion is focused on relevant aspects associated to the coexistence of bainite and martensite, in particular considering that prior research indicates that the presence of lower bainite on tempered martensitic structure is beneficial for the mechanical properties.

It is well established that the steel chemistry is one of the most important factors governing the phase transformation temperatures, which in turn are dependent on the stabilization of the parent austenite phase [129]. This is why the vast majority of equations to predict the $M_s$ and $B_s$ temperatures are mainly based on the chemical composition [130]. However as demonstrated in this research, the transformation temperatures are also affected by changes in cooling rate. Although, it is noteworthy to mention that, similar relations between start transformation temperatures and cooling rate on low alloy steels have been reported elsewhere [131].

As observed on the phase transformation temperatures corresponding to the industrial cooling curves, the $B_s$ *(bainite start)* temperature of the continuous cooling curves obtained by dilatometry also showed an increasing trend with a decreasing cooling rate. As mentioned in the previous chapter, it can be argued that this increase in Bs temperature could be due to an increase on the diffusion atomic coefficient at higher transformation temperatures [117]. It can also be observed that the increasing $B_s$ temperature due to the decreasing cooling rate is accompanied by a decrease in the $M_s$ temperature at the intermediate cooling region of the diagram. The variation on the $M_s$ and $B_s$ temperatures associated to the changes in cooling rates are in fact reflected on the different proportions of martensite and bainite obtained after continuous cooling as illustrated in *Table 5-1*, where, as the cooling rate is decreased from

2°C/s to 0.3°C/s, the amount of martensite decreases with a corresponding increase in the fraction of bainite. In this sense, Bohemen et al., [129] observed that an increasing fraction of bainite induced a decrease in the martensite-start temperature on a 41Cr4 low alloy steel submitted to continuous cooling. As explained by the Bohemen, the reason why martensite start transformation decreases with increasing fraction of bainite might be due to the mechanical stabilization of the remaining austenite. The origin of mechanical stabilization is the shape change associated with the bainitic transformation which causes the accumulation of dislocations in the surrounding austenite.

In the decade of the 1980's, Tomita and Okabayashi [132, 133, 134] initially reported that the presence of bainite in a martensitic structure increases the strength and toughness of quenched and tempered low and medium alloy steels. They postulated that the mechanism responsible for this enhancement would be associated with a grain size refinement of the austenite by the lower bainitic sheaves. As explained in reference [135], the carbon partitioning promoted by bainite would consequently increase the strength of the martensite by refining its packet structure. Furthermore, the constraint associated to the deformation of bainite by the surrounding martensite (stronger) would also lead to a strengthening effect on the bainitic structure [136].

According to the experimental data developed by Tomita and Kobayashi in reference [134] the optimal mix proportion of lower bainite and tempered martensite related to a peak of strength in 0.40% C-Ni-Cr-Mo steel, would be approximately 20% lower bainite - 80% tempered martensite. As seen in *Table 5-1*, similar proportions of bainite and martensite were developed on the specimen cooled at 1°c/s, associated to 100-P condition. According to this theory, it would be reasonable to expect superior strength properties on the thin section of the ring segment quenched in polymer identified as 100-P condition. This assumption will be confirmed in the following chapter.

# 6 Effect of Industrial Cooling rate on Microstructure and Mechanical Properties of Large Forging Segments

## 6.1 Introduction

This chapter presents the results from the three segments quenched in water, polymer and vegetable oil after tempering treatment at 590°C for 10 hours. As discussed in the previous section, with the exception of condition 100-W, where the as-quench microstructure predicted was predominately lath martensite, all the other predicted conditions showed different proportions of martensite and bainite. The tempering treatment is of particular importance since it improves the strength-toughness balance of low alloy steels by promoting carbide precipitation and reducing stress concentrations on martensite. On the contrary, bainite is less sensitive to tempering treatment than martensite, where the major changes observed on tempered bainite are associated to a slight coarsening of cementite precipitates. In this regard, the main objective of this chapter was to investigate the influence of the different mixtures of microstructures produced during industrial heat treatment, on the strength and toughness of three forged segments made of AISI 8630 Modified low alloy steel. Particular attention was paid to the morphological and orientation relationships differences of the carbides precipitates between the martensitic and bainitic structures.

## 6.2  Results

### 6.2.1  Morphology of Tempered Microstructures

#### 6.2.1.1  *Optical Microscopy*

Optical microscopy was carried out in order to get a first insight into the microstructures after tempering treatment. However, due to the complexity of the tempered microstructures, the characterization was further complemented by SEM in order to distinguish the main features of the various microstructures produced after industrial heat treatment. Figure 6-1 shows optical microstructures of the normalized, quenched and tempered ring segments. For the fast cooling rates / short cooling times produced on the thin sections of the ring segments, a fine microstructure with an acicular morphology was obtained for 100-W, 100-P and 100-O conditions. In this sense, Hoseiny et al. [137] and Penha et al. [19] reported similar morphologies for martensitic and bainitic structures after quenching and tempering treatments. Prior research [48] on quenched and tempered low alloy steels indicates that tempered martensite and lower bainite share some morphological similarities when observed under the optical microscope. Consequently, these similarities complicated the differentiation between these two structures when observed under the optical microscope. On the contrary, for the slow cooling rates / long cooling times produced on the thick sections of the ring segments, mixed microstructures with acicular and granular morphologies were obtained for 250-W, 250-P and 250P conditions. The granular morphology detected in the thick sections has also been reported by Du et al. [138]. It is clear that optical microscopy is not capable to reveal the main characteristics of the various microstructures mainly due to the small size of their metallurgical features, however as seen in next section, SEM technique was employed to clarify the main features of the microstructures developed after industrial heat treatment.
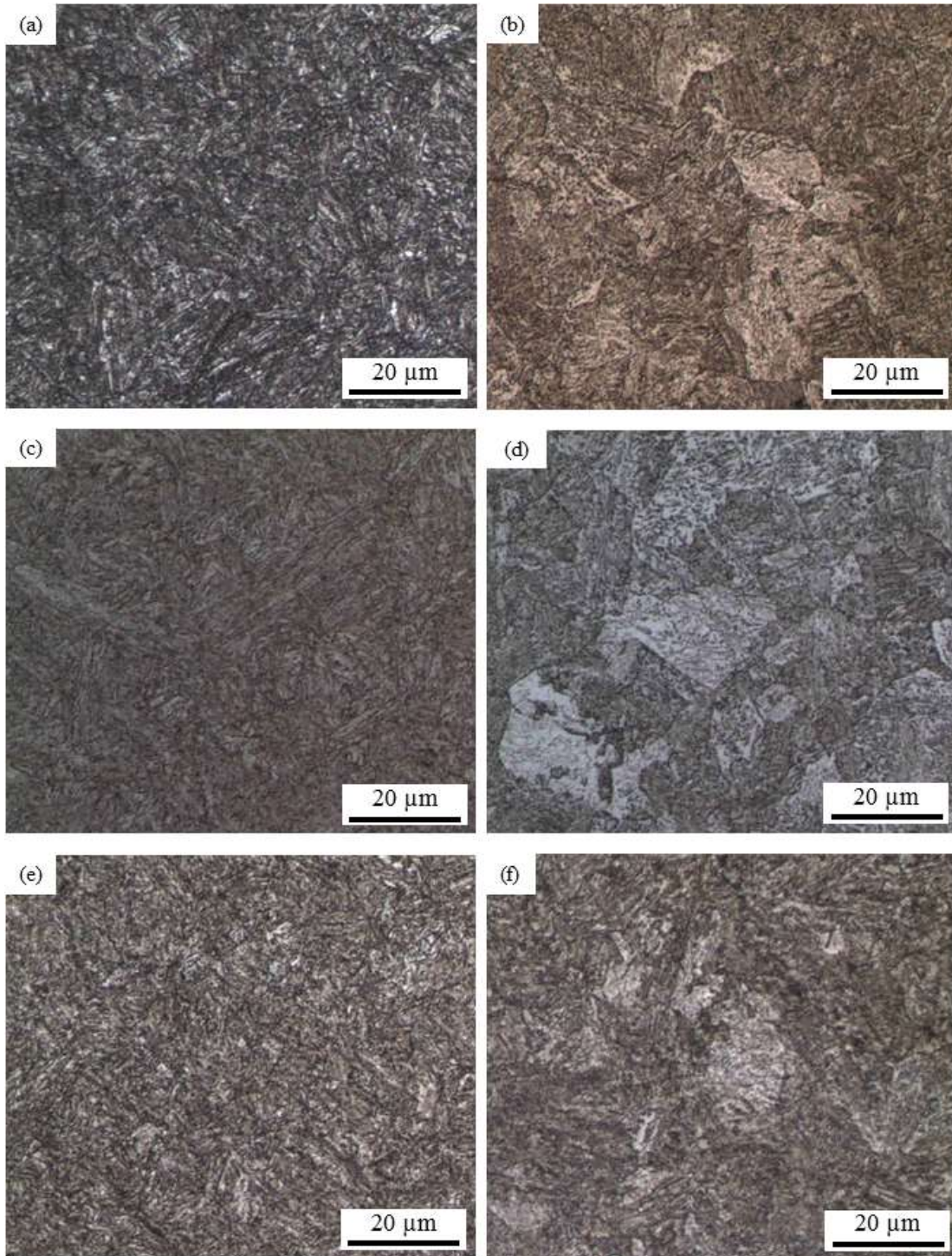
Figure 6-1: Optical micrographs for (a) 100-W, (c) 100-P and (e) 100-O conditions, showing a fine microstructure with an acicular morphology, whereas (b) 250-W, (d) 250-P and 250-O conditions show a mixed microstructure with acicular and granular regions.

*6.2.1.2 Scanning Electron Microscopy*

Tempered martensite and tempered lower bainite were the main microstructures observed on the six conditions studied, although it should be emphasized that distinguishing between tempered martensite and tempered bainite using FEG-SEM technique has a certain level of difficulty due the similarities shared by these two constituents after tempering treatment. In addition a nonclassical bainite morphology was also found on 250-P condition. The nature of the formation of this microstructure is discussed into more detail in section 6.3.1.

*Figure 6-2* and *Figure 6-3* illustrates high magnification SEM micrographs emphasizing the main morphological characteristics of the tempered martensite and tempered lower bainite produced under industrial heat treatment conditions, whereas Figure *6-4* illustrates the non-classical morphology of bainite found in 250-P condition. Finally, *Figure 6-5* to *Figure 6-10*, display low magnification SEM micrographs of all the microstructures in order to observe them in a broader perspective.

*Figure 6-2*, shows tempered martensite which consists of multivariant (crystallographic variant) carbide precipitation within the martensite laths and extensive precipitation on the lath boundaries [139, 57]. In this sense, Hoseiny et al. [137] determined, by means of TEM-EDS, that $M_3C$ carbides are precipitated after quenching and tempering of a low alloy steel with chemical composition (wt. %) of 0.36% C, 1.97% Cr and 1.0% Ni. In general, $M_3C$ carbide is known as cementite and it is transformed from ε-carbide during tempering. Additionally, it can be observed how carbides are orientated in two main directions (Widmanstätten arrays, [57]) within the laths and along the lath boundary in the axial direction. Accordingly, this morphology and carbide distribution are characteristics of tempered martensite.

*Figure 6-3* displays tempered lower bainite which, unlike tempered martensite, consists of carbide precipitates arranged in a single crystallographic variant (Bagaryatski orientation relationship, [57]) within the bainitic laths. Furthermore, the absence of inter-lath carbides on its boundaries can also be observed. These observations are agreement with those of Caballero et al. [125]. As stated by Bhadeshia [57], in lower bainite carbides precipitate from a carbon supersaturated ferrite adopting a single orientation at 60° from the lath axis.

As the cooling rate further decreased, and non-classical morphology of bainite became visible on 250-P condition. As seen in Figure *6-4*, this so-called featureless bainite consists of coarse carbides on the prior austenite grain size and a mixture of elongated and blocky carbide precipitates randomly distributed within the bainitic matrix.

The tempered microstructures corresponding to the 100 mm cross section of the ring segments quenched in water, polymer and vegetable oil are displayed in *Figure 6-5* to *Figure 6-7*. 100-W condition, with a $\lambda$ parameter of 154 s ($CR_{MAX}$ = 2.17 °C/s) consists of full tempered martensitic structure with interlath and intralath fine cementite precipitates. 100-P condition with a $\lambda$ parameter of 231 s ($CR_{MAX}$ = 1.52°C/s) presumably shows mixtures of tempered martensite and tempered bainite. It can be argued that 100-O condition with a $\lambda$ parameter of 253 s ($CR_{MAX}$ = 1.60°C/s) also shows mixtures of tempered martensite and tempered bainite but with lower bainite fraction as discussed in previous chapter 5.

The tempered microstructures corresponding to the 250 mm cross section of the ring segments quenched in water, polymer and vegetable oil are displayed in *Figure 6-8* to *Figure 6-10*. As seen in these figures, the microstructures of the 250-W, 250-P and 250-O might consist of tempered martensite and tempered bainite with cooling times, $\lambda$ of 387 ($CR_{MAX}$ = 0.85°C/s), 515 ($CR_{MAX}$ = 0.65°C/s), and 608 s ($CR_{MAX}$ = 0.60°C/s), respectively. A similar tendency was also observed on the thick cross sections were as cooling time increases, the amount of tempered martensite is reduced while at the same time the amount of tempered bainite is increased. Furthermore, extensive carbide precipitation at the austenite grain boundaries is also observed on 250-P and 250-O conditions. During the FEG-SEM evaluation it could be observed that the average carbide size thickness for tempered martensite, tempered lower bainite and featureless bainite were 0.04, 053 and 0.081 µm respectively.
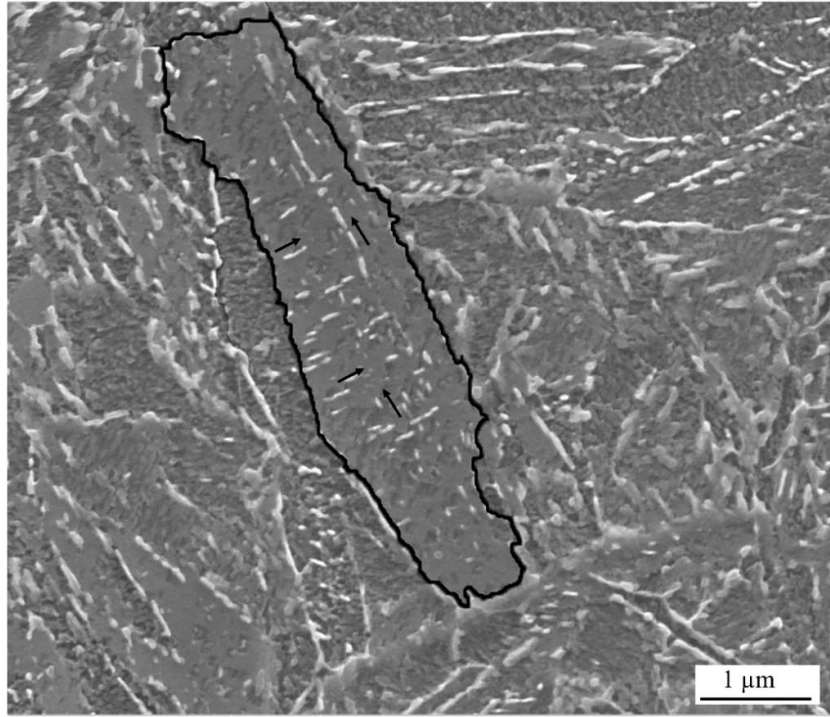
Figure 6-2: SEM micrograph of tempered martensite observed in 100-P condition.
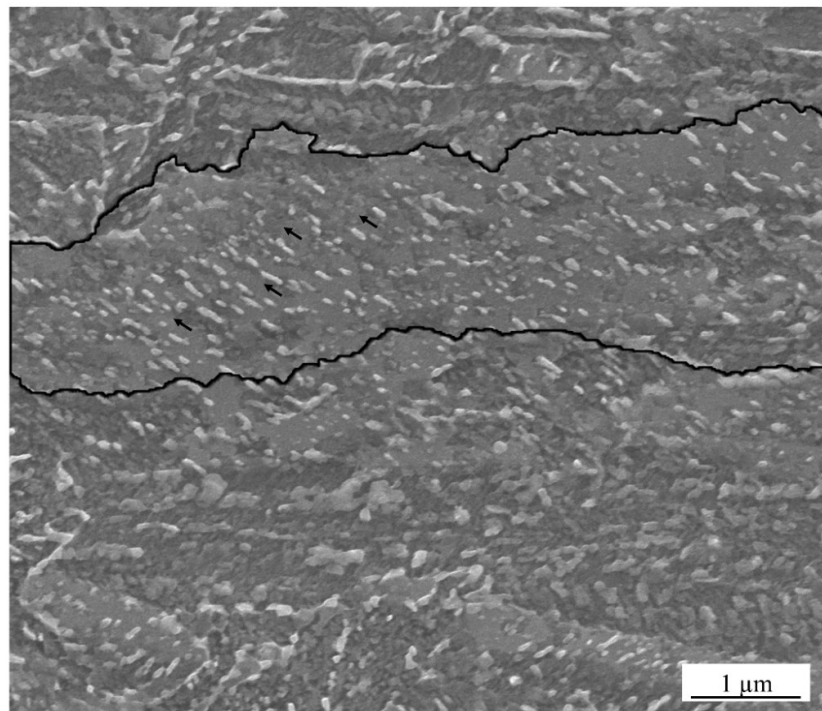


Figure 6-3: SEM micrograph of tempered lower bainite observed in 100-O condition.
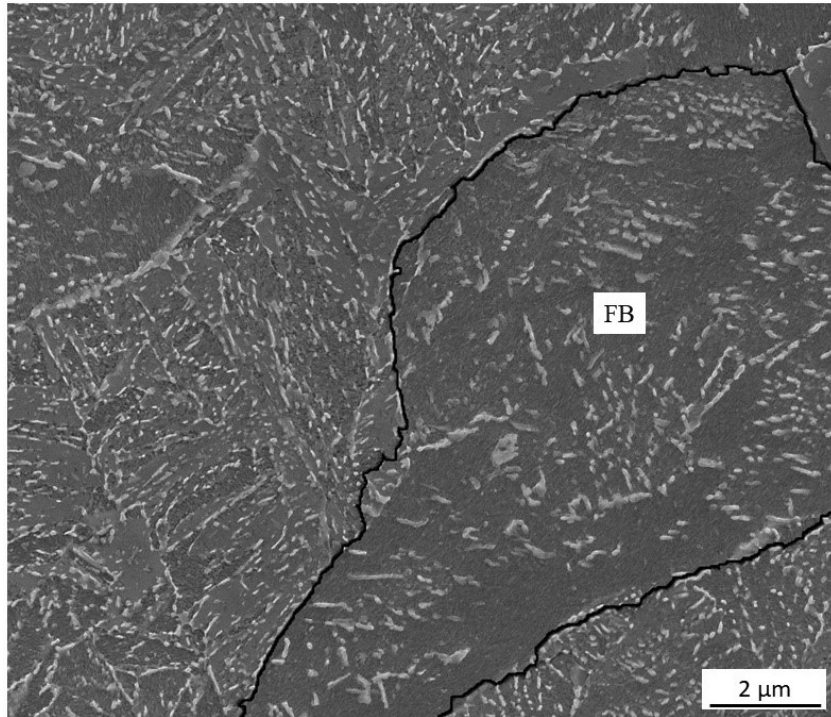
Figure 6-4: SEM micrograph showing "featureless" bainite found in 250-P. (FB) featureless bainite.
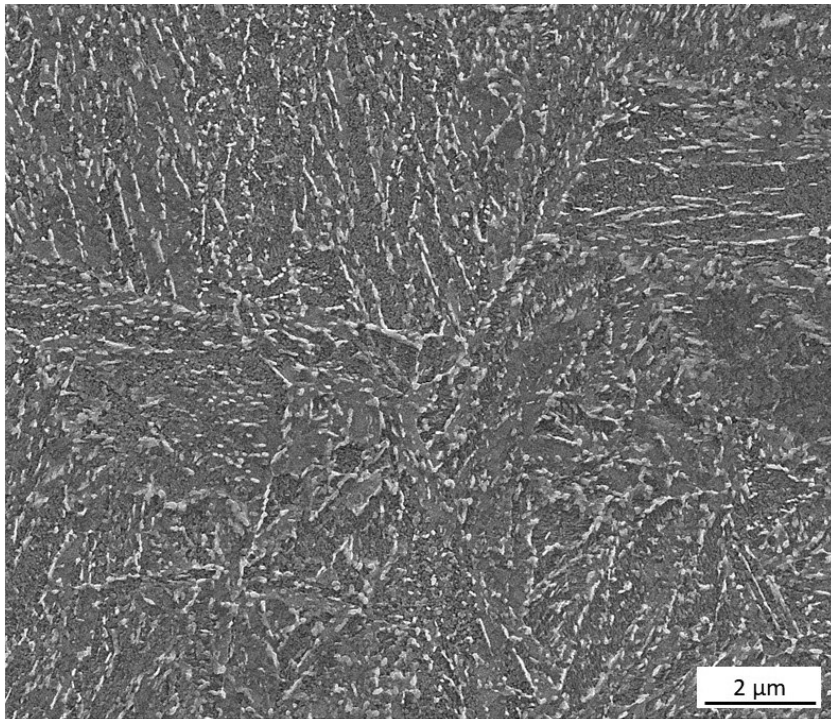


Figure 6-5: SEM micrograph corresponding to 100-W condition, showing a full tempered martensitic structure.
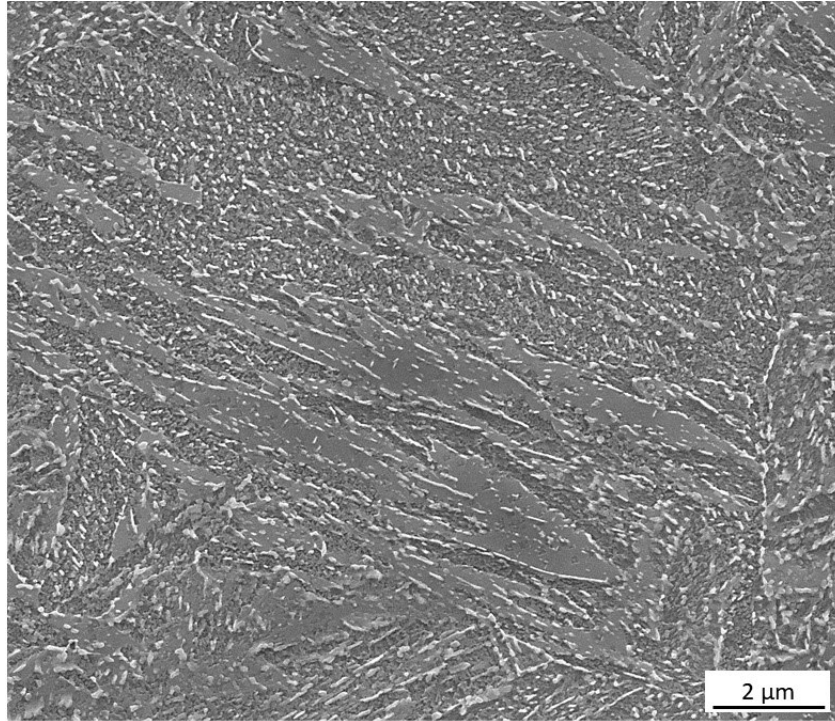
Figure 6-6: SEM micrograph corresponding to 100-P condition, showing distribution of tempered microstructures (martensite and bainite).
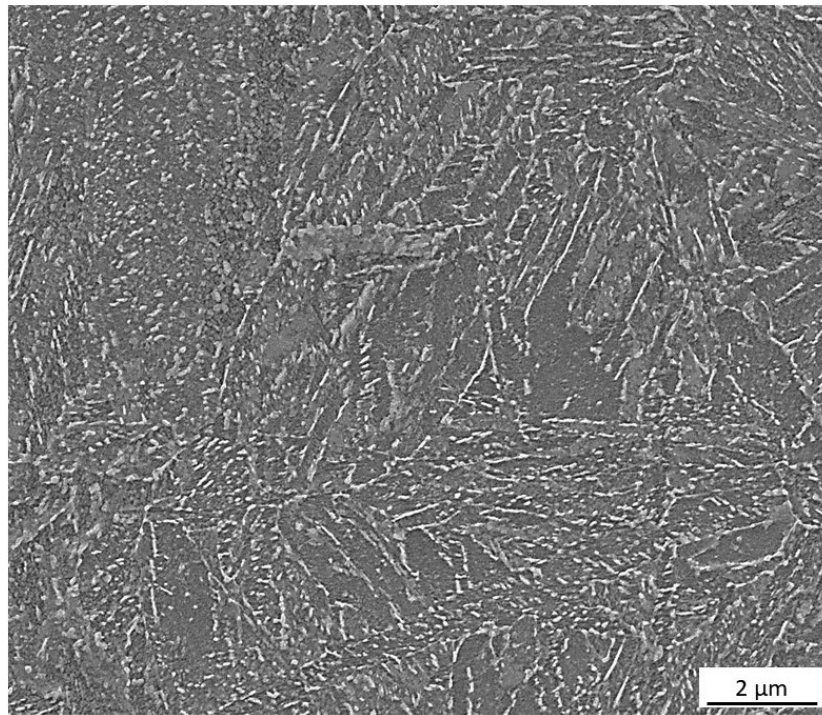


Figure 6-7: SEM micrograph corresponding to 100-O condition, showing distribution of tempered microstructures (martensite and bainite).
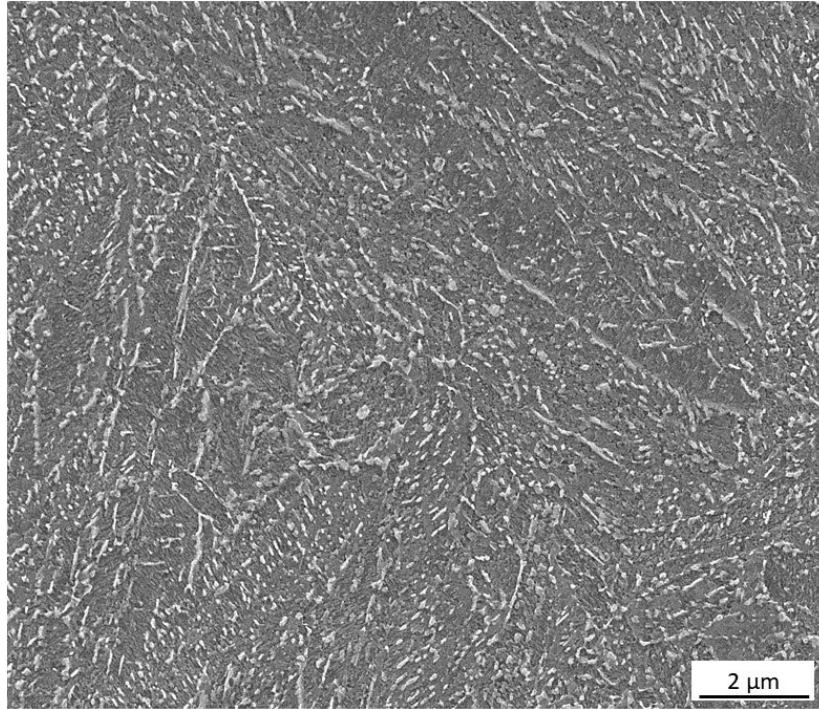
Figure 6-8: SEM micrograph corresponding to 250-W condition, showing distribution of tempered microstructures (martensite and bainite).
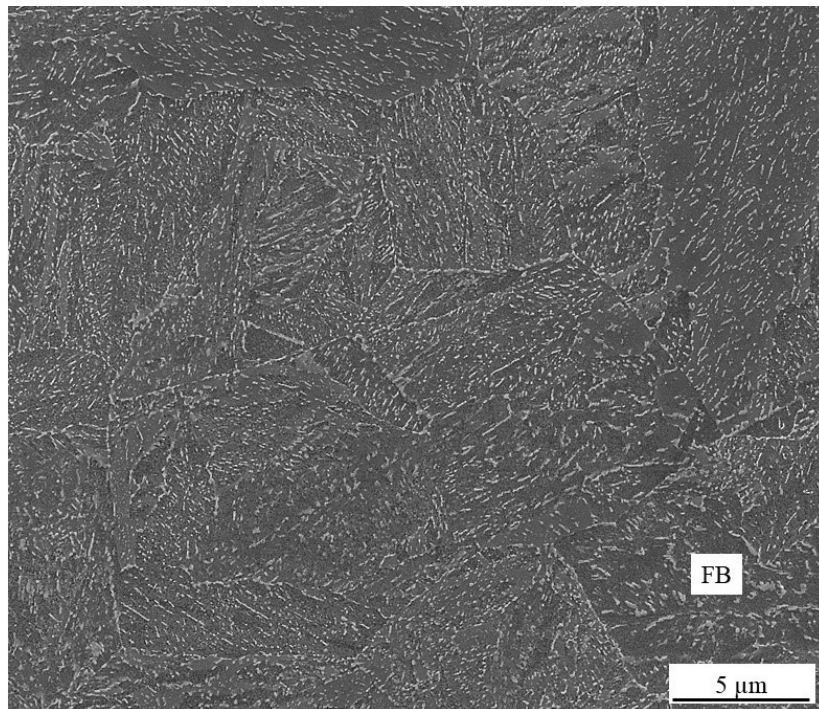


Figure 6-9: SEM micrograph corresponding to 250-P condition, showing tempered lower bainite along with featureless bainite (FB).
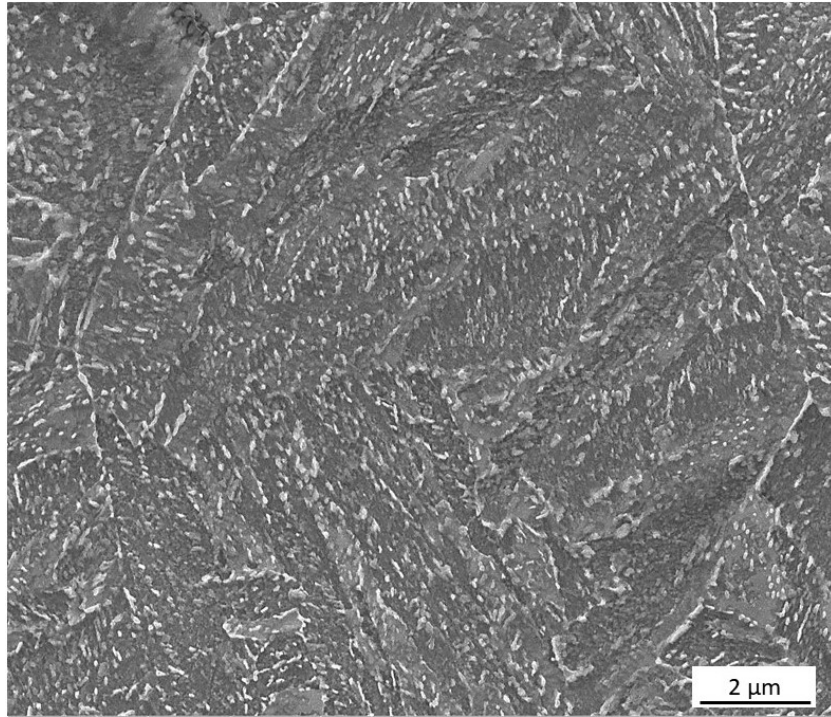
Figure 6-10: SEM micrograph corresponding to 250-O condition, showing mostly tempered lower bainite.

### 6.2.2 Tensile Properties

The yield strength (YS), and ultimate tensile strength (UTS) properties for the various thickness-cooling conditions are illustrated in *Figure 6-11*. Initially it can be seen that all the conditions resulted in yield strength values over 760 MPa, which complies with the minimum yield strength level of the material specification for the selected component. Correspondingly the UTS values also were well above the minimum UTS requirement (900 MPa) as per the material specification. The YS and UTS values of the three 100 mm cross sections varied from 925 to 979 MPa, 1041 to 1065 MPa respectively, whilst the YS and UTS of the three 250 mm sections varied from 839 to 924 MPa, 989 to 1040 MPa. Overall, the maximum YS and UTS was achieved in 100-O. On the other hand, the minimum YS and UTS were achieved in 250-P, this behaviour was unexpected, as aqueous polymer showed faster cooling conditions as compared to the cooling conditions produced in 250-O (slower cooling condition). The reasons associated to the unexpected strength and toughness results are thoroughly discussed in section 6.3.2.

### 6.2.3 Impact Properties

The CVN impact energy properties for the various thickness-cooling conditions are provided in *Figure 6-12*. Initially it can be seen that all the conditions resulted in impact values over 42 J, which complies with the impact energy level of the material specification for the selected component. The CVN values of the three 100 mm cross sections varied from 83 to 98 J, whilst the CVN values of the three 250 mm sections varied from 76 to 85 J. The maximum CVN impact energy was achieved in 100-P. On the other hand, the minimum CVN impact value was achieved in 250-P, again this was unexpected as aqueous polymer showed faster cooling conditions as compared to the cooling conditions produced in 250-O (slower cooling condition).
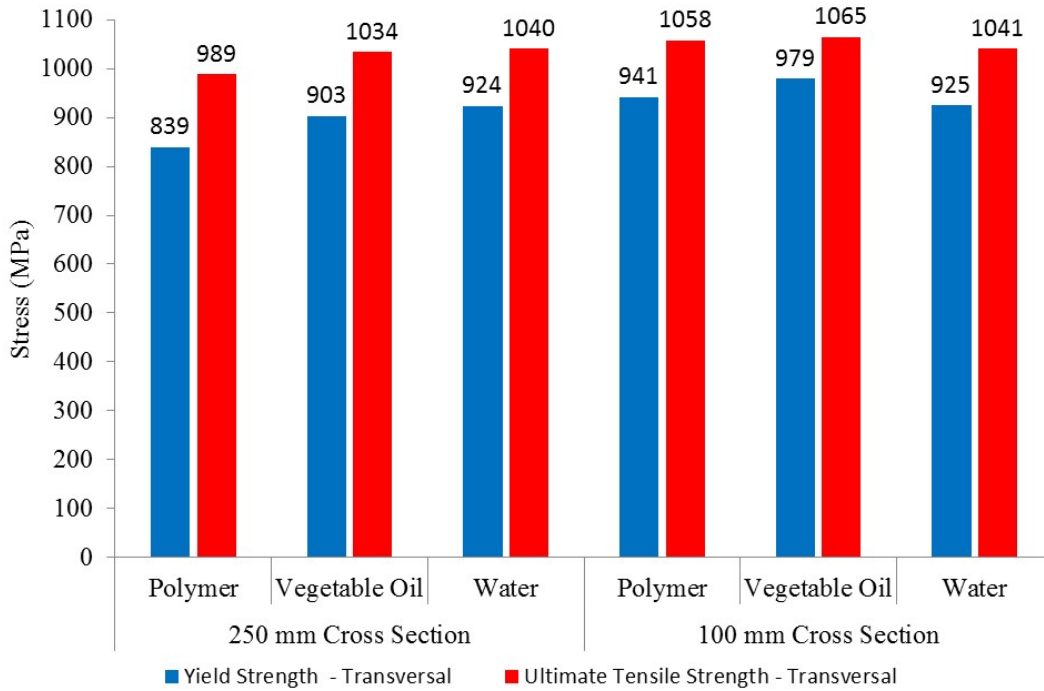
Figure 6-11: Tensile properties of the tested material at room temperature.
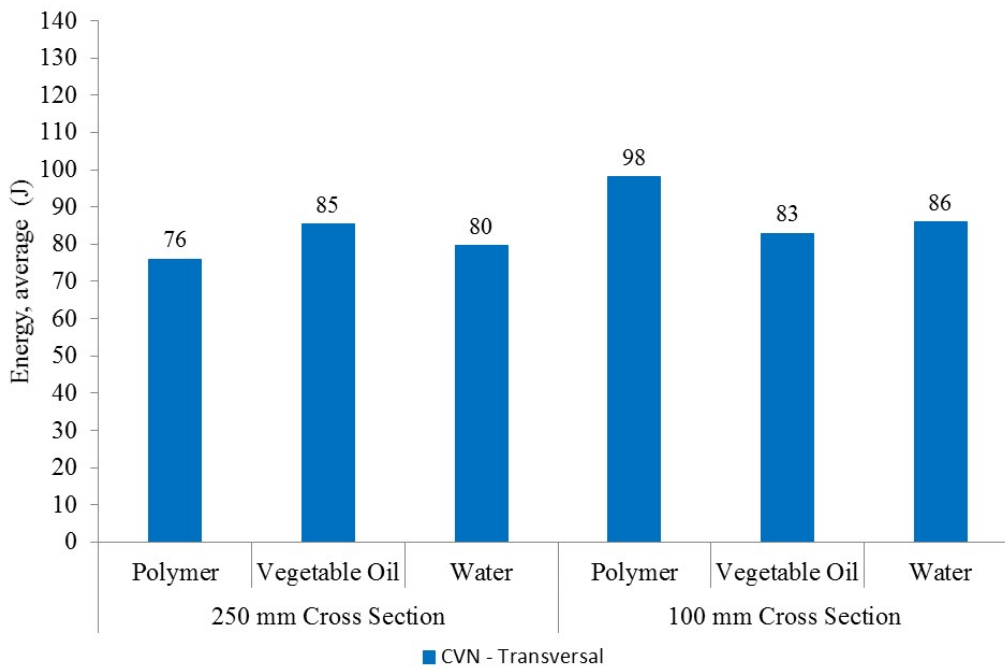


Figure 6-12: Impact properties of the tested material at -30°C.

As seen in *Table 6-1* no relationship is observed between the cooling parameters ($CR_{MAX}$ and $\lambda$) and the mechanical properties. This inconsistency between the cooling conditions and mechanical properties, along the unexpected results described above might be explained in terms of the microstructural changes produced after industrial heat treatment. This will be explain later in section 6.3.2 after discussing the effects of quenching and tempering on the microstructural evolution.

| Identification | CR $_{Max}$ (°C /s) | $\lambda$ (s) | Yield Strength (MPa) | Ultimate Tensile Strength (Mpa) | CVN Impact Energy (J) |
|---|---|---|---|---|---|
| 100W | 2.17 | 154 | 925 | 1041 | 86 |
| 100P | 1.52 | 231 | 941 | 1058 | 98 |
| 100O | 1.6 | 253 | 979 | 1065 | 83 |
| 250W | 0.85 | 387 | 924 | 1040 | 79 |
| 250P | 0.65 | 515 | 839 | 989 | 75 |
| 250O | 0.6 | 608 | 903 | 1034 | 85 |

Table 6-1: Tensile and CVN Impact properties at RT and -30°C respectively.

## 6.2.4 CTOD Properties

As briefly explained in section 3.5.4, the specimens for CTOD testing were selected based on the yield strength values produced by the different thickness-cooling conditions. In this sense, the minimum (839 MPa / 250-P) and maximum (979 MPa / 100-O) yield strengths where selected along with two locations (925 MPa / 100-W and 941 MPa / 100-P) which showed intermediate values between the maximum and minimum yield strengths.

CTOD fracture toughness results are provided in *Table 6-2*. A first observation is that the CTOD value for all the conditions varied from 0.242 to 0.249 mm. it is evident that this variation is almost negligible and it can be argued that CTOD parameter for all the conditions is almost the same, regardless of the changes in yield strength. In addition, it is noteworthy to mention that these CTOD values were very close to 0.25 mm which corresponds to the aim value originally proposed by the company.

Additionally, the stable crack extensions (ductile tearing fracture) for 100-W, 100-P 100-0 and 250-P conditions were 2.30, 1.48, 2.35 and 2.44 mm respectively. In line with the observations made for the CTOD values, the stable crack extension was also very similar for all the

conditions with the only exception of 100-P which resulted in a crack extension value of 1.48 mm. Furthermore, the maximum forces for 100-W, 100-P 100-0 and 250-P conditions were 111.45, 108.57, 116.57 and 111.13 kN respectively.

Finally, as illustrated in the force - displacement curves provided in Appendix E, the 100-W, 100-O and 250-P specimens experienced a gradual decrease in load immediately after reaching maximum force without fracturing (no complete separation). This behaviour could be an indication of a relatively high ductility on the specimens even after reaching maximum load. On the contrary, 100-P specimen immediately break into two parts after reaching its maximum load.

| Identification | Yield Strength (MPa) | CTOD, $\delta$ (mm) | Stable crack extension, $\Delta$ (mm) | Maximum load (kN) |
|---|---|---|---|---|
| 100W | 925 | 0.246 | 2.30 | 111.45 |
| 100P | 941 | 0.242 | 1.48 | 108.57 |
| 100O | 979 | 0.249 | 2.35 | 116.57 |
| 250P | 839 | 0.243 | 2.44 | 111.13 |

Table 6-2: CTOD properties tested at $^{\circ}0$ C. Yield strengths values are included for reference.

In summary, it can be argued that irrespective of the yield strength variations associated the different thickness-cooling conditions, the CTOD values were almost the same for the various studied conditions, and more importantly they were very close to the aimed value originally proposed for this research project. In this sense, one question arises immediately: what are the reasons behind the similarity in CTOD properties for different thickness-cooling conditions? As seen in section 6.3.4, this question is addressed in terms of the microstructural evolution not only during heat treatment but as well during the previous manufacturing operations.

Additionally, it is interesting to note that 100-P specimen showed the lowest values of stable crack extension and maximum load, although it should be pointed out that these variations do not alter significantly its corresponding CTOD value. However as further explained in section 6.3.4 , these variations were associated to chemical segregation remaining after industrial heat treatment.

*6.2.4.1 CTOD Fracture Surface Analysis*

In view of the complexity of the relationships between CTOD fracture toughness and microstructure, a detailed fracture surface analysis was carried out on the C (T) specimens in order to clarify the fracture mechanisms controlling the performance of large forgings heat treated under industrial conditions. In this sense *Figure 6-13*, illustrates the typical fracture modes observed in all the C(T) specimens extracted from the selected thickness-cooling conditions, whereas *Figure 6-14* to *Figure 6-16*, display high magnification fractographs of the ductile, transition and cleavage regions for each condition evaluated.

The characteristic fracture modes observed in the four C (T) specimens are illustrated in *Figure 6-13*. A dimple structure, characteristic of ductile fracture was observed immediately after the fatigue precrack tip as illustrated in *Figure 6-13* (a). Frequently, this ductile fracture mode is identified as ductile tearing zone or stable crack extension and it's a consequence of the blunting process taking place at the fatigue precrack tip during crack growth [140, 141].
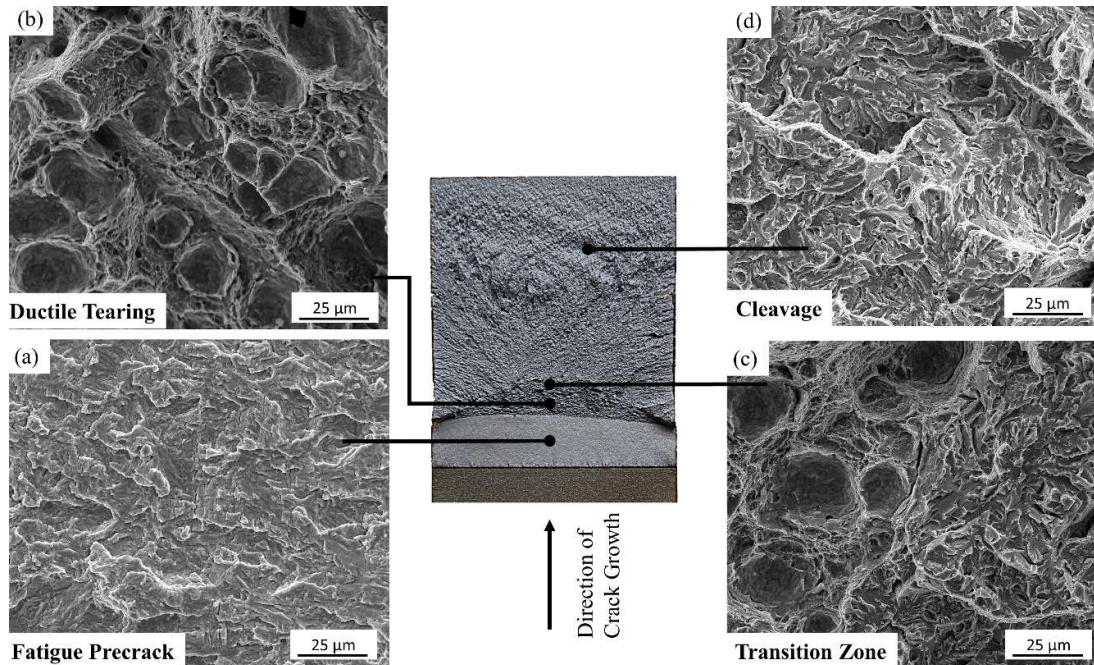


Figure 6-13: Typical fracture modes observed on the fracture surface of 100-O specimen quenched in aqueous polymer and tempered at 590°C: (a) Fatigue precrack, (b) Ductile tearing zone, (c) Ductile-Cleavage transition zone  and (d) cleavage zone.

Hausild et al. [141], investigated the effect of ductile tearing on fracture energy at 0°C and 90°C of an A508 Cl. Steel, their results suggest a correlation between the ductile area and fracture toughness of C (T) specimens tested at 0°C, i.e., higher ductile area leads to higher fracture toughness. However, no such correlation was found on the C (T) specimens tested at -90°C.

As the ductile crack front propagates through the specimen, eventually a transition between the ductile tearing and cleavage zones becomes evident as displayed in *Figure 6-13* (b). As elucidated by Soboyejo and co-workers [140], this zone is of relevance since in general, the critical CTOD value is reached in this transition region. As explained by the same author in reference [140], the rationale behind the occurrence of a critical CTOD value in the aforementioned region can explained by the interruption of the stable ductile tearing imposed by cleavage cracking. The above mentioned cleavage cracks initiate ahead of the ductile zone, and propagate in the opposite direction of the crack growth until they coalesce with the ductile tearing zone as elucidated in *Figure 6-13* (c). Finally, *Figure 6-13* (d) shows a representative area of the cleavage fracture observed in all the C (T) specimens which fracture mode is predominantly transgranular.

As described in section 2.7.2.4, ductile fracture mechanism involves the nucleation growth and coalescence of voids. In addition, as explained by Broek et al. [142], second particles such as non-metallic inclusion are preferred initiation sites for void nucleation. In this regard, as illustrated in *Figure 6-14* , some non-metallic inclusions (dotted square) were observed inside the voids structure associated to the stable ductile tearing. The diameter of the non-metallic inclusions varied from 2 to 5 μm in all the specimens. The chemical composition of the non-metallic inclusions was not determined as this sort of analysis is out of the scope of the present work. However, according to the chemical composition of the selected steel, sulphides (MnS, CaS), and oxides (MnO, MgO, Ca) non-metallic inclusions are usually presented in the selected steel after solidification process.

Considering that the size and distribution of non-metallic inclusions are in fact not significantly affected by changes in cooling rate during quenching, it is therefore expected that the ductile tearing zones produced on all the specimens are very similar between each other.

The transition from the ductile tearing to cleavage fracture for the 100-W, 100-P, 100-O and 250-P specimens is illustrated in *Figure 6-15*. As seen in this figure, all the specimens display a well-defined transition zone where cleavage cracking interrupts the stable crack extension which correspondingly represents the region in which critical CTOD is obtained. Brittle fracture surfaces of the C (T) specimens corresponding to all the studied conditions are shown in *Figure 6-16*. 100-W, 100-O and 250-P conditions display a similar fracture mode, which can be defined as a transgranular quasi-cleavage mode. This fracture mode is characteristic of a ductile material and its fracture surface it's distinguished by the presence of concave facets, micro-cracks and areas of dimple rupture, which form tear ridges with the cleavage steps. On the contrary, as illustrated in *Figure 6-16* (b), 100-P condition shows a well-defined cleavage fracture mode which unlike all the conditions consists of large and flat-like facets. In addition, dimple rupture was occasionally observed on the fracture surface of this specimen as illustrated in *Figure 6-17*. In this type of fracture mode the cleavage facets are flatter than those of quasi-cleavage fracture and its chevron patterns are usually pointing to the fracture origin [143]. According to the observations of Balart and Knott the fracture mode differences between 100-P and the rest of conditions could be associated to microstructural variations associated to changes in carbide size distribution. In this sense, triggering brittle fracture, involves a number of factors which contribute to the nucleation and propagation of cleavages cracks. Under the application of external load, microcracks are generated ahead of the macroscopic crack. These microcracks in turn are developed at carbide precipitates which serve as cleavage nucleation sites as explained by Ritchie et al. [144].Correspondingly, these discontinuities act as stress risers contributing to exceed the atomic bond strength therefore promoting cleavage crack nucleation. If the stress ahead of the macroscopic crack is higher than the fracture stress ($\sigma_f$) the microcrack propagates into the matrix leading to cleavage fracture [81].

In summary, it can be argued that inclusions (void nucleators) and carbides (crack nucleators) are the main microstructural features associated to the different fracture mechanisms observed under the different thickness-cooling conditions. Although, it also true that a correlation exists between the packet size (sub-grain structure) and facet size. However, the work of Johnson and Becker [145], clearly indicates that the main characteristic controlling the fracture toughness of tempered bainitic structures is the distribution of and size of the carbide precipitates.
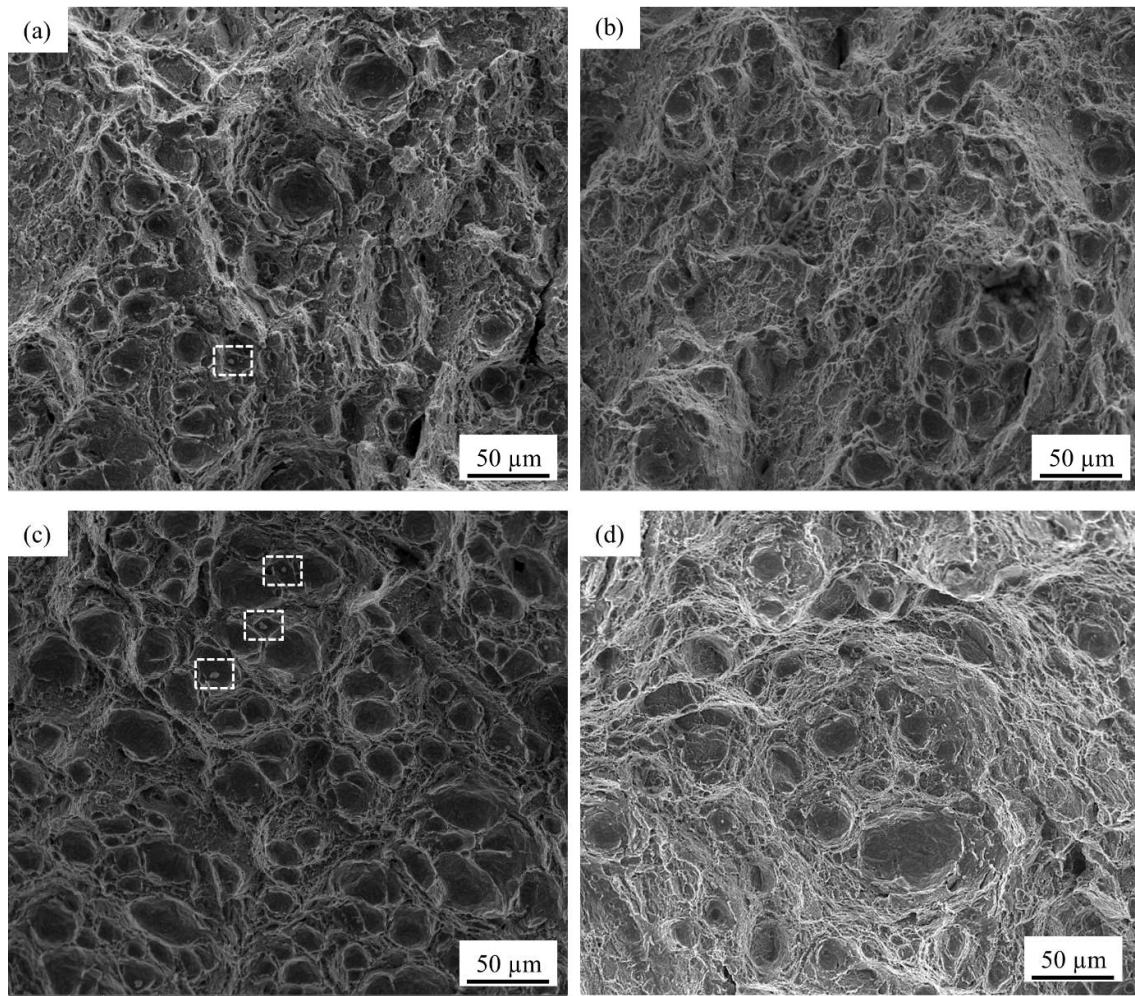
Figure 6-14: SEM fractographs of ductile tearing zones on (a) 100-W, (b) 100-P, (c) 100-O and (d) 250-P.
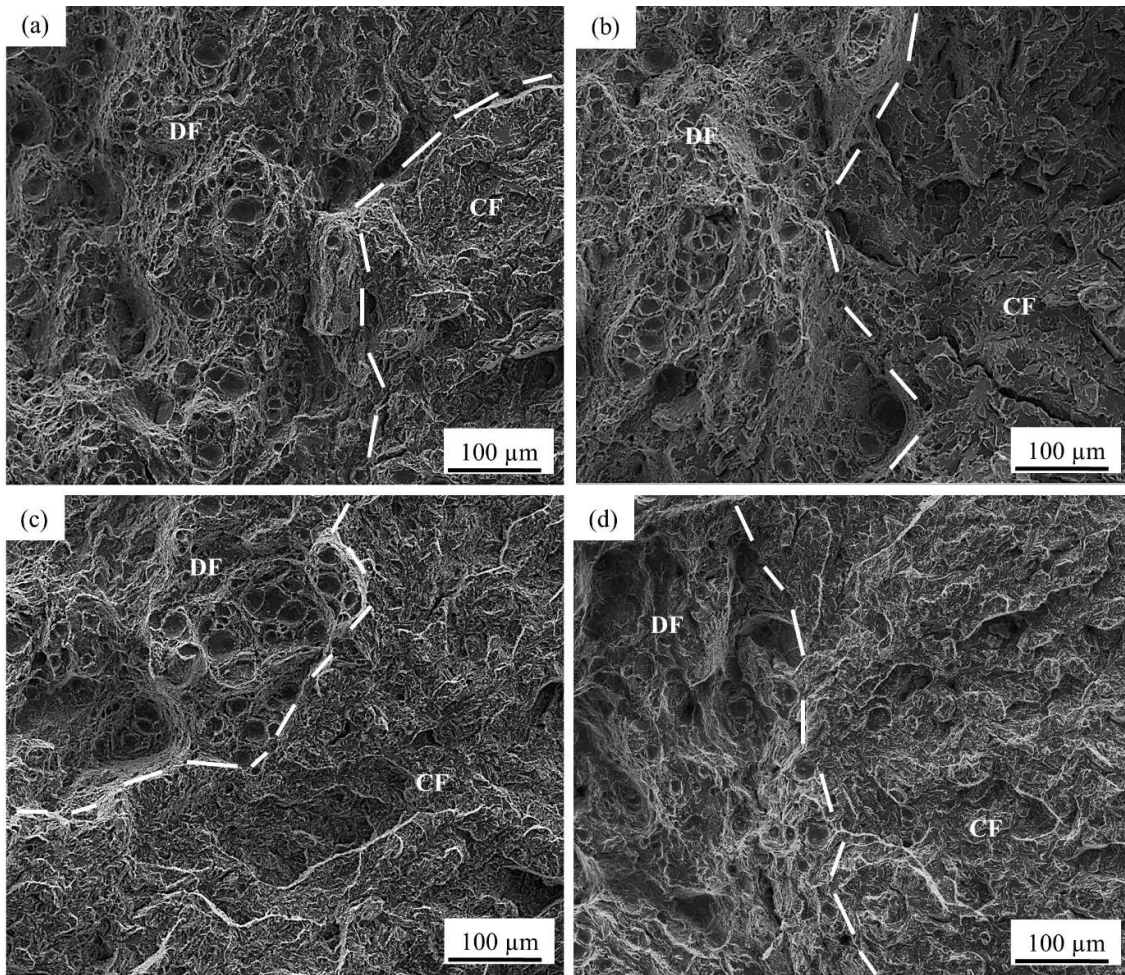
Figure 6-15: SEM fractographs of ductile tearing cleavage transition zones on (a) 100-W, (b) 100-P, (c) 100-O and (d) 250-P.
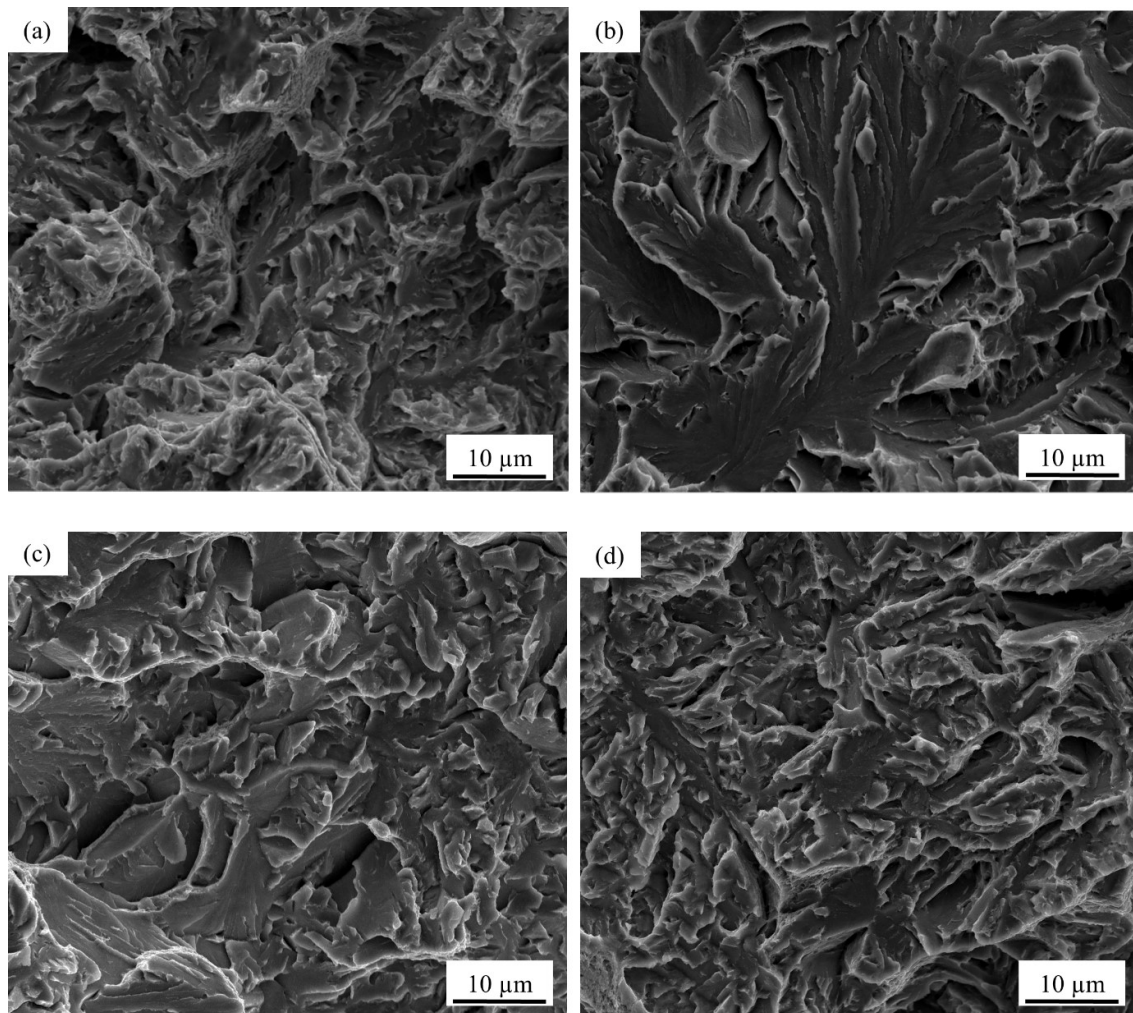
Figure 6-16: SEM fractographs of cleavage fracture zones on (a) 100-W, (b) 100-P, (c) 100-O and (d) 250-P.
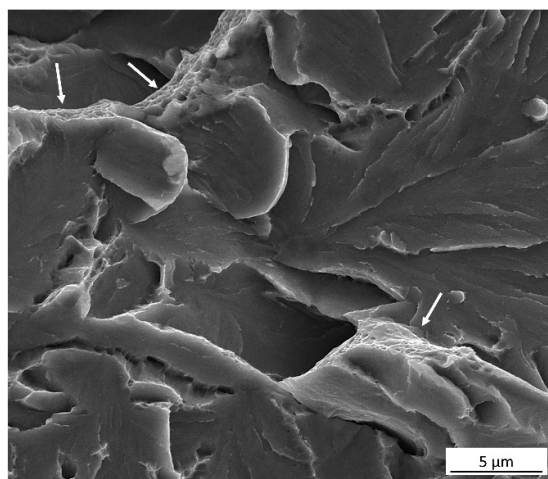


Figure 6-17: Dimple rupture (white arrows) forming tear ridges or steps between cleavage facets on 100-P condition.

*6.2.4.2   Subsurface Microstructures near to initiation sites*

In order to identify the main microstructural features controlling the CTOD fracture toughness, a microstructural evaluation was carried out near to the ductile-brittle transition zone in all the C (T) specimens since this is the area in which critical CTOD is obtained. Initially, an attempt was made to locate cleavage initiation sites in the different specimens analysed, however, as seen in Figure 6-18, only in the specimen corresponding to 250-P condition a cleavage initiation site was located. As explained by Bowen et al. [146], the reason for this difficulty to find initiation sites could be associated to a reduced sampling volume characteristic of sharp crack specimens. In this sense, Lin and Ritchie [147] defined the sampling zone as: "the volume of material within the plastic zone required to ensure the presence of an eligible particle where the fracture criterion can be met". As seen in this figure it can be seen how cleavage initiation site is located ahead of the ductile tearing zone. In addition, non-metallic inclusions with average size of 3μm can also be observed near to initiation site in Figure 6-18 (c) and (d), nevertheless these features cannot be regarded as the main features triggering cleavage since they are in fact located at the bottom of dimple voids associated to ductile fracture. As mentioned previously, the reason why the non-metallic inclusion are not potential initiation sites for cleavage could be associated to the fact that the higher stresses are located further ahead of the blunted precrack tip (and not near to the inclusions) therefore it might be unlikely triggering cleavage promoted by non-metallic inclusion.

The microstructure of the cross-section near to the cleavage initiation site is illustrated in *Figure 6-19* and *Figure 6-20*. In these figures, it can be observed how the cleavage crack paths are mainly changed by the prior austenite grain boundaries or occasionally by the sub-grain boundaries additionally, it can also be observed how the cleavage cracks are arrested by the prior austenite grain boundaries or by the sub-grain boundaries. These observations are in line with the work of Kim et al. [148], in which it is demonstrated the packet substructure determines the cleavage fracture unit.
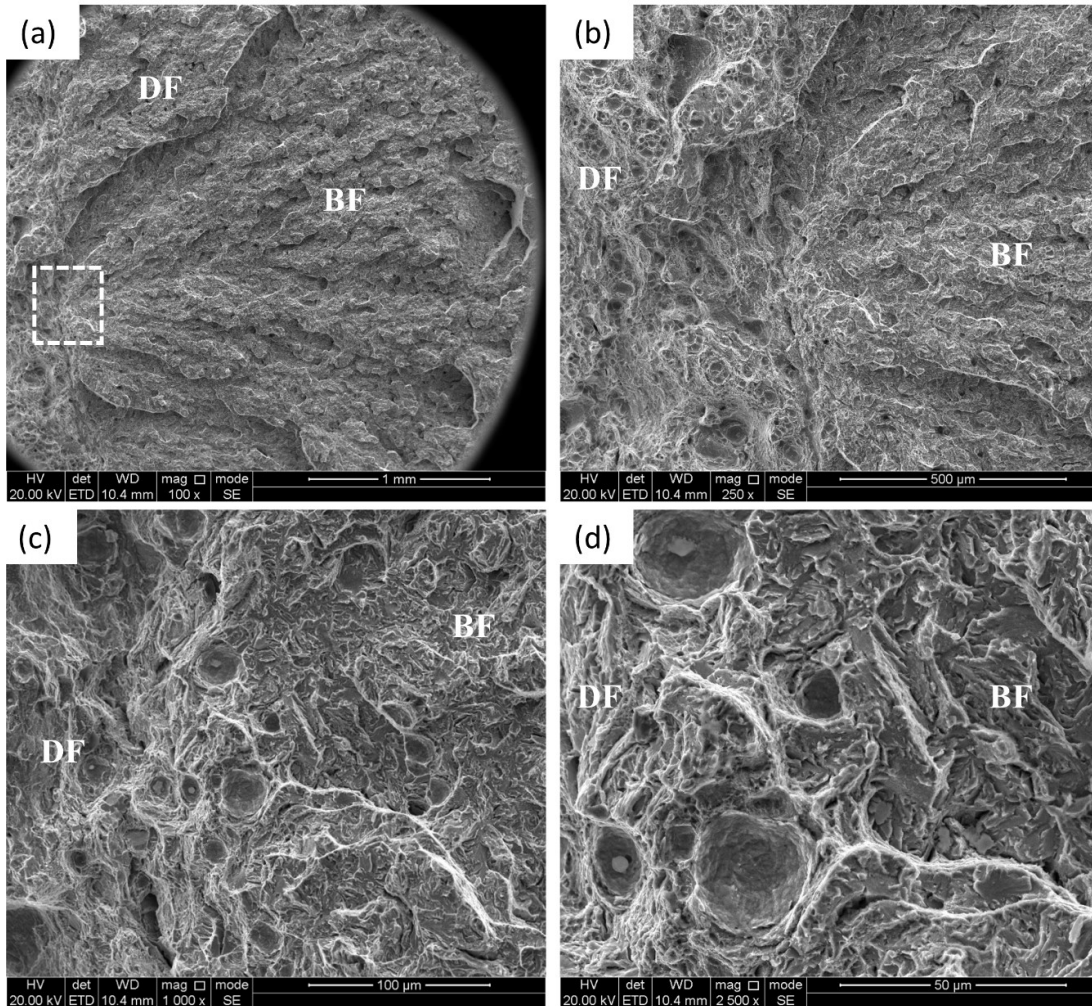
Figure 6-18: SEM micrographs of the main cleavage initiation site in the precracked C (T) specimen 250-P condition showing: (a) cleavage initiation area ahead of the precrack tip, (b) ductile and brittle fracture near to initiation site, (d) and (c) detail of the fracture initiation site.
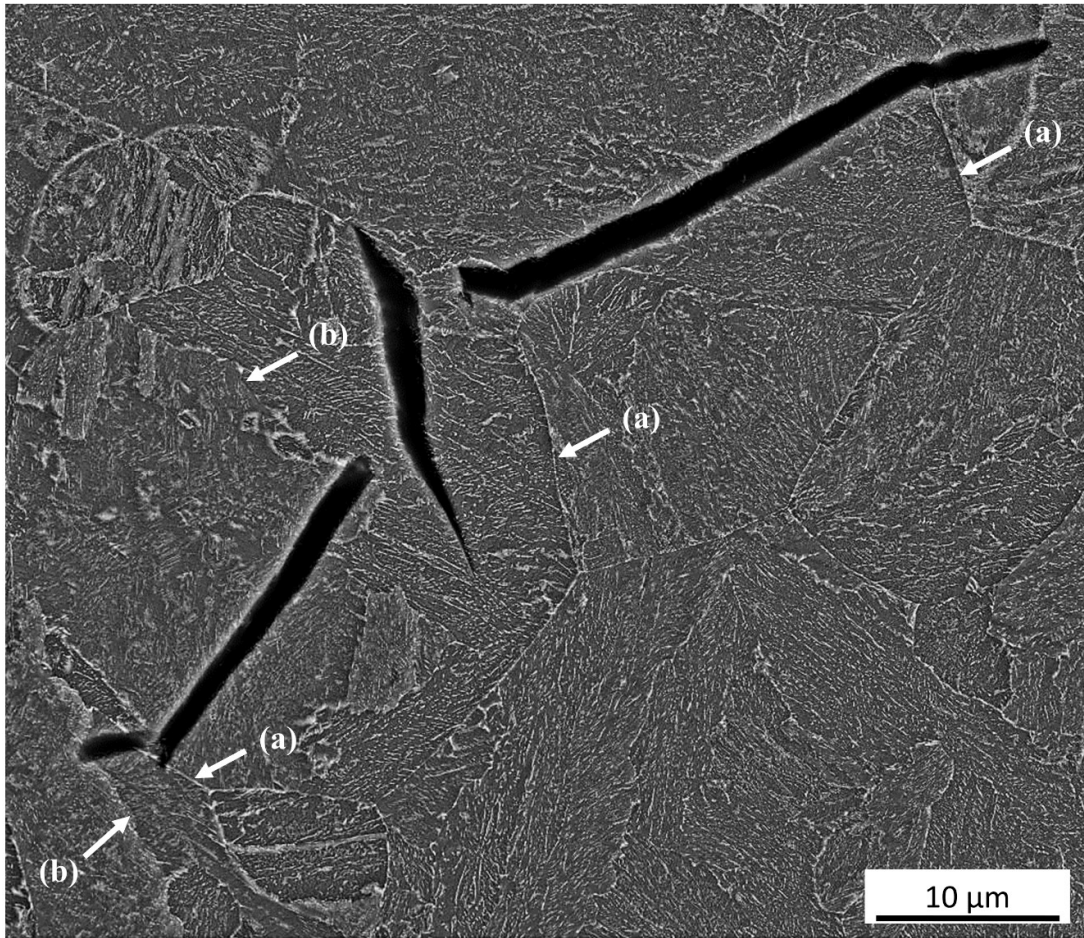
Figure 6-19: SEM micrograph of the cross-sectioned area beneath the fracture surface of the precracked C (T) specimen 250-P condition, showing the crack propagation path changed by (a) prior austenite grain boundaries and (b) sub-grain boundaries. It is also noted that cleavage cracks are arrested by packet boundaries.
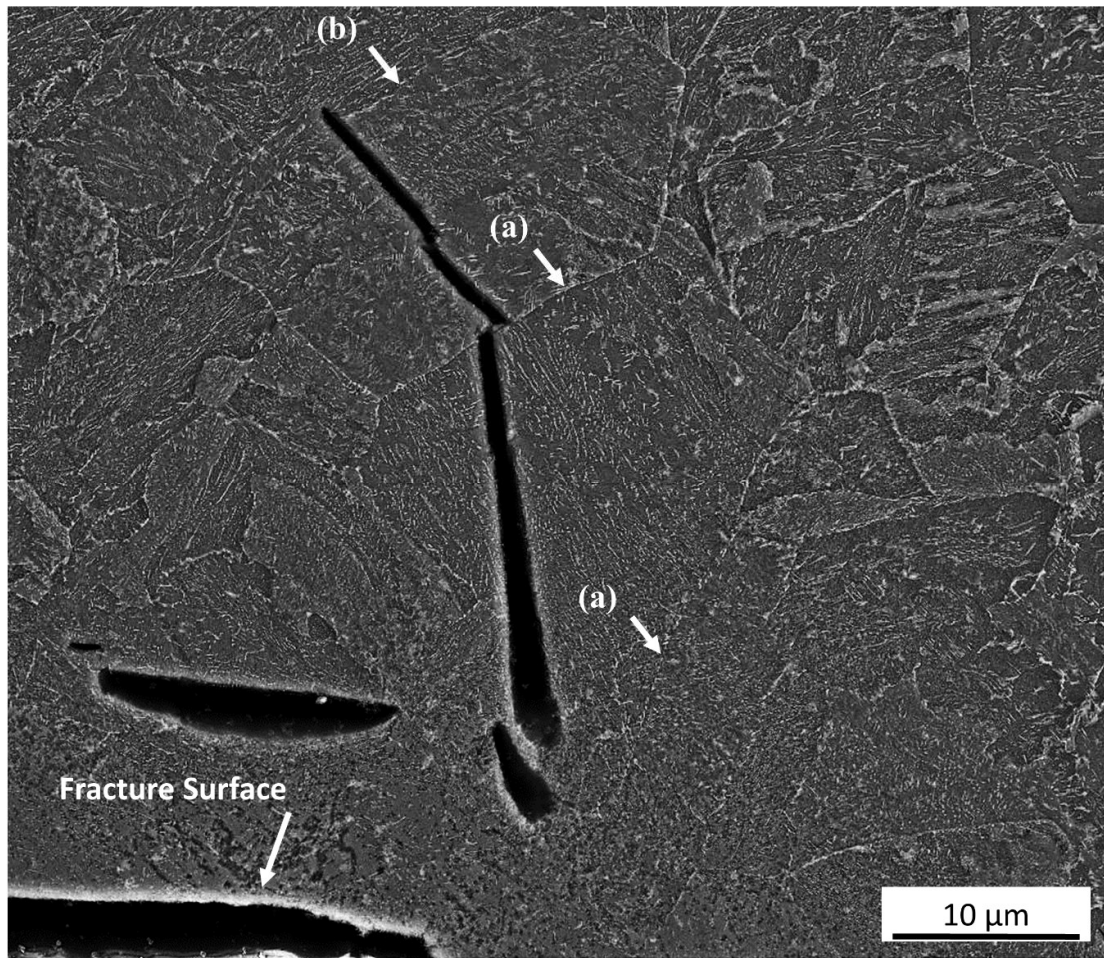
Figure 6-20: SEM micrograph of the cross-sectioned area beneath the fracture surface of the precracked C (T) specimen 250-P condition, showing the crack propagation path changed by (a) prior austenite grain boundaries and (b) sub-grain boundaries. It is also noted that cleavage cracks are arrested by packet boundaries.

## 6.3 Discussion

### 6.3.1 Effect of industrial heat treatment on Microstructural evolution

As described in Chapter 5, the microstructural evolution during quenching is greatly influenced by the applied cooling rate. In turn, the strength and toughness behaviour is determined by the microstructures produced after quenching and tempering. In this regard, it can be elucidated that the fast cooling rate produced on the thin section of the ring segment quenched in water (100-W) promote the formation a fully martensitic structure (see *Figure 6-5*), which as explained by Bhadeshia and Khan [149], begins its formation at imperfections of the austenite (parent phase) such as dislocation arrays. As per CCT diagram in Chapter 5, constant cooling rates greater than 1°C/s are required to allow to formation of a full martensitic structure during industrial quenching by avoiding the bainitic nose of the diagram. It is noteworthy to mention the formation of full martensite in 100-W condition it is not only dependent on the high heat transfer rates produced by water, but also is affected by the thin wall of the ring segment which contributes with relatively high heat removals rates in comparison, for example, with the thick wall of the ring segment (250-W). A seen in *Figure 6-6* to *Figure 6-10*, the rest of the conditions; 100-P-100-O, 250-W, 250-P and 250-O, resulted mostly in the formation of mixed structures of tempered martensite and tempered bainite. Correspondingly, mixtures of martensite and bainite can be obtained between 1 and 0.3°C/s, according to the CCT diagram in Chapter 5. In this regard, the formation of these microstructures under industrial quenching can be explained by the heat transfer conditions produced by the type of quenchant and the cross section of each ring segment. The effect of the type of quenchant and cross section size on the cooling conditions produced during industrial quenching were already discuss in detail in section 4.3.2. As observed in *Table 5-1*, as the constant cooling rate decreased from 1 to 0.3°C, lower bainitic structure become visible and its phase fractions increases as the cooling rate is further decreased. At the same time the volume fraction of tempered martensite decreased with a decreasing cooling rate. Regarding the bainitic transformation during quenching, it has been addressed by Bohemen et al. [129] that its formation strongly depends on the prior austenite grain size, however in the present research the prior austenite grain size it is assumed to be in a similar range considering that, in principle, the austenitizing conditions (temperature –time) were the same for the three ring segments quenched in water, polymer and vegetable oil.

Although, it should be pointed out that the heating rates during austenitizing process were not necessarily the same since the three ring segments were austenitized in different furnaces with correspondingly different heating rate capacities.

As explained in section 2.6.2, tempering treatment is of great importance for the determination of the mechanical properties, where the main mechanism occurring during the tempering of martensite is the precipitation of carbides while the tempering of bainite mainly involves a slight coarsening effect of the carbides precipitates already formed during quenching. As described in 6.2.1.2, the carbide precipitates in tempered martensite were finer than those of tempered bainite. This aspect is of considerable relevance since the size and distribution of carbides represent one of the main factors controlling the fracture toughness of low alloy steels [97]. There are a couple of explanations associated to observed differences between the carbide size precipitates of tempered martensite and tempered bainite. In principle, the bainitic structure is already coarse before tempering treatment due to the autotempering process occurring during quenching [57] and any additional *re-tempering* only further contributes to its coarsening process. On the contrary the precipitation of carbides in the martensitic structure in fact begins during actual tempering treatment. However as explained in section 2.6.2, bainite is less sensitive to tempering treatment in comparison with martensite. The second aspect is associated to the high transformation temperatures of bainite in comparison with those of martensite. As explained by Albrecht et al [150], at high transformation temperatures the diffusion rate is also high, leading to precipitation of coarse cementite which nucleates and grows from the carbon supersaturated ferrite. In addition, a relation between the cooling rate and transformation temperatures can be observed either for the exponential (industrial quenching) and constant (CCT) cooling where, as the cooling rate decreased the transformation temperature for bainite is increased. Considering this, it can be concluded that high transformation temperatures and slow cooling rates associated to the formation of bainite in combination with the industrial tempering treatment are the main factors contributing to the slightly coarse carbide precipitates compared to those of tempered martensite.

Another important difference between tempered martensite and tempered lower bainite can be observed in *Figure 6-2* and *Figure 6-3*. The lack of interlath precipitates it is evident on tempered bainite, where only intralath precipitation is observed. On the contrary, extensive interlath precipitates are observed between the laths of tempered martensite.

For martensite, this behaviour can be explained in terms of its nucleation and growth mechanisms during tempering where interlath, intralath and grain boundaries are preferential sites for the nucleation and growth of carbides [39]. The explanation for the precipitation behaviour on bainite obeys to its kinetic of phase transformation, where the slow diffusion rates (in comparison, for example with those of upper bainite) allow the penetration of some carbon in the bainitic ferrite which in turn promotes the formation of fine intralath rather than interlath precipitates. As seen in *Figure 6-9* and *Figure 6-10*, extensive carbide precipitation can be elucidated at the prior austenite grain boundaries of 250-P and 250-O. As described in reference [151], the reason for this could be associated to longer time available for carbides to precipitate along the grain boundaries due to the high diffusion rates associated to high transformation temperatures / slow cooling rates produced under the aforementioned conditions.

Another important aspect observed in 250-P was the formation of a so-called featureless bainite, as observed in Figure *6-4*. The reason for the formation of this microstructure on the thick section of the ring segment quenched in polymer is not clear. However, Pickering and Bhadeshia [90] observed that macrosegregation generated during the solidification of large ingots might lead to the formation of unexpected microstructures after quenching and tempering. It is also reported in this work, that during tempering at 645°C for 6 h, the austenite-martensite island formed during quenching decomposes into mixtures of ferrite and cementite. It was reported as well that these austenite-martensite islands were found in segregated regions. In addition, Habraken and Economopoulos [152] revealed that nonclassical bainites can be formed during continuous cooling, including carbide-free acicular bainite, and granular bainite. Interestingly, as explained by Samuel and co-workers [153] granular bainite consists of a bainitic-ferrite matrix with martensite-austenite islands which upon tempering, decompose into mixtures of ferrite and cementite. Based on the previous context, it could be argued that possibly, the presence of featureless bainite observed in 250-P could be due to chemical segregation from ingot solidification which promotes the formation of non-uniform microstructures after heat treatment. Further analysis might be required to determine the type of segregation (enrichment or depletion) and the segregated chemical elements associated to the formation of this microstructure. Presumably this so called featureless bainite could be in fact associated to mixtures of ferrite and cementite after tempering treatment.

Finally, it is well known that upon quenching treatment, martensite and bainite might contain certain amounts of retained austenite. Nevertheless, as seen in the previous section no evidence of retained austenite was found on the different tempered conditions studied. The reason for this is due to the fact that any austenite retained after quenching is decomposed during tempering at temperatures above 400°C and transformed into mixtures of ferrite and cementite, the above, bearing in mind that the ring segments were tempered at 590°C [53].

## 6.3.2   Effect of Microstructure on Tensile Properties

The first observation that becomes clear from the YS and UTS results (*Figure 6-11*) is that despite the changes in cooling rate produced by the different cooling media during quenching, the resultant properties were similar for both the thin and thick cross sections of the ring segments. The above, considering the expected scatter inherent in an industrial process. These similarities can be discussed in terms of the microstructures produced after quenching and tempering. By analysing the microstructures (section 6.2.1.2) developed on the ring segments after industrial quenching, and as well the microstructures obtained on the CCT diagram (section 5.2), it is evident that the similarities observed on the YS and UTS are associated to the formation of different mixtures of tempered martensite and tempered bainite for both, the thin and thick cross sections of the ring segments, with the only exception of 100-W which microstructure consisted of full martensite. The question which arises now, is how similar properties can be obtained with full tempered martensite (100-W) and mixtures of tempered martensite and tempered bainite (100-P, 100-0, 250-W, 250-P and 250-O). This question was addressed by Ohmori et al. [154], they demonstrated that tempered duplex structures (martensite and bainite) are capable to reach strength levels as high as full tempered martensite. The high strength levels reached by the dual microstructure can be explained by the fact that the bainitic laths partition the austenite grain size, therefore producing a refining effect on the overall microstructure. Interestingly, when analysing the YS and UTS values produced on the 100 cross section of the three ring segments as described in section 6.2.2, it can be observed how the YS and UTS properties of 100-W condition were lower than those of 100-P and 100-O conditions. In fact, these two conditions developed the highest YS and UTS values of all the conditions studied.

The superior YS and UTS properties experienced on 100-P and 100-O could be explained by the combined effect of the following aspects: the first aspect is associated with the argument already explained before regarding the refining effect on the PAGBs caused by the presence of bainitic laths. The second aspect, is associated to the resistance to dislocation motion promoted by the fine distribution of small carbide precipitates in tempered martensite as explained by Balart and Knott [155] .

On the other hand, when analysing the YS and UTS properties produced on the 250 mm cross section of the three ring segments, it can be seen that these results are slightly inferior than those corresponding to the 100 cross sections. Additionally, it can also be observed that the YS and UTS decreased in order of water, polymer and vegetable oil. On his work about the cleavage fracture toughness on tempered martensitic Ni–Cr–Mo steels, Kim et al. [128] observed that yield strength is increased as the amount tempered martensite increases in the Ni–Cr–Mo low alloy steel. As explained by the author, the reason for the improvement on yield strength is due to a packet-refining mechanism provided by tempered martensite after tempering treatment. Hence, it could be argued that the decreasing amount of tempered martensite (small carbides) observed on 250-W, 250-P and 250-O respectively, along with the increasing amount of tempered bainite (large carbides) could be the main microstructural aspects responsible for the slightly inferior strength properties observed on the 250 mm cross section of the three ring segments. Nevertheless, it is important to mention that the featureless bainite observed on 250-P condition could have also contributed to the reduced YS and UTS properties displayed on 250-P, which in fact were the lowest strength values among all of the thickness-cooling conditions. The detrimental effect of the featureless bainite could due to the inability of its coarse carbide precipitates to restrict the movement of dislocations, therefore promoting a reduction in strength properties.

It can be concluded that the strength properties industrially produced on the 100 and 250 mm cross sections of the ring segments after quenching (W, P and O) and tempering, are surprisingly very similar and well above the material specification. In general, these similarities could be explained in terms of the microstructures produced after quenching in which, regardless of the cross section (100 or 250 mm) or the quenching media (water, polymer and vegetable oil), similar microstructures (mixtures of tempered martensite and tempered bainite) were formed on the ring segments after heat treatment.

Although, it also true that the small differences observed between each conditions could be related to the different fractions of tempered martensite and tempered bainite which provide fine carbide precipitates and packet refining correspondingly.

Interestingly, the higher tensile and impact properties of all the thickness-cooling conditions evaluated were produced with mixtures of tempered martensite and tempered martensite with proportions of 85% (TM) -15 %( TB). These results are in line with experimental data reported by Tomita and Okabayashi in references [133, 134, 132].In this context, it can be summarized that the main factors controlling the strength properties could be the distribution and size of carbide precipitates in which tempered martensite (mean carbide size: 0.04 μm) unlike tempered bainite (mean carbide size: 0.053 μm) provides slightly higher strength properties. Finally, it should be also noted that, the strength properties can also be affected by the formation of unexpected microstructures such as the featureless bainite observed on 250-P condition, which formation might be attributed to the effects of the chemical segregation as discussed 6.2.1.2.

### 6.3.3 Effect of Tempered Microstructures on Impact Properties

As observed in the strength properties, the impact properties (CVN) for all the cooling conditions are also similar and within material specification. However, a higher scatter is observed on the CVN values compared to the scatter observed on the tensile properties, this scatter could be attributed to a higher sensitivity of this mechanical testing to the specimen geometry associated to the stress distributions during mechanical testing. The blunt notch region of the CVN specimen induces a stress field ahead of the notch of higher magnitude in comparison with the round tensile specimen. Consequently, the higher stresses ahead of the notch are more capable to effectively induce cracking on small carbides precipitates, this, considering the fact that the smallest particles require the largest stresses to promote fracture. On the contrary as explained by Lin and Ritchie [147] the lowest stresses with the large sampling zone in the tensile testing might not be sufficient to sample small carbides and in consequence producing cracking only on the large carbide precipitates which could be more uniformly distributed.

In addition, the difference between the maximum (100-P), minimum (250-P) and average (rest of conditions) CVN values can be explained in terms of different microstructures produced after industrial heat treatment. In line with the tensile properties, 100-P condition also produced the highest impact properties. As mentioned previously, the reason for the superior strength-toughness properties developed on 100-P could be due to the mixtures of tempered martensite and tempered martensite with proportions of 85%(TM) -15%(TB) produced under this conditions which as mentioned could be related to the combined effect of the refining mechanism on the PAGBs and to the fine distribution of small carbide precipitates in tempered martensite. As explained by Hausild et al [141], cleavage fracture on CVN testing is controlled by the presence of second phase particles which can induced "local stress amplifications" so it can be deduced that the fine precipitates observed on 100-P condition could have contributed to reduce the possibility of triggering cleavage fracture, therefore increasing the impact energy. On the other hand, as explained by Chakrabarti and co-workers in reference [156], the grain size is also important since once cleavage crack is nucleated, the grain boundaries are able to control the crack propagation. Regarding the 250-P condition, as with the strength properties, the impact properties were also the lowest of all the thickness-cooling conditions. The explanation for this, is essentially the same as that given for the strength properties, which related to the formation of featureless bainite decorated with randomly distributed coarse carbides.

### 6.3.4 Effect of Tempered Microstructure on CTOD Properties

The first question that naturally arises regarding the CTOD properties is why, despite the variation in yield strength produced by the different thickness-cooling conditions, the resultant CTOD properties were virtually the same as illustrated in *Table 6-2*. Furthermore, considering that at first glance, CTOD and CVN can be regarded as toughness measurements, the CTOD results raises the question of why there is not a correlation between CTOD and CVN properties. As seen below these questions are discussed in terms of the stress gradients ahead of the macroscopic crack for each specimen and the microstructural features eligible for fracture.

As indicated by Shin and co-workers [157], it is well known that from a mechanical perspective, yield strength is proportional to CTOD, this proportionality should be rationalized considering that yield strength, essentially indicates the point in which the material starts to deform plastically. In this sense, it is clear that if the plastic deformation is increased the CTOD parameter increases, since with the application of load the material deforms plastically instead of fracturing. Based on this proportionality, the offshore designers sometimes impose a restriction in the maximum yield strength of subsea forgings for deep-water applications. This could be explained by the fact that a high yield strength can result in a plastic flow that could be higher than the fracture stress therefore leading to brittle fracture or a low CTOD parameter. This is in fact the reason why many offshore designers prefer keeping the yield strength at low values to avoid compromising the CTOD parameter. All these arguments are certainly true, however Qiu et al. [158], demonstrated that although there exists a relationship between yield strength and CTOD, this one is not linear but rather exponential as illustrated in Figure 6-21. As seen in this figure, the red square roughly indicates the region in which the present CTOD values would be hypothetically located on this plot, from this perspective it could be argued that the reason why no relation between YS and CTOD is observed on the studied conditions, is because the variation in the yield strengths properties is not high enough to generate a significant change on the CTOD properties.
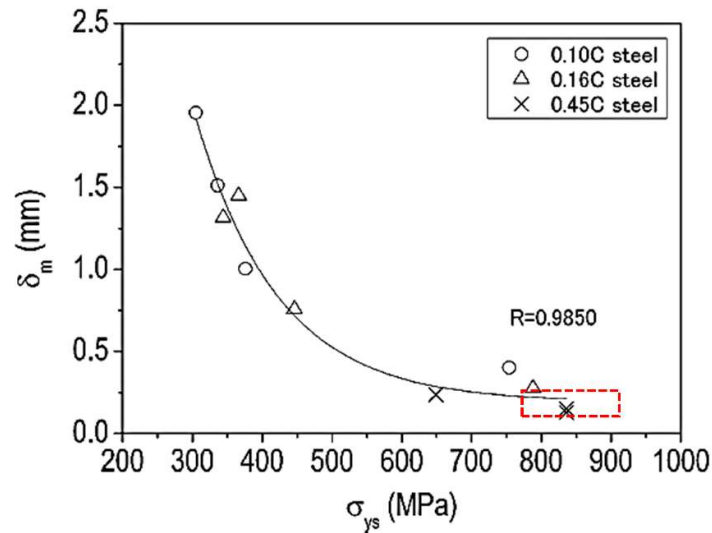
Figure 6-21: Plot of CTOD against yield strength for 0.10% C, 0.16% C, and 0.45% C ferrite-cementite steels heat treated to produce different grain size. R, represents the correlation coefficient and the red square roughly indicates the area corresponding to the CTOD values obtained on the present work. (From, Hai Qiu et al., Influence of Grain Size on the Ductile Fracture Toughness of Ferritic Steel, ISIJ International, Vol. 54 (2014), No. 8, pp. 1958–1964)


Now, it would be prudent to approach the similarity in CTOD results from a mechanical-microstructural perspective. As mentioned previously the stress field produced by either a round tensile specimen or a blunt-notch (CVN) specimen, can in fact activate different microstructural features, i.e., depending on the stress field ahead of the notch, different microstructural features can be eligible to trigger cleavage or ductile fracture. This also applies for the CTOD testing which possesses a sharp crack.

As illustrated in *Figure 6-22*, the fracture stresses can fluctuate considerably in function of the specimen geometry. This in turn has an effect on the sampling volume, for instance, it has been validated that the sampling zone of a CTOD specimen, which contains a sharp crack, is significantly smaller than the sampling zone of a CVN specimen with a blunt notch. In other words, it can be interpreted that the fracture process on a CTOD specimen relies on the small carbide precipitates due to the higher stresses induced on the small sampling zone by the sharp crack, whereas the fracture process on CVN specimens depends on the large carbide precipitates due to the lower stresses induced on the large sampling zone by the sharp crack.

The above considering the basic mechanism in which higher stresses are required to fracture small particles whereas lower stresses are required to fracture large particles. In view of this scenario, it is reasonable to argue that one of the reasons why the CTOD properties were similar, regardless of the different microstructures, is because the group of "small" carbides, either on the tempered martensite, tempered bainite or featureless bainite were within a similar size range, which lead to similar CTOD parameters. In the same fashion, it can be inferred that the CVN properties showed a higher scatter probably due to a higher variation in the group of "large" carbide precipitates in the larger sampling zone.
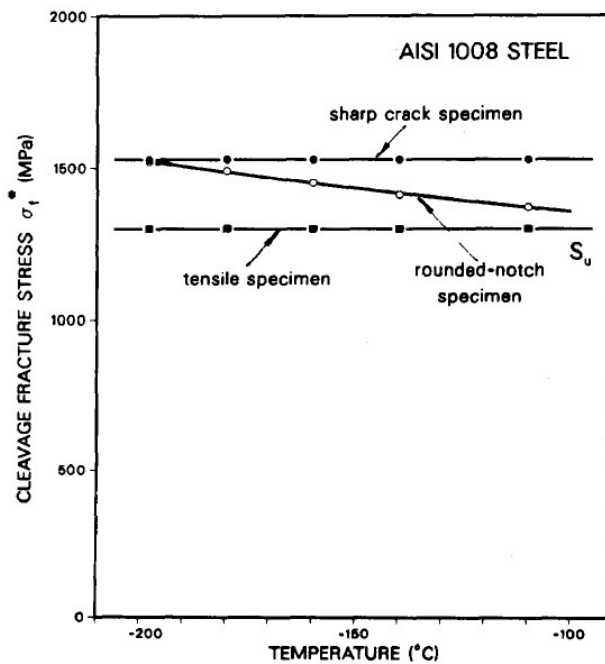


Figure 6-22: Model predictions of the critical microscopic fracture stress, for cleavage fracture in AISI 1008 steel ahead of a sharp-crack (i.e. K,.), rounded-notch (i.e. Charpy) and uniaxial tensile ductility specimens. S, is the lower bound strength (of the largest observable particle) *[147]*.

In spite of the similar CTOD results observed on the three conditions, attention was drawn to 100-P condition which showed a smaller stable crack extension and a lower maximum load compared to those of 100-W, 100-O and 250-P. Clearly, the smaller stable crack extension would mean that cleavage cracks ahead of the ductile zone, presumably nucleated and propagated before than the rest specimens therefore stopping the stable crack extension and maximum load earlier than the rest of the conditions.

Considering this, cross sections corresponding to 100-W and 250-P specimens were metallographically prepared and assessed under the optical microscope. As seen in *Figure 6-23* and *Figure 6-24*, the results indicate that the C (T) specimen related to 100-P conditions presented a higher level of segregation compared to that of 100-W and 250-P conditions. As previously discussed in section 2.8.2, chemical segregation can lead to the formation of enriched zones with alloying elements such as chromium, therefore promoting the formation of hard phases, such as martensite, which in this case would be a sort of low-tempering martensite with characteristics of brittleness, high yield strength and higher internal stresses, and potentially, a preferred site for nucleation of cleavage cracking.

| Transgranular cleavage | Transgranular quasi-cleavage | Transgranular quasi-cleavage |

100-P
δ (CTOD) = 0.242
Δa = 1.48 mm
Max Load: 108.57 kN

250-P
δ (CTOD) = 0.243
Δa = 2.44 mm
Max Load: 111.13 kN

100-W
δ (CTOD) = 0.246
Δa = 2.30 mm
Max Load: 111.45 kN
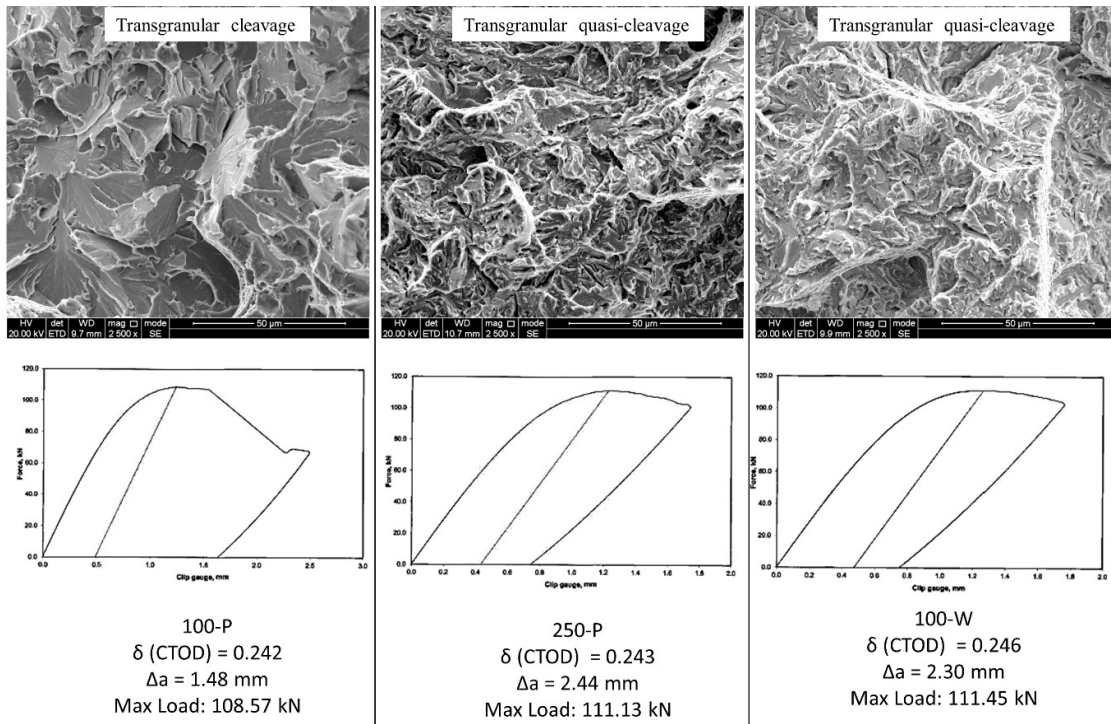
Figure 6-23: Illustration of CTOD fracture surfaces and corresponding Force – Displacements plots for 100-P, 250-P and 100-W conditions.
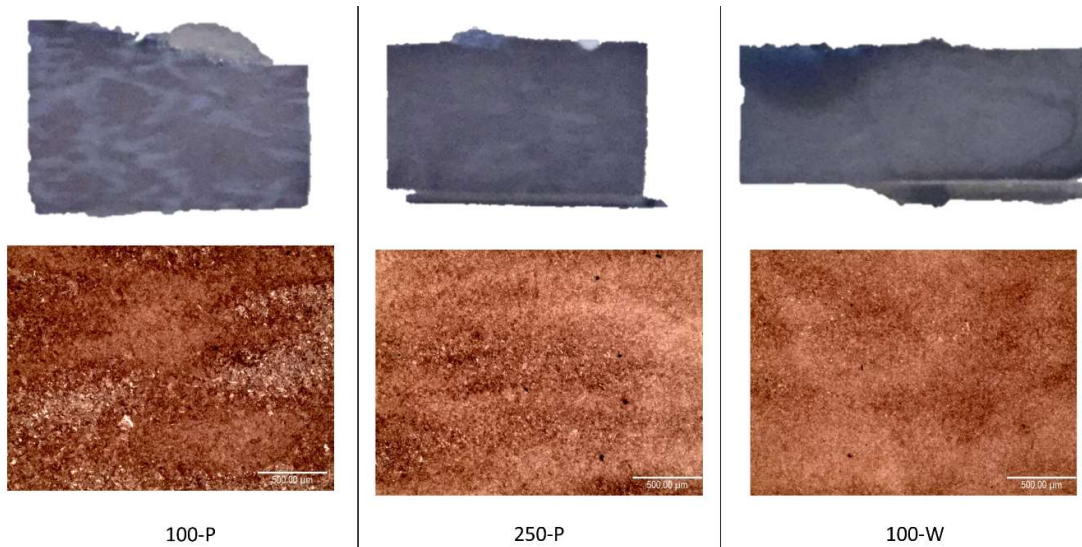


100-P

250-P

100-W

Figure 6-24: Illustration of macrostructure and microstructures observed on a 5 mm section of CTOD specimens corresponding to 100-P, 250-P and 100-W conditions. The three specimens were equally etched with 3% Nital (3 s) and 10% Sodium Metabisulfite solution (20 s).

*6.3.4.1   Implications*

The outcomes of the present research suggest that the fracture mechanism governing the CTOD properties of the three conditions can be regarded as ductile fracture toughness since no evidence of pop-in events (cleavage cracks) were observed on the load-displacement (see Appendix E) plots before reaching maximum load. Presumably, the reason why no pop-in events (cleavage cracks) were observed before reaching maximum load is because the non-metallic inclusions present on the different specimen do not reach the critical size to nucleate a cleavage crack. In this sense, Bowen and co-workers [146], determined a lower critical size of 9µm on low alloy steels to prevent cleavage fracture. In addition, it can be elucidated that the ductile fracture is governed by the critical fracture strain once the plastic strain ahead of the crack tip reached a critical value. The application of monotonic load result in crack opening promoted by the blunting process. Non-metallic inclusions are preferred initiation sites during stable crack extension, and the stable tearing process is related to the decohesion of the non-metallic inclusions from the ferritic matrix. Once decohesion is completed, microvoid coalescence mechanism becomes the main fracture mode. After this process, the transition from ductile tearing to cleavage fracture takes place when the hydrostatic stresses reach a critical value for cleavage crack nucleation. As elucidated by Lin and Ritchie [147], the sharp crack on the C (T) specimen give rise to a complex stress distribution ahead of the macroscopic crack. These high stresses in combination with a relatively small sampling zone implicate that the dominant particle or group of particles are the small carbide precipitates. Presumably, the similar dimensions of the small carbides precipitates during quenching and tempering of the bainitic and martensitic structure resulted on of similar CTOD parameters for the different thickness-cooling conditions studied. Finally, it should be recognised that given the dimension of the experimental forgings and the industrial conditions, it is clear that segregation is determinant for the obtention of uniform mechanical properties along the part, regardless of the quenching media or tempering process.

# 7 Summary and Outlook of the Project

## 7.1 Summary

As mentioned before, the structural integrity of large scale forgings employed in the energy sector is strongly affected by key processing parameters involved in the manufacture of these components. Considering this, the aim of the present research was to study the effects of cooling rate on the microstructure and mechanical properties of an AISI 8630M low alloy steel heat treated under industrial conditions. It is recognized that, at an industrial level, major microstructural changes occur at the centre of the cross section of the forging due to the combined effect of steel-making, forging and heat treatment processes. Therefore, large-scale experimental forgings were industrially heat treated and subsequently evaluated and characterised. The key findings for each chapter were as follows:

### *Chapter 4: Effect of Water, Aqueous Polymer and Vegetable Oil Quenchants on Cooling Characteristics of Ring Segments Industrially Heat-Treated*

1. Cooling curve analysis led to the conclusion that for both the thin and thick cross-sections of the forging, water and vegetable oil produced the fastest, and slowest cooling times, whereas intermediate cooling times between those of water and vegetable oil were achieved by aqueous polymer.

2. The time to cool from 800 to 500˚C the thin cross sections quenched in water, polymer and vegetable oil, was 154, 231 and 253 s, respectively. Further, the time to cool from 800 to 500˚C the thick cross sections quenched in water, polymer and vegetable oil, was 387, 515 and 608 s, respectively.

3. Vapour phase, nucleate boiling and convective heat transfer stages were generally observed on the ring segments quenched in water, polymer and vegetable oil. The maximum cooling rate and phase transformation zone were found to be located within the boiling phase regime. The boiling point of water and aqueous polymer was found to be approximately 100˚C and marked the beginning of the convective heat transfer.

4. The estimated start transformation temperatures on the thin cross-section were between 350 and 410°C, whereas the ones corresponding to the thick cross section were between 460 and 480°C. These temperature ranges were later confirmed to be associated the formation of bainite and martensite during industrial quenching.

5. Cooling conditions are also affected by the thickness of the forging. Longer cooling times were observed on the thin sections compared to thick ones due to a reduced heat flow associated with a larger cross section. A more uniform cooling pattern was also observed on the thick cross sections apparently associated to a higher stability of the vapour film on the thick sections of the ring segments.

### Chapter 5: *Development of a Continuous Cooling Transformation Diagram for and AISI 8630 Modified Low Alloy Steel using Dilatometry*

1. Successful, identification of microstructural constituents was carried out by means of scanning electron microscopy and dilatometry. The microstructures formed in continuously cooled specimen were degenerated pearlite, ferrite, granular bainite, lower bainite and martensite, depending on the applied cooling rate.

2. Mixtures of degenerated pearlite, bainite, and small amounts of ferrite and M/A constituent were observed at cooling rates between 0.01 and 0.03°C/s, whereas, full bainitic microstructure was perceived at cooling rates between 0.05 and 0.2°C/s. In addition, from 0.3 to 1°C/s, a mixture of bainite and martensite was the dominant microstructural constituent. Finally, a full martensitic structure appeared at cooling rates above 2°C/s.

3. Pearlite – Ferrite mixtures were formed at average temperatures between 700 and 600°C. Average bainite start and finish temperatures in the range of full bainitic structure (0.05 and 0.2°C/s) were 490 and 300°C respectively. Whereas, average martensite start and finish temperatures in the range of full martensitic structure (higher than 2°C/s) were 330 and 170°C respectively.

4.  Within the bainite-martensite mixed zone, it was found that the fraction of lower bainite increases along with a decreasing cooling rate with a corresponding decrease in martensite fraction. Also, the bainitic start temperature increases with decreasing cooling rate accompanied by a decrease in the martensite start temperature.

5.  The superimposing of the industrial cooling curves on the CCT diagram revealed that the majority of the thickness-cooling conditions fell within the mixed region of martensite and bainite (0.03 to 1˚C/s), with the only exception of 100-W condition which cooling curve fell between continuous cooling rates of 1 and 2 ˚C/s associated to a full martensite structure.

## *Chapter: 6 Effect of Industrial Cooling rate on Microstructure and Mechanical Properties of Large Forging Segments*

1.  With the exception of condition 100-W, in which the microstructure was predominately tempered martensite, the rest of conditions predominantly exhibited a microstructure consisting of mixtures of tempered martensite and tempered bainite after industrial heat treatment.

2.  As previously observed in the CCT specimens, the industrially heat treated specimens corresponding to the different thickness-cooling conditions also exhibited an increasing bainitic fraction with a decreasing cooling rate accompanied by a corresponding decrease in the martensitic fraction.

3.  The microstructure of tempered martensite consisted of multivariant (crystallographic variant) carbide precipitation within the martensite laths and extensive precipitation on the lath boundaries, whereas the tempered bainitic structure displayed a lower type morphology with carbide precipitates arranged in a single crystallographic variant (Bagaryatski orientation relationship) within the bainitic lath.

4.  In general, it was elucidated that the strength and impact toughness properties industrially produced on the 100 and 250 mm cross sections of the ring segments after quenching (W, P and O) and tempering, were similar and well above the material specification. Although, the  higher strength and impact toughness values were

observed at mixtures of tempered martensite and tempered bainite with proportions of 85%(TM) -15%(TB) in line with the observations of Tomita and Okabayashi [133, 134, 132]. The subtle differences observed between each thickness-cooling conditions could be related to the variation on the distribution and size of carbide precipitates and packet substructure associated the different fractions of tempered martensite and tempered bainite with changes on cooling rate.

5. Small amounts of a featureless microstructure became visible on 250-P condition which consisted of coarse carbides along the prior austenite grain size and a mixture of elongated and blocky carbide precipitates randomly distributed within the bainitic matrix. The formation of this microstructure remained unclear, however it could be associated with the decomposition of granular bainite during tempering promoted by chemical segregation from the ingot solidification process. Furthermore, the lower strength and impact values observed on 250-P conditions were found to be associated to the presence of this so-called featureless microstructure.

6. The CTOD properties for the selected specimens were very similar regardless of the yield strength and microstructure. This would be an indication that the variation in the yield strengths properties and carbide size distribution were not high enough to generate a significant change on the CTOD properties.

7. The fracture mechanisms governing the CTOD properties of the three conditions were found to be associated to ductile fracture since no evidence of pop-in events (cleavage cracks) were observed on the load-displacement plots before reaching maximum load.

8. Finally, it is noteworthy to mention that in spite of the fact that vegetable oil provided the slow quench rates if compared with those water or aqueous polymer quenchants, the mechanical properties produced by this quenchant were similar to those produced by water and polymer quenching. As such, this finding indicates the possibility of using vegetable oil as potential replacement for water or aqueous polymer within the studied conditions

## 7.2   Economic Impact of the Research

In view of the results obtained with vegetable oil, where it was demonstrated that in spite of it's slow heat extraction rates characteristics, the aforementioned bio-quenchant is in fact capable to develop similar properties in large scale forgings, compared with those produced with commercial quenchants such as water a aqueous polymer solutions; it is therefore necessary to elucidate the potential savings in using vegetable oil as an alternative cooling media for material grades with similar composition as the AISI 8630M low alloy steel.

1. Cost of quench tank body with complete engineering and agitation system:

- Vegetable Oil (bio-temproil® ) : 501,000 €
- Aqueous solution with  23% concentration of polymer: 805,000 €

It can be clearly seen that the cost of a quenching tank system for vegetable oil media is cost-effective in monetary terms (37% less expensive than polymer) when compared with a quenching tank for polymer solution purposes. The reason behind this is due to the fact that, a larger quenching tank and a more complex agitation system is mandatory when polymer solutions is the desired option.

2. Cost of quenchants for the first filling:

- Vegetable Oil (bio-temproil® ) : 826,500 €
- Aqueous solution with  23% concentration of polymer: 276, 000 €

Although the initial investment for the first filling using vegetable oil is more expensive than polymer solution it is also true that the ROI (Return on investment) after the third year would be around 60,000 € (3% difference between vegetable oil and polymer solutions) , with an annual average return of 3-5% over the subsequent years.

3. In addition, there are other factors that might represent potential savings if vegetable oil is used as alternative quenching media in the forging industry:

a) Cost per Year on 30,000 Tons Basis (after first filling):

- Vegetable Oil (bio-temproil®): 174,000 €.
- Aqueous solution with 23% concentration of polymer: 270, 000 €.

b) Minimum distortion and cracking issues. (No re-works needed such as straightening operations).

c) Homogeneous hardness distribution.

d) Cost of waste product for disposal:

- Vegetable Oil (bio-temproil®): 85,500 €.
- Aqueous solution with 23% concentration of polymer: 480, 000 €.

e) Reduced $CO_2$ emissions (eco-conception): Fixed price 2017 of $CO_2$ equivalent = 6 €/ Ton.

## 7.3   Suggestions for Future Work

•       Quantitative and qualitative measurements of carbide precipitates were not carried out due to time limitations, however, considering the relevance of carbide thickness as preferred sites for the nucleation and propagation of cleavage cracks, and in-depth analysis of this metallurgical aspect would further expand the understanding of the effects of carbide precipitation on the mechanical properties of industrially heat treated large forgings. A combination of transmission electron microscopy (TEM), energy dispersive spectroscopy (EDS) and X-ray diffraction can be used to determine the morphology, spatial distribution, and elemental composition of carbide precipitates.

•       As discussed in Chapter 6, the detrimental effect of segregation was evidenced by the low strength and impact toughness properties found on the thick section of the ring segment quenched in aqueous polymer (250-P). Considering this, it's clear that more research is required in order to determine the influence of segregated elements on the formation of unexpected microstructures after quenching and tempering under industrial conditions. As reported in reference [90] electron probe microanalysis (EPMA) represent a potential technique to perform chemical analysis either on segregated and non-segregated areas.

•       Considering the expected scatter in fracture toughness, a larger number of CTOD tests on the different locations of the forging would be desirable aiming to increase the representativeness of the CTOD results associated to the different thickness-cooling conditions evaluated. It would also be desirable to explore the possibility of developing an alternative fracture toughness testing, which allows to reduce costs associated to the CTOD testing. As elucidated in Appendix F, an initial attempt was made to develop a low-cost CTOD procedure by exploring the validity of Crack Tip Opening Angle (CTOA) as a geometry independent fracture parameter using digital image correlation (DIC) technique on a series of sub-size specimens. Continuing research on this line of thought would potentially facilitate the evaluation of the structural integrity of large scale forgings by means of fracture toughness testing.

# 8 Appendix A: Chemical Composition Certified Test Report

**ELLWOOD QUALITY STEELS COMPANY**

A PENNSYLVANIA BUSINESS TRUST
700 MORAVIA STREET, NEW CASTLE, PA 16101

Page 1

EQS

(724) 658-6788
Teletax (724) 658-6802

## CERTIFIED TEST REPORT

Date: 2/17/14

Report of Tests of: (2), 48" X 148" - Grade 8630M Ingot(s)

For Company: Frisa Forjados S.A. DE C.

Valentin G. Rivero #127

MEXICO 66350

Customer's Order: FF-12471

Date of Order: 1/3/14

Our Shop Order: 105120

Specification:

## CHEMICAL ANALYSIS

| Heat # | C | Mn | P | S | Si | Ni | Cr | Mo | V | Cu | Al | Hppm | Ti | As |
|--------|------|------|------|-------|-------|------|------|-------|------|-------|------|------|------|------|
| AM781 | .33 | .95 | .007 | .001 | .30 | .84 | .99 | .40 | .005 | .14 | .026 | 1.0 | .003 | .004 |
| | Sn | Co | W | Pb | B | Sb | Nb | Ca | Zr | N | | | | |
| | .009 | .013 | .009 | .0001 | .0001 | .001 | .002 | .0010 | .002 | .0091 | | | | |

The material was melted using the electric furnace-ladle refined-vacuum degassed process and was subsequently bottom poured.

The material has been melted using a fine grain melt practice capable of meeting ASTM 7 or finer.

The material was calcium treated for inclusion shape control.

CE(Nb) = .83

V+Nb+Ti = .010

DI = 8.5" per ASTM A255 for grain size 7.

Ingot Hardness: 206 BHN

Capable of 25ppm max. Oxygen.

The material was produced in accordance with the EQS Quality Manual dtd. 1/1/14, Rev. 2 which meets the intent of the latest revisions to ISO 9001:2008, ISO 10012-1, MIL-I-45208, NCA-3800, and 10-CFR-50 App. B for quality assurance, inspection and calibration systems.

The material is capable of meeting the JK microcleanliness requirements given below when tested in accordance to ASTM E45.

| | A | B | C | D |
|-------|-----|-----|-----|-----|
| Thin | 2.0 | 1.5 | 2.0 | 1.5 |
| Heavy | 1.5 | 1.0 | 1.0 | 1.5 |

I certify that the reported results and statements of this certificate represent the actual attributes of the material furnished and are in full compliance with all purchase order specification requirements. The recording of false, fictitious or fraudulent statements or entries on this document may be punishable as a felony under Federal Statutes. During the manufacturing process, tests, and inspections, the material did not come in direct contact with mercury or any of its compounds nor with any mercury containing devices employing a single boundary of containment. No welding or weld repair was performed on this material. The material was produced free of radioactive elements.

Gregory J. Morgan
Quality Engineer

167

# 9 Appendix B: Quenching Simulations

Model Properties:
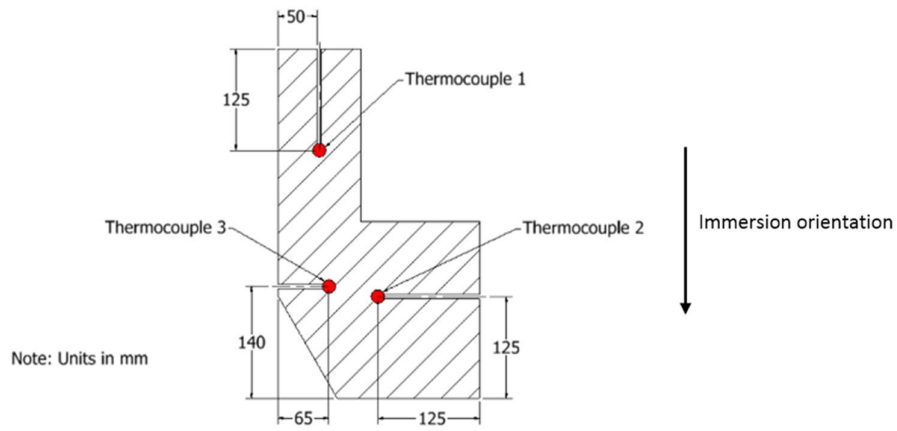


Mesh arrangement and selected zones for simulation:
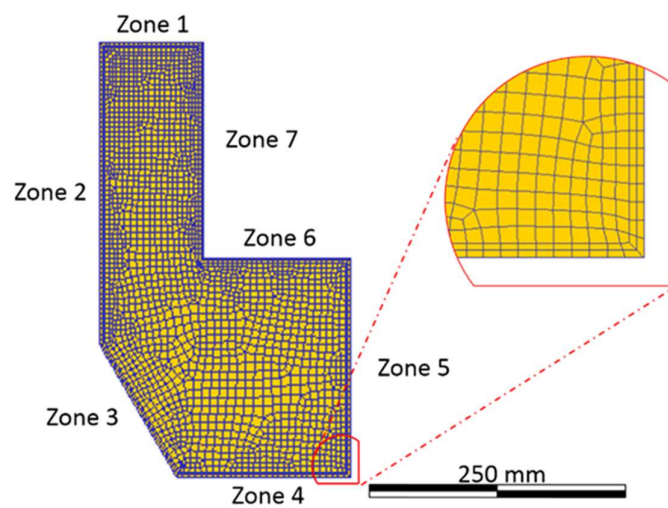
Flow chart for the determination of HTC using DEFORM:
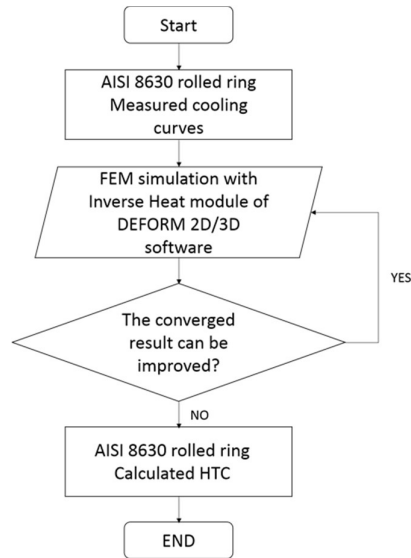


Calculated HTC (Heat Transfer Coefficient) for the different zones, divided by: a) vertical; b) horizontal; c) external; d) internal,
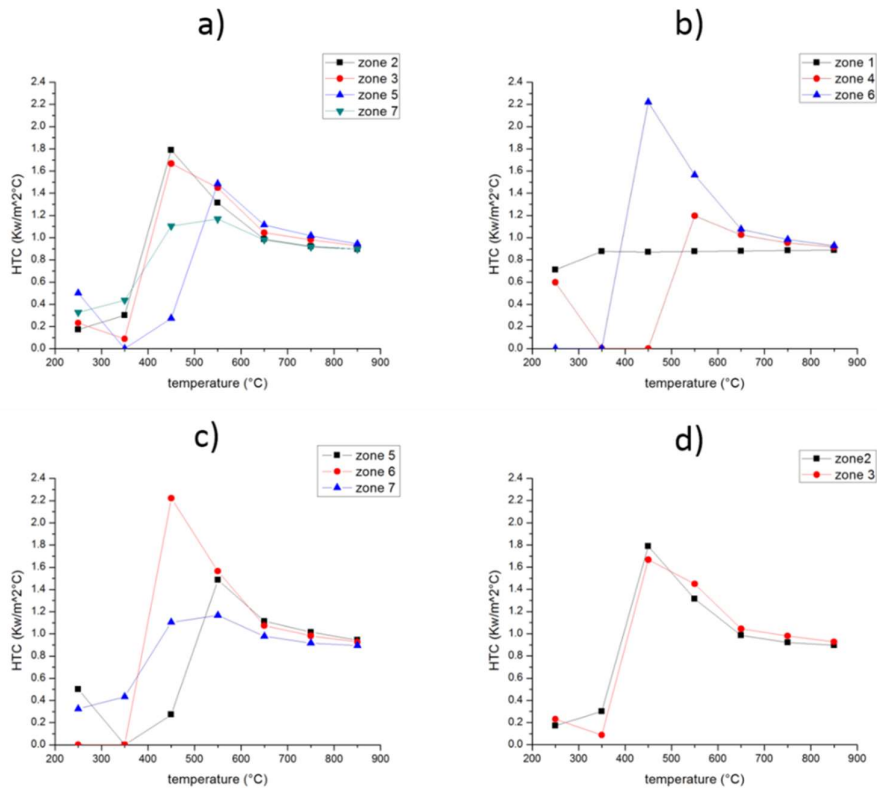
Cooling Rate Simulation (Full Scale Ring):
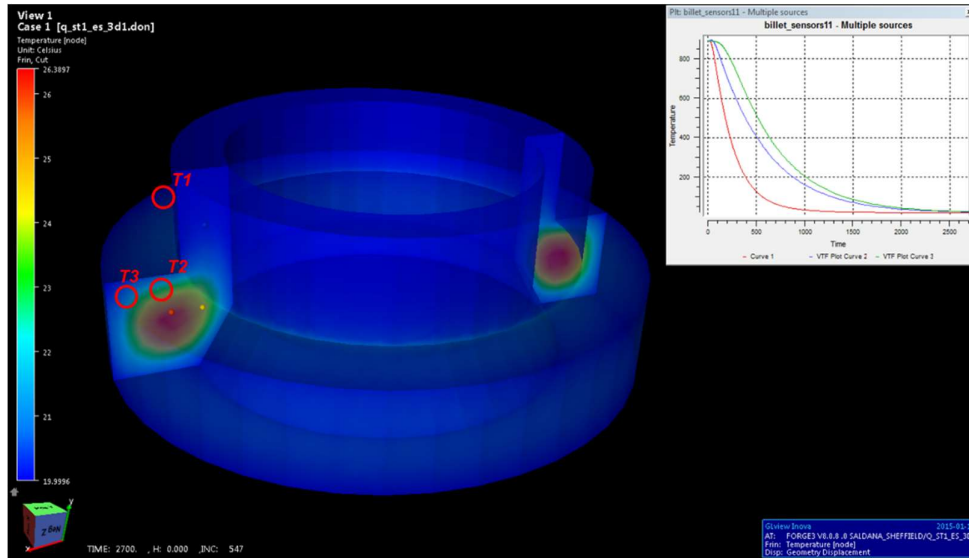


Cooling Rate Simulation (Segment Ring):
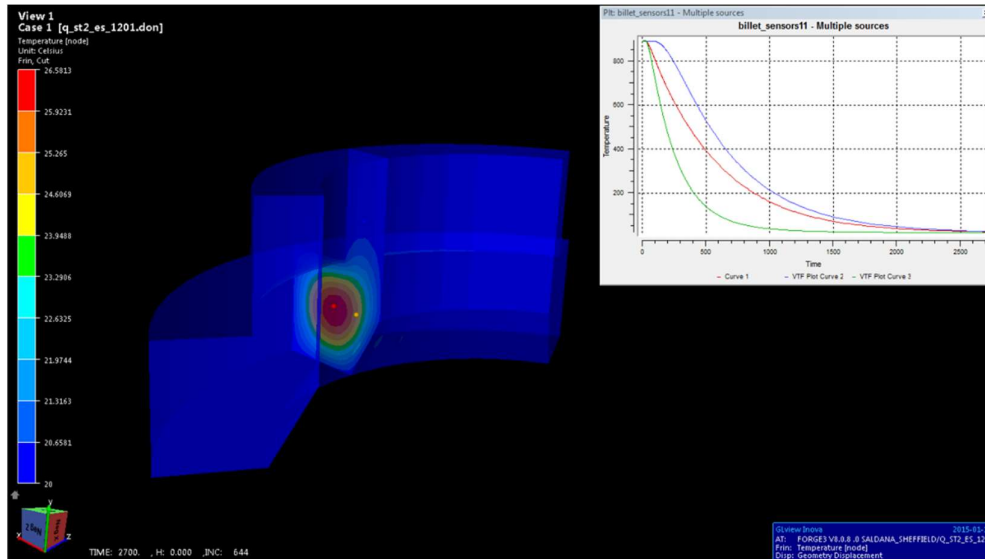
# 10 Appendix C:   Smart-Quench System
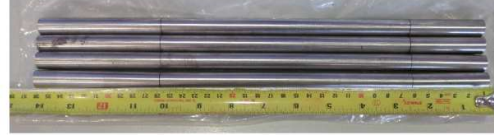


2.- Steel probes before quenching.



3.- Steel probes after quenching.



4.- Different Cooling Media.

1.- Smart Quench Testing Equipment.

# 11 Appendix D: C(T) Specimen Drawing

# 12 Appendix E: CTOD Test Results

100-P Condition:

## TWI

## CT FRACTURE TEST 30054 M01-01

| Test date | 23/06/2015 | | Client | FRISA |
|---|---|---|---|---|
| Technician | Jerry Godden | | Project leader | Fabio Pulvirenti |
| Test machine | INSTRON 8500 B107 | | Investigator's signature | |
| Control mode | Displacement | | Compiled by | Phillip Cossey |

### SPECIMEN DETAILS

| | | |
|---|---|---|
| Force, F | 108.57 | kN |
| Width, W | 50.010 | mm |
| Thickness, B | 24.960 | mm |
| Crack length, $a_0$ | 25.252 | mm |
| Yield strength | 956 | MPa |
| Young's modulus | 190 | GPa |
| Poisson's ratio | 0.300 | |
| Test temperature | 0.0 | °C |

### RESULTS

| | | |
|---|---|---|
| $\delta$ | 0.242 | mm |
| K @ calculation point | 190.8 | MPa.m$^{1/2}$ |
| $F_{max}/F_Q$ | 1.84 | |
| $K_Q$ | 103.63 | MPa.m$^{1/2}$ |
| Total area under Force v Clip | 88.27 | kNmm |
| J0 from SINGLE CLIP | 347.59 | kJ/m² (N/mm) |
| Plastic area Force v CMOD | 47.41 | kNmm |
| Type of result | $\delta/J_u$ | |
| | | |
| Test standard | BS 7448: Part 1: 1991 | |
| Result qualified to standard(s) | NO | |

### LOWER CLIP GAUGE VALUES

| | | |
|---|---|---|
| Knife edge height | 0.00 | mm |
| Vg | 1.239 | mm |
| Vp | 0.486 | mm |

### UPPER CLIP GAUGE VALUES

| | | |
|---|---|---|
| Knife edge height | NA | mm |
| Vg | NA | mm |
| Vp | NA | mm |

100-P Condition:

## CT FRACTURE  TEST 30054 M01-01

Diagram of
fracture face



| Specimen width, W | 50.010 | mm |
| Specimen thickness, B | 24.960 | mm |
| Machined notch depth, M | 20.530 | mm |
| Surface crack length, $a_{S1}$ | 24.520 | mm |
| Surface crack length, $a_{S2}$ | 24.760 | mm |
| $a_{max}$ | 25.520 | mm |
| $a_{min}$ | 24.480 | mm |

Comments

W

B

| Measurement Line | Fatigue crack length $a_f$, mm | Slow stable crack extension + fatigue crack $a_p$, mm | Slow stable crack extension including stretch zone, $\Delta_a$, mm |
|---|---|---|---|
| 1 | 24.480 | 24.480 | 0.000 |
| 2 | 24.870 | 25.670 | 0.800 |
| 3 | 25.240 | 27.150 | 1.910 |
| 4 | 25.400 | 27.540 | 2.140 |
| 5 | 25.500 | 27.770 | 2.270 |
| 6 | 25.520 | 27.410 | 1.890 |
| 7 | 25.470 | 27.090 | 1.620 |
| 8 | 25.300 | 26.540 | 1.240 |
| 9 | 24.950 | 24.950 | 0.000 |
| Weighted Average | 25.252 | 26.736 | 1.484 |

Measured by:   Phillip Cossey

Signed:

250-P Condition:

**TWI**

## CT FRACTURE  TEST 30054 M01-02

| | | | |
|---|---|---|---|
| Test date | 23/06/2015 | Client | FRISA |
| Technician | Jerry Godden | Project leader | Fabio Pulvirenti |
| Test machine | INSTRON 8600 8107 | Investigator's signature | |
| Control mode | Displacement | Compiled by | Phillip Cossey |

### SPECIMEN DETAILS

| | | |
|---|---|---|
| Force, F | 111.13 | kN |
| Width, W | 49.910 | mm |
| Thickness, B | 24.960 | mm |
| Crack length, $a_0$ | 25.473 | mm |
| Yield strength | 854 | MPa |
| Young's modulus | 190 | GPa |
| Poisson's ratio | 0.300 | |
| Test temperature | 0.0 | °C |

### RESULTS

| | | |
|---|---|---|
| $\delta$ | 0.243 | mm |
| K @ calculation point | 198.8 | MPa.m$^{1/2}$ |
| $F_{max}/F_Q$ | 1.70 | |
| $K_Q$ | 117.06 | MPa.m$^{1/2}$ |
| Total area under Force v Clip | 87.24 | kN.mm |
| J0 from SINGLE CLIP | 348.96 | kJ/m² (N/mm) |
| Plastic area Force v CMOD | 43.17 | kN.mm |
| Type of result | $\delta J_m$ | |
| Test standard | BS 7448: Part 1: 1991 | |
| Result qualified to standard(s) | NO | |

### LOWER CLIP GAUGE VALUES

| | | |
|---|---|---|
| Knife edge height | 0.00 | mm |
| Vg | 1.226 | mm |
| Vp | 0.433 | mm |

### UPPER CLIP GAUGE VALUES

| | | |
|---|---|---|
| Knife edge height | NA | mm |
| Vg | NA | mm |
| Vp | NA | mm |



LVGENPLOT V 1.29 02-Apr-2015        Page 4 of 5        SI/FRA/F/1 Rev0.0 June 2002

TWI Ltd, Granta Park, Great Abington, Cambridge, CB21 6AL, Cambridgeshire, UK, Tel 01223 899000
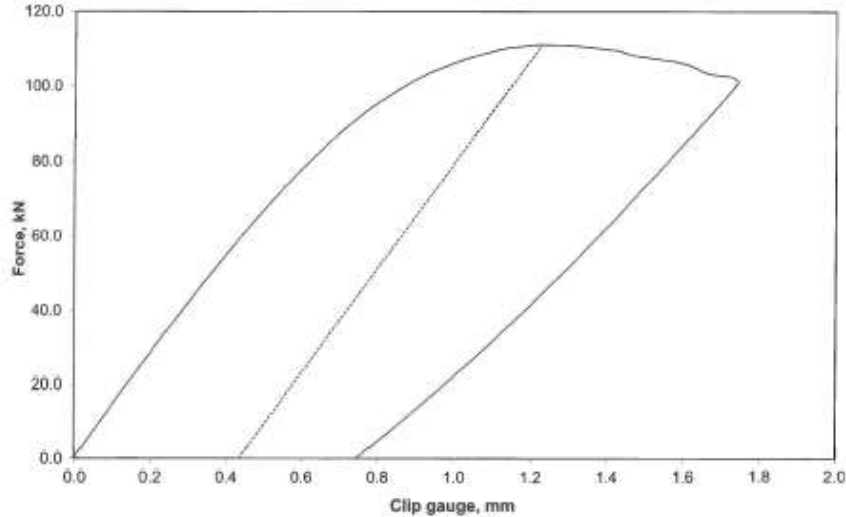
250-P Condition:

30054 M01 02 BS 7448 PART 1 TEST RESULTS  18/01/2016  08:47

## CT FRACTURE  TEST 30054 M01-02

Diagram of
fracture face

1  2  3  4  5  6  7  8  9

| | |
|---|---|
| Specimen width, W | 49.910  mm |
| Specimen thickness, B | 24.960  mm |
| Machined notch depth, M | 20.520  mm |
| Surface crack length, $a_{s1}$ | 24.660  mm |
| Surface crack length, $a_{s2}$ | 24.830  mm |
| $a_{max}$ | 25.760  mm |
| $a_{min}$ | 24.800  mm |

W

Comments

B

| Measurement Line | Fatigue crack length $a_0$, mm | Slow stable crack extension + fatigue crack $a_p$, mm | Slow stable crack extension including stretch zone, $\Delta_a$, mm |
|---|---|---|---|
| 1 | 24.800 | 24.800 | 0.000 |
| 2 | 25.270 | 26.650 | 1.380 |
| 3 | 25.530 | 28.120 | 2.580 |
| 4 | 25.680 | 29.040 | 3.360 |
| 5 | 25.760 | 29.400 | 3.640 |
| 6 | 25.710 | 29.450 | 3.740 |
| 7 | 25.580 | 29.010 | 3.430 |
| 8 | 25.370 | 26.720 | 1.350 |
| 9 | 24.970 | 24.970 | 0.000 |
| Weighted Average | 25.473 | 27.909 | 2.436 |

Measured by:   Phillip Cossey                Signed: _____

LVGENPLOT V 1.29 02-Apr-2015            Page 5 of 5            SI/FRA/F/1 Rev0.0 June 2002

100-W Condition:

TWI

## CT FRACTURE  TEST 30054 M01-03

| Test date | 23/06/2015 |
|---|---|
| Technician | Jerry Godden |
| Test machine | INSTRON 8500 B107 |
| Control mode | Displacement |

| Client | FRISA |
|---|---|
| Project leader | Fabio Pulvirenti |
| Investigator's signature | pp. M. Hadeth |
| Compiled by | Phillip Cossey |

### SPECIMEN DETAILS

| Force, F | 111.45 | kN |
|---|---|---|
| Width, W | 49.920 | mm |
| Thickness, B | 24.980 | mm |
| Crack length, $a_0$ | 25.431 | mm |
| Yield strength | 940 | MPa |
| Young's modulus | 190 | GPa |
| Poisson's ratio | 0.300 | |
| Test temperature | 0.0 | °C |

### RESULTS

| $\delta$ | 0.246 | mm |
|---|---|---|
| K @ calculation point | 198.8 | MPa.m$^{1/2}$ |
| $F_{max}/F_Q$ | 1.68 | |
| $K_Q$ | 118.37 | MPa.m$^{1/2}$ |
| Total area under Force v Clip | 91.63 | kNmm |
| J0 from SINGLE CLIP | 365.18 | kJ/m$^2$ (N/mm) |
| Plastic area Force v CMOD | 47.67 | kNmm |
| Type of result | $\delta U_m$ | |

| Test standard | BS 7448: Part 1: 1991 |
|---|---|
| Result qualified to standard(s) | NO |

### LOWER CLIP GAUGE VALUES

| Knife edge height | 0.00 | mm |
|---|---|---|
| Vg | 1.281 | mm |
| Vp | 0.472 | mm |

### UPPER CLIP GAUGE VALUES

| Knife edge height | NA | mm |
|---|---|---|
| Vg | NA | mm |
| Vp | NA | mm |

100-W Condition:

## CT FRACTURE  TEST 30054 M01-03

Diagram of
fracture face

| Specimen width, W | 49.920 mm |
| Specimen thickness, B | 24.960 mm |
| Machined notch depth, M | 20.420 mm |
| Surface crack length, $a_{S1}$ | 24.320 mm |
| Surface crack length, $a_{S2}$ | 24.720 mm |
| $a_{max}$ | 25.760 mm |
| $a_{min}$ | 24.540 mm |

Comments

W

B

| Measurement Line | Fatigue crack length $a_{0}$, mm | Slow stable crack extension + fatigue crack $a_{p}$, mm | Slow stable crack extension including stretch zone, $\Delta_{a}$, mm |
|---|---|---|---|
| 1 | 24.540 | 24.540 | 0.000 |
| 2 | 25.010 | 26.290 | 1.280 |
| 3 | 25.360 | 28.150 | 2.790 |
| 4 | 25.600 | 29.340 | 3.740 |
| 5 | 25.720 | 29.350 | 3.630 |
| 6 | 25.760 | 29.120 | 3.360 |
| 7 | 25.760 | 28.230 | 2.470 |
| 8 | 25.520 | 26.640 | 1.120 |
| 9 | 24.890 | 24.890 | 0.000 |
| Weighted Average | 25.431 | 27.729 | 2.299 |

Measured by:    Phillip Cossey

Signed: _____

100-O Condition:

TWI

## CT FRACTURE TEST 30054 M01-04

| Test date | 12/01/2016 |
|---|---|
| Technician | Jerry Godden |
| Test machine | INSTRON 8500 B107 |
| Control mode | Displacement |

| Client | FRISA |
|---|---|
| Project leader | Matthew Haslett |
| Investigator's signature | M Haslett |
| Compiled by | J Godden |

### SPECIMEN DETAILS

| Force, F | 116.57 | kN |
|---|---|---|
| Width, W | 50.040 | mm |
| Thickness, B | 25.010 | mm |
| Crack length, $a_0$ | 24.986 | mm |
| Yield strength | 994 | MPa |
| Young's modulus | 190 | GPa |
| Poisson's ratio | 0.300 | |
| Test temperature | 0.0 | °C |

### RESULTS

| $\delta$ | 0.249 | mm |
|---|---|---|
| K @ calculation point | 200.8 | MPa.m$^{1/2}$ |
| $F_{max}/F_Q$ | 1.67 | |
| $K_Q$ | 120.41 | MPa.m$^{1/2}$ |
| Total area under Force v Clip | 96.87 | kNmm |
| J0 from SINGLE CLIP | 376.55 | kJ/m² (N/mm) |
| Plastic area Force v CMOD | 50.81 | kNmm |
| Type of result | $\delta/J_n$ | |
| Test standard | BS 7448: Part 1: 1991 | |
| Result qualified to standard(s) | NO | |

### LOWER CLIP GAUGE VALUES

| Knife edge height | 0.00 | mm |
|---|---|---|
| Vg | 1.271 | mm |
| Vp | 0.481 | mm |

### UPPER CLIP GAUGE VALUES

| Knife edge height | NA | mm |
|---|---|---|
| Vg | NA | mm |
| Vp | NA | mm |

TWI Ltd, Granta Park, Great Abington, Cambridge, CB21 6AL, Cambridgeshire, UK, Tel 01223 899000

100-O Condition:

## CT FRACTURE  TEST 30054 M01-04

Diagram of
fracture face

1 2 3 4 5 6 7 8 9

| | |
|---|---|
| Specimen width, W | 50.040  mm |
| Specimen thickness, B | 25.010  mm |
| Machined notch depth, M | 20.440  mm |
| Surface crack length, $a_{s1}$ | 24.340  mm |
| Surface crack length, $a_{s2}$ | 24.400  mm |
| $a_{max}$ | 25.240  mm |
| $a_{min}$ | 24.280  mm |

W

Comments

B

| Measurement Line | Fatigue crack length $a_q$, mm | Slow stable crack extension + fatigue crack $a_p$, mm | Slow stable crack extension including stretch zone, $\Delta_a$, mm |
|---|---|---|---|
| 1 | 24.280 | 24.710 | 0.430 |
| 2 | 24.820 | 25.770 | 0.950 |
| 3 | 25.100 | 27.760 | 2.660 |
| 4 | 25.240 | 28.770 | 3.530 |
| 5 | 25.220 | 29.100 | 3.880 |
| 6 | 25.220 | 28.870 | 3.650 |
| 7 | 25.060 | 28.000 | 2.940 |
| 8 | 24.880 | 25.840 | 0.960 |
| 9 | 24.410 | 24.450 | 0.040 |
| Weighted Average | 24.986 | 27.336 | 2.351 |

Measured by:   Jerry Godden            Signed: _____

# 13 Appendix F: Digital Image Correlation (DIC) Analysis

Methodology for computing stress intensity factor $K_Q$ and $K_{IC}$ according to ASTM E399-12

- The load-displacement record during the experiment is obtained.
- A line with slope equal to 0.95 of the slope of the initial linear portion of the load-displacement (P-V) record is drawn.
- The line drawn intersects the P-V curve at point $P_Q$.
- If $P_{max}/P_Q \leq 1.10$ then $K_Q$ is estimated by the following equation:

$$K_Q = \frac{P_Q}{\sqrt{BB_N}\sqrt{W}} f\left(\frac{\alpha}{W}\right) \qquad \text{where:}$$

- $B_N$, B are the thicknesses of the specimen in the grooved and non-grooved area, respectively
- $\alpha$, W are the crack size and specimen width as defined in the standard
- f is a function of the ratio $\alpha/W$ (further information available in the standard):

- $K_Q$ equals to $K_{IC}$ if $\qquad 2.5\left(K_Q/\sigma_Y\right)^2 < W - \alpha$

where $\sigma_Y$ is the yield strength of the material

**Methodology for computing critical Crack Tip Opening Angle (CTOA) with DIC according to ASTM E2472-12**

- A particular crack tip location and deformed image, DI, for analysis is selected.
- A reference deformed image RI is chosen.
- In the region of 0.5 to 1.5 mm behind the crack tip in image DI, pairs of subsets* above and below the crack line are selected which are a distance $r_i$ behind the crack tip. Subsets must be close to the crack line.
- The crack opening displacement vector ($u_i$ for upper and $l_i$ for the lower subset) for each small subset is computed using DIC.
- A CTOA value is calculated for each pair of subsets at a distance of $r_i=1$mm behind the crack tip using the equation below:

$$\text{CTOA} = \psi_i = 2\tan^{-1}\frac{u_i - l_i}{2r_i}$$

- The average CTOA value in the steady-state region of the $\psi$~crack length plot is the critical CTOA $\psi_{crit.}$
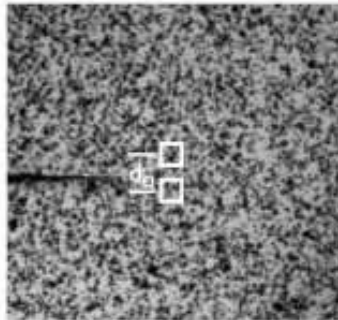


(a) Image of current crack tip region          (b) Image after crack extension
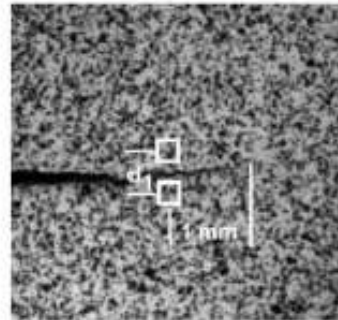
20 mm Sub-Size C(T) Specimen:

15 mm Sub-size C(T) Specimen  - DIC Analysis
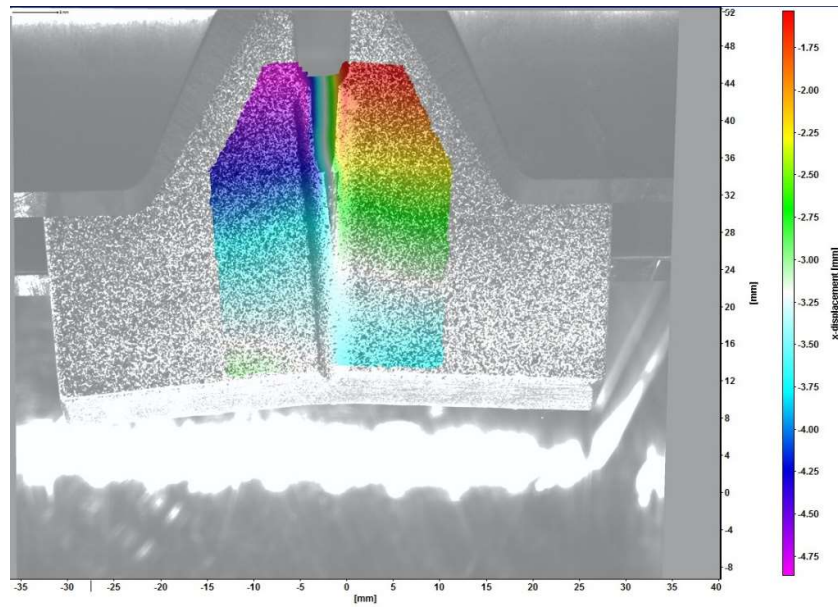
X-Displacement:



20 mm Sub-Size C(T) Specimen - DIC Analysis
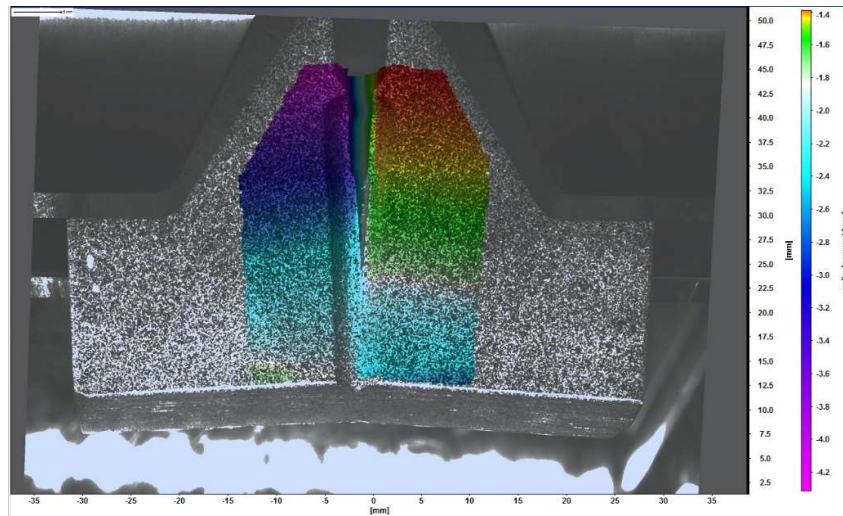
X-Displacement:

25 mm Sub-Size C(T) Specimen - DIC Analysis
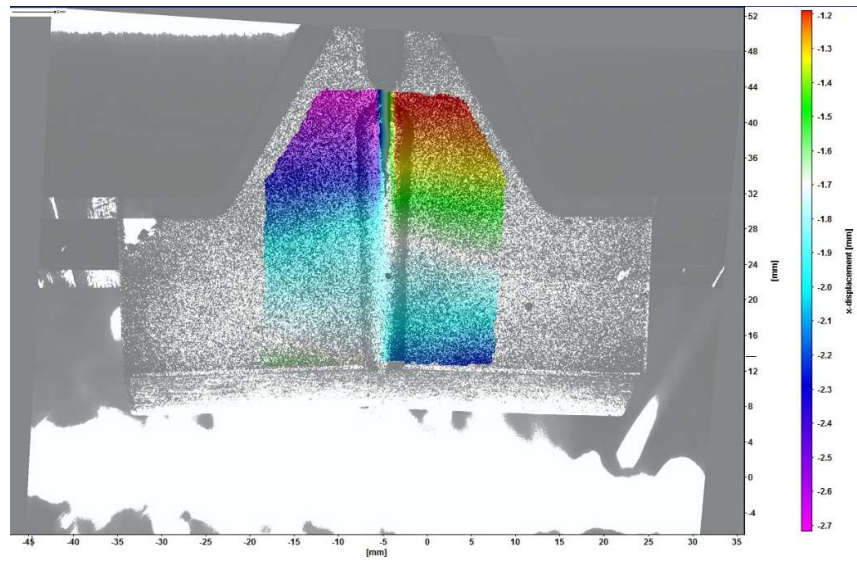
X-Displacement:



15 mm Sub-Size C(T) Specimen - DIC Analysis
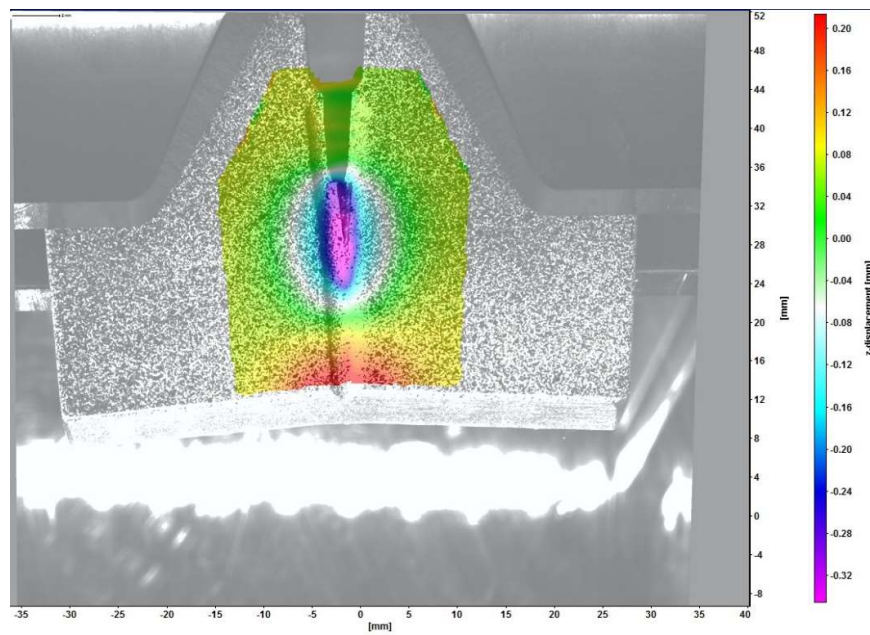
Z-Displacement:

20 mm Sub-Size C(T) Specimen - DIC Analysis
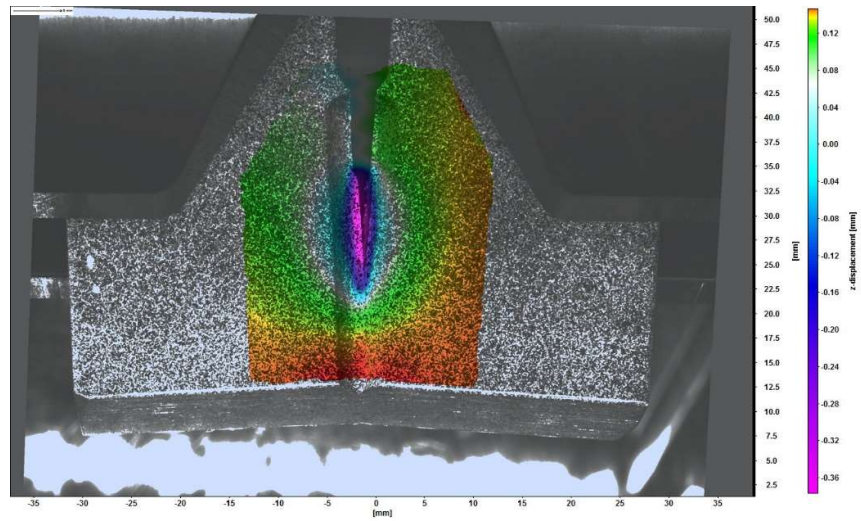
Z-Displacement:



25 mm Sub-Size C(T) Specimen - DIC Analysis

Z-Displacement:
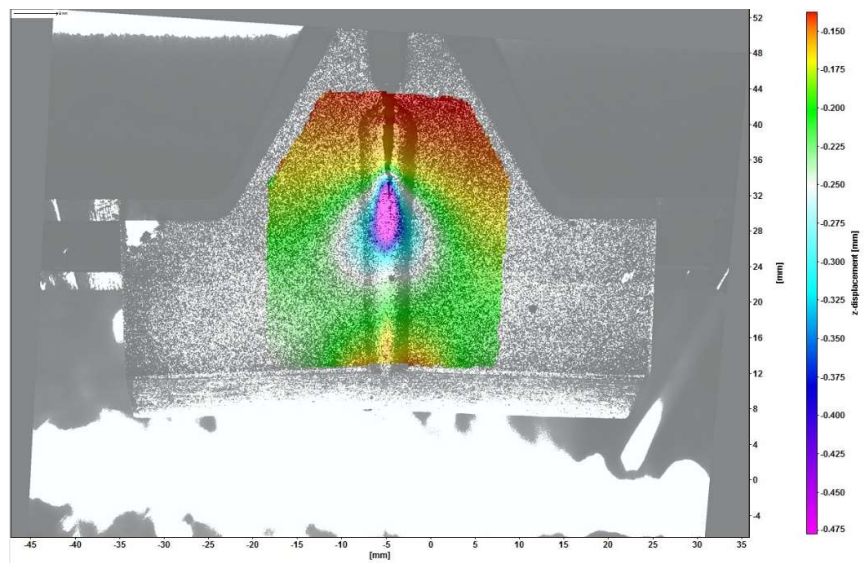
# 14 References

[1]     K. Chung-Gil and L. Sang-Seop, "Heat treatment conditions of low carbon steel part used in the deep sea," in *Proceedings of the ASME 2010 29th International Conference on Ocean, Offshore and Arctic Engineering OMAE2010*, June 6-11, 2010, Shanghai, China, 2010.

[2]     "Trendsetterengineering.com," 2016. [Online]. Available: http://www.trendsetterengineering.com/connection-systems/. [Accessed 27 August 2016].

[3]     P. Layus, P. Kah, J. Martikainen, M. Pirinen, E. Khlushova and A. Ilyin, "European and Russian Metals for Arctic Offshore Structures," in *Proceedings of the Twenty-third (2013) International Offshore and Polar Engineering*, Anchorage, Alaska, USA, June 30–July 5, 2013, 2013.

[4]     J. D. Burk and C. L. Ribardo, "Thunder Horse - Materials, Weldings and Corrosion Challenges and Solutions," in *2010 Offshore Technology Conference*, Houston,Texas, USA, 3-6 May 2010, 2010.

[5]     J. Knott, "Brittle fracture in structural steels: perspectives at different size-scales," *Phil. Trans. R. Soc. A,* 2015.

[6]     L. Muehlenbachs, M. A. Cohen and T. Gerarden, "The impact of water depth on safety and environmental performance in offshore oil and gas production," *Energy Policy,* vol. 55, pp. 699-705, 2013.

[7]     "Subsea Systems," FMC Technologies, [Online]. Available: http://www.fmctechnologies.com/en/SubseaSystems/Technologies/SubseaProduct ionSystems/TieInAndFlowlines/VerticalAndHorizontalTieInSystems/HorizontalTi eIn.aspx. [Accessed 10 10 2016].

[8]     A. Bahrami, N. Zettlemoyer and W. Vangeertruyden, "Rationalization of Toughness Requirements for Subsea Forgings," in *Proceedings of the ASME 2015 34th International Conference on Ocean, Offshore and Arctic Engineering*, May 31-June 5, 2015, St. John's, Newfoundland, Canada, 2015.

[9]     G. E. Totten, C. E. Bates and N. A. Clinton, Handbook of quenchants and quenching technology, Materials Park, OH: ASM International, 1993.

[10]     T. P. Kumar, "Influence of Steel Grade on Surface Cooling Rates and Heat Flux during Quenching," *Journal of Materials Engineering and Performance,* vol. 22 (7), 2013.

[11]     B. Lišcic, H. M. Tensi, L. C. F. Canale and G. E. Totten, Quenching theory and technology. Second Edition, Taylor and Francis Group, LLC, 2010.

[12]     H. Pous-Romero, J. Talamantes-Silva, S. S. Al-Bermani, H. K. D. H. Bhadeshia and B. P. Wynne, "The prediction of toughness and strength in high integrity forgings," in *19th International Forgemasters Meeting 2014*, 2014.

[13]     T. Baker, F. Kavishe and J. Wilson, "Effect of non-metallic inclusions on cleavage fractyre," *Materials Science and Technology,* vol. 2, pp. 576-582, 1986.

[14]     T. Jin, Z. Liu and Y. Cheng, "Effect of non metallic inclusions on hydrogen-induced cracking of API5L X100 steel," *International Journal of Hydrogen Energy,* vol. 35, no. 15, pp. 8014-8021, 2010.

[15]     G. J. Manzo and B. E. Gabrielsson, "The Fundamentals of High Quality Bottom-Poured Ingot Production and Their Implementation at Ellwood Uddeholm Steel Company," in *The Third CISEI Ingot Metallurgy Symposium*, Pittsburgh, Pennsylvania, 1990.

[16]     S.-H. Hsiang and H.-L. Ho, "Investigation of the influence of various process parameters on the radial forging processes by the finite element method (FEM)," *The International Journal of Advanced Manufacturing Technology,* vol. 23, no. 9, pp. 627-635, 2004.

[17]     Q. Ma, Z.-q. Lin and Z.-q. Yu, "Prediction of deformation behavior and microstructure evolution in heavy forging by FEM," *The International Journal of Advanced Manufacturing Technology,* vol. 40, no. 3, pp. 253-260, 2009.

[18]     "Thelibraryofmanufacturing.com," 2016. [Online]. Available: http://thelibraryofmanufacturing.com/forging.html. [Accessed 24 August 2016].

[19]     R. Neves Penha, J. Vatavuk, A. A. Couto, S. A. de Lima Pereira, S. A. de Sousa and L. d. C.F. Canale, "Effect of chemical banding on the local hardenability in AISI 4340 steel bar," *Engineering Failure Analysis,* vol. 53, pp. 59-68, 2015.

[20]     K. Shah, B. Kiefer and J. Gavigan, "Finite Element Simulation of Internal Void Closure in Open-Die Press Forging," *Advanced Manufacturing Processes,* pp. 501-506, 2007.

[21]     "Scotforge.com," [Online]. Available: http://www.scotforge.com/Why-
         Forging/Forging-101. [Accessed 26 August 2016].

[22]     N. A. Ali, "Thermomechanical processing of 34CrNiMo6 steel for Large Scale
         Forging (Doctoral Dissertation)," Sheffield, 2013.

[23]     C. W. Li, L. Z. Han, X. M. Luo, Q. D. Liu and J. F. Gu, "Effect of tempering
         temperature on the microstructure and mechanical properties of a reactor pressure
         vessel steel," *Journal of Nuclear Materials,* vol. 477, pp. 246-256, 2016.

[24]     G. E. Totten, Ed., Steel Heat Treatment Handbook,, CRC Taylor & Francis Group,
         2007.

[25]     G. Krauss, Steel: processing, structure and performance, ASM International, 2005.

[26]     N. Kozlov and O. Keßler, "Influencing on liquid quenching by surface
         structuring," *International Journal of Thermal Sciences,* vol. 101, pp. 133-142,
         2016.

[27]     G. Ramesh and K. N. Prabhu, "Wetting and Cooling Performance of Vegetable
         Oils during Quench Hardening," *Heat Transfer-Asian Research,* vol. 45, no. 4, pp.
         342-357, 2016.

[28]     H. Hasan, M. Peet, . J. Jalil and H. Bhadeshia, "Heat transfer coefficients during
         quenching of steels," *Heat and Mass Transfer,* vol. 47, no. 3, pp. 315-321, 2011.

[29]     B. Hernandez-Morales, H. Vergara-Hernandez, G. Solorio-Diaz and G. Totten,
         "Experimental and Computational Study of Heat Transfer During Quenching of
         Metallic Probes," in *Evaporation, Condensation and Heat transfer*, Intechopen,
         2011.

[30]     S. S. Sahay, G. Mohapatra and G. Totten, "Overview of Pearlitic Rail Steel:
         Accelerated Cooling, Quenching, Microstructure, and Mechanical Properties,"
         *Journal of ASTM International,* 2009.

[31]     K. N. Prabhu and G. Ramesh, "Wetting kinetics, kinematics and heat transfer
         characteristics of pongamia pinnata vegetable oil for industrial heat treatment,"
         *Applied Thermal Engineering,* vol. 65, no. 1-2, pp. 433-446, 2014.

[32]     R. Ikkene, . Z. Koudil and M. Mouzali, "Cooling Characteristic of Polymeric
         Quenchant: Calculation of HTC and Prediction of Microstructure and Hardness,"

*Journal of Materials Engineering and Performance,* vol. 23, no. 11, pp. 3819-3830, 2014.

[33]  E. C. d. Souza, M. R. Fernandes, S. C. Augustinho, L. d. C. F. Canale and G. E. Totten, "Comparison of Structure and Quenching Performance of Vegetable Oils," *Journal of ASTM International,* vol. 6, no. 9, 2009.

[34]  K. N. Prabhu and P. Fernandes, "omparative study of heat transfer and wetting behaviour of conventional and bioquenchants for industrial heat treatment," *International Journal of Heat and Mass Transfer,* vol. 51, no. 3-4, pp. 526-538, 2008.

[35]  S. King, A. Fletcher and F. Allen, "On the Quenching Characteristics of Polyalkylene Glycol Solutions in Water," *Materials Science and Engineering,* no. 95, pp. 247-257, 1987.

[36]  N. I. Kobasko, E. Carvalho de Souza, L. d. C. F. Canale and G. E. Totten, "Vegetable Oil Quenchants: Calculation and Comparison of," *The Cooling Properties of a Series of Vegetable Oils,* vol. 56, no. 2, pp. 131-142, 2010.

[37]  J. Župan, T. .. Filetin and D. Landek, "The effect of TiO2 nanoparticles on fluid quenching characteristics," *International Heat Treatment and Surface Engineering,* vol. 6, no. 2, pp. 56-60, 2012.

[38]  G. Ramesh and K. Prabhu, "Review of thermo-physical properties, wetting and heat transfer characteristics of nanofluids and their applicability in industrial quench heat treatment," *Nanoscale Research Letter. A SprinerOpen Journal,* 2011.

[39]  H. Bhadeshia and R. Honeycombe, Steels, Microstructure and Properties, Elsevier Ltd, 2006.

[40]  P. Hughes and W. Flores, "The Effects of Large Scale Forgings and Heat Treatment on the Mechanical Performance of Mooring Connectors," in *2010 Offshore Technology Conference*, Houston, Texas, USA 3-6 May 2010., 2010.

[41]  M. Fontecchio, M. Maniruzzaman and R. D. Sisson, Jr., "The Effect of Bath Temperature and Agitation Rate on the Quench Severity of 6061 Aluminum in Distilled Water," in *Surface Engineering Coatings and Heat Treatments 2002: Proceedings of the 1st ASM International Surface Engineering and the 13th IFHTSE Congress (ASM International)*, 2003.

[42]     R. Ikkene, Z. Koudil and M. Mouzali, "Measurement of the Cooling Power of Polyethylene Glycol Aqueous Solutions Used as Quenching Media," *Journal of ASTM International,* vol. 7, no. 2, 2010.

[43]     N. Chen, B. Liao, J. Pan, Q. Li and C. Gao, "Improvement of the flow rate distribution in quench tank by measurement and computer simulation," *Materials Letters,* vol. 60, no. 13-14, pp. 1659-1664, 2006.

[44]     M. Tajima, T. Maki and K. Katayama, "Study of Heat Transfer Phenomena in Quenching of Steel (Effect of latent heat of phase transformation)," *Bulletin of JSME ,* vol. 28, no. 242, 1985.

[45]     P. Fernandes and K. N. Prabhu, "Effect of section size and agitation on heat transfer during quenching of AISI 1040 steel," *Journal of Materials Processing Technology,* vol. 183, no. 1, pp. 1-5, 2007.

[46]     K. N. Prabhu and G. Ramesh, "Effect of thermal conductivity and viscosity on cooling performance of liquid quench media," *International Heat Treatment and Surface Engineering,* vol. 8, no. 1, pp. 24-28, 2014.

[47]     A. Abdollah-zadeh and A. Salemi, "The effect of tempering temperature on the mechanical properties and fracture morphology of a NiCrMoV steel," *Materials Characterization,* vol. 59, no. 4, pp. 484-487, 2008.

[48]     S. K. Mandal, Steel Metallurgy: Properties, Specification and Applications, McGraw-Hill, 2015.

[49]     H. Arabi, S. Mirdamadi and A. Abdolmaleki, "Temper Embrittlement Sensitivities of 3Cr–1Mo and 2.25Cr–1Mo Low Alloy Steels," *ISIJ International,* vol. 47, no. 9, pp. 1363-1367, 2007.

[50]     ASM Handbook, Volume 4. Heat Treating, ASM International, 1995.

[51]     L. C. Canale, X. Yao, J. Gu and G. E. Totten, "A historical overview of steel tempering parameters," *International Journal of Microstructure and Materials Properties,* vol. 3, 2008.

[52]     N. Bogh, "Quench Tank Agitation Design Using Flow Modeling," in *Proceeding of International Heat Treating Conference*, Schaumburg, Illinois, 1994.

[53]     C. G. Andres, F. Caballero, C. Capdevila and L. Alavarez, "Application of dilatometric analysis to the study of solid–solid phase transformations in steels," *Materials Characterization,* vol. 48, pp. 101-111, 2002.

[54]     J. Pacyna, "Interpretations of Cooling Dilatograns In The Range of The Bainitic and Martensticis Transformations," *Archives of Metallurgy And Materials,* vol. 59, no. 4, 2014.

[55]     B. Marini, X. Averty, P. Wident, P. Forget and F. Barcelo, "Effect of the bainitic and martensitic microstructures on the ardening and embrittlement under neutron irradiation of a reactor pressure vessel steel," *Journal of Nuclear Materials,* vol. 465, pp. 20-27, 2015.

[56]     V. D. Eisenhüttenleute, Ed., Steel - A Handbook for Materials Research and Engineering: Volume 1: Fundamentals (v. 1), vol. 1.

[57]     H. Bhadeshia, Bainite in Steels, 2nd ed., IOM Communications Ltd, 2001.

[58]     H. Bhadeshia, Effect of Stress and Strain on Formation of Bainite in Steels, H. J. McQueen,, E. V. Konpleva and N. D. Ryan, Eds., Canadian Institute of Mining, Minerals and Petroleum, Montreal, Canada, 1996.

[59]     S. Nambu, N. Shibuta, M. Ojima, J. Inoue, T. Koseki and H. Bhadeshia, "In situ observations and crystallographic analysis of martensitic transformation in steel," *Acta Materialia,* vol. 61, no. 13, pp. 4831-4839, 2013.

[60]     G. Thomas and G. Kusinski, "Lath (Packet) Martensite Revisited," in *Steel Heat Treating in the New Millenium: An Internationals Symposium in Honor of Professor George Krauss.*, 2000.

[61]     L. Fielding, "The Bainite Controversy," *Material Science and Technology,* vol. 29, no. 4, pp. 383-399, 2013.

[62]     H. Bhadeshia and D. Edmonds, "The Mechanism of Bainite Formation in Steels," *Acta Metallurgica,* vol. 28, pp. 1265-1273, 1980.

[63]     B. P. J. Sandvik, "The bainite reaction in Fe-Si-C alloys," *Metallurgical and Materials Transactions A,* vol. 13A, p. 777–787, 1982.

[64]     R. Hehemann, Phase Transformations, Metal Park, Ohio: ASM, 1970.

[65]     K. Sugimoto , N. Usui, M. Kobayashi and S. Hashimo, "Effects of volume fraction and stability of retained austenite on ductility of TRIP-aided dual phase steels," *ISIJ International,* vol. 32, p. 1311–1318, 1992.

[66]     W. Song, J. Appen, P. Choi, R. Dronskowski, D. Raabe and W. Bleck, "Atomic-scale investigation of ε and θ precipitates in bainite in 100Cr6 bearing steel by atom probe tomography and ab initio calculations," *Acta Materialia,* vol. 61, no. 20, pp. 7582-7590, 2013.

[67]     B. Bramfitt and J. Speer, "A Perspective on the Morphology of Bainite," *METALLURGICAL TRANSACTIONS A,* vol. 21A, 1990.

[68]     F. Caballero, H. Roelofs, S. Hasler, C. Capdevila, J. Chao and J. Cornide, "Influence of bainite morphology on impact toughness of continuously cooled cementite free bainitics steels," *Materials Science and Technology,* 2011.

[69]     A. Barbacki, "The role of bainite in shaping mechanical properties of steels," *Journal of Materials Processing Technology,* vol. 53, pp. 57-63, 1995.

[70]     X. Zhang and J. Knott, "Cleavage fracture in bainitic and martensitic microstructures," *Acta Materialia,* vol. 47, no. 12, pp. 3483-3495, 1999.

[71]     A. Di Schino and C. Guarnaschelli, "Effect of microstructure on cleavage resistance of high-strength quenched and tempered steels," *Materials Letters,* pp. 1968-1972, 2009.

[72]     B. P. Wynne, E. I. Saldana-Garza, B. P. Wynne, R. Cerda-Rojas and R. D. Mercado-Solis, "Effect of Different Quench Media on the Microstructure and Mechanical Properties of Large-scale Low Alloy Steel Forgings," in *16th International Conference Metal Forming 2016*, Krakow, Poland, 2016.

[73]     "voestalpine Steel Division," 2016. [Online]. Available: voestalpine Steel Division. [Accessed 22 September 2016].

[74]     W. D. Callister Jr. and D. G. Rethwisch, Fundamentals of Materials Science and Engineering. An Integrated Approach, John Wiley & Sons, Inc., 2008.

[75]     J. Billingham, J. Sharp, J. Spurrier and P. Kilgallon, "Review of the performance of high strength steels used offshore," Health and Safety Executive (HSE)., 2003.

[76]     ASM Handbook, Mechanical Testing and Evaluation. Volume 8, ASM International, 2000.

[77] N. Abd-Allah, M. El-Fadaly, M. Megahed and A. Eleiche, "Fracture Toughness Properties of High-Strength Martensitic Steel within a Wide Hardness Range," *Journal of Materials Engineering and Performance,* vol. 10(5), pp. 576-585, 2001.

[78] A. Rossoll, C. Berdin and C. Prioul, "Determination of the Fracture Toughness of a Low Alloy Steel by the Instrumented Charpy Impact Test," *International Journal of Fracture,* vol. 115, no. 3, pp. 205-226, 2002.

[79] R. O. Ritchie, B. Francis and W. L. Server, "Evaluation of Toughness in AISI 4340 Alloy Steel Austenitized at Low and High Temperatures," *Metallurgical Transactions A,* vol. 7A, 1976.

[80] "ASTM A370-07. Standard Test Methods and Definitions for Mechanical Testing of Steel Products," ASTM International, 2007.

[81] T. Anderson, Third Edition, FRACTURE MECHANICS, Fundamental and Applications, CRC Press, 2005.

[82] P. Zelenak, "CTOD Size Matters," 28 October 2011. [Online]. Available: https://ewi.org/ctod-size-matters/. [Accessed 2 10 2016].

[83] J. H. Chen, G. Z. Wang, Q. Wang and Y. G. Liu, "Effect of sizes of ferrite grains and carbide particles on toughness of notched and precracked specimens of low-alloy steels," *International Journal of Fracture,* pp. 223-241, 2004.

[84] *BS7448-1, Fracture Mechanics Toughness Tests. Method for Determination of KIC, Critical CTOD and Critical J Values of Metallic Materials,* London, UK: British Standards, 1991.

[85] Y. Kayamori, T. Inoue and T. Tagawa, "A Comparison Between BS7448-CTOD and ASTM E1290-CTOD in Linepipes," in *8th International Conference on Ocean, Offshore and Arctic Engineering. OMAE 2009*, May 31 - June 5, 2009 Honolulu, Hawaii, USA, 2009.

[86] J. Gan, Q. Yu, W. Wu and J. Le, "Fracture Toughness Evaluation For Welded Joints Of High Strength Steel Through CTOD Test," in *29th International Conference on Ocean, Offshore and Arctic Engineering OMAE 2010*, June 6-11, 2010, Shanghai, China, 2010.

[87]     A. Pineau and B. Tanguy, "Advances in cleavage fracture modelling in steels: Micromechanical, numerical and multiscale aspects," *Comptes Rendus Physique,* vol. 11, no. 3-4, pp. 316-325, 2010.

[88]     ASM Handbook, Volume 19, Fatigue and Fracture, ASM International, 1996.

[89]     J. D. Verhoeven, "A review of microsegregation induced banding phenomena in steels," *Journal of Materials Engineering and Performance,* vol. 9, no. 3, pp. 286-296, 2000.

[90]     E. J. PICKERING and H. BHADESHIA, "Macrosegregation and Microstructural Evolution in a Pressure-Vessel Steel," *METALLURGICAL AND MATERIALS TRANSACTIONS A,* vol. 45A, 2014.

[91]     S. Mahalingam and P. E. J. Flewitt, "The Influence of Grain Size on Brittle Crack Propagation," *Journal of Physics: Conference Series,* vol. 371, 2012.

[92]     M. Zikry and T. Hatem, "Modeling of Lath Martensitic Microstructures and Failure Evolution in Steel Alloys," *Journal of Engineering Materials and Technology,* vol. 131, no. 4, 2009.

[93]     C. Wang, M. Wang, J. Shi, W. Hui and H. Dong, "Effect of microstructural refinement on the toughness of low carbon martensitic steel," *Scripta Materialia,* vol. 58, pp. 492-495, 2008.

[94]     N. J. Kim and A. H. Nakagawa, "Effective grain size of dual-phase steel," *Materials Science and Engineering,* vol. 83, no. 1, pp. 145-149, 1986.

[95]     K.-H. Lee, S.-g. Park, M.-C. Kim, B.-S. Lee and D.-M. Wee, "Characterization of transition behavior in SA508 Gr.4N Ni–Cr–Mo low alloy steels with microstructural alteration by Ni and Cr contents," *Materials Science and Engineering A,* vol. 529, pp. 156-163, 2011.

[96]     J. Janovec, A. Výrostková and A. Holý, "The Influence of Tempering Conditions on Microstructure and Carbide Formation in 0.3C–1.1Mn–0.3Mo–0.2Cr Steel," *Canadian Metallurgical Quarterly,* vol. 33, no. 2, pp. 227-232, 1994.

[97]     P. Bowen, S. G. Druce and J. F. Knott, "Effects of Microstructure On Cleavage Fracture In Pressure Vessel Steel," *Acta Metallurgica,* vol. 34, no. 6, pp. 1121-1131, 1986.

[98]     L. Hao, M. Sun and D. Li, "The influence of composition segregation to the microstructrue and mechanical properties of SA508-3 steel," *Advanced Materials Research,* Vols. 146-147, p. 1017121, 2011.

[99]     "Omega Data Loggers," Omega, [Online]. Available: http://www.omega.com/. [Accessed 19 October 2016].

[100]    "Type K Thermocouple Calibration," Mosaic-Industries, [Online]. Available: http://www.mosaic-industries.com/.

[101]    "Standard Test Methods for Tension Testing of Metallic Material. ASTM E8/E8M − 16a," ASTM International.

[102]    "Standard Test Methods for Notched Bar Impact Testing of Metallic Materials. E23 − 16b," ASTM International.

[103]    G. F. Vander Voort, "Revealing Prior-Austenite Grain Boundaries in Heat Treated Steels (Article)," [Online]. Available: http://www.georgevandervoort.com/.

[104]    "Standard Test Methods for Determining Average Grain Size. ASTM E112 - 13," ASTM International.

[105]    S.-G. Park, K.-H. Lee, K.-D. Min, M.-C. Kim and B.-S. Lee, "Characterization of Phase Fractions and Misorientations on Tempered Bainitic/Martensitic Ni-Cr-Mo Low Alloy RPV Steel with Various Ni Content," *Met. Mater. Int,* vol. 19, no. 1, pp. 49-54, 2013.

[106]    G. Ramesh and N. Prabhu, "Effect of Polymer Concentration on Wetting and Cooling Performance During Immersion," *Metallurgical and Materials Transactions B,* vol. 47, no. 2, pp. 859-881, 2016.

[107]    "Standard Test Method for Determination of Cooling Characteristics of Quench Oils by Cooling Curve Analysis, ASTM D6200 - 01(2012)," ASTM International.

[108]    "Standard Test Method for Determination of Cooling Characteristics of Aqueous Polymer Quenchants by Cooling Curve Analysis with Agitation (Tensi Method), ASTM D6482 - 06(2016)," ASTM International.

[109]    "Industrial quenching oils -- Determination of cooling characteristics -- Nickel-alloy probe test method, ISO 9950: 1995".

[110]    M. Atkins, Atlas of continuous cooling transformation diagram for engineering steels, England: American Society for Metals, 1980.

[111]   K. N. Prabhu and P. Fernandes, "Heat Transfer During Quenching and Assessment of Quench Severity," *Journal of ASTM International Selected Technical Papers STP1523 Quenching and Cooling, Residual Stress and Distortion Control,* vol. 6, no. 1, pp. 1-17, 2009.

[112]   S. Ma, Characterization of the performance of mineral oil based quenchants using CHTE Quench Probe System,MSc Dissertation.

[113]   T. Teljeko and A. Buczek, "Investigation of heat transfer coefficient during quenching in various," *International Journal of Heat and Fluid Flow,* vol. 44, pp. 358-364, 2013.

[114]   M. Reich and O. Kessler, "Quenching Simulation of Aluminum Alloys Including Mechanical Properties of the Undercooled States," *Materials Performance and Characterization,* vol. 1, no. 1, pp. 1-18, 2012.

[115]   H. Vergara-Hernández and B. Hernández-Morales, "A novel probe design to study wetting front kinematics during forced convective quenching," *Experimental Thermal and Fluid Science,* vol. 33, no. 5, pp. 797-807, 2009.

[116]   C. Gupta, G. Dey, J. Chakravartty, D. Srivastav and S. Banerjee, "A study of bainite transformation in a new CrMoV steel under continuous cooling conditions," *Scripta Materialia,* vol. 53, no. 5, pp. 559-564, 2005.

[117]   S. Zhao, D. Wei, R. Li and L. Zhang, "Effect of Cooling Rate on Phase Transformation and Microstructure of Nb-Ti Microalloyed Steel," *Materials Transactions,* vol. 55, no. 8, pp. 1274-1279, 2014.

[118]   R. Cerda, M. de la Garza, M. P. Guerrero-Mata and R. Colas, "Study of Heat Treated Large Hot Rolled Steel Rings," in *Proceedings from the 6th International Quencing and Control of Distortion Conference*, September 9–13, 2012, Chicago, Illinois, USA, 2012.

[119]   F. Oliveira, M. Andrade and A. Cota*, "Kinetics of austenite formation during continuous heating in a low carbon steel," *Materials Characterization,* vol. 58, no. 3, pp. 256-261, 2007.

[120]   B. J. Park, J. M. Choi and K. J. Lee, "Analysis of phase transformations during continuous cooling by the first derivative of dilatation in low carbon steels," *Materials Characterization,* vol. 64, pp. 8-14, 2012.

[121]    S. Lee, H. Na and B. Kim, "Effect of Niobium on the Ferrite Continuous-Cooling-Transformation (CCT) Curve of Ultrahigh-Thickness Cr-Mo Steel," *Metallurgical and Materials Transactions A,* vol. 44, no. 6, pp. 2523-2332, 2013.

[122]    S. Shanmugam, R. Misra, T. Mannering, D. Panda and S. Jansto, "Impact toughness and microstructure relationship in niobium-and vanadium-microalloyed steels processed with varied cooling rates to similar yield strength," *Materials Science and Engineering: A,* vol. 437, no. 2, pp. 436-445, 2006.

[123]    L. Habraken, "Proceedings of the Fourth International Conference on Electron Microscopy,," in *Springer Verlag*, Berlin, Germany, 1958.

[124]    Z. Qiao, Y. Liu, L. Yu and Z. Gao, "Formation mechanism of granular bainite in a 30CrNi3MoV steel," *Journal of Alloys and Compounds,* vol. 2009, no. 475, pp. 560-564, 2009.

[125]    F. G. Caballero, M. J. Santofimia, C. Garcia-Mateo and C. Garcia de Andres, "Time-Temperature-Transformation Diagram within the Bainitic Temperature Range in a Medium Carbon Steel," *Materials Transactions,* vol. 45, no. 12, pp. 3272-3281, 2004.

[126]    H. Bhadeshia, "Martensite and Bainite in Steels : Transformation Mechanism & Mechanical Properties," *J. Phys. IV France, IVth European Symposium on Martensitic Transformations,* vol. 07, no. C5, pp. 367-376, 1997.

[127]    K. Radwański, "Structural characterization of low-carbon multiphase steels merging advanced research methods with light optical microscopy," *Archives of Civil and Mechanical Engineering,* vol. 16, no. 3, pp. 282-293, 2016.

[128]    K.-H. Lee, S.-G. Park, M.-C. Kim and B.-S. Lee, "Cleavage fracture toughness of tempered martensitic Ni–Cr–Mo low alloy steel with different martensite fraction," *Materials Science and Engineering: A,* vol. 534, pp. 75-82, February 2012.

[129]    S. van Bohemen and J. Sietsma, "The kinetics of bainite and martensite formation in steels during cooling," *Materials Science and Engineering: A,* vol. 527, no. 24-25, pp. 6672-6676, 2010.

[130]    M. Gomez, L. Rancel, E. Escudero and S. F. Medina, "Phase Transformation under Continuous Cooling Conditions in Medium Carbon Microalloyed Steels," *Journal of Materials Science & Technology,* vol. 30, no. 5, pp. 511-516, 2014.

[131]   M. Nikravesh, M. Naderi and G. Akbari, "Influence of hot plastic deformation and cooling rate on martensite and bainite start temperatures in 22MnB5 steel," *Materials Science and Engineering: A,* vol. 540, no. 1, pp. 24-29, 2012.

[132]   Y. Tomita and K. Okabayashi, "Mechanical properties of 0.40 pct C-Ni-Cr-Mo high strength steel having a mixed structure of martensite and bainite," *Metallurgical Transactions A,* vol. 16, no. 1, pp. 73-82, 1985.

[133]   Y. Tomita and K. Okabayashi, "Heat treatment for improvement in lower temperature mechanical properties of 0.40 pct C-Cr-Mo ultrahigh strength steel," *Metallurgical Transactions A,* vol. 14, no. 11, pp. 2387-2393, 1983.

[134]   Y. Tomita and K. Okabayashi, "Improvement in lower temperature mechanical properties of 0.40 pct C-Ni-Cr-Mo ultrahigh strength steel with the second phase lower bainite," *Metallurgical Transactions A,* vol. 14, no. 2, pp. 485-492, 1983.

[135]   C. Liu and P. Kao, "Tensile properties of a 0.34C-3Ni-Cr-Mo-V steel with mixed lower-bainite-martensite structures," *Materials Science and Engineering,* pp. 171-177, 1992.

[136]   C. Young and H. Bhadeshia, "Strength of Illixtures of bainite and Illartensite," *Materials Science and Technology,* pp. 209-214, 1994.

[137]   H. Hoseiny, U. Klement, P. Sotskovszki and J. Andersson, "Comparison of the microstructures in continuous-cooled and quench-tempered pre-hardened mould steels," *Materials and Design,* vol. 32, no. 1, pp. 21-28, 2011.

[138]   H. Ma, Z. Liu, C. Du, H. Wang, X. Li, D. Zhang and Z. Cui, "Stress corrosion cracking of E690 steel as a welded joint in a simulated marine atmosphere containing sulphur dioxide," *Corrosion Science,* vol. 100, pp. 627-641, 2015.

[139]   H. Hoseiny, F. G. Caballero, R. M'saoubi and B. Högman, "The Influence of Heat Treatment on the Microstructure and Machinability of a Prehardened Mold Steel," *Metallurgical and Materials Transactions A,* vol. 46A, 2015.

[140]   W. Soboyejo, J. Zhou, J. Crompton and et al., "An investigation of the fracture behavior of coarse grained heat-affected zones in A707 steel welds," *Metallurgical and Materials Transactions A,* vol. 32, no. 3, pp. 533-545, 2001.

[141]   P. Haušild, I. Nedbal, C. Berdin and C. Prioul, "he influence of ductile tearing on fracture energy in the ductile-to-brittle transition temperature range," *Materials Science and Engineering: A,* vol. 335, no. 1-2, pp. 164-174, 2002.

[142]   D. Broek, "The Role of Inclusions in Ductile Fracture and Fracture Toughness," in *Symposium on Fracture and Fatigue at the School of Engineering and Applied Science George Washington University*, Washington, D.C., May 3-5, 1972, 1972.

[143]   A. Venugopal Reddy, Investigation of Aeronautical and Engineering Component Failures, CRC Press, Technology & Engineering. , 2004.

[144]   R. Ritchie, J. Knott and J. Rice, "On the relationship between critical tensile stress and fracture toughness in mild steel," *J. Mech. Phys. Solids,* vol. 21, pp. 395-410, 1973.

[145]   D. Johnson and W. Becker, "Toughness of Tempered Upper and Lower Bainitic Microstructures in a 4150 Steel," *Journal of Materials Engineering and Performance,* vol. 2, no. 2, 1993.

[146]   P. Bowen, M. Ellis, M. Strangwood and J. Knott, "Micromechanisms of Brittle Fracture in 2 1/4Cr-1Mo Weld Metal," in *Fracture Control of Engineering Structures- ECF 6.*

[147]   T. Lin and R. O. Ritchie, "On the Effect of Sampling Volume on the Microscopic Cleavage Fracture Stress," *Engineering Fracture Mechanics,* vol. 29, no. 6, pp. 697-703, 1988.

[148]   S. Kim, S. Lee and B. S. Lee, "Effects of grain size on fracture toughness in trasition temperature region of Mn-Mo-Ni low alloy steels," *Materials Science and Engineering A,* vol. 359, no. 1-2, pp. 198-209, 2003.

[149]   H. Bhadeshia and S. Khan, "Kinetics of Martensitic Transformation in Partially Bainitic 300M Steel," *Materials Science and Engineering,* no. A129, pp. 257-272, 1990.

[150]   J. Albrecht, J.-E. Bertilsson and B. Scarlin, "The Fracture Toughness of Actual and Simulated Large Rotor Forgings Made from 3.5Ni Steel," in *Steel Forgings, ASTM STP 903, E. G. Nisbett and A. S. Melilli, Eds., American Society for Testing and Materials*, Philadelphia, 1986.

[151]   T. Dorin, N. Stanford, A. Taylor and H. Peter, "Effect of Cooling Rate on Phase Transformations in a High-Strength Low-Alloy Steel Studied from the Liquid Phase," *Metallurgical and Materials Transactions A,* vol. 46, no. 12, pp. 5561-5571, 2015.

[152]    L. Habraken and M. Economopoulos, "Bainitic microstructures in," *In: Transformation and hardenability in steels. Ann Arbor, MI: Climax Molybdenum Co,* pp. 69-107, 1967.

[153]    F. Samuel, D. Daniel and O. Sudre, "Further investigations on the microstructure and mechanical behaviour of granular bainite in a high strength, low alloy steel: Comparison of ferrite-pearlite and ferrite-martensite microstructures," *Materials Science and Engineering,* vol. 92, pp. 43-62, 1987.

[154]    Y. Ohmori, H. Ohtani and T. Kunitake, "Tempering of the Bainite/Martensite Duplex Structure in a Low-Carbon Low Alloy Steel," *Metal Science,* vol. 8, no. 1, pp. 357-366, 1974.

[155]    M. Balart and J. Knott, "Low temperature fracture properties of DIN 22NiMoCr37 steel in fine-grained bainite and coarse-grained tempered embrittled martensite microstructures," *Engineering Fracture Mechanics,* vol. 75, no. 8, pp. 2480-2513, 2008.

[156]    D. Chakrabarti, M. Strangwood and D. Claire, "Effect of Bimodal Grain Size Distribution on Scatter in Toughness," *Metallurgical and Materials Transactions A,* vol. 40, no. 4, pp. 780-795, 2009.

[157]    M. Kang, H. Kim, S. Lee and S. Y. Shin*, "Correlation of Microstructure with Tensile and Crack Tip Opening Displacement Properties at Low Temperatures in API Linepipe Steels," *Metals and Materials International,* vol. 21, no. 4, pp. 628-638, 2015.

[158]    H. Qiu, T. Hanamura and S. Torizuka, "Influence of Grain Size on the Ductile Fracture Toughness of Ferritic Steel," *ISIJ International,* vol. 54, no. 8, pp. 1958-1964, 2014.

[159]    M. T. Welsch, D. Bruch and E. Østby, "Forgings for Low Temperature Applications – Influences of the Alloying Concept and Advanced Forging Procedures on Impact Strength and Fracture Toughness," Maui, Hawaii, USA, 2011.

[160]    J. Sinczak, J. Majta, M. Glowacki and M. Pietrzyk, "Prediction of mechanical properties of heavy forgings," *Journal of Materials Processing Technology,* Vols. 80-81, pp. 166-173, 1998.

[161]  B. Coterell, "The past, present, and future of fracture mechanics," *Engineering Fracture Mechanics,* vol. 59, no. 5, pp. 533-553, 2002.

[162]  D. Spriestersbach, P. Grad and E. Kerscher , "Influence of different non-metallic inclusion types on the crack initiation in high-strength steels in the VHCF regime," *International Journal of Fatigue,* vol. 64, pp. 114-120, 2014.

[163]  Y.-K. Lee, M. Kang and M. Jung, "Finite-element simulation of quenching incorporating improved transformation kinetics in a plain medium-carbon steel," *Acta Materiala,* vol. 60, no. 2, pp. 525-536, 2012.

[164]  T. P. Kumar, "Coupled Analysis of Surface Heat Flux, Microstructure Evolution, and Hardness during Immersion Quenching of a Medium Carbon Steel in Plant Conditions.," *Materials Performance and Characterization,* vol. 1, no. 1, pp. 1-22, 2012.

[165]  E. Carvalho de Souza, R. M. Fernandes, S. C. Augustinho, L. de Campos Franceschini Canale and G. E. Totten, "Comparison of Structure and Quenching Performance of Vegetable Oils," *Journal of ASTM International,* vol. 6, no. 9, 2009.

[166]  R. Klueh, N. Evans, P. Maziasz and V. Sikka, "Creep-rupture behavior of 3Cr–3W–V bainitic steels," *International Journal of Pressure Vessels and Piping,* vol. 84, no. 1-2, pp. 29-36, 2007.

[167]  H. Zhang, X. Cheng, B. Bai and H. Fang, "The tempering behavior of granular structure in a Mn-series low carbon steel," *Materials Science and Engineering A,* vol. 528, no. 3, pp. 920-924, 2011.

[168]  E. Hall, "The deformation and ageing of mild steel: III discussion of results," *Proc Phys Soc London.,* vol. B64, pp. 747-53, 1951.

[169]  N. Petch, "The cleavage of polycrystals," *J Iron Steel Inst.,* vol. 174, pp. 25-8, 1953.

[170]  K. Andrews, "Empirical Formulae for the Calculation of Some Transformation Temperatures," *JISI,* vol. 203, pp. 721-727, 1965.

[171]  E. Mazancova and K. Mazanec, "Physical metallurgy characteristics of the M/A constituent formation in granular bainite," *Journal of Materials Processing Technology,* pp. 287-292, 1997.